

Magazine of Civil Engineering

98(6), 2020

ISSN
2712-8172





ПОЛИТЕХ
Санкт-Петербургский
политехнический университет
Петра Великого

Инженерно-строительный институт
Центр дополнительных профессиональных программ
195251, г. Санкт-Петербург, Политехническая ул., 29,
тел/факс: 552-94-60, www.stroikursi.spbstu.ru,
stroikursi@mail.ru

**Приглашает специалистов организаций, вступающих в СРО,
на курсы повышения квалификации (72 часа)**

Код	Наименование программы	Виды работ*
Курсы по строительству		
БС-01-04	«Безопасность и качество выполнения общестроительных работ»	п.1,2, 3, 5, 6, 7, 9, 10, 11, 12, 13, 14
БС-01	«Безопасность и качество выполнения геодезических, подготовительных и земляных работ, устройства оснований и фундаментов»	1,2,3,5
БС-02	«Безопасность и качество возведения бетонных и железобетонных конструкций»	6,7
БС-03	«Безопасность и качество возведения металлических, каменных и деревянных конструкций»	9,10,11
БС-04	«Безопасность и качество выполнения фасадных работ, устройства кровель, защиты строительных конструкций, трубопроводов и оборудования»	12,13,14
БС-05	«Безопасность и качество устройства инженерных сетей и систем»	15,16,17,18,19
БС-06	«Безопасность и качество устройства электрических сетей и линий связи»	20,21
БС-08	«Безопасность и качество выполнения монтажных и пусконаладочных работ»	23,24
БС-12	«Безопасность и качество устройства мостов, эстакад и путепроводов»	29
БС-13	«Безопасность и качество выполнения гидротехнических, водолазных работ»	30
БС-14	«Безопасность и качество устройства промышленных печей и дымовых труб»	31
БС-15	«Осуществление строительного контроля»	32
БС-16	«Организация строительства, реконструкции и капитального ремонта. Выполнение функций технического заказчика и генерального подрядчика»	33
Курсы по проектированию		
БП-01	«Разработка схемы планировочной организации земельного участка, архитектурных решений, мероприятий по обеспечению доступа маломобильных групп населения»	1,2,11
БП-02	«Разработка конструктивных и объемно-планировочных решений зданий и сооружений»	3
БП-03	«Проектирование внутренних сетей инженерно-технического обеспечения»	4
БП-04	«Проектирование наружных сетей инженерно-технического обеспечения»	5
БП-05	«Разработка технологических решений при проектировании зданий и сооружений»	6
БП-06	«Разработка специальных разделов проектной документации»	7
БП-07	«Разработка проектов организации строительства»	8
БП-08	«Проектные решения по охране окружающей среды»	9
БП-09	«Проектные решения по обеспечению пожарной безопасности»	10
БП-10	«Обследование строительных конструкций и грунтов основания зданий и сооружений»	12
БП-11	«Организация проектных работ. Выполнение функций генерального проектировщика»	13
Э-01	«Проведение энергетических обследований с целью повышения энергетической эффективности и энергосбережения»	
Курсы по инженерным изысканиям		
И-01	«Инженерно-геодезические изыскания в строительстве»	1
И-02	«Инженерно-геологические изыскания в строительстве»	2,5
И-03	«Инженерно-гидрометеорологические изыскания в строительстве»	3
И-04	«Инженерно-экологические изыскания в строительстве»	4
И-05	«Организация работ по инженерным изысканиям»	7

*(согласно приказам Минрегионразвития РФ N 624 от 30 декабря 2009 г.)

**По окончании курса слушателю выдается удостоверение о краткосрочном повышении
квалификации установленного образца (72 ак. часа)**

Для регистрации на курс необходимо выслать заявку на участие, и копию диплома об образовании по телефону/факсу: 8(812) 552-94-60, 535-79-92, , e-mail: stroikursi@mail.ru.

Magazine of Civil Engineering

SCHOLAR JOURNAL

ISSN 2712-8172

Свидетельство о государственной регистрации:
Эл № ФС77-77906 от 19.02.2020,
выдано Роскомнадзором

Специализированный научный журнал. Выходит с
09.2008.

Включен в Перечень ВАК РФ

Индексируется в БД Scopus

Периодичность: 8 раз в год

Учредитель и издатель:

Санкт-Петербургский политехнический университет
Петра Великого

Адрес редакции:

195251, СПб, ул. Политехническая, д. 29

Главный редактор:

Екатерина Александровна Линник

Научный редактор:

Виталий Владимирович Сергеев

Заместитель главного научного редактора:

Галина Леонидовна Козинец

Редакционная коллегия:

PhD, проф. Т. Аввад;
д.т.н., проф. М.И. Бальзанников
д.т.н., проф. А.И. Белостоцкий;
к.т.н., проф. А.И. Боровков;
д.т.н., проф. А. Бородинец;
PhD, проф. М. Велькович;
PhD, проф. Р.Д. Гарг;
PhD, М.Р. Гарифуллин;
Dr.-Ing, проф. Т. Грис;
д.т.н., проф. Т.А. Дацюк;
д.т.н., проф. В.В. Елистратов;
Dr.-Ing., проф. Т. Кэрки;
д.т.н., проф. Д.В. Козлов;
д.т.н., доцент С.В. Корниенко;
д.т.н., проф. Ю.Г. Лазарев;
д.т.н., проф. М.М. Мухаммадиев;
Dr.-Ing. Habil., проф. Х. Пастернак;
Dr.-Ing., проф. Ф. Рёгинер;
д.т.н., проф. Т.З. Султанов;
д.т.н., проф. М.Г. Тягунов;
акад. РАН, д.т.н., проф. М.П. Федоров;
Dr.-Ing., проф. Д. Хеэц;
д.г.-м.н. А.Г. Шашкин;
д.т.н. В.Б. Штильман

Дата выхода: 26.10.2020

© ФГАОУ ВО СПбПУ, 2020

© Иллюстрация на обложке: Илья Смагин

Magazine of Civil Engineering

SCHOLAR JOURNAL

ISSN 2712-8172

Peer-reviewed scientific journal

Start date: 2008/09

8 issues per year

Publisher:

Peter the Great St. Petersburg Polytechnic University

Indexing:

Scopus, Russian Science Citation Index (WoS),
Compendex, EBSCO, Google Academia, Index
Copernicus, ProQuest, Ulrich's Serials Analysis System,
CNKI

Corresponding address:

29 Polytechnicheskaya st., Saint-Petersburg, 195251,
Russia

Editor-in-chief:

Ekaterina A. Linnik

Science editor:

Vitaly V. Sergeev

Deputy chief science editor:

Galina L. Kozinetc

Editorial board:

T. Awwad, PhD, professor
M.I. Balzannikov, D.Sc., professor
A.I. Belostotsky, D.Sc., professor
A.I. Borovkov, PhD, professor
A. Borodinets, Dr.Sc.Ing., professor
M. Veljkovic, PhD, professor
R.D. Garg, PhD, professor
M. Garifullin, PhD, postdoctorant
T. Gries, Dr.-Ing., professor
T.A. Datsyuk, D.Sc., professor
V.V. Elistratov, D.Sc., professor
T. Kärki, Dr.-Ing., professor
D.V. Kozlov, D.Sc., professor
S.V. Korniyenko, D.Sc., professor
Yu.G. Lazarev, D.Sc., professor
M.M. Muhammadiev, D.Sc., professor
H. Pasternak, Dr.-Ing.habil., professor
F. Rögener, Dr.-Ing., professor
T.Z. Sultanov, D.Sc., professor
M.G. Tyagunov, D.Sc., professor
M.P. Fedorov, D.Sc., professor
D. Heck, Dr.-Ing., professor
A.G. Shashkin, D.Sc.
V.B. Shtilman, D.Sc.

Date of issue: 26.10.2020

© Peter the Great St. Petersburg Polytechnic University.

All rights reserved.

© Coverpicture – Ilya Smagin

Contacts:

E-mail: mce@spbstu.ru

Web: <http://www.engstroy.spbstu.ru>

Contents

Sagdiev, Kh.S., Teshabayev, Z.R., Galiaskarov, V.A., Yuvmitov, A.S. Centrifugal modeling of underground polymer pipes under temperature effect	9801
Huynh, T.-P., Ho, N.-T., Bui, P.-T., Do, N.-D., Nguyen, T.-C. Mechanical-thermal characteristics of foamed ultra-lightweight composites	9802
Sychova, A.M., Zarin, S.V., Matskevich, A.V. Theory of determining the frequency of natural oscillations of span structures	9803
Ibragimov, R.A., Korolev, E.V., Deberdeev, T.R. Mechanical activation in the production of lime-sand mixtures	9804
Marshdi, Q.S.R., Al-Sallami, Z.H.A., Zaichenko, N.M. Effect of multicomponent modifier on the properties of cement pastes formulated from self-compacting concrete	9805
Shaikezhan, A, Anuarova, A.D., Antonovic, V. Cement slurry from electro-phosphoric slag	9806
Zhao, Q.Q., Zhang, H.T., Fediuk, R.S., Wang, J.W. Antiskid prediction model for cement pavements in seasonal frost regions	9807
Gerasimova, E., Galyamichev, A., Dogru, S. Stress-strain state of Insulated Glass Unit in structural glazing systems	9808
Derabla, R, Sajedi, F. Behavior of heat treated self-compacting mortar cured in seawater	9809
Al-Rousan, R. The shear behavior of CFRP Strengthened RC beams	9810
Sabri, M.M., Shashkin, K.G. The mechanical properties of the expandable polyurethane resin based on its volumetric expansion nature	9811
Yurchenko, V.V., Peleshko, I.D. Improved gradient projection method for parametric optimisation of bar structures	9812



Centrifugal modeling of underground polymer pipes under temperature effect

Kh.S. Sagdiev*, Z.R. Teshabayev, V.A. Galiaskarov, A.S. Yuvmitov

Institute Mechanics and Seismic Resistance of the Structures named M.T. Urazbaev Academy of science of the Republic of Uzbekistan, Tashkent, Uzbekistan

* E-mail: imssan@mail.ru

Keywords: centrifugal modeling, polymer pipes, temperature effect, pipe-soil interaction, structure model, scale factors, experiment technique, measuring complex, strain gauge sensor

Abstract. Experimental study of underground polymer pipes under temperature effect is developed in this paper by the method of centrifugal modeling to study the process of polymer pipes elongation depending on the depth of laying and physical and mechanical properties of soil. The method is based on the use of centrifugal installation with PC and software. The experiments were carried out in a centrifuge with an effective radius of centrifuge rotation at a working scale of modeling $n = 40$. Experimental studies were carried out at various laying depths of the underground polymer pipes. In the process of conducting experiments, the polymer pipe model was subjected to various temperature influences. The temperature effect on the polymer pipe model was created using an electric spiral. As a result, it is established that the process of polymer pipes elongation over time under soil pressure and temperature factor has a non-linear character; the value of the absolute strain depending on the laying depth and the temperature factor may differ by several times.

1. Introduction

In the life support system for the population, the pipes made from various materials and of various configurations are widely used as water pipelines, gas pipelines, oil pipelines, for transportation of toxic and explosive substances in various industries and manufactures.

Pipelines are widely used in the cities, between the cities and populated localities and in the recent decades have been widely used between the countries. Therefore, pipelines are often called "life lines" and this shows, that pipelines play an important role in human life. Due to the enormous length and wide geographical distribution, the pipelines are located at different laying depths in complex ground conditions and under water, in cross profile areas with tectonic faults and in zones of different seismic intensity; they are exposed to great exploitative and seismic hazard. Due to the fact that pipelines play a significant role in country's economy, much attention has been paid to their reliable operation, ensuring their seismic safety during the exploitation.

Pipes, as a conducting system, have a rather complex structure, consisting of the straight line and curved line areas, intersections nodes and fixing elements. Depending on the complexity of the pipeline system designs, considerable length and wide geographical location the pipelines are subject to various seismic hazards, such as destruction, soil liquefaction, wave propagation process, pipe-soil interaction, pipe displacement relative to soil, pipe separation from soil, etc.

To solve these problems, a regularity of strain was established. Many researchers from different countries have studied the issues of seismic effect on the pipelines stress state. Here we present some results of other researchers, close to the subject of the proposed study. As is known, earthquakes can pose a threat to the structure integrity of buried pipelines. As a result of constant soil strain around the pipeline in a quasistatic way, not necessarily associated with high seismic intensity, the earthquake aftermath can cause serious damage. Analysis of the effect of earthquakes showed, that the damage in linear steel pipelines was caused by permanent soil strain, such as fracture movements, landslides, lateral compression caused by soil



strain; only a few pipelines were damaged as a result of wave propagation [1, 2]. For example, such pipelines were damaged during earthquakes in San Fernando [3], in Kobe [4], in Kojaeli [5] and in Chi-Chi [6].

Studies of the seismic stress state of buried pipelines are based on certain assumptions that allow simulating consideration process with some simplifications, the process requires further refinement. In the study of the stress state of underground pipelines under seismic effect, the main point is to simulate the process of the pipe interaction with surrounding soil. A seismic analysis of soil interaction with a pipe of finite length based on the Winkler model has been carried out and the approach is focused on account for axial strains, since bending strains in a buried pipe due to wave propagation have usually a second-order effect [7]. To solve the problems of the joint seismic vibrations of the underground pipeline and elastic soil, it is assumed that a slippage occurs at the boundary and the shear stresses arising on it are proportional to the relative displacement of soil and pipeline particles or their relative velocities of motion [8]. On the basis of the Hamilton-Ostrogradsky variational principle a system of equations was obtained and the stress state of the pipeline was studied, taking into account the displacement relative to the soil medium under arbitrary direction of seismic effect [9]. The problem of dynamic stability of underground pipelines of finite length, located in water-saturated soils [10] has been solved, the effect of geometric and mechanical characteristics of a pipeline on dynamic stability of the "soil-pipe" system has been revealed. The dependence of interaction coefficient of a polymer pipe with soil was experimentally determined using data obtained at longitudinal vibrations of underground polymer pipelines under seismic loads [11].

In recent years the effect of wave propagation on the buried pipeline with a curved axis and their interaction with soil was studied in several publications. Numerical analysis of underground pipeline seismic behavior at right angle of bending showed an increase in strain in a curved section with increasing radius of curvature [12]. Using the elastic model, the quasi-static problems of pipes response at right angle of bending to Rayleigh waves were solved and the effect of some basic parameters, such as the wavelength and soil strain was determined [13].

In [14], mechanical reaction of continuous (welded) underground steel pipelines, crossing active seismic faults was considered. These pipelines are subject to strains due to axial, shear and bending loads, and create high stresses and strains in critical places that can lead to a pipe breakage. The studies in [15] were based on modeling the "soil-pipeline" system using nonlinear finite elements, taking into account inelastic behavior of surrounding soil, the soil-pipe interaction and contact, the development of the large inelastic strains in steel pipeline, the distortion of the pipeline cross-section and possible local strain and internal pressure. At various soil parameters, both for cohesive and non-cohesive soils, the effect of the diameter-thickness ratio of the pipeline and the stress-strain of the steel material were studied.

In addition to the above numerical studies one can cite separate experimental studies for studying the stress state of buried polyethylene pipelines [16, 17, 18]. An experimental study was conducted on a centrifuge based on the modeling the pipeline response to a seismic discontinuity. During the tests the effect of the fault type, fault angle of displacement on mechanical behavior of the pipeline was studied, as well as the effect of the pipeline laying depth and diameter, the moisture content in soil.

In [19] the issue of the interaction effect on the stress-strain state of underground structures in the form of a rigid body with a base soil was studied. Viscoelastic characteristics of the bodies interaction were determined by theoretical and experimental studies and the graphs of viscoelastic characteristics interaction were plotted.

The results of experimental studies of physico-mechanical properties of the centrifuged and vibrated samples were given in [20]. The properties of inhomogeneity of a fresh concrete mix were evaluated to determine the changes in water-cement ratio, residual water content and density along the thickness of the centrifuged sample, as well as the changes in strength properties of hardened concrete. As a result, a numerical experiment to study the carrying capacity of the centrifuged supports of the power lines was conducted, taking into account the obtained dependence of the change in concrete strength along the wall thickness of the product.

In [21], an issue of temperature wave propagation along the wall of the hollow cylinder with an abrupt change in temperature of internal medium arising from the motion cessation or circulation of a heated flow was considered. An algorithm for calculating the temperature field by a numerical method was shown using an explicit finite-difference scheme of enhanced accuracy under cylindrical symmetry conditions, under boundary conditions of the first kind. The results of calculation of the temperature wave penetration depth were given by the considered algorithm depending on time passed after thermal effect.

The results of numerical solutions of underground and aboveground structures spatial problem taking into account the work of the surrounding infinite massif in homogeneous and inhomogeneous areas were given by a combined method [22–24].

In [25] the definition of rational parameters of the developed compensating device of the pipeline in a triangular form was given using the computational-experimental research methods. The coefficient of the

compensating device form refinement was obtained by computational-experimental research methods, structurally performed using the curved pipe bends, to reduce longitudinal compressive force arising from temperature difference to the level of the overall stability of the pipeline in longitudinal direction.

An aspect of numerical simulation to assess the possibility of the centrifugal modeling of the solute substances in adsorptive, radionuclide and reactive solutions [26] was studied. As a result, it was shown that it is possible to conduct centrifugal experiments to evaluate physical processes or chemical reactions.

In the above scientific studies the actual problems of underground pipeline-soil interaction under temperature effects have not been experimentally studied. So, the study of underground pipeline-soil interaction using the method of the centrifugal modeling is of great scientific and practical interest.

2. Methods

2.1. The methods to conduct experimental studies

Conducting field experiments to study the stress-strain state of pipelines and determine the parameters of pipeline interaction with surrounding soil requires large capital expenditures and a long period of time. Besides, creating dynamic and static loads identical in each series of experiments is extremely difficult [27]. These difficulties in experimental studies can be overcome if to proceed to model experiments, in particular, to use the method of centrifugal modeling – one of the most progressive experimental modeling methods [28]. In the most complex cases, which are beyond the approximate mathematical modeling and to check the results of calculations and design, experimental modeling is used, in which centrifugal modeling is practically the only procedure that could predict the state of the system over time [29].

Currently, the centrifugal modeling method is widely used in various fields of science and technology. Centrifugal modeling as a method is rapidly developing in the world; the importance of the method in construction has increased significantly; extensive material has been accumulated that is directly related to the solution of actual practical problems [30, 31].

Modeling is a tool to study the state of objects and the processes occurring in them. In physical modeling, the system under study (a full-scale structure) is reproduced using an equivalent system (model of the structures, as a rule, having a smaller size). At the same time, natural processes are reproduced in the model in such a way as to obtain the necessary information in the most reliable, simple, quick and cheap way, and in some cases even more completely than when observed on a full-scale object or by calculation.

However, at ordinary physical modeling of earth structures, the nonlinear relationship between stresses and strains distorts the entire picture of the stress state of the model compared to a full-scale object, the strength in a small model increases. In this case, as a rule, only qualitative information about the object can be most easily obtained. In order to achieve complete similarity between the model and the structure (to ensure equality of stresses and strength and proportionality of strains) and to obtain the necessary quantitative information about the object, it is necessary to increase the weight per unit volume of the model material.

Only one method opens up this possibility – the method of centrifugal modeling, which is qualitatively different from other methods of physical modeling. The qualitative and fundamental difference of the centrifugal modeling method is as follows:

- in centrifugal modeling, the material of full-scale objects is used in models;
- the model is placed in the field of centrifugal forces (similar to the gravitational field), which increases the weight of a unit volume of the model material;
- in a model located in the field of centrifugal forces, a stress state is created which is identical to the one in a full-scale object.

All this ensures the complete preservation of the physical nature of phenomena and processes under study. Compared with the natural conditions, only the time scale of their occurrence changes; this makes the centrifugal modeling method progressive and most effective. Using this method, it is possible to make significant additions to the calculations, in many cases to get more accurate results; in some cases this method allows researchers to solve such complex and not studied until now issues that so far are beyond research either by analytical (calculated) way or by field observations.

Principal relationships. The centrifugal force field (used as a force field, similar to a gravitational one) created by the centrifugal machine has n times greater intensity; here n is the linear scale of modeling

$$n = \sqrt{\frac{\omega^2 R_{ef}}{g} + 1}, \quad (1)$$

where ω is the angular velocity of the centrifuge; R_{ef} is the effective radius of rotation; g is the gravitational acceleration.

The model of the structure is placed in the field of centrifugal forces, so far from the axis of rotation and the intensity of the centrifugal field is taken so significant that the influence of gravitational forces that distort the field of forces in modeling can be neglected.

The main point of the method can be understood from the following simple example. When modeling static stresses under structure own weight, it is necessary to satisfy the condition

$$\gamma H = idem, \quad (2)$$

where γ is the weight per unit volume of material (soil); H is the thickness of the soil layer.

For the natural conditions (full-scale conditions)

$$\gamma_n = m_v g, \quad (3)$$

where γ_n is the force acting per unit volume of material (soil) in the gravitational field, m_v is the mass of a substance per unit volume.

The acceleration can be changed by causing inertial forces in the system (model) under consideration, for which the system must be subjected to some acceleration i . Then the total acceleration vector of the model is:

$$a_m = g + i \quad (4)$$

and

$$\gamma_m = m_v a_m \quad (5)$$

where, γ_m is the force acting on a unit volume of this material (soil) in the model in total force field of inertia and gravity.

If the model is done n times less than a full-scale structure, then according to (2) the equality of stresses is expressed by

$$\gamma_n H = \gamma_m \frac{H}{n} \quad (6)$$

or

$$\gamma_m = \gamma_n n \quad (7)$$

Substituting (3) and (5) in (7), we get

$$m_v a_m = n m_v g, \quad a_m = g n \quad (8)$$

that is, the basic rule of centrifugal modeling under considered conditions is that the model is affected by volume forces that exceed the force of gravity as many times as the model is smaller than the actual structure [29].

With this method of modeling, the quantitative characteristics of the phenomena and processes observed in the model are directly transferred to the natural conditions through appropriate scale factors, in particular:

$$\ell_n = n \ell_m; \quad S_n = n^2 S_m; \quad V_n = n^3 V_m; \quad P_n = n^2 P_m; \quad \sigma_n = \sigma_m; \quad \gamma_n = \frac{1}{n} \gamma_m; \quad (9)$$

$$T_n = T_m; \quad t_n = n t_m; \quad (t_n = n^2 t_m),$$

where ℓ is the length; S is the area; V is the volume; P is the force; σ is the stress; γ is the volume weight; T is the temperature; t is time; n , m are the indices corresponding to the full-scale structure and the model.

In case of modeling the motion of mechanical system, time t in centrifugal modeling will be n times less than in natural conditions, while in modeling the processes with viscous strains it will be n^2 times less. Varying the speed of rotation of the centrifuge, according to (2) the desired simulation scale can be selected. An account of all possible errors associated with the measurement accuracy and with the accuracy of the gravitational field modeling is given in [30–32].

Currently, the use of polymer pipes to convey various media (water, gas, oil, etc.) is growing rapidly. This is due to the advantages of the pipes made of polymer materials as compared to metal pipelines. Therefore, studies of the polymer pipe behavior under various static and dynamic loads are relevant. With this in mind, we have investigated the effect of the temperature factor on the stability of polymer pipes laid in the ground at various depths.

The proposed experimental research technique can be used to study the behavior of underground pipelines made of various materials, taking into account their geometric parameters and soil conditions under temperature effect.

2.2. Experimental studies

Experimental studies of polymer pipes under temperature effect have been carried out on a modernized centrifugal installation of the Institute of Mechanics and Seismic Stability of Structures of the Academy of Sciences of the Republic of Uzbekistan. The existing measuring complex based on the light-beam oscillographs was replaced by a new recording system “sensor + amplifier + analogous digital converter + personal computer + software”. The created program of sensor signals registration allowed us to avoid the use of photographic paper and chemical processing, to significantly reduce the processing time and to observe the experiment in real time on the computer monitor. The results of instrumental measurements in numerical and graphical form are given immediately after the end of the experiment. The data obtained during the experiment are saved as files and can be reused later.

A four-channel measuring complex was used to conduct model experiments on a centrifugal unit. Three measuring channels were intended for recording signals from strain gauges installed on the object under study and one channel for recording the centrifuge speed using an optical sensor.

It should be noted that in recent decades, the use of polymer pipes for transporting various media (water, gas, oil, etc.) has increased rapidly. This is due to the advantages of the pipes made from polymeric materials when compared to metal pipelines. Therefore, the studies of the behavior of polymer pipes under various static and dynamic loads are relevant.

With this in mind we have investigated the effects of the temperature factor on the strain in polymer pipes embedded in ground at different depths. The experiments have been carried out in a centrifuge with an effective radius of rotation $R_{ef} = 1.75$ m, with a working scale of modeling $n = 40$ (Fig. 1). Experiments have been carried out using the carriage 1 (Fig. 2, a) with dimensions: working section length – 35.2 cm; working section width – 23.8 cm; working section height – 30.0 cm.

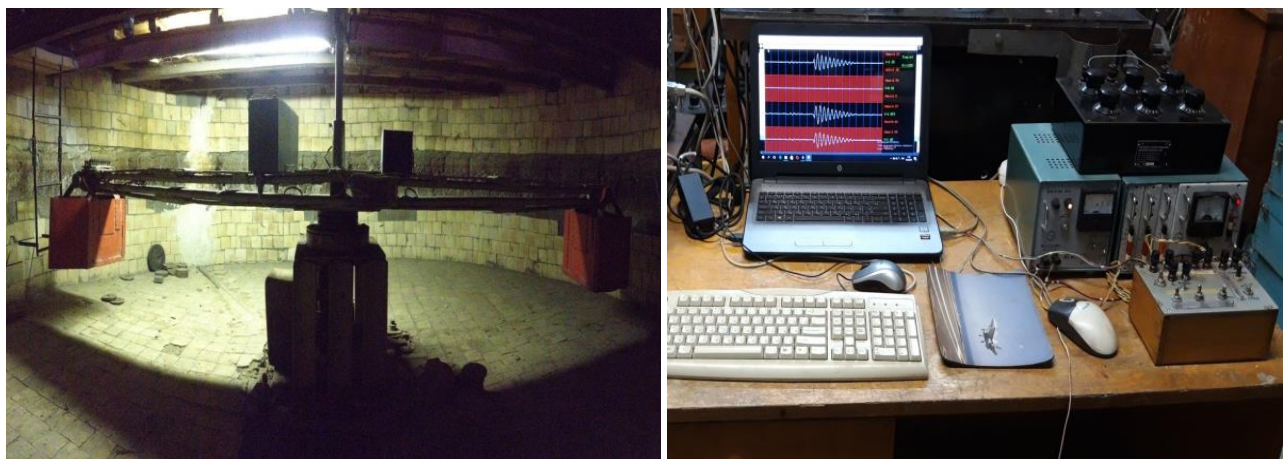
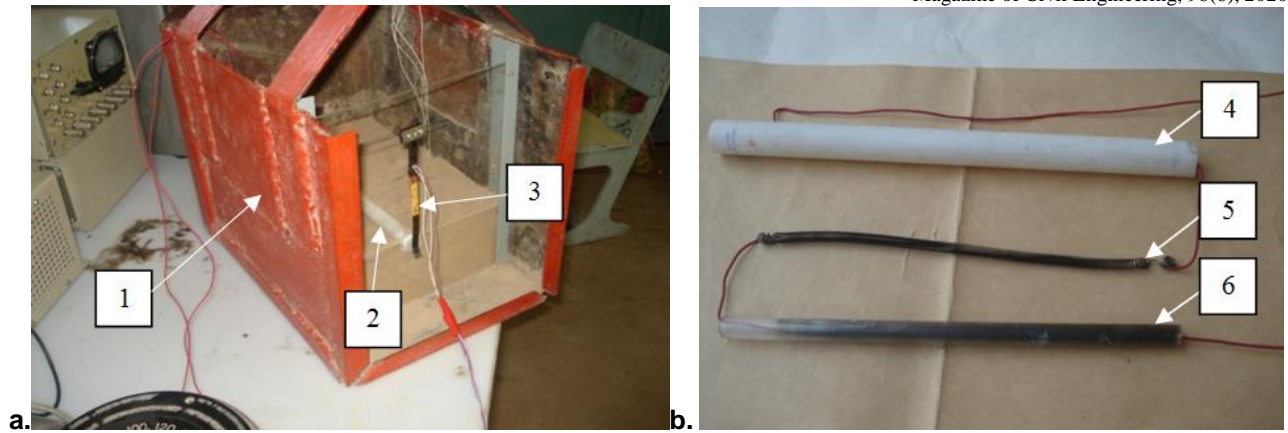


Figure 1. General view of a centrifugal installation with a measuring complex.



**Figure 2. (a) – a carriage with a tube model located on an earth base:
1 – a centrifuge carriage; 2 – a tube model; 3 – a displacement sensor.
(b) – a tube model with heating system: 4 – a tube model; 5 – a spiral, 6 – a quartz tube**

A polymer tube 4 (Fig. 2, b) was used as an experimental sample (tube model P4004T) with the following geometrical dimensions: total tube length $l_m = 28.2$ cm, outer diameter of the tube $d_{1m} = 2.2$ cm, internal diameter of the tube $d_{2m} = 1.5$ cm, tube wall thickness $\Delta_m = 0.35$ cm, working section length of the tube $l_m = 26.3$ cm.

Accordingly, the geometrical dimensions in full-scale conditions are: the total length of the pipe $l_n = 11.28$ m, the outer diameter of the pipe $d_{1n} = 0.88$ m, the internal diameter of the pipe $d_{2n} = 0.60$ m, the wall thickness of the pipe $\Delta_n = 0.14$ m, the working section length $l_n = 10.52$ m.

Characteristic features of the sample material of polymer pipeline of P4004T brand are as follows: density $9.41\text{--}1.53$ kN/m³, tensile yield strength 23000 kN/m² and elongation of 250% .

To carry out the experiments, a quartz tube 6 (Fig. 2, b) was placed inside a model made of a polymer tube to isolate and uniformly distribute the temperature along the contour. Inside the quartz tube, a spiral 5 was placed (Fig. 2, b), which heated up the system to the desired temperature, the value of which was controlled by the LATR autotransformer.

To determine the laws of temperature change under different heating conditions, preliminary an experiment has been conducted with a tube located on soil surface. A loamy soil of disturbed structure with a volume weight of $\gamma = 14.5$ kN/m³ and moisture-content $W = 9\%$ was chosen as the soil sample. One end of the tube model was rigidly fixed, and the other end could move freely along the tube axis. The displacements of the free end of the tube model ΔZ have been recorded using a strain gauge, calibrated in advance. When voltage was applied to the electric coil, the model of the tube heated up and lengthened, and the change in tube temperature ΔT has been determined from the relation:

$$\Delta Z_n = \alpha \cdot \Delta T \cdot Z, \quad (10)$$

where ΔZ is the elongation of the tube determined from the calibration data, Z is the tube length at room temperature, α is the coefficient of temperature expansion of the tube material $\alpha = 1.5 \times 10^{-4}$ 1/deg.

Having determined the law of temperature variation over time, the experiments then have been carried out to determine the displacements of a model of an underground hot-water system made of polymer pipes at different depths of embedment in soil. So, in a compacted soil, by centrifuging for 30 minutes (which in nature conditions corresponds to 33 days), a foundation was built up on which the model of tube 2 was bedded (Fig. 2, a), and then it was filled up with soil. One end of the tube was fixed rigidly in the centrifuge carriage a specially made strain gauge sensor 3 was installed at the second free end to measure the tube displacements relative to soil at various temperatures.

At the level of the upper part of the pipe model, a sensor was installed to measure the soil pressure on the pipe. Before heating the tube, the filling was compacted by rotating the centrifuge for 25-30 minutes.

The values of displacements of the model of underground hot-water system under temperature changes depending on the voltage on the heating element have been determined by the readings of the computer based on the calibration data. The depth of laying the model pipe in the experiments was changed from 3.0 to 9.0 cm, which in full-scale conditions corresponds to the depth of laying from 1.2 to 3.6 meters. According to the results of the experiments and analysis of the data obtained, graphs of changes in the tube elongation were constructed for different heating modes and depths.

3. Results and Discussion

Fig. 3 shows the dependences of polymer tube elongations over time after stabilization of the centrifuge rotation at different depths and voltage variations on the heater.

Fig. 3 (a) shows the dependences of the tube elongation over time when the centrifuge is rotated within 20-25 minutes: curves 1, 3, 5 correspond to the elongations of the tube lying on the soil surface; curves 2, 4, 6 correspond to tube elongation located at a depth of $H_m = 3$ cm. Curves (1, 2), (3, 4), (5, 6) are obtained when the tube is heated, caused by a change in voltage on the heater at 15 V, 10 V, 5 V, respectively.

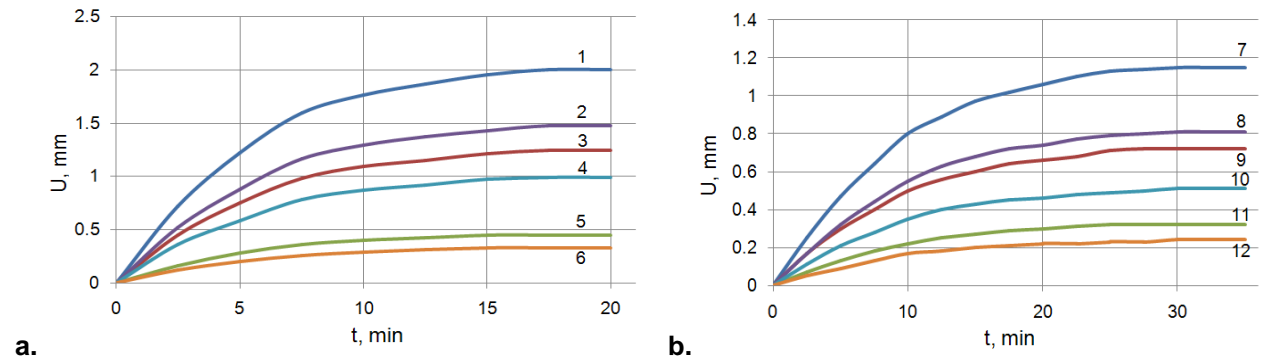


Figure 3. The dependence of polymer tube elongations over time on the voltage change in the heater at different depths.

Fig. 3 (b) shows the dependences of the tube elongation over time, located at the depth $H_m = 6$ cm (curves 7, 9, 11) and $H_m = 9$ cm (curves 8, 10, 12), caused by a voltage change on the heater. Curves (7, 8), (9, 10), (11, 12) are obtained by rotating the centrifuge for 30-35 minutes at the voltage of the heater 15 V, 10 V, 5 V respectively.

The instrumental data obtained show that the tube elongates with the temperature increase, and the tube deformation at the beginning of its heating process for 15-20 minutes is non-linear; then at constant temperatures, the tube displacements reach the maximum values and remain constant. The elongation of the tube lying on the soil surface differs significantly from the one of the embedded tube, depending on the depth. In general, with an increase in the depth of the tube, its elongation decreases markedly depending on the temperature acting on it.

Fig. 4 shows the change in soil pressure depending on the depth of the tube embedment at centrifuge rotation for 25-30 minutes. As seen from the figure, at the beginning of centrifuge rotation the soil pressure on the tube increases almost in direct proportion. During the first minutes, when the centrifuge begins its rotation, the pressure increases minimally. After 4 minutes of acceleration and stabilization of the rotational speed of the centrifuge, the pressure in soil is increasing for about 13 minutes; this is associated with soil compaction. The experiment shows an increase in soil pressure on the structure and its tendency to its asymptotic value depending on the duration of the centrifugal forces.

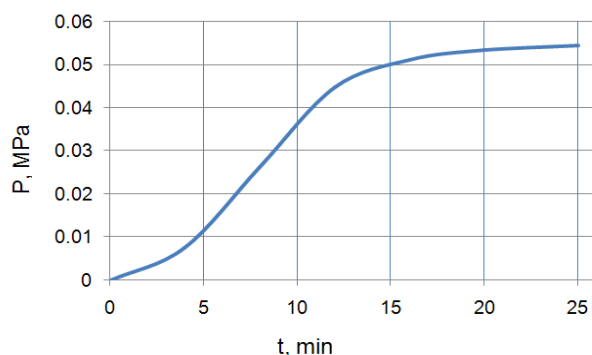


Figure 4. Pressure changes in soil depending on the tube depth.

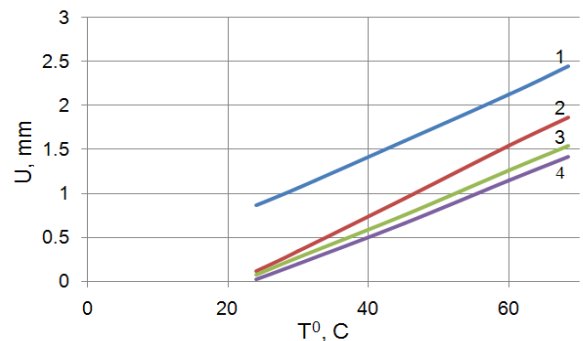


Figure 5. Dependence of tube elongation on temperature at different depths:
1 – free location; 2 – $H_m = 3.0$ cm;
3 – $H_m = 6.0$ cm; 4 – $H_m = 9.0$ cm.

Fig. 5 shows the dependences of the tube model elongation on temperature at different depths of its embedment: 1 – at free location on the soil surface; 2, 3, and 4 – at depths of embedment $H_m = 3.0$ cm,

$H_m = 6.0$ cm and $H_n = 9.0$ cm respectively, which in nature laying depth corresponds to $H_n = 1.2$ m, $H_n = 2.4$ m и $H_n = 3.6$ m.

At constant value of the tube depth its elongation increases with an increase in temperature, and at constant values of temperature with an increase in soil pressure, the elongation of the tube decreases depending on its depth.

4. Conclusion

As a result of the present work, the following conclusions can be outlined:

1. With an increase in the depth of the polymer tube at the same temperature, the tube elongation decreases markedly. At a constant temperature $T = 60^\circ \text{C}$, the tube displacement in a free state is at $H_m = 0$ cm, $U_m = 2.1$ mm; at $H_m = 3.0$ cm, $U_m = 1.6$ mm; at $H_m = 6.0$ cm, $U_m = 1.35$ mm; and at $H_m = 9.0$ cm, $U_m = 1.2$ mm, which as a percentage is 76 %, 64 % and 57 % of the free state of tube displacement.
2. With an increase in the temperature effect at the same depth, the tube elongation increases. At a constant depth of tube embedment $N_m = 6.0$ cm, at an increase in temperature from $T = 30^\circ \text{C}$ to 60°C , the tube elongation increases from 0.26 mm to 1.3 mm.
3. With an increase in depth the values of soil pressure on the tube increase, tending to a certain asymptote.
4. The developed measuring system to record experimental data using a computer as a recording device made it possible to observe the experiment in real time and store the data obtained from the sensors in files.
5. The results obtained can be used in calculation and design of underground polymer pipelines for earthquake resistance.
6. In the future, the authors will conduct extensive research on this topic with various samples of polymer pipelines under various ground and temperature conditions.
7. At the moment, in scientific literature there are no results of experimental studies on underground polymer pipelines using the centrifugal modeling method. Therefore, the research results are not compared with the results of other scientific studies.

References

1. Ariman, T., Muleski, G.E. A review of the response of buried pipelines under seismic excitations. *Earthquake Engineering and Structural Dynamics*. 1981. No. 9. Pp. 133–151.
2. Liang J., Sun S. Site effects on seismic behavior of pipelines. *Pressure Vessel Technology*. 2000. No.122(4). Pp.469–475.
3. Desmod, T.P., Power, M.S., Taylor, C.L., Lau, R.W. Behavior of large-diameter pipeline at fault crossings. *ASCE, TCLEE*. 1995. No. 6. Pp. 296–303.
4. Nakata, T., Hasuda, K. Active fault in 1995 Hyogoken Nanbu Earthquake. *Kagaku*. 1995. No. 65. Pp. 127–142.
5. Earthquake Engineering Research Institute. Kocaeli. Turkey Earthquake of August 17. EERI Special Earthquake Report. 1999.
6. Takada, S., Nakayama, M., Ueno, J., Tajima, C. Report on Taiwan Earthquake. RCUS, Earthquake Laboratory of Kobe University. 1999. Pp. 2–9.
7. Virginia Corrado, Berardino D'Acunto, Nicola Fontana, Maurizio Giugni. Inertial Effects on Finite Length Pipe Seismic Response. *Hindawi Publishing Corporation Mathematical Problems in Engineering*. 2012. Vol.2012, Article ID 824578, 14 pages. [//dx.doi.org/10.1155/2012/824578](https://doi.org/10.1155/2012/824578).
8. Israilov, M., Mardonov, B., Rashidov, T. Seismodynamics of an Underground Pipeline in Nonideal Contact with Soil Effect of Sliding on Dynamic Stresses. *Applied Mechanics and Technical Physics*. 2016. Vol. 57. Issue 6. Pp. 1126–1132.
9. Bekmirzaev, D.A., Rashidov, T.R. Mathematical Simulation and Solution of the Problem of Seismo-Dynamics of Underground Pipelines. *Engineering & Technologies*. 2015. Vol. 8. Issue 8. Pp. 1046–1055.
10. Rashidov, T.R., An, E.V. Issledovaniye ustoychivosti podzemnogo truboprovoda s uchetom geometricheskoy nelineynosti pri prodolnom nagrujenii [Study of the stability of the underground pipeline with account into to geometric nonlinearity with longitudinal loading]. *Soil Mechanics and Foundation Engineering*. 2017. No. 2. Pp. 7–11. (rus)
11. Rashidov, T.R., Nishonov, N.A. Seysmodinamika podzemnih polimernih truboprovodov s peremennimi koeffitsientami vzaimodeystviya [Seismic dynamics of the underground polymer pipelines with variable interaction coefficients]. *Soil Mechanics and Foundation Engineering*. 2016. No. 3. Pp. 34–38. (rus)
12. Saberi, M., Arabzadeh, H., Keshavarz, A. Numerical Analysis of Buried Pipelines with Right Angle Elbow under Wave Propagation. *Procedia Engineering*. 2011. Vol. 14. Pp. 3260–3267.
13. McLaughlin, P.M., O'Rourke, M. Strain in Pipe Elbows Due to Wave Propagation Hazards. *Technical Council on Lifeline Earthquake Engineering Conference. TCLEE 2009*.
14. Lillig, D.B., Newbury, B.D., Altstadt, S.A. The second ISOPE strain-based design symposium. In *Proceedings of the International Society of Offshore and Polar Engineering Conference*. Osaka, Japan. 2009.
15. Vazouras, P., Karamanos, S.A., Dakoulas, P. Finite element analysis of buried steel pipelines under strike-slip fault displacements. *Soil Dynamics and Earthquake Engineering*. 2010. Vol. 30. Pp. 1361–1376.

16. Ha, D., Abdoun, T.H., O'Rourke, M.J., Symans, M.D., O'Rourke, T.D., Palmer, M.C., et al. Buried high-density polyethylene pipelines subjected to normal and strike-slip faulting a centrifuge investigation. *Canadian Geotechnical Journal*. Vol. 45. Issue 12. Pp. 1733–1742.
17. Ha, D., Abdoun, T.H., O'Rourke, M.J., Symans, M.D., O'Rourke, T.D., Palmer, M.C., Stewart, H.E. Centrifuge Modeling of Earthquake Effects on Buried High-Density Polyethylene (HDPE) Pipelines Crossing Fault Zones. *Geotechnical and Geoenvironmental Engineering*. 2008. Vol. 134. Issue 10. Pp. 1501–1515.
18. Ha, D., Abdoun, T.H., O'Rourke, M.J., Symans, M.D., O'Rourke, T.D., Palmer, M.C., Stewart, H.E. Factors Influencing the Behavior of Buried Pipelines Subjected to Earthquake Faulting. *Soil Dynamics and Earthquake Engineering*. 2009. Vol. 29. Pp. 415–427.
19. Khojmetov, G.Kh., Bekmirzaev, D.A., Yuvmitov, A.S. Determination of Viscosity Parameters in Rigid Body-Soil Interaction. *European Science Review*. 2016. Vol. 1–2. Pp. 163–165.
20. Dedukh, D.A., Schsuzkiy, V.L., Kuzmenko, A.A. Spun concrete properties of power transmission line supports. *Magazine of Civil Engineering*. 2017. No. 75(7). Pp. 37–51. DOI: 10.18720/MCE.75.4
21. Samarin, O.D. The temperature waves motion in hollow thick-walled cylinder. *Magazine of Civil Engineering*. 2018. No. 78(2). Pp. 161–168. DOI: 10.18720/MCE.78.13
22. Chernysheva, N.V., Kolosova, G.S., Rozin, L.A. Combined Method of 3^d Analysis for Underground Structures in View of Surrounding Infinite Homogeneous and Inhomogeneous Medium. *Magazine of Civil Engineering*. 2016. 62(2). Pp. 83–91. DOI: 10.5862/MCE.62.8
23. Yarashov, J., Usarov, M., Ayubov, G. Study of longitudinal oscillations of a five-storey building on the basis of plate continuum model. *E3S Web of Conferences*. 2019. 97. 04065.
24. Toshmatov, E., Usarov, M., Ayubov, G., Usarov, D. Dynamic methods of spatial calculation of structures based on a plate model. *E3S Web of Conferences*. 2019. 97. 04072.
25. Kozhaeva, K.V. Influence of the compensating device parameters on the underwater pipeline stability. *Magazine of Civil Engineering*. 2018. No. 80(4). Pp. 24–36. DOI: 10.18720/MCE.80.3
26. Huanhuan, Q. Centrifugal Modeling and Validation of Solute Transport within Unsaturated Zone. *Magazine of Water*. 2019. No. 11. Pp. 1–21. DOI: 10.3390/w11030610
27. Rashidov, T.R., Khojmetov, G.H. Seysmostoykost podzemnih truboprovodov [Seismic resistance of the underground pipelines]. Tashkent: Fan. 1985. 152 p. (rus)
28. Pokrovskiy, G.I., Fedorov, I.S. Tsentrobejnoe modelirovanie v stroitel'nom dele [Centrifugal modeling in construction]. M.: Stroyizdat. 1968. 247 p. (rus)
29. Feodorov, I.S., Melnik, V.G., Teytelbaum, A.I., Savvina, V.A. Teoriya i praktika tsentrobejnogo modelirovaniya v stroitel'stve [Theory and practice of centrifugal modeling in construction]. M.: Stroyizdat, 1984. 248 p. (rus)
30. Pokrovskiy, G.I., Feodorov, I.S. Tsentrobejnoe modelirovanie v gornom dele [Centrifugal modeling in mining]. M.: Nedra. 1969. 270 p. (rus)
31. Yakovleva, T.G., Ivanova, D.I. Modelirovanie prochnosti i ustoychivosti zemlyanogo polotna [Modeling the strength and stability of the road bed]. M.: Transport, 1980. 253 p. (rus)
32. Teshabaev, Z.R. Eksperimentalnoe issledovanie vzaimodeystviya podzemnih sooruzheniy s gruntom metodom tsentrobejnogo modelirovaniya [Experimental study of the interaction of the underground structures with the ground by the method of the centrifugal modeling]: Abstract of Cand. diss. Tashkent: 1986. 20 p. (rus)

Contacts:

Khamidulla Sagdiev, imssan@mail.ru

Zohidjon Teshabayev, imssan@mail.ru

Viktor Galiaskarov, instmech@uznet.net

Anvar Yuvmitov, anvar.sayfullaevich@mail.ru

© Sagdiev, Kh.S., Teshabayev, Z.R., Galiaskarov, V.A., Yuvmitov, A.S., 2020



DOI: 10.18720/MCE.98.2

Mechanical-thermal characteristics of foamed ultra-lightweight composites

T.-P. Huynh^{a,*}, N.-T. Ho^b, P.-T. Bui^{c,d}, N.-D. Do^e, T.-C. Nguyen^f

^a Can Tho University, Can Tho City, Viet Nam

^b VSB Technical University of Ostrava, Ostrava, Czech Republic

^c Ho Chi Minh City University of Technology, Ho Chi Minh City, Viet Nam

^d Viet Nam National University Ho Chi Minh City, Ho Chi Minh City, Viet Nam

^e National Taiwan University of Science and Technology, Taipei City, Taiwan

^f Le Quy Don Technical University, Ha Noi City, Viet Nam

* E-mail: htphuoc@ctu.edu.vn

Keywords: composite, cement, fly ash, compressive strength, thermal behavior, microstructure

Abstract. Turning waste into construction materials recently gets much attention from the researchers in the world due to the advantages of not only the eco-friendly environment but also the positive enhancement of material characteristics. Thus, this study investigates the feasibility of the use of a ternary mixture consisting of cement, ground granulated blast-furnace slag (GGBFS), and fly ash (FA) for producing foamed ultra-lightweight composites (FULC) with the designed dry density of approximately 700 kg/m³. The FULC specimens were prepared with various FA/GGBFS ratios (16/24, 20/20, and 24/16) and foaming agent/water ratios (1/60, 1/80, 1/100, and 1/120). The constant water-to-binder ratio of 0.2, cement content of 40 % by mass, and superplasticizer dosage of 0.2 % by mass were applied for all FULC mixtures. Properties of the FULC specimens were evaluated through laboratory tests of compressive strength, dry density, thermal conductivity, water absorption, and thermal behavior following the relevant ASTM standards. Additionally, both the microstructure observation and cost analysis of all FULC mixtures was performed. Test results show that reducing GGBFS content resulted in a reduction in the compressive strength, dry density, thermal conductivity, and cost of the FULC. A similar trend could be observed when reducing the concentration of foam in the FULC mixtures. As the results, the 28-day compressive strength, dry density, thermal conductivity, water absorption, and cost of the FULC were in the ranges of 4.41–5.33 MPa, 716–729 kg/m³, 0.163–0.182 W/mK, 41.5–48.5 %, and 15.3–20.9 USD/m³, respectively. Furthermore, the FULC exhibited excellent performance under fire conditions as the maximum temperature at the internal surface of the FULC and the normal brick walls were 122 °C and 318 °C after 120 minutes of firing, respectively. Consequently, both GGBFS and FA had enormous potential for the production of FULC.

1. Introduction

Vietnam is facing the demand for housing because of the increase in population density, while the land for construction is limited. That is the reason for the existence of high-rise buildings or skyscrapers, which solves the issues involving human shelter as well as land use. On account of these problems, the solutions are pointed to resolve the situation that buildings have to face up to the heavy-weight and such things as comfort. Foam concrete (FC) is invented to serve sustainable development and respond the human life, and FULC is one of the possible products involving to FC. FC is known as durable, lightweight construction materials, which provide the construction industry lots of advantages by decreasing cost, insulation capacity, and fire resistance of structures [1].

On the other hand, the cost of materials is crucial concerned having a significant effect on the construction; it occupies nearly 60 % of the total cost of building construction [2]. The using of FC can

Huynh, T.-P., Ho, N.-T., Bui, P.-T., Do, N.-D., Nguyen, T.-C. Mechanical-thermal characteristics of foamed ultra-lightweight composites. Magazine of Civil Engineering. 2020. 98(6). Article No. 9802. DOI: 10.18720/MCE.98.2



This work is licensed under a CC BY-NC 4.0

replace a brick wall to lighten the weight of the building and to cheapen the foundation cost. The smooth surface of foam concrete reduced the cost for plastering as well as construction price. Moreover, the lowering of the air-conditioning cost is in parallel with the reduction of heat flow [3]. Containing an amount of pore (having a total volume of at least 20 %) and having a lot of artificial air-void trapped inside its specimens by using a suitable foaming agent are the excellent characteristics of FULC [4, 5]. The use of FULC provides impressive performance to the building, for the structure of FULC create insulations from heat and act as sound-proof [1]. It is well-known as perfect, an insulating material that is going to hit wide distribution in construction.

Nowadays, scientists have been investigating the enhancement of FULC properties to find out and maximize the application. That FULC productions have been using day by day, the scientific research on FULC will continue to exploit its characteristics to improve construction development. There are ranges of scientific journals that investigate the production of FULC, to mention that FC has advantages of thermal insulation properties, fire-resistant, and durability [6–8]. The idea of increasing the level of thermal protection and improving the humidity regime using a wall made of lightweight materials has been well-applied by Russian researchers [9, 10]. Thus, FULC is invented to serve sustainable development and respond the human life. Having said that FULC is a potential material that can multiply research to discover the leading topic. In spite of the application are widening, the production of FULC gradually become tougher, which is due to the scarcity of input material such as cement. The issues related to cement production are becoming seriously because of environmental problems. Currently, the world's annual demand uses more than 4 billion tons of cement [11], not mentioned it exhaust approximately (5 % CO₂) [12] to the environment. Coupled with the growth of the industry, the ongoing conduct of research topics on using industrial waste to minimize a substantial environmental agent and maximize the production of construction material has been continuing. These studies on FC by using industrial waste that can be mentioned such as the addition of ultrafine GGBFS provided an increase in the compressive strength of FC when using GGBFS as partial cement replacement [13] or the substitution of sand by FA in FC mixes lower foam volume because of FA fineness [14].

This investigation focuses on the combination of blended binders, including FA, GGBFS, and ordinary Portland cement (OPC) to manufacture and aim to assess the characteristics of FULC. The topic thereby contributes to the science of FULC in particular and concrete in general.

2. Materials and Methods

2.1. Materials

Type-I OPC conforming to ASTM C150, GGBFS conforming to ASTM C989, and FA conforming to ASTM C618 were used as the binder materials in this study. Specific gravities and chemical compositions of cement, GGBFS, and FA are listed in Table 1.

As can be seen, cement and GGBFS comprised CaO and SiO₂ majorly, whereas high content of SiO₂ and Al₂O₃ was found in FA. Fig. 1 shows the particle size distribution of GGBFS and FA. Fig. 2 shows the morphology of raw materials consisting of GGBFS and FA by using scanning electron microscopic (SEM). It can be seen that GGBFS had irregular shapes, while FA contained a lot of spherical particles with different sizes.

Table 1. Specific gravity and chemical compositions of raw materials.

Properties		Cement	GGBFS	FA
Specific gravity		3.15	2.92	2.26
Chemical composition (wt.%)	SiO ₂	20.0	35.6	55.3
	Al ₂ O ₃	4.2	11.3	22.7
	Fe ₂ O ₃	3.1	0.5	5.9
	CaO	62.4	41.0	5.7
	MgO	4.2	6.5	1.6
	K ₂ O	0.4	0.6	1.5
	Na ₂ O	0.3	0.3	3.8
	L.O.I*	1.75	4.71	2.74

*L.O.I – loss on ignition

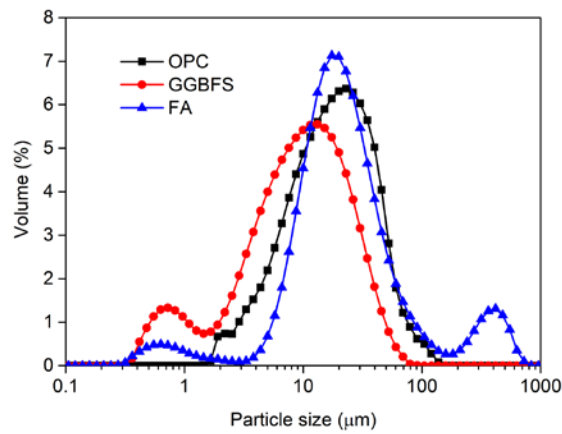
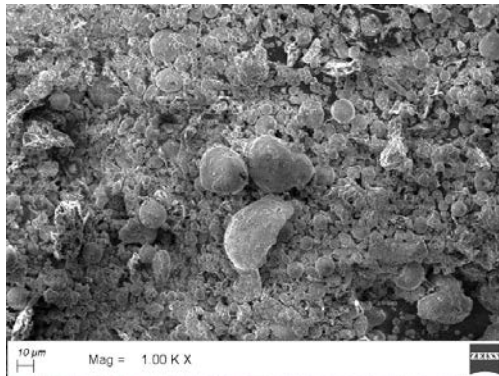
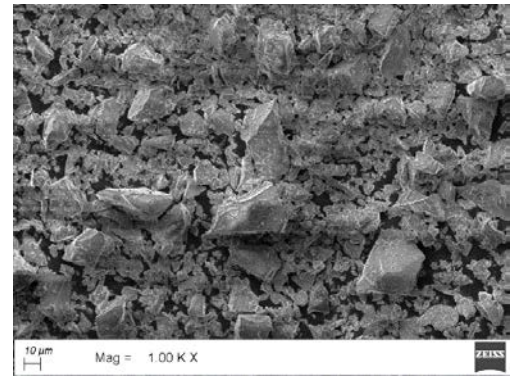


Figure 1. Particle size distribution of raw materials.



(a) FA



(b) GGBFS

Figure 2. SEM images of raw materials.

The mineralogical compositions of GGBFS and FA were determined by using X-ray diffraction (XRD), as shown in Fig. 3. The non-crystalline phase existed in the GGBFS structure without any peak whereas the high intensity of quartz was found in FA, which is considered as crystalline phase.

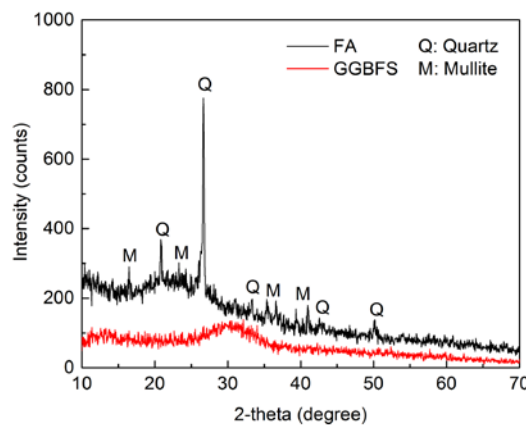


Figure 3. XRD patterns of raw materials.

In this study, the pale brown liquid EABASSOC foaming agent with a specific gravity of 1.02 and pH (in solution) of 6.7 and type-G superplasticizer (SP) sourced from China with a specific gravity of 1.34 were used for the preparation of FULC samples.

2.2. Mixture proportions

Six mixture proportions are prepared in this study, as shown in Table 2. Constant percentages of foam, water, and SP contents were 5, 16, and 0.2 % by mass of FULC, respectively. The content of 40 % cement by weight of FULC was kept constant to assess the influence of FA and GGBFS on properties of FULC. The proportions of FA and GGBFS were in the range of 16–24 % by mass of FULC. It was reported that the foaming agent/water (F/W) ratio affects the formation of the void and porosity of FULC. Therefore,

the F/W ratios of 1/60, 1/80, 1/100, and 1/120 were prepared to evaluate the effects of the F/W on the characteristics of FULC.

Table 2. Mixture proportions of FULC.

Materials	% by mass					
	M1	M2	M3	M4	M5	M6
Cement	40	40	40	40	40	40
FA	16	20	24	20	20	20
GGBFS	24	20	16	20	20	20
Foam	5	5	5	5	5	5
Mixing water	16	16	16	16	16	16
SP	0.2	0.2	0.2	0.2	0.2	0.2
F/W*	1/80	1/80	1/80	1/60	1/100	1/120

*F/W – foaming agent-to-water ratio

2.3. Mixing procedure and specimen preparation

All of the materials were kept in anti-moisture bags to prevent the moisture before mixing. The foam was initially generated from different F/W ratios (as shown in Table 2) using a foam generator. After making the foam, the mixing procedures can be started as follows: Firstly, cement, FA, and GGBFS were dry mixed uniformly in a laboratory mixer for 1 min. Mixing water with SP was then gradually added to the dry mixture and allowed to mix for 2 min to obtain a uniform fresh mixture. Finally, the foam was added to the fresh mixture and mixed for another 2 min to get a homogenous fresh paste.

After mixing, the fresh pastes were cast in 50-mm-per-side cube-shaped molds, as seen in Fig. 4. The surfaces of the specimens were then sealed with plastic films to avoid water loss. All specimens were de-molded for 24 h after casting and cured in water until the designated test ages. The finished products were put in laboratory conditions and remolded after 24 h. Right that, all FULC specimens were cured at room condition until the day of testing.



Figure 4. FULC specimens.

2.4. Test methods

Compressive strength of FULC specimens was tested at the ages of 3, 7, 14, and 28 days according to ASTM C109, which can be considered as the modified standard for testing compressive strength of the prepared 50x50x50 mm FULC specimens.

After the compression test, the small pieces obtained from the broken FULC specimens were used for analyzing their microstructure by scanning electron microscopy (SEM). The experiment was performed following the guidelines of Hwang and Huynh [15]. In addition, density, water absorption, and voids of specimens were measured per ASTM C642. The thermal conductivity (TC) was recorded using a portable device model ISOMET 2014 as described by Hwang and Tran [16] to measure the correlation between density and porosity as well as the voids inside FULC.

It is noted that three specimens of each FULC mixture were subjected to each test, and the average value of the three specimens was reported.

2.5. The temperature distribution in the wall by a finite element model

Heat transfer through walls is the energy transmission process that involves objects having different temperatures. The heat transfer typically goes following three different patterns, including heat conduction, heat convection, and thermal radiation. Therefore, modeling of heat transfer must consider the whole solid bodies of a wall, as well as the convection and radiation between the substantial mass of the wall and the external heating sources [17].

Basic equations of heat transfer as described in equation (1) [18, 19]:

$$\lambda \nabla^2 T = \rho c \frac{\partial T}{\partial t}, \quad (1)$$

where: λ is the thermal conductivity, W/(m.K); c is the specific heat, J/(kg.K); ρ is the density, kg/m³; $\nabla^2 T = \text{div}(\text{grad } T)$ is the Laplace temperature operator.

A variety of boundary conditions, including temperature conditions, heat flow conditions, convection boundary conditions, radiation boundary conditions is often solved in heat transfer analysis. In this study, temperature conditions and convection boundary conditions were used as boundary conditions to solve the problem of heat transfer and equation (2) can be described as follows [20]:

$$q_c = h(T_c - T), \quad (2)$$

where: $T_c = T_c(t)$ is the temperature of the convective medium, °C; $T = T(t)$ is the temperature of the solid surface, °C; h is the convection coefficient, W/(m².K).

The wall of size 3.3×1.1×0.1 m was modeled in ANSYS APDL software. The specific heat, thermal conductivity, and density of brick walls were given as a function of temperature in the range $20 \leq T \leq 1200$ °C. For simplicity in computational analysis, according to studies [21–23], this simulation assumes the average value of specific heat, thermal conductivity, and density, as given in Table 3. The temperature profile of the wall was plotted by exposing the wall to the standard fire curve ISO 834, as shown in Fig. 5.

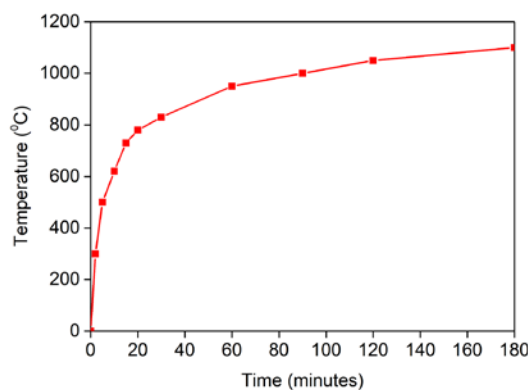


Figure 5. Temperatures versus time curves of standard fire curve ISO 834.

Table 3. Material properties.

No.	Property	FULC wall*	Normal brick wall
1	Thermal conduction coefficient, W/(m.K)	0.380	1.25
2	Specific heat, J/(kg.K)	0.85	0.92
3	Density, kg/m ³	716	2090
4	Convection coefficient, W/(m ² .K)	25	25

*FULC – foamed ultra-lightweight composite

Furthermore, the thermal conductivity of the FULC wall was compared with that of the normal brick wall under fire conditions to evaluate the thermal characteristics of FULC. It is noted that normal brick is one of the most popular and widely used construction materials in Vietnam. Therefore, it is chosen for the comparison with the FULC in order to demonstrate the advantages of using FULC instead of normal brick in terms of thermal behavior.

3. Results and Discussion

3.1. Compressive strength

Compressive strength development of the FULC specimens with various FA/GGBFS ratios is shown in Fig. 6. It can be seen that the FA/GGBFS ratio affected the compressive strength of FULC. The higher the FA/GGBFS ratio, the lower the compressive strength, regardless of age curing. There was an increase in the compressive strength of FULC when using the smaller amount of FA and higher amount of GGBFS (i.e., the higher FA/GGBFS ratio). The increase in compressive strength was due to the existence of FA and GGBFS, which filled the voids between grains and contributed to the better size distribution of the matrix, resulting in a reduction of porosity (as can be observed in Fig. 8) and thereby, improving compressive strength [24, 25]. In addition, Wang et al. [24] and Tangpagasit et al. [26] previously reported that the reactions between reactive SiO_2 and Al_2O_3 available in source materials and $\text{Ca}(\text{OH})_2$ formed from cement hydration created secondary hydration products such as C-S-H and C-A-S-H. The amount of these products increased over time, and they filled voids inside FULC, resulting in the denser structure. This may be a possible explanation for the strength results obtained in the present study.

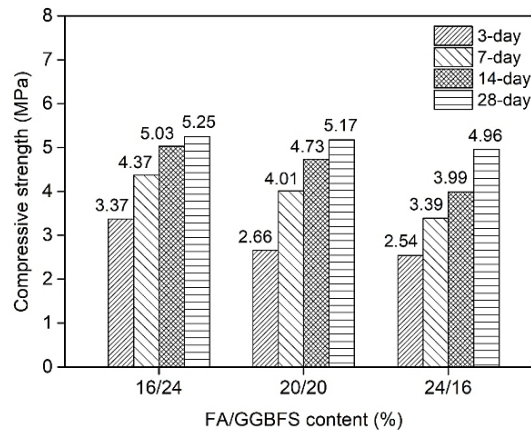


Figure 6. Compressive strength development of the FULC specimens with various FA/GGBFS ratios.

In general, the use of a higher amount of foam negatively affects the compressive strength of the FULC specimens, especially at the early ages [27]. The effect of F/W ratios on the compressive strength of FULC specimens is shown in Fig. 7. The high amount of foam (i.e., the low F/W) decreased the compressive strength of FULC. This behavior was due to an increase of void volume and the negative influence of foam on the pore size distribution and the quality of binding skeleton, resulting in a decrease in the final strength of the porous matrix [28, 29].

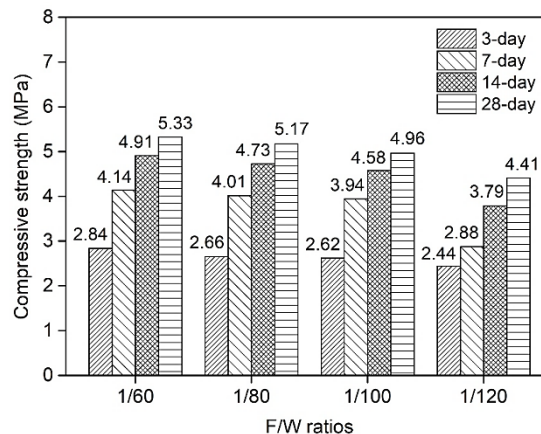


Figure 7. Compressive strength development of the FULC specimens with different F/W ratios.

3.2. Microstructure

The microstructure of FULC samples was shown in Fig. 8 by using a scanning electron microscopy technique (SEM). As seen in Fig. 8(a), M1 remained the unreacted GGBFS particles with angular shapes that formed the non-homogeneity structure inside the FULC specimen. The appearance of GGBFS and a suitable superplasticizer decreased air-void spaces and narrowed air-void size distributions [30]. Fig. 8(c) shows that the higher amount of unreacted FA particles. It indicates that FA played a role as an inert component, instead of pozzolanic material. The filler role of FA resulted in a more uniform distribution of pores and prevented from merging and overlapping of pores at higher foam content [31].

In addition, the air-void spaces were formed when adding the high amount of foam to FULC specimens, as shown in Fig. 8(b), (d), (e), and (f). The expansion of internal pores volume gradually exposed as seen in Fig. 8(d), (b), (e), and (f) with the use of FW at the levels of 1/60, 1/80, 1/100, and 1/120, respectively. Thus, the inclusion of foam restructured and changed characteristics through the formation of bubbles inside the FULC specimen. It leads to increase porosity and thus minimize TC property of the FULC. The previous research proved that the properties of foam concrete have no relation with air-void shape because of the approximately same shape of all air voids and independence of foam volume [31]. Cebeci [32] also proved that the large voids do not change the characteristics of the fine pore structure of hardened cement paste. Moreover, it is found that the amount of foaming agent used affected not only the physical properties but also the production cost of the FULC.

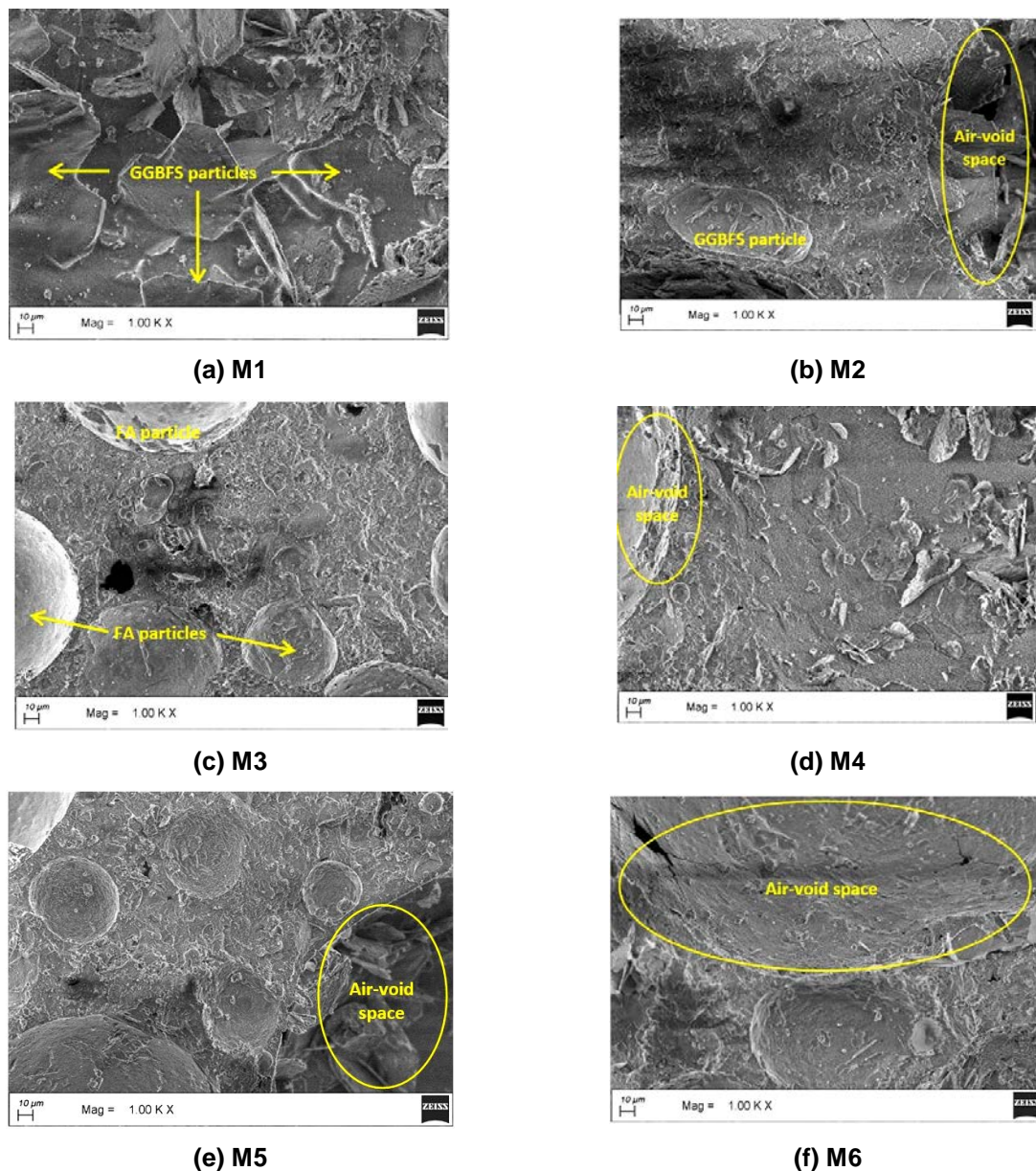


Figure 8. SEM images of the FULC specimens at 28 days.

3.3. Dry density and water absorption

Table 4 lists the engineering properties of FULC mixtures. The density of all of the FULC specimens was in the range of 716–728 kg/m³. The higher the foam amount, the lower the density of FULC. The inclusion of foam released air-entrapped parts leaving the void spaces and increased the porosity inside the FULC structure. As a result, the density of FULC specimens reduced, and their water absorption increased. Moreover, the introduction of foam leads to the reduction of FULC production cost significantly from 20.9 USD/m³ for FULC with F/W = 1/60 to 15.3 USD/m³ for FULC with F/W = 1/120 (Table 4).

Table 4. Engineering properties of the FULC specimens.

Mixtures	Dry density (kg/m ³)	Thermal conductivity (W/mK)		Water absorption (%)	Cost (USD/m ³)
		SSD*	OD**		
M1	726	0.454	0.178	44.4	18.6
M2	721	0.445	0.175	45.7	18.0
M3	717	0.438	0.168	46.9	17.5
M4	728	0.495	0.182	41.5	20.9
M5	719	0.441	0.171	46.7	15.6
M6	716	0.380	0.163	48.5	15.3

*SSD – saturated surface dry condition; **OD – oven dry condition

Although it can be seen the relationship between the dry density of the FULC and its compressive strength and water absorption rate through the data provided in Table 4 and Fig. 6 and 7, these relationships are clearly displayed in Fig. 9 and 10.

Fig. 9 shows the relationship between dry density and compressive strength. It can be expressed by equation (3) with $R^2 = 0.93$:

$$y = 1248.4 - 232.6x + 25.3x^2. \quad (3)$$

It is reasonable that the higher dry density of the FULC was proportional to its higher compressive strength value. As aforementioned, the lower the amount of foam in the FULC mixtures, the lower the porosity of the FULC samples. Thus, the denser structure of the FULC samples resulted in the higher dry density, which consequently leads to the higher compressive strength of the FULC samples, as can be seen in Fig. 9.

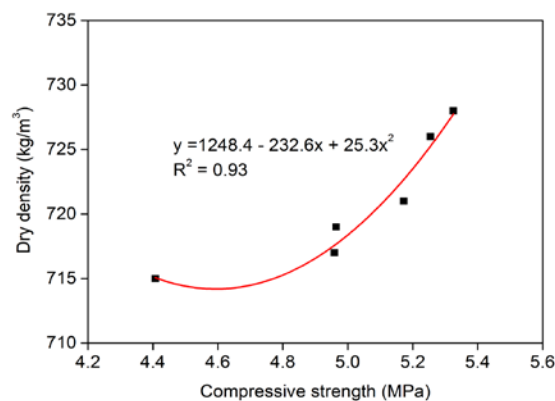


Figure 9. The relationship between dry density and compressive strength of the FULC specimens at 28 days.

Moreover, Fig. 10 shows the relationship between dry density and water absorption. There was an adverse relationship between dry density and water absorption, as shown in a representative equation (4) with $R^2 = 0.91$:

$$y = 523.2 + 10.9x - 0.14x^2. \quad (4)$$

The negative correlation is due to the characteristics of FA, whose crystal contained a considerable amount of quartz phase. Hence, the involvement of FA in the chemical reaction of the system is limited and thus releasing the gaps inside the FULC structure. The excessive addition of foaming agent commonly created air-voids and thereby, resulting in the low density and the low compressive strength [31]. Furthermore, the air-void parameters, including volume, size, and spacing, influenced strength and density [31]. It was also found that the air-void size distribution is one of the essential micro-properties affecting the strength of foam concrete [33].

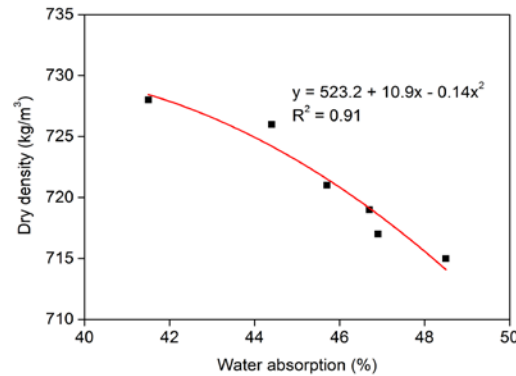


Figure 10. The relationship between dry density and water absorption of the FULC specimens at 28 days.

3.4. Thermal conductivity

The 28-day TC values recorded for the FULC specimens at both saturated-surface-dry (SSD) and oven-dry (OD) conditions are given in Table 4.

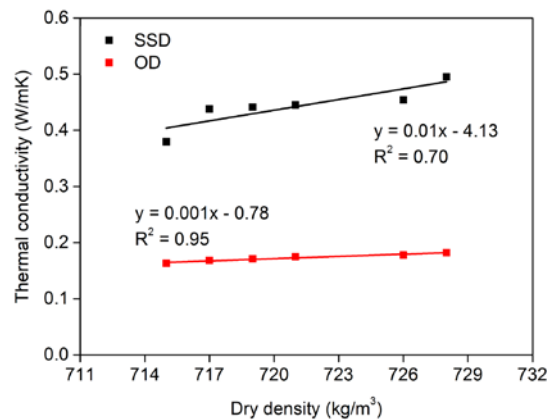


Figure 11. The relationship between dry density and thermal conductivity of the FULC specimens at 28 days.

As the results, the TC values were in the range of 0.380–0.495 W/(m.K) and 0.163–0.182 W/(m.K) for the FULC specimens in SSD and OD conditions, respectively. Thus, the SSD-TC of the FULC specimens was about 2.5 times higher than the OD-TC of the FULC specimens. This finding is supported by the previous results reported by Kim et al. [34] as the TC was proportional to the moisture of the specimens. The TC results from Table 4 also reveal that the effect of FA/GGBFS ratios on the TC of the FULC specimens was less significant than the impact of F/W ratios TC of the FULC specimens. Papa et al. [35] previously reported that higher void volume resulted in lower TC of the material. On the other hand, Fig. 11 shows the linear correlation between TC and the dry density of FULC specimens at the age of 28 days as higher dry density was associated with higher TC values.

3.5. The behavior of FULC under fire condition

To create the finite element models in ANSYS APDL software, multiple tasks have to be completed for the model to run correctly. In this thermal model plane, 55 was used for the wall. This element is available in the elements library of ANSYS APDL, as shown in Fig. 12.

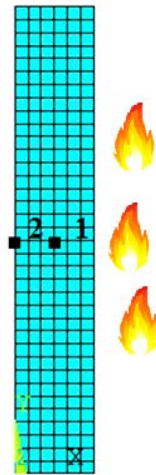


Figure 12. Finite element model.

Temperature distribution in the wall exposed to fire depended on space and time. The temperature of the points (Node 1 – the center of the wall and Node 2 – the inside surface of the wall) for the two types of walls, including the FULC wall and normal brick wall, was analyzed as shown in Fig. 13.

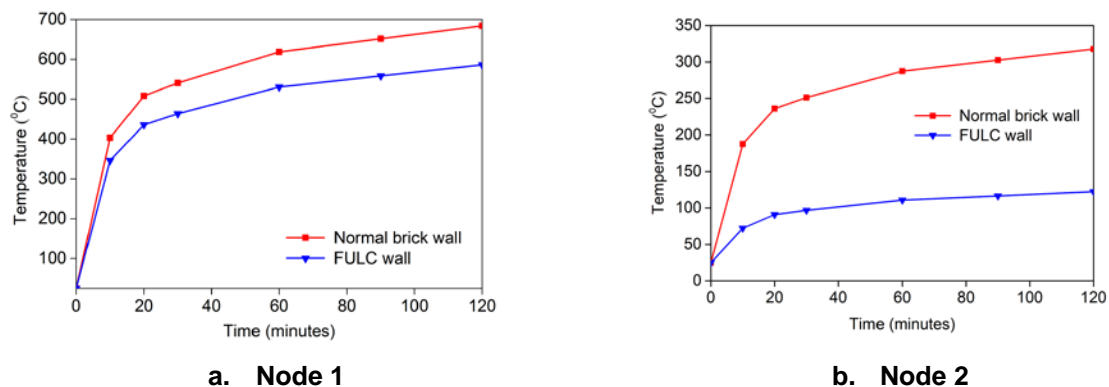


Figure 13. The temperature at Node 1 (a) and Node 2 (b) in the FULC wall and normal brick wall.

It is easy to observe the difference of temperature distribution between the center (Node 1) and outer points (Node 2) of the FULC wall and the normal brick wall. After 120 minutes of fire, the variation of maximum temperature at the center and surface of the normal wall brick and the FULC wall was 14.30 % and 61.49 %, respectively. As expected, the FULC wall had better insulation performance than the normal wall brick. This behavior is in good agreement with the result of the TC test.

4. Conclusions

The feasibility of the use of a ternary mixture of cement, GGBFS, and FA for producing FULC was investigated in this study. The mechanical and thermal properties of FULC were further evaluated. The following conclusions can be made based on the experimental outcomes:

1. 28-day compressive strength of the FULC ranged from 4.41 to 5.33 MPa, which can be classified as Grade 5.0 of foamed lightweight concrete as stipulated by TCVN 9029–2017 Vietnamese standard. There was an increase in the compressive strength of the FULC (from 4.96 MPa to 5.25 MPa) when using the lower amount of FA and a higher amount of GGBFS. Moreover, the inclusion of a higher amount of foam negatively affected the compressive strength of the FULC specimens as the reduced strength from 5.33 MPa to 4.41 MPa was observed.
2. Dry density and water absorption of the FULC at 28 days were in the ranges of 716–729 kg/m³ and 41.5–48.5 %, respectively. The higher the foaming agent amount, the lower the density, and the higher the water absorption rate of the FULC.
3. After 28 days, the thermal conductivity of the FULC in SSD and OD conditions were in the ranges of 0.380–0.495 and 0.163–0.182 W/mK, respectively. The inclusion of more foam resulted in more void volume and thus lower TC value. Foam contributed to the comfort of the building by lowering thermal

transfer. Furthermore, it is interesting to find that the effect of FA/GGBFS ratios on the TC of the FULC specimens was less significant than the effect of F/W ratios TC of the FULC specimens.

4. After 120 minutes under fire, the maximum temperature at the center of the FULC wall and the normal brick wall was 317.7 and 122.30 °C, respectively. Whereas, the maximum temperature at the outer surface of the FULC wall and the normal brick wall was 684.0 and 586.20 °C, respectively. Thus, The FULC exhibited better performance under fire conditions in comparison with the normal brick.

5. It could be observed from the SEM images of the FULC specimens that the air-void spaces were formed when adding a high amount of foam to FULC specimens. On the other hand, the foam not only affected the physical properties of FULC but also lowered the cost for the production of FULC when taking into account the effectiveness of optimization of the content of the use of a foaming agent. The material cost of the FULC mixtures ranged from 15.3–20.9 USD/m³.

6. Consequently, industrial waste products such as GGBFS and FA can be potentially used for the production of FULC. In future work, the characteristic of FULC incorporating various types of waste materials should be investigated to enhance the background of the present study.

5. Acknowledgment

The authors would like to express the sincere thanks to Huynh's research group at Can Tho University, Vietnam, for their kind assistance provided during the experimental works.

References

1. Othuman, M.A., Wang, Y.C. Elevated-temperature thermal properties of lightweight foamed concrete. *Construction and Building Materials*. 2011. 25(2). Pp. 705–716.
2. Kerali, A.G. Durability of compressed and cement-stabilised building blocks. [Online]. System requirements: Adobe Acrobat Reader. URL: <https://pdfs.semanticscholar.org/0796/d37441d7120d683f0388c40c4e557ef248ad.pdf> (date of application: 13.08.2019).
3. Kumar, N.V., Arunkumar, C., Senthil, S.S. Experimental study on mechanical and thermal behavior of foamed concrete. *Materials Today: Proceedings*. 2018. 5(2). Pp. 8753–8760.
4. Mydin, M.A.O., Wang, Y.C. Mechanical properties of foamed concrete exposed to high temperatures. *Construction and Building Materials*. 2012. 26(1). Pp. 638–654.
5. Lim, S.K., Tan, C.S., Lim, O.Y., Lee, Y.L. Fresh and hardened properties of lightweight foamed concrete with palm oil fuel ash as filler. *Construction and Building Materials*. 2013. 46. Pp. 39–47.
6. Pacheco-Torgal, F. Eco-efficient construction and building materials research under the EU Framework Programme Horizon 2020. *Construction and Building Materials*. 2014. 51. Pp. 151–162.
7. Zhang, Z., Provis, J.L., Reid, A., Wang, H. Geopolymer foam concrete: An emerging material for sustainable construction. *Construction and Building Materials*. 2014. 56. Pp. 113–127.
8. Jones, M.R., McCarthy, A. Preliminary views on the potential of foamed concrete as a structural material. *Magazine of Concrete Research*. 2005. 57(1). Pp. 21–31.
9. Korniyenko, S.V., Vatin, N.I., Gorshkov, A.S. Thermophysical field testing of residential buildings made of autoclaved aerated concrete blocks. *Magazine of Civil Engineering*. 2016. 4. Pp. 10–25.
10. Korniyenko, S.V. Advanced hygrothermal performance of building component at reconstruction of S. Radonezhskiy temple in Volgograd, MATEC Web of Conferences. 2016. 53.
11. Olivier, J.G., Maenhout, G.J., Muntean, M., Peters, J.A.H.W. Trends in global CO₂ emissions: 2016 report. [Online]. System requirements: Adobe Acrobat Reader. URL: <https://www.pbl.nl/sites/default/files/cms/publicaties/pbl-2016-trends-in-global-co2-emissions-2016-report-2315.pdf> (date of application: 13.08.2019).
12. Mikulčić, H., Klemeš, J.J., Vujanović, M., Urbanec, K., Duić, N. Reducing greenhouse gasses emissions by fostering the deployment of alternative raw materials and energy sources in the cleaner cement manufacturing process. *Journal of Cleaner Production*. 2016, 136. Pp. 119–132.
13. Gowri, R., Anand, K.B. Utilization of fly ash and ultrafine GGBS for higher strength foam concrete. *IOP Conference Series: Materials Science and Engineering*. 2018. 310.
14. Nambiar, E.K.K., Ramamurthy, K. Influence of filler type on the properties of foam concrete. *Cement and Concrete Composites*. 2006. 28(5). Pp. 475–480.
15. Hwang, C.L., Huynh, T.P. Effect of alkali-activator and rice husk ash content on strength development of fly ash and residual rice husk ash-based geopolymers. *Construction and Building Materials*. 2015. 101. Pp. 145–155.
16. Hwang, C.L., Tran, V.A. Engineering and durability properties of self-consolidating concrete incorporating foamed lightweight aggregate. *Journal of Materials in Civil Engineering*. 2016. 28(9).
17. Oluwale, O., Joshua, J., Nwagwo, H. Finite element modeling of low heat conducting building bricks. *Journal of Minerals and Materials Characterization and Engineering*. 2012. 11. Pp. 800–806.
18. Nguyen, T.C., Luu, X.B. Reducing temperature difference in mass concrete by surface insulation. *Magazine of Civil Engineering*. 2019. 88(4). Pp. 70–79.

19. Lam, T.V., Nguyen, T.C., Bulgakov, B.I., Anh, P.N. Composition calculation and cracking estimation of concrete at early ages. Magazine of Civil Engineering. 2018. 82(6). Pp. 136–148.
20. Chuc, N.T., Lam, T.V., Bulgakov, B.I. Designing the composition of concrete with mineral additives and assessment of the possibility of cracking in cement-concrete pavement. Materials Science Forum. 2018. 931. Pp. 667–673.
21. Fakury, R.H., Casas, E.B.L., Júnior, F.P.F., Abreu, L.M.P. Numerical analysis of the Eurocode assumptions for temperature distribution in composite steel and concrete beams. Mecánica Computacional. 2002. XXI. Pp.1998–2008.
22. Jacob, B., Balaji, A., John, E. Behaviour of concrete structures under fire - a comparative study between IS 456: 2000 and finite element software ANSYS. American Journal of Engineering Research. 2013. 3. Pp. 62–66.
23. Casano, G., Piva, S. Transient heat conduction in a wall exposed to a fire: an analytic approach. Journal of Physics: Conference Series. 2017. 796(1). 11 p.
24. Wang, A., Zhang, C., Sun, W. Fly ash effects: III. The micro aggregate effect of fly ash. Cement and Concrete Research. 2004. 34(11). Pp. 2061–2066.
25. Aghaeipour, A., Madhkan, M. Effect of ground granulated blast furnace slag (GGBFS) on RCCP durability. Construction and Building Materials. 2017. 141. Pp. 533–541.
26. Tangpagasit, J., Cheerarot, R., Jaturapitakkul, C., Kiattikomol, K. Packing effect and pozzolanic reaction of fly ash in mortar. Cement and Concrete Research. 2005. 35(6). Pp. 1145–1151.
27. Kearsley, E.P., Wainwright, P.J. The effect of high fly ash content on the compressive strength of foamed concrete. Cement and Concrete Research. 2001. 31(1). Pp. 105–112.
28. Kearsley, E.P., Wainwright, P.J. The effect of porosity on the strength of foamed concrete. Cement and Concrete Research. 2002. 32(2). Pp. 233–239.
29. Hajimohammadi, A., Ngo, T., Mendis, P., Kashani, A., van Deventer, J.S.J. Alkali activated slag foams: The effect of the alkali reaction on foam characteristics. Journal of cleaner production. 2017. 147. Pp. 330–339.
30. Jiang, J., Lu, Z., Niu, Y., Li, J., Zhang, Y. Study on the preparation and properties of high-porosity foamed concretes based on ordinary Portland cement. Materials & Design. 2016. 92. Pp. 949–959.
31. Nambiar, E.K.K., Ramamurthy, K. Air-void characterisation of foam concrete. Cement and Concrete Research. 2007. 37(2). Pp. 221–230.
32. Cebeci, O.Z. Pore structure of air-entrained hardened cement paste. Cement and Concrete Research. 1981. 11(2). Pp. 257–265.
33. Kearsely, E.P., Visagie, M. Specialist techniques and materials for construction. 1999. 11 p.
34. Kim, K.H., Jeon, S.E., Kim, J.K., Yang, S. An experimental study on thermal conductivity of concrete. Cement and Concrete Research. 2003. 33(3). Pp. 363–371.
35. Papa, E., Medri, V., Kpogbemabou, D., Morinière, V., Laumonier, J., Vaccari, A., Rossignol, S. Porosity and insulating properties of silica-fume based foams. Energy and Buildings. 2016. 131. Pp. 223–232.

Contacts:

Trong-Phuoc Huynh, htphuoc@ctu.edu.vn

Nguyen-Trong Ho, ntrong.ho@gmail.com

Phuong-Trinh Bui, buiphuongtrinh@hcmut.edu.vn

Ngoc-Duy Do, dongocduy29@gmail.com

Trong-Chuc Nguyen, ntchuc.mta198@gmail.com



Theory of determining the frequency of natural oscillations of span structures

A.M. Sychova*, S.V. Zarin, A.V. Matskevich

Military Space Academy named after A.F. Mozhaysky, Saint Petersburg, Russia

* E-mail: amsychova@yandex.ru

Keywords: cracks, reinforced concrete span structure, vibrodiagnostics, natural oscillation frequency, Griffith energy approach

Abstract. The article is devoted to the development of mathematical dependence of determination the natural oscillation frequencies of reinforced concrete span structures according to the physical, mechanical, geometric and energy characteristics of their elements and materials. Carrying out and processing the results of the experimental studies as well as the analysis of literature revealed the ways of reducing the error of the existing mathematical dependences in determining the natural oscillation frequencies of the span structures. The use of Griffith's energy approach, the account of the nonlinear law of stiffness changes and the subsequent approximation of the experimental data made it possible to reduce the error of the mathematical dependence in the process of determination the natural oscillation frequencies of span structures by 4.4 times. The effect obtained makes it possible to apply the developed mathematical dependence to monitor the technical condition of the reinforced concrete span structures and the numerical determination of the boundaries of their technical condition categories.

1. Introduction

The object of research is span-bearing reinforced concrete structures, which make up 40% of the total volume of building structures. One of the ways to assess their technical condition is vibration diagnostics.

Today vibrodiagnostics is an extremely popular is an extremely popular method of technical monitoring because it gives the possibility to assess the technical condition of different systems. Also it can be used to assess seismic loads on buildings and structures, both of natural (earthquakes, wind loads) [1, 2] and of man-made origin (aircraft take-off, launch of space rockets, traffic, etc.) [3].

Among the advantages of vibrodiagnostics the reduced (compared to other methods of nondestructive control) errors [4, 5] can be called. In addition, the natural oscillations frequency as a diagnostic feature of vibrodiagnostics takes into account the physico-mechanical, geometric, structural and other factors that characterize the decrease of the bearing capacity of the structural element in the assemblage.

By means of vibrodiagnostics the technical condition of various buildings and structures [6–8] can be assessed. On the one hand, they include unique buildings, such as launch facilities of rocket and space complexes, the source of structural vibrations in them being the launch of the carrier rocket [9]. On the other hand, it can be buildings of historical heritage [10, 11], bridge structures [12, 13] or concrete columns [14], the source of oscillation in them is the load of man-made origin (technoseismic).

In the process of assessing the technical condition category of buildings and structures the relationship of diagnostic signs of vibrodiagnostics with defects and destruction occurring in structures is of special interest [15].

The article [16] gives the analysis of the results of the vibration method used to determine the degree of damage in the structures. The software module developed for the localization of these damages is also given. The article shows that the natural frequencies of structure vibration, as well as the forms of their



oscillations are the most important characteristics that allow to obtain information about the state of the structure.

In [17] a new feature is developed and proposed for the vibration methods – the index of damage. This step has been done in order to detect and locate damage in composite beams. The new method is compared with similar methods, for example, the deformation energy method.

The article [18] discusses the possibility of using the computational and intelligent methods of structural monitoring of the composite materials. It is emphasized that the composite materials, unlike metal, can have an ideal appearance without visible damage, although they may have many microdefects inside. In this case, it is necessary to use the SHM (Structural Health Monitoring) system.

In [19] the problem of damage detection in building constructions at external excitation is considered. The paper proposes a new index called the modal participation coefficient which is obtained on the basis of experimental data on the environmental vibration assessment.

In article [20] it is shown that at the origin of microcracks or at the development of the main crack in a structure the potential energy of deformation which can create an acoustic signal is released. This signal can be recorded on the surface of the product as an acoustic emission.

As the literature review shows, the relationship of vibrodiagnostic features with the characteristics of defects and damages formed in the structure during operation, as well as with the energy of crack formation has not been considered up to date.

In addition, there is no data concerning the relationship of diagnostic features with the structure, phase composition of the construction material, as well as the presence of microdefects in it which are not detected during the visual inspection.

The present international normative documents [21, 22] do not include the quantitative indicators that determine the categories of technical condition of buildings and structures and the safety of their operation.

The existing methods of quality monitoring of the building structure technical condition require the determination of a large number of physical and mechanical characteristics and geometric parameters of elements and materials of structures for control calculations. The access to building structures for determining these characteristics is difficult in most of the buildings and structures in use (ceramic tiles, plaster, drywall, flooring, suspended ceilings, etc.).

Then it will be urgent to develop the quantitative characteristics of the transition of one category of the technical condition of the structure into another, which will increase the accuracy and efficiency of determining its technical condition. The basis of the development is the experimental determination of the natural oscillation frequency.

The goal of the study: to increase the reliability of monitoring the technical condition of load-bearing reinforced concrete structures by using vibration diagnostics.

Research problem: on the basis of the conducted experimental studies, we obtain a mathematical dependence of the natural vibration frequency of span structures on the physical-mechanical, geometric, and energy characteristics of their elements and materials; error of the obtained mathematical dependence should be significantly reduced in comparison with the existing ones.

2. Methods

From the analysis of the literature it follows that the accumulation of defects and damages in the span concrete beam causes a decrease in its rigidity and the frequency of its own oscillations under the load action [23].

Analysis of the possibility of calculating the natural oscillation frequency of the structure shows that there is an analytical formula for determining the dependence of the natural oscillation frequency of span structures on a number of parameters, including the spatial stiffness of the section (1), [24]. However, the error in the determination of the natural oscillation frequencies for this dependence is as high as 35 %.

$$\lambda = \frac{\phi}{L_0^2} \sqrt{\frac{D}{m}}, \quad (1)$$

where $D = EI$ is spatial stiffness of the structure (it changes at the formation and the development of defects and damages), Nm^2 ; E is reduced modulus of elasticity of the material of construction, Pa ; I is moment of inertia of the cross section, m^4 ; ϕ is dimensionless frequency factor depending on the type of the construction

and the method of its fixing; L_0 is construction span, m; m is the structure mass distributed in the span per unit length (takes into account the actual load on the structure), Hsec^2/m^2 .

The task of the study was to develop a mathematical formula of determining the frequency of natural oscillations of span concrete structures with reduced error for its further application to control their technical condition.

The main scientific idea of the work is as follows.

1. To date the following relationship, Formula (2), is used to calculate the spatial stiffness D in Formula (1). This dependence makes it possible to determine the value of stiffness only at the final stage of the structure operation, Fig. 1, due to the fact that it takes into account the physical and mechanical characteristics of the structure's material prior to their destruction.

$$D = E_b \left(I + I_s \alpha + I_s' \alpha' \right), \quad (2)$$

where E_b is the deformation module of the compressed concrete, Pa; I is the moment of inertia of the concrete section relative to the center of gravity of the reduced cross-section of the element, m^4 ; I_s, I_s' is moments of inertia of the cross-sectional areas, respectively, of the stretched and compressed reinforcement relatively to the center of gravity of the reduced cross-section of the element, m^4 ; α is coefficient of reduction of reinforcement to concrete.

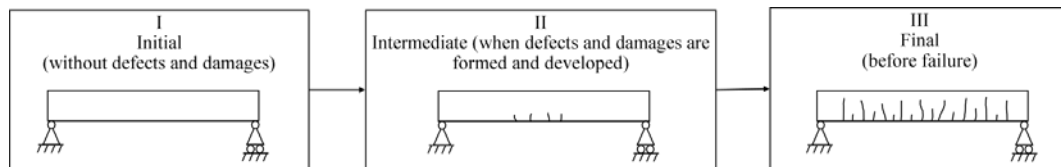


Figure 1. Stages of the span structure operation.

The work suggested that to reduce large errors in the determination of the natural oscillation frequency (Formula 1) it is necessary to consider the stiffness changes over the full life cycle of the construction, which in turn will allow to take into account nonlinear work of concrete during the operation of long-span structures. This can be realized if we take into account the law of rigidity variability in the process of calculation.

In the Formula 1 the paper proposes to use the dependence in order to calculate the spatial stiffness (3), [9]. The choice is dictated by the fact that it includes the law of rigidity variability. This law is based on the force approach and is taken into account by the value of the ratio of the bending moment from the external load to the limiting bending moment perceived by the cross section (M/M_{\max}).

$$D = kD_0 \left\langle 1 - \left[1 - \frac{D_{\min}}{kD_0} \right] \frac{M}{M_{\max}} \right\rangle, \quad (3)$$

where k is correction factor depending on the duration of the load; D_0 is stiffness of the cross section of the element under the assumption of a linear relationship between stresses and strains and the absence of cracks, Nm^2 ; D_{\min} is the minimum value of the section stiffness in the state preceding its destruction, Nm^2 ; M is bending moment from the external load, Nm ; M_{\max} is the ultimate bending moment resisted by the section, Nm .

In addition, this mathematical dependence deals with two stiffness: the stiffness of the cross section of the element under the assumption of a linear relationship between loads and strains and the absence of cracks, D_0 , and the minimum value of the stiffness of the section in the state preceding its destruction, D_{\min} .

It is assumed that the use of Formula (3) in Formula (1) will lead to a significant reduction in the error in determining the natural oscillation frequencies of span structures. This effect should be especially evident at the initial and final stage of the design, since the dependence (3) includes the rigidity of the structure, D at these stages of its operation. But, since the law of rigidity variability (M/M_{\max}) is based on the force approach which does not reflect the nonlinear operation of concrete at the intermediate stage of the structure operation the error is likely to change insignificantly.

2. It is assumed that since the decrease in the frequency of natural oscillations and spatial stiffness is connected with the formation of defects and damage, then in the dependence (3) it is necessary to use the energy law reflecting the mechanics of destruction of the construction material. Further reduction of the error can be realized by using energy rather than force approach, for example Griffith's approach [24] (Formula 4)

in order to reflect the law of rigidity variability. This dependence is derived by Griffith for brittle materials which are known to include concrete.

$$\Delta U = 2l\gamma, \quad (4)$$

where l is crack length, m; γ is surface crack energy, Nm.

The energy approach can take into account not only the geometric characteristics of structures (in terms of l) but also the physical and chemical characteristics of the material (in terms of γ). Their joint contribution will allow to take into account the nonlinear operation of concrete and reduce the error of numerical determination of the natural oscillation frequency of span structures.

3. Results and Discussion

To confirm the assumptions made in the work it is necessary to solve the following steps:

1) while determining (on the basis of experimental data) the frequency of natural oscillations of the span structures by substituting Formula (3) in Formula (1), Formula (5) obtained allows to assess the magnitude of the error

$$\lambda = \phi \sqrt{\frac{kD_0 \left\langle 1 - \left[1 - \frac{D_{\min}}{kD_0} \right] \frac{M}{M_{\max}} \right\rangle}{mL_0^4}}; \quad (5)$$

2) to carry out the experimental investigations in order to establish the relationship between the natural frequency of the span structures and the energy of destruction according to Griffith, and correspondingly, the characteristics that are reflected in this formula: defects and damages emerging in construction is indicator l and physico-chemical characteristics of the materials of these structures is figure γ .

3) to identify the type of function describing the nonlinearity of changes in the law of stiffness variability based on Griffith's energy approach; to derive a new mathematical dependence and determine the magnitude of its error.

In accordance with the tasks stated, at the first stage the experimental studies were carried out in order to establish the relationship between the natural oscillation frequency of the structure and the index M/M_{\max} (Formula 3).

The experiment was carried out on the reinforced concrete beams of factory production 1 PB-10-1P, their parameters being shown in Table 1 and Fig. 2 and 3.

Table 1. Geometrical and physical-mechanical parameters of beams 1 PB-10-1P and their elements.

Brand	Dimensions, mm									Weight, kg	E_b , MPa	E_s , MPa
	L	L_0	b	b'	h	h_0	a	a'	d			
1 PB-10-1P	1030	930	120	80	65	53	12	18	4	20	3×10^4	2×10^5

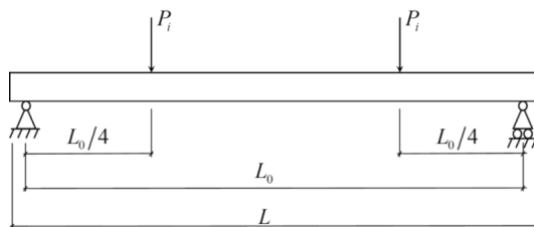


Figure 2. The rated scheme of the beam's 1 PB-10-1P.

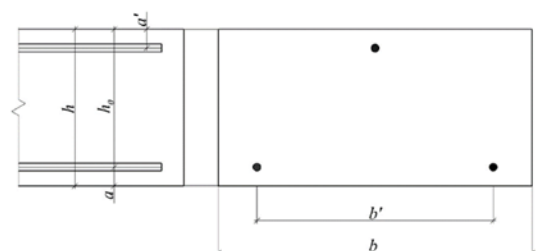


Figure 3. The beam cut 1 PB-10-1P.

To ensure a constant bending moment in the middle of the span the rated scheme shown in Fig. 2 was used.

At the initial stage the sample without defects and damages was fixed on the stand (Fig. 4) and the first forms of natural oscillations of the sample were excited while determining its natural frequencies (Fig. 5) with the device VIC-3-2.



Figure 4. Fixing the test sample on the stand.



Figure 5. Excitation of the first forms of the sample oscillation with the determination of its natural frequencies.

Next, a step-by-step application a static load to the sample was performed (Fig. 6) on the test press IP-100 with the increments of not more than 10 % of the destructive load, followed by a repetition of the initial stage. At the final stage a destructive load was applied to the sample and the natural oscillation frequency of the beam was estimated.



Figure 6. Load application to the sample according to the diagram (Figure 2).

The readings obtained were recorded into the table. After each step of load application the value M/M_{\max} was calculated and a map of defects was drawn up: the total length of the cracks was determined; the spalling of the concrete compressed zone, the pulling of the reinforcement and its rupture in the stretched zone, and so on were fixed.

Then the dependence of the beam natural oscillation frequency on the ratio value of the bending moments was constructed, M/M_{\max} , Fig. 7.

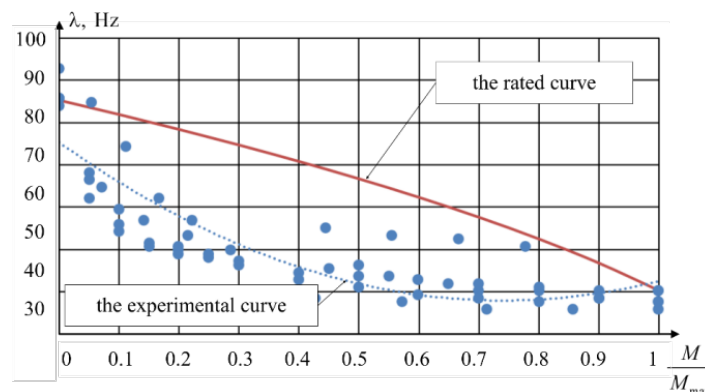


Figure 7. The rated and experimental graphs of the dependence of the natural oscillation frequency on the relative bending moment.

As we can see from the figure, the error of the rated determination of the natural oscillation frequency in accordance with the proposed Formula (5) at the initial (without defects) and final (before destruction) stage of the construction operation is greatly reduced (as shown by the comparison of experimental and calculated data, from 35 to 8 %, i.e. 4.4 times), which confirmed earlier assumptions and differs significantly from the

results of other authors [4]. From the figure it also follows that, unlike the experimental curve, the rated one has a linear character. This special feature may be the reason why the error of the mathematical model remains the same at the intermediate stage of operation of the beam, which also confirms the assumptions made. This implies the need to move to a nonlinear form of dependence describing the law of stiffness changes in Formula 5. Proceeding from the nature of the experimental curve, it is assumed to be described by the exponential dependence properly.

At the second stage, in accordance with the tasks of the study, it was necessary to establish a correlation between the frequency of natural vibrations of the beam and the energy of destruction according to Griffith and the geometric and physical-chemical characteristics of the beam's material (reinforced concrete).

Table 2 shows the relationship obtained on the basis of the experimental data between the natural oscillation frequency of the span beam and the relative length of the cracks formed in it when the load is applied. This relationship is obtained in the work for the first time. The presence of cracks was assessed visually. The table shows that with an increase in the relative length of cracks during the transition from the initial to the final stage of the beam operation the frequency of the natural oscillations is reduced by 2.1 times.

Table 2. The relationship between the natural oscillation frequency of the beam and the relative cracks length.

The natural frequency, λ , Hz	82	72	63	57	50	45	42	41	40	38	38
Relative total cracks length	0	0.1	0.2	0.3	0.4	0.5	0.6	0.7	0.8	0.9	1

Then, in order to identify the relationship of the natural oscillation frequencies of the span structures with the presence of microdefects in them and with the physical and chemical properties of the materials of these structures, electron microscopy of the samples (Fig. 8) at the initial and the final stages of the span structure, as well as their derivatographic analysis (Fig. 9, Table 3) were performed.

However it was assumed that the magnitude λ will be interconnected not only with the length of the visually defined crack but with the presence of microcracks, their contribution to the process of reducing the bearing capacity and the subsequent destruction of the concrete beam being very large. In other words, if there are no visible cracks on the surface of the concrete, and the number of invisible microcracks increases and the bearing capacity of the span structure falls, this effect will affect the value of the frequency of its own oscillations.

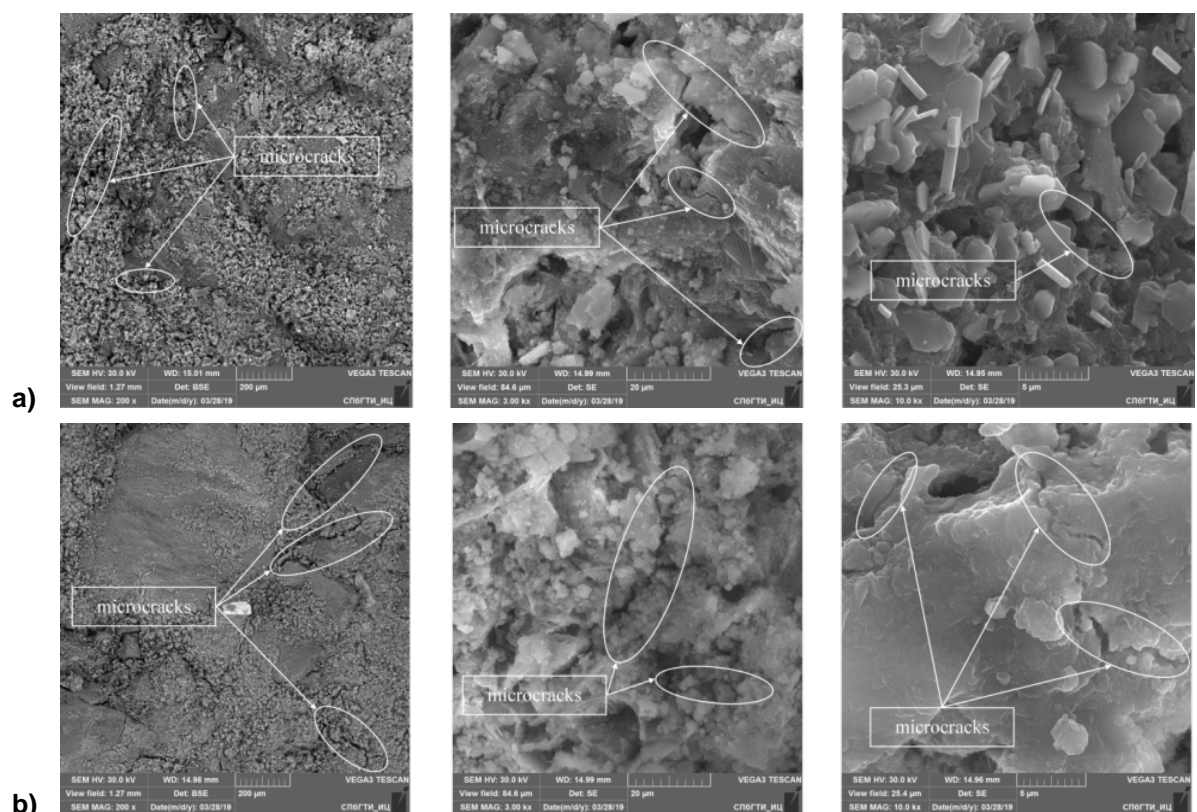


Figure 8. Results of concrete samples data processing by means of the electron microscopy: a) the initial stage of the structure operation, b) the final stage of the structure operation.

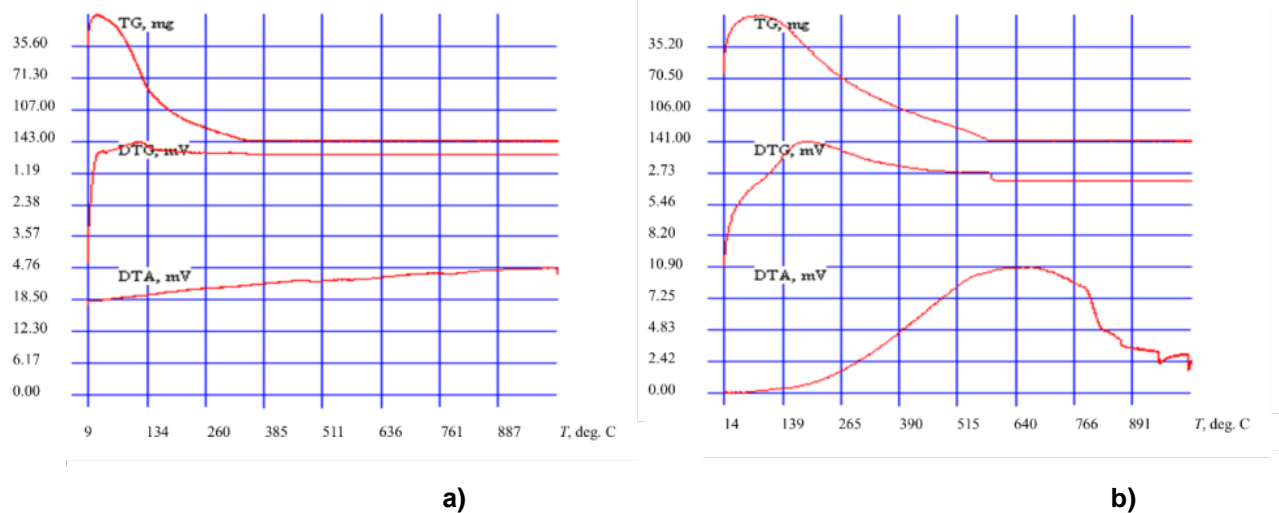


Figure 9. Data of the derivatographical analysis of samples:
a) the initial stage of structure operation, b) the final phase of structure operation.

According to the results of analysis of microscopic tests the relative density of microcracks, ρ_{rel} , m^{-1} , as the ratio of the total length of cracks of the structure to its surface area was obtained (Table 3).

Table 3. Results of physical and chemical analysis of samples.

Stage of the structure operation	Natural oscillation frequency, Hz	Total density of macrocracks, ρ_{rel} , m^{-1}	Total density of microcracks, ρ_{rel} , m^{-1}	Loss of water in the gel phase
Initial	85	0	6800	67
Final	40	22	77109	33

Table 3 shows that the total density of microcracks increases by more than an order of magnitude with a decrease in the natural oscillation frequency of the span structure by 2.1 times. In this case the total density of microcracks increases only by 2 times. This may indicate that the presence of macrocracks plays an important role in reducing the frequency of natural vibrations of the concrete structure and this value can reflect the internal invisible processes of destruction in the material.

The derivatographic analysis of the samples carried out showed that the amount of water in the gel phase at the final stage of the structure's operation as regards the initial one falls by 2 times. This fact can probably be explained by the fact that the gel phase as a component of the cement stone of the span beam is more brittle in relation to other phases and is a source of the formation and development of cracks. In this case the destruction of this phase occurs as shown also by the decrease in the amount of chemically bound water in it [25].

Physical and chemical studies carried out confirm the assumption about the interrelation of both geometric and physico-chemical characteristics of the material with the frequency of natural oscillations of the superstructure made from this material. These results are obtained for the first time.

Further it was necessary to determine the value of the surface energy of cracks included in Griffith's formula. Due to the complexity of determining this value on the edge angle of wetting because of the capillary-porous structure of the concrete, a search was made for the physical value of the material surface by which it can be determined. Analysis of the literature data showed that when increasing the surface hardness of non-metallic inorganic materials their surface energy also increases [26].

It was suggested that if we derive a mathematical relationship between these indicators, then after measuring the hardness of the crack surface, it is possible to determine its surface energy.

Proceeding from the above mentioned conclusions, the results of the approximation of the experimental data (Fig. 10) gave the possibility to obtain for the first time the empirical dependence of the surface energy of nonmetallic bodies of different nature on their hardness according to Mohs scale, Formula (6).

$$\gamma = 0.35e^{0.32H} \text{ Mohs}. \quad (6)$$

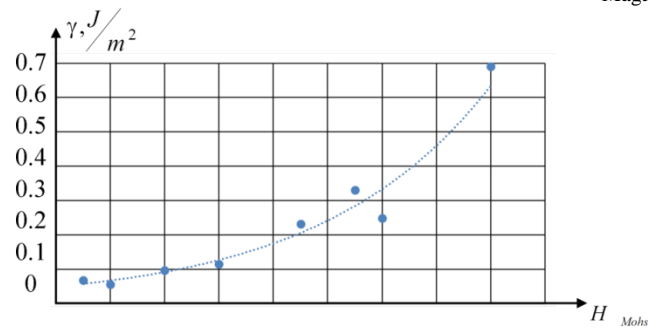


Figure 10. Dependence of surface energy of non-metallic materials on their hardness according to Mohs scale.

The dependence obtained was used to calculate the surface energy of cracks in the experimental beam, which allowed to calculate the relative failure energy according to Griffith, $\Delta U/\Delta U_{\max}$.

At the third stage, the mathematical processing of experimental data by using the regression analysis was carried out in order to identify the type of function describing the nonlinearity of the change of the law of stiffness variability on the basis of Griffith's energy.

The output parameter and the variable factors are shown in Table 4.

As an output parameter the stiffness variable function obtained from Formula (5) was used.

Table 4. Initial data for the construction of mathematical equations.

$Y = \frac{kD_0 - \frac{\lambda^2 L_0^4 m}{\phi^2}}{kD_0 - D_{\min}}$	the stiffness variability function
$X_1 = \frac{P}{P_{\max}}$	the relative load
$X_2 = \frac{n}{n_{\max}}$	the relative number of cracks
$X_3 = \frac{\Delta U}{\Delta U_{\max}}$	the relative energy according to Griffith
$X_4 = \frac{a_{crc}}{a_{crc_{\max}}}$	the relative crack's width

Linear and exponential types of equations were used in the construction of the models. For the convenience of the coefficients comparison in the regression equations relative variable parameters were used.

The obtained regression equations of various types and classes are given below. For each equation the calculated and tabular values of Fisher's criterion are given, by means of their comparison the adequacy of the equations obtained was estimated.

A linear model describing the individual influence of each of the four factors X_1, X_2, X_3, X_4

$$Y = 0.68 - 0.04X_1 + 0.93X_2 - 2.40X_3 + 0.80X_4. \quad (5)$$

Fisher's criterion rated is 2.92.

Fisher's criterion table $F(60.56) = 1.55$.

$2.92 > 1.55$, hence the model describes the experimental data adequately.

An exponential model describing the individual influence of each of the four factors X_1, X_2, X_3, X_4

$$Y = e^{0.02 - 3.54 X_1 + 2.67 X_2 - 6.53 X_3 + 1.62 X_4}. \quad (6)$$

Fisher's criterion rated is 24.01.

Fisher's criterion table $F(60.56) = 1.55$.

$24.01 > 1.55$, therefore, the model describes the experimental data adequately and properly.

From the Formulas (7 and 8) it follows that the most significant factor is the relative energy of crack formation according to Griffith, and the nonlinear exponential dependence (8) is more adequate according to Fisher's criterion in regard to the linear one, which confirms the previously stated assumption.

Further, we approximate the experimental data by the least squares method to obtain the dependence of the natural frequency of the structures on the relative Griffith energy, Formula 9.

$$\lambda = \phi \sqrt{\frac{kD_0 \left\langle 1 - \left[1 - \frac{D_{\min}}{kD_0} \right] \left(1 - e^{-5 \frac{\Delta U}{\Delta U_{\max}}} \right) \right\rangle}{mL_0^4}}. \quad (9)$$

The experimental and new calculated curves obtained from the approximation results are shown in Fig. 11. The figure shows that the error has significantly decreased (as shown by the comparison of experimental and calculated data, the error has decreased up to 8 % at all stages of the structure operation), which confirms the previously stated assumption. In comparison with the existing mathematical dependence [7], the error is reduced by 4.4 times.

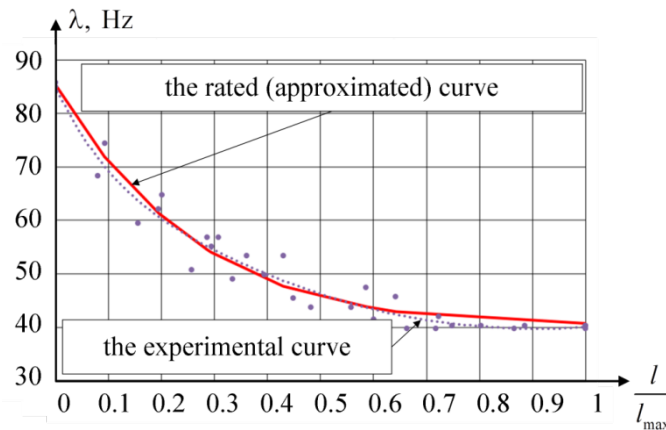


Figure 11. The dependence of the natural oscillation frequency of the beam on the relative energies according to Griffith.

The validity of the obtained model application for the real structures and buildings is justified by the application of the theory of similarity [9]:

- 1) the physical similarity of the mathematical dependence developed is taken into account by the corresponding coefficients in Formulas 1 and 3 which it includes;
- 2) the law of the stiffness variability on the basis of Griffith energy used in the mathematical dependence developed is chosen in the form of dimensionless quantity.

4. Conclusions

1. On the basis of Griffith's energy approach the mathematical dependence of the determination of the natural oscillation frequency of the span structures is developed.
2. It is shown that the error of the mathematical dependence developed is reduced by 4.4 times in comparison with the existing formulas.
3. It is shown that the value of the natural oscillation frequency of the span beam is reduced by 2.1 times in the presence of defects and destruction at the final stage of its operation in regard to the initial one.
4. According to the physico-chemical investigations it is shown that at the final stage of the structure operation the relative density of microcracks in the span beam increases by an order of magnitude in regard

to the initial stage, the relative density of macrocracks increases by 2 times, the amount of gel water being reduced by 2 times.

5. For the first time the mathematical formula linking the surface energy of nonmetallic inorganic materials with the hardness of their surface is obtained.

References

1. Tang, T., Yang, D., Wang, L., Zhang, J., Yi, T. Design and application of structural health monitoring system in long-span cable-membrane structure. *Earthquake Engineering and Engineering Vibration*. 2019. Vol. 18. No. 2. Pp. 461–474.
2. Vatin, N.I., Ivanov, A.Y., Rutman Y.L., Chernogorskiy, S.A., Shvetsov, K.V. Earthquake engineering optimization of structures by economic criterion. *Magazine of Civil Engineering*. 2017. No. 8. Pp. 67–83. URL: <https://doi.org/10.18720/MCE.76.7>
3. Mirsaidov, M.M., Abdikarimov, R.A., Vatin, N.I., Zhgutov, V.M., Khodzhaev, D.A., Normuminov, B.A. Nonlinear parametric oscillations of viscoelastic plate of variable thickness. *Magazine of Civil Engineering*. 2018. 82(6). Pp. 112–126. DOI: 10.18720/MCE.82.11
4. Ulybin, A.V. On the Choice of concrete strength inspection methods of ready-built structures. *Magazine of Civil Engineering*. 2011. 4(22). Pp. 10–15. DOI: 10.5862/MCE.22.1
5. Holmin, M.S., Ulybin, A.V., Frolov, A.V. The deviation in the calculation of the load-carrying ability of the slabs in the survey of buildings. *Construction of Unique Buildings and Structures*. 2017. 4(55). Pp. 20–35. DOI: 10.18720/CUBS.55.2
6. Gatti, M. Elastic period of vibration calculated experimentally in buildings hosting permanent GPS stations. *Earthquake Engineering and Engineering Vibration*. 2018. Vol. 17. No. 3. Pp. 607–625.
7. Savin, S.N. Dynamic monitoring of building structures on the example of the concert hall "Pushkinskiy" ramp in Moscow. *Magazine of Civil Engineering*. 2012. 7(33). Pp. 58–62.
8. Gong, T., Li, Q., Wang, W. Evaluation of the fishbone model in simulating the seismic response of multistory reinforced concrete moment-resisting frames. *Earthquake Engineering and Engineering Vibration*. 2019. Vol. 18. Issue 2. Pp. 315–330.
9. Sycheva, A.M., Zarin, S.V., Mackevich, A.V., Aleshichev, S.E., Abu-Hasan, M.S. Opredelenie tekhnicheskogo sostoyaniya proletrykh konstrukcij po chastote sobstvennykh kolebanij [Evaluation of technical state of superstructures based on natural vibration frequency]. *Transportnoe stroitel'stvo*. 2019. No. 3. Pp. 25–28. (rus)
10. Comanducci, G., Cavalagli, N., Gioffré, M., Trequattrini, M., Ubertini, F. Ambient vibration testing of a monumental fountain by contact and non-contact sensing techniques. *Procedia Engineering*. 2017. Vol. 199. Pp. 3338–3343.
11. Saisi, A., Gentile, C., Ruccolo, A. Static and dynamic monitoring of a Cultural Heritage bell-tower in Monza. *Procedia Engineering*. 2017. Vol. 199. Pp. 3356–3361.
12. Song, S., Qian, Y., Liu, J., Xie, X., Wu, G. Time-variant fragility analysis of the bridge system considering time-varying dependence among typical component seismic demands. *Earthquake Engineering and Engineering Vibration*. 2019. Vol. 18. Issue 2. Pp. 363–377.
13. Zhou, Z. Vibration-based Damage Detection of Bridge Superstructures. Saarbrücken, 2008. 300 p.
14. Lyapin A., Shatilov Y. Vibration-based damage detection of the reinforced concrete column. 2nd International Conference on Industrial Engineering. Chelyabinsk, 2016. Pp. 1867–1871. URL: <https://doi.org/10.1016/j.proeng.2016.07.184>
15. Sokolov, V., Musorina, T., Starshinova, E., Popovych, I. Assessment stability and informative of diagnostic matrix in analysis states of reinforced concrete slab. [Online]. MATEC Web of Conferences. St. Petersburg, 2016. URL: <https://doi.org/10.1051/matec-conf/20167304016>
16. Lyapin, A., Shatilov, Y. Vibration-Based Damage Detection of Steel Pipeline Systems. In book: *Non-destructive Testing and Repair of Pipelines*. Luxembourg, 2018. Pp.63–72. URL: https://doi.org/10.1007/978-3-319-56579-8_5
17. Manoach, E., Warminski, J., Kloda, L., Teter, A. Numerical and experimental studies on vibration based methods for detection of damage in composite beams. *Composite Structures*. 2017. Vol. 170. Pp. 26–39. URL: <https://doi.org/10.1016/j.compstruct.2017.03.005>
18. Sebastião, S., Cunha, Jr., Díaz, Y., Gomes, G., Alexandrino, P. The use of intelligent computational tools for damage detection and identification with an emphasis on composites. *Composite Structures*. 2018. Vol. 196. Pp. 44–54. DOI: 10.1016/j.compstruct.2018.05.002
19. Park H., S., Oh B., K. Damage detection of building structures under ambient excitation through the analysis of the relationship between the modal participation ratio and story stiffness. *Journal of Sound and Vibration*. 2018. Vol. 418. Pp. 122–143. URL: <https://doi.org/10.1016/j.jsv.2017.12.036>
20. Nikol'skij, S.G. Ekspress-metod kontrolya erozii betona [Express method of concrete erosion control]. *Magazine of Civil Engineering*. 2008. No. 2(2). Pp. 39–44. (rus)
21. ISO 2394: General principles on reliability for structures, ISO/TC 98/SC 2 N. International Organization for Standardization, 2015.
22. EN 1990:2001. Eurocode. Basis of structural design. Brussels: CEN, 2002. 89 p.
23. Zarin, S.V., Ischakov, Sh.Sh., Kovalev, F.E. On the probability of the development of the diagnostic feature of decline the bearing capacity of structures under random dynamic loads. *International Multi-Conference on Industrial Engineering and Modern Technologies «FarEastCon»*. Vladivostok, 2019. URL: <https://doi.org/10.1088/1757-899X/463/3/032010>
24. Babkov, V.V., Mohov, V.N., Kapitonov, S.M., Komohov, P.G. *Strukturoobrazovanie i razrushenie cementnykh betonov* [Structure formation and destruction of cement concretes]. Ufa: UPK, 2002. 376 p.
25. Svatovskaya, L.B., Sychova, A.M., Sychov, M.M. Silica sol properties for construction. [Online]. MATEC Web of Conferences, St. Petersburg, 2018. URL: <https://doi.org/10.1051/matecconf/201819303034>
26. Sychova, A.M., Svatovskaya, L.B., Starchukov, D.S., Soloviova, V.Y., Gravit, M.V., The improving of the concrete quality in a monolithic clip. *Magazine of Civil Engineering*. 2018. No. 4. Pp. 3–14. DOI: 10.18720/MCE.80.1

Contacts:

Anastasia Sychova, amsychova@yandex.ru

Sergey Zarin, sergeyzarin27091989@gmail.com

Andrey Matskevich, andmats@yandex.ru

© Sychova, A.M., Zarin, S.V., Matskevich, A.V., 2020



DOI: 10.18720/MCE.98.4

Mechanical activation in the production of lime-sand mixtures

R.A. Ibragimov^a, E.V. Korolev^b, T.R. Deberdeev^c

^a Kazan State University of Architecture and Engineering, Kazan, Russia

^b Saint Petersburg State University of Architecture and Civil Engineering, St. Petersburg, Russia

^c Kazan National Research Technological University, Kazan, Russia

* E-mail: rusmag007@yandex.ru

Keywords: aggregates, mortar, mechanical properties, hydration, energy efficiency

Abstract. This paper presents a review of the author's research of the effect of different grinding units' on the physical and chemical profile and geometry of quartz powders. Thus, when quartz sand is being treated in a vortex layer machine for 3–5 minutes, the mean particle size decreases from 235 to 6–7 μm , and the maximum size – from 498 to 81–77 μm . In this case, the specific surface area of the quartz powder, determined by the BET method, is 1.14–1.5 times larger than that of the powder obtained in other grinding units. It was shown that only the treatment of quartz sand in the vortex layer machine allows identifying this process as mechanical activation. The same positive results were obtained when treating building lime in the machine. There is an intensification of the building lime hydration process observed. The rational treatment time of the lime-sand compounds mixture in the vortex layer machines is 5 minutes. For compounds obtained from such mixtures at the age of 28 days, an increase in compressive strength by 209 % and bending strength by 172 % is observed. A decrease in the porosity of the compounds by 24 % was also found. Increasing the time of treatment of a lime-sand mixture in the vortex layer machine for more than 5 minutes has shown a slight effect on the physical and mechanical properties of the materials obtained.

1. Introduction

The actual problem for the construction industry is to increase strength and durability of construction composites. One of key propriety area is the increase of physical and mechanical properties of lime-sand compounds, reducing the energy intensity of production. In compliance with topic of this article the subject of investigation is to study the effect of treatment of lime-sand and quartz powder on the physical and mechanical properties.

Nowadays, various types of grinding mills and disintegrators are used for grinding raw components [1]. It is known that during the grinding process the dispersion of particles, the roughness of their surface and, in some cases, the crystallinity degree of the raw components coating surface are being changed. These changes affect the interfacial intensity of physiochemical processes, which often leads to accelerated hydration and hardening of inorganic binder compounds [2–6].

Therefore, with all other things being equal (dispersion, component type), the impact of the grinding equipment type on the strength properties of the building compound seems natural. In particular, they tried to explain the different strengths of lime-sand materials by the different shape of quartz powder particles, their different structural strength and different solubility both in water and in different environments, etc. [7].

The paper [8] gives a hypothesis which associates the compounds strength with the quantity, speed and inter-beat intervals of disintegrator grinding bodies.

The papers [9, 10] present the results of a comparison of different grinding machines, including the vortex layer machine, and testify that the strength of the obtained building compounds primarily depends on the machine power rating and the treatment time. The frequency and velocity of the working bodies' impacts on the mill charge is secondary.

The paper [11, 12] highlights that the type of a grinding machine significantly affects the surface properties of the powder obtained from quartz sand. Thus, in a ball mill the surface of the specified powder is



smooth and flawless, in a centrifugal mill – the particles are sharp-edged and have a large number of cracks. In a bowl mill the powder contains a large number of sharp-edged grains.

The main task of materials science is to search new technological methods for the increase stability and durability of lime-sand compounds, reduce energy intense technique.

The study purposes were determination of the effect of lime-sand in VLM on surface area and morphology and also determination of the influence of mixed girding with lime-sand on the physical and mechanical properties.

According to the study purposes the following tasks were appointed:

- to indicate properties of quartz sand by the dependence of the type of grinding machine;
- to determine the effect of the treatment duration of lime-sand in VLM on temperature change kinetics in the slaking time;
- to established banding and compression strength of lime-sand products by treatment of lime-sand in VLM.

2. Research methods

A natural consequence of the previously established patterns is the dependence of the reactive capacity of the quartz powder on the crystallinity degree of the quartz surface layer and the total surface of the powder in contact with the medium (that is, taking into account the surface roughness, the presence of cracks). In a certain variation range of these powder properties, an increase in the compound strength should be observed (this statement is a consequence of the general theory of composite materials). Moreover, for each compounding “hydraulic binder – quartz powder” system the variation range properties will be individual. Therefore, of particular interest is the study of the “building lime – quartz powder” system, the components of which were treated in the vortex layer machine (VLM). The design and the treatment technique of components in the VLM are presented in the paper [13].

For the research, the 1st grade building calcium quicklime meeting the requirements of EN 459-1:2010 “Building lime – Part 1: Definitions, specifications and conformity criteria”. The quartz powder was obtained from the quartz sand of the Kama-Ustinsky field deposit, which meets the requirements of DIN EN 12620-2008 “Aggregates for concrete”. The quartz sand fineness modulus is 1.2.

A size-consist analysis of the quartz powder was carried out on a Shimadzu SALD-2300 laser light scattering particle size analyzer.

The median diameter D50 (the average diameter with respect to which half of all sample particles by mass will be larger and the other smaller) and the diameter D98 (diameter with respect to which 98 % of all sample particles by mass will be smaller) were chosen as the main size distribution index. For the original quartz sand, the D50 value is 234.6 μm , and D98 is 498.4 μm .

The indicated quartz sand is also characterized by the dependence of the grain geometry on the type of grinding machine (Table 1). To obtain a quartz powder with roughly the same specific surface area, the grinding time in mills was 45–117 minutes, and in the VLM – only 5 minutes.

Table 1. Quartz powder properties depending on the type of grinding machine.

Property	Grinding machine type			
	ball	bowl	centrifugal	VLM
Specific surface area, m^2/kg	230 \pm 20	250 \pm 20	253 \pm 20	254 \pm 20
Specific area under BET, m^2/kg	6540	7120	8670	9860
Particles size, μm :				
– D98	120	85	75	77
– D50	12	8	6	6
Roughness coefficient	28.4	28.5	34.3	38.8

The data analysis (Table 1) shows that for quartz sand treated in various types of machines, the specific surface area and the average equivalent particle diameter differ slightly. The research results obtained by the BET method indicate that the specific surface area of the quartz powder treated in the VLM is 1.14–1.51 times larger than the specific surface area of the quartz powder treated in other studied machines. This indicates the formation of a rougher surface of the quartz powder treated in the VLM. The quantitative parameter characterizing the formation of a rough surface is the roughness coefficient (Table 1), equal to:

$$k_s = \frac{S_{ud,BET}}{S_{ud,g}}, \quad (1)$$

where $S_{ud,g}$ is the specific surface area, calculated according to the size-consist using the classical geometric formula establishing the relationship between the particle diameter and its specific surface; $S_{ud,BET}$ is the specific surface area determined by the BET method.

3. Results and Discussion

A logical consequence of an increase in the phase interface area is an increase in the number of reaction products formed at the interface boundary. Here, the authors purposely do not rely on “increase in reactive capacity”, “increase in activity”, etc. as the indicated terms (reactive capacity, activity) for processes running at the interface phase boundary depend not only on the contact area (extensive factor according), but also on the change rate in the substance physical properties (intensive factor according to [14]).

The specified features are clearly demonstrated in Fig. 1 and 2. Fig. 1 shows optical micrographs of quartz powder grains, and Fig. 2 – images obtained using the Auger microprobe JAMP-9500F (JEOL).

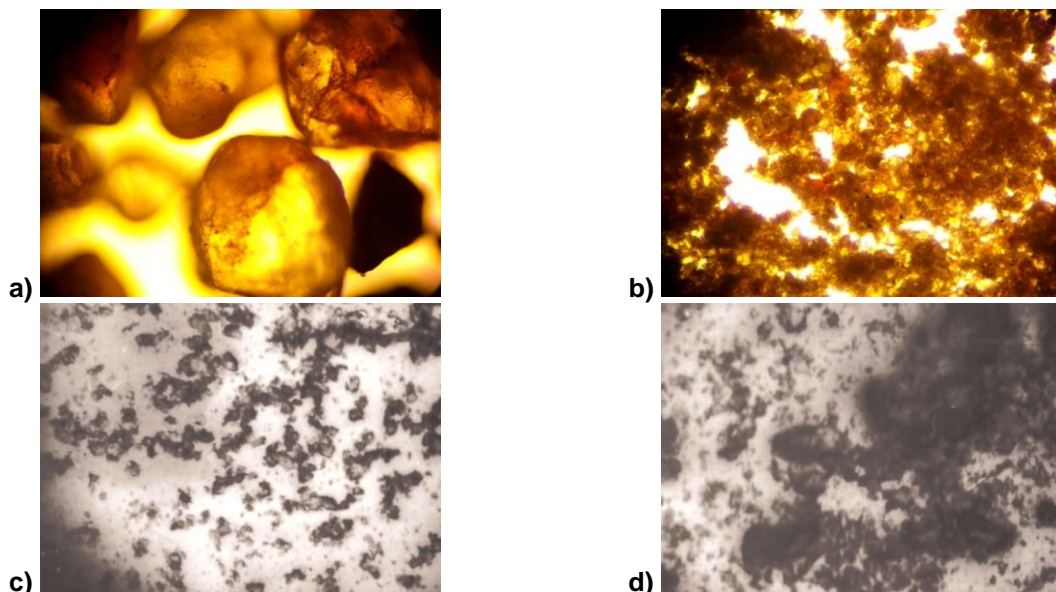


Figure 1. Micrographs of quartz powder grains (magnification 100*):
a) quartz sand grains; b) quartz powder after grinding for 5 minutes in the VLM;
c) the same in a centrifugal mill; d) the same in a ball mill

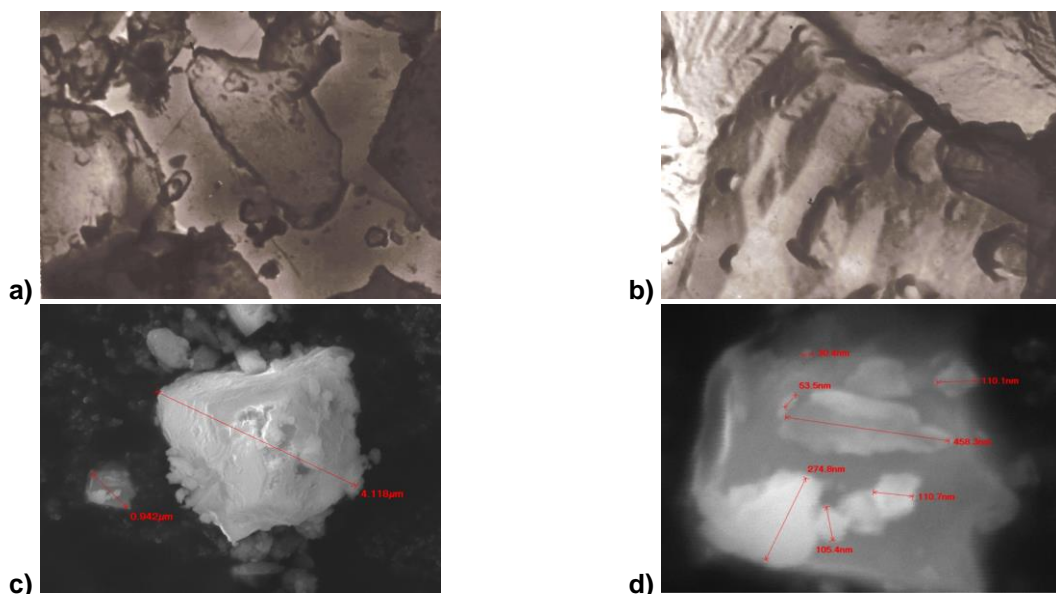


Figure 2. Electronic images of quartz powder grains:
a) treated in a ball mill (4000*); b) the same in a centrifugal mill (20000*);
c) the same in the VLM (10000*); d) the same in the VLM (75000*).

The particles of quartz powder treated in a ball mill have a smooth, flawless surface, which proves the grinding effect. The surface of the powder milled in a centrifugal mill is shard-edged with a fracturing pattern indicating the splitting action of the grinding machine. There are inclusions in the particles of quartz powder, indicating the impact effect during treatments in a centrifugal mill.

The particles of quartz powder treated in the VLM have a layer-like structure, a high degree of surface roughness, a large extended network of cracks, as well as impact-resulted inclusions. A feature of VLM-treatment is that when grinding quartz sand particles, separation occurs along individual conglomerates (Fig. 2 c), and not along cleavage surfaces, as it is in the case of ball and centrifugal mills (Fig. 2 a, b), which illustrates the VLM power rating.

The physical change of the silica in the powders obtained can be estimated by the change in its solubility. The silica content by dissolution in alkalis was defined. The results are presented in Table 2.

Table 2. The content of alkali-soluble soluble silica in the obtained powders treated in various grinding machines.

Grinding machine type	Alkali-soluble soluble silica content			
	Time after grinding*, days			
	0	10	20	30
Ball	0.0110 /	0.0093 /	0.0093 /	0.0093 /
	$1.68 \cdot 10^{-6}$	$1.42 \cdot 10^{-6}$	$1.42 \cdot 10^{-6}$	$1.42 \cdot 10^{-6}$
Bowl	0.0130 /	0.0110 /	0.0110 /	0.0110 /
	$1.83 \cdot 10^{-6}$	$1.54 \cdot 10^{-6}$	$1.54 \cdot 10^{-6}$	$1.54 \cdot 10^{-6}$
Centrifugal	0.0180 /	0.0167 /	0.0167 /	0.0167 /
	$2.08 \cdot 10^{-6}$	$1.93 \cdot 10^{-6}$	$1.93 \cdot 10^{-6}$	$1.93 \cdot 10^{-6}$
VLM	0.0320 /	0.0290 /	0.0290 /	0.0290 /
	$3.24 \cdot 10^{-6}$	$2.94 \cdot 10^{-6}$	$2.94 \cdot 10^{-6}$	$2.94 \cdot 10^{-6}$

Notes: the numerator presents the content of alkali-soluble soluble silica in wt. %; and the denominator – the same in % / m²; * – the powders were stored under natural conditions.

The presented data (Table 2) clearly point to an increase in solubility of alkali-soluble silica for powders treated in the VLM. Given the natural dependence of the solubility of the substance on the contact area [15–20], the criterion confirming this conclusion is written as:

$$k_p = \left(\frac{S_{ud,n}}{S_{ud,i}} - 1 \right) \cdot \left(\frac{C_i}{C_n} - 1 \right), \quad (2)$$

where the index “n” indicates the parameters of the base powder (in this case, the powder treated in a ball mill); C standing for the content of alkali-soluble silica.

The values of k_p are presented in Table 3.

Table 3. Values of the k_p criterion.

Property	Grinding machine type			
	ball	bowl	centrifugal	VLM
k_p criterion	-	0.96	0.72	1.83

As can be seen from Table 3, an increase in solubility is observed only for quartz powder treated in the VLM more intensively as compared with an increase in the powder total surface (Table 1).

After storage under natural conditions, in all cases there is a decrease in the alkali-soluble silica content. The most intense decrease in alkali-soluble silica is observed for powders treated in ball and bowl mills, 15.5 and 15.4 % respectively. The lowest value of this parameter is observed for a centrifugal mill – 7.2 %, for the VLM – 9.4 %. These changes are observed only after 10 days of storage of the powders, and then stabilization is observed.

Summarizing the data presented, we can conclude that VLM quartz powder treatment is a very effective way leading to the formation of a quartz powder with a highly rough surface. The VLM treatment conditions have a natural effect on the particle size distribution of quartz powder: an increase in the VLM treatment time leads to a shift in the distribution maximum to the area of smaller sizes (Fig. 3). It should be noted that the

maximum is diffused with almost uniform distribution of various diameters particles after treating quartz powder in the VLM during 3 minutes.

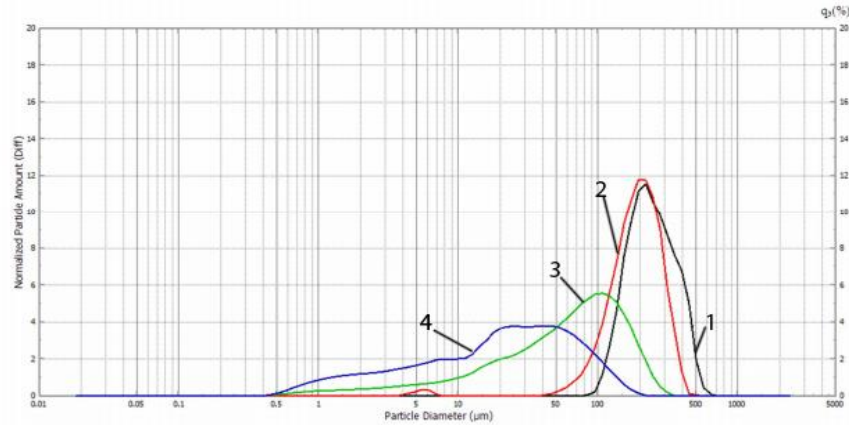


Figure 3. Quartz powder particles distribution: 1 – not VLM-treated; 2 – VLM-treated for 20 sec.; 3 – the same during 1 min; 4 – the same during 3 min.

In addition, it is significant that there is a fairly rapid decrease in both the average and maximum particle sizes in the VLM. Thus, when quartz powder is treated for 3 minutes, the average particle size D50 decreases from 235 to 7 μm, and D98 – from 498 to 81 μm.

Such influence on quartz powder should affect the properties of the structural formation of the “building lime – quartz powder” system. Such properties at the first stage were the temperature and the lime slaking time. The determination methods were in accordance with EN 459-2:2010 “Building lime – Part 2: Test methods”.

Additionally, the effect of both VLM-treatments and its duration (3 and 5 min) were studied. The temperature change kinetics of the lime test is presented in Fig. 4, showing an increase in the temperature and a reduction in the slaking time with an increase in the VLM-treatment time. The change in the qualitative-quantitative characteristics/the rate of reaching the maximum temperature:

$$\mathcal{Q} = T_{\max} / t(T_{\max}), \quad (3)$$

(here T_{\max} – is the maximum temperature; $t(T_{\max})$ is the time to reach the maximum temperature) demonstrates an increase in the chemical reaction rate of $\text{Ca}(\text{OH})_2$. Thus, for the original building lime $\dot{\nu}_0 = 29.8^\circ\text{C}/\text{min}$, for building lime treated in the VLM, $\dot{\nu}_3 = 38.0$ и $\dot{\nu}_5 = 52.7^\circ\text{C}/\text{min}$ respectively, 3 and 5 min.

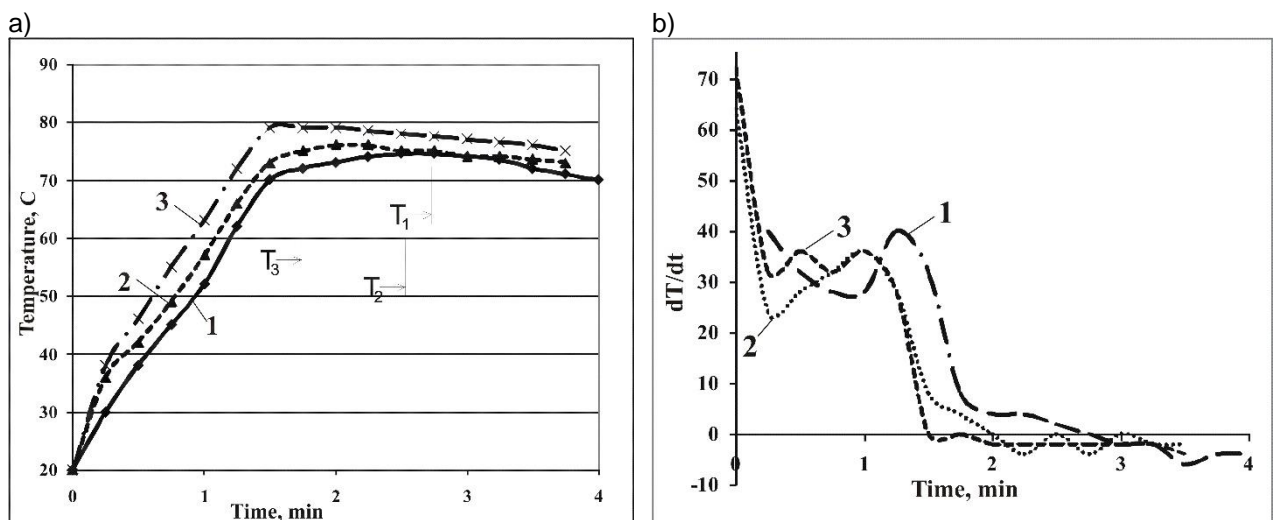


Figure 4. Kinetics of heat generation during a lime slaking treatment (a) and the dependence of dT/dt on the hydration time (b): 1 (T_1) – original building lime; 2 (T_2) – treated for 3 min in a VLM; 3 (T_3) – the same for 5 min (T_i – lime slaking time).

Another important kinetics feature of Fig. 4 is the presence of sections at $T = f(t)$, characterized by different changing rates (Table 4).

Table 4. Parameters of kinetic dependences of heat generation during the slaking of lime treated in a VLM.

Type of lime	Sections characteristics											
	Section I			Section II			Section III			Section IV		
	k_I	$T_{max}, ^\circ\text{C}$	$t(T_{max}), \text{min}$	k_{II}	$T_{max}, ^\circ\text{C}$	$t(T_{max}), \text{min}$	k_{III}	$T_{max}, ^\circ\text{C}$	$t(T_{max}), \text{min}$	k_{IV}	$T_{max}, ^\circ\text{C}$	$t(T_{max}), \text{min}$
Original	32	52	1	36	70	1.5	3.6	74.5	2.75	–	–	–
VLM-treated for 3 min	64	36	0.25	26	49	0.75	32	73	1.5	1.6	75	2.75
VLM-treated for 5 min	72	38	0.25	32.8	79	1.5	-1.2	77.5	2.75	–	–	–

The presented data on kinetics of the heat generation during the slaking of lime lead to the conclusion that the lime treated in a VLM is characterized by a more intense interaction with water in the initial hydration period: in the first section, the k_I coefficient is greater than the same indicator for the original lime. Moreover, very valuable information is contained in the dependence $dT/dt = f(t)$ presented in Fig. 4 b, which demonstrates that the processes of VLM-treated lime interacting with water are significantly more intense. The above follows not only from the value of dT/dt , but also from the amplitude and frequency of oscillations dT/dt in the time interval 0–2 min. Such temperature fluctuations are typical for the building lime hydration kinetics. The peculiarity of the building lime treated in the VLM is the shift of the velocity of the temperature peak to the origin of coordinates (for VLM treatments during 3 minutes) and an increase in the number of peaks for VLM treatments during 5 min should be noted that for the building lime treated in a VLM, a shift in time of reaching $dT/dt = 0$ is also observed. In consequence, for the original building lime, this condition is satisfied at $t_0 = 2.75$ min, for VLM-treated lime – 2.25 and 1.75 minutes for treatments during 3 and 5 minutes respectively.

Y. Khint proved the possibility to obtain silicalcite in different disintegrators. These devices are technically complex. Moreover, the rapid wear of the titanium alloy pins has led to the loss of the initial leading position of these machines in mechanical activation.

In this regard, we have obtained data on the effect of joint VLM treatment of building lime and quartz sand on the kinetics of changes in the strength of lime-sand products, hardened in natural conditions (Table 5) for the first time. The ratio of quartz sand to lime was taken equal 3:1. The strength of lime-sand products, the content of unhydrated grains were determined in accordance with EN 459-2:2010 "Building lime – Part 2: Test methods".

Table 5. Banding and compression strength of lime-sand products.

Time of VLM activation, min	Average strength values, MPa, in days								Average density, kg/m ³	Porosity, %	Unhydrated lime grains content, %
	2		3		7		28				
	<i>R_{bt}</i>	<i>R_b</i>	<i>R_{bt}</i>	<i>R_b</i>	<i>R_{bt}</i>	<i>R_b</i>	<i>R_{bt}</i>	<i>R_b</i>			
0	<u>0.31</u> 100 %	<u>1.5</u> 100 %	<u>0.51</u> 100 %	<u>2.4</u> 100 %	<u>0.67</u> 100 %	<u>3.2</u> 100 %	<u>1.2</u> 100 %	<u>5.3</u> 100 %	1530±31	16.4±0.3	3.8
1	<u>0.35</u> 113 %	<u>1.77</u> 118 %	<u>0.56</u> 110 %	<u>2.7</u> 112 %	<u>0.73</u> 109 %	<u>3.6</u> 112 %	<u>1.3</u> 108 %	<u>5.8</u> 109 %	1545±31	15.8±0.3	3.3
2	<u>0.38</u> 123 %	<u>2.08</u> 138 %	<u>0.64</u> 125 %	<u>3.26</u> 136 %	<u>0.83</u> 124 %	<u>4.32</u> 135 %	<u>1.46</u> 122 %	<u>7.0</u> 132 %	1555±31	15.2±0.3	2.1
3	<u>0.42</u> 135 %	<u>2.4</u> 160 %	<u>0.68</u> 133 %	<u>3.72</u> 155 %	<u>0.91</u> 136 %	<u>4.99</u> 156 %	<u>1.65</u> 138 %	<u>8.2</u> 155 %	1560±31	14.3±0.3	0.9
4	<u>0.48</u> 155 %	<u>2.74</u> 182 %	<u>0.77</u> 151 %	<u>4.32</u> 180 %	<u>1.04</u> 155 %	<u>5.71</u> 178 %	<u>1.79</u> 149 %	<u>9.5</u> 179 %	1560±31	13.5±0.3	0.3
5	<u>0.56</u> 181 %	<u>3.2</u> 213 %	<u>0.91</u> 178 %	<u>5.25</u> 219 %	<u>1.19</u> 177 %	<u>7.01</u> 219 %	<u>2.07</u> 172 %	<u>11.1</u> 209 %	1570±31	12.8±0.3	0
8	<u>0.56</u> 181 %	<u>3.28</u> 218 %	<u>0.92</u> 180 %	<u>5.28</u> 220 %	<u>1.20</u> 179 %	<u>7.03</u> 220 %	<u>2.07</u> 172 %	<u>11.5</u> 217 %	1570±31	12.5±0.3	0

Notes: R_{bt} – is the ultimate bending strength, R_b – is the ultimate compression strength showing the absolute value of the indicator in the numerator and the relative one in % of the control in the denominator.

Table 5 shows that the maximum strength values of lime-sand compounds are observed after 5 minutes of a VLM-treatment of dry mixtures. For these compounds at the age of 28 days, the compressive strength increases by 209 %, and bending – by 172 % compared with the control composition. A further increase in the VLM treatment time almost never leads to significant changes.

A typical feature of all compounds obtained is a relatively lower rate of increase in the bending strength than in compression. With an increase in VLM-treatment time, a decrease in the porosity of lime-sand compounds up to – 24 % relative to the control composition is observed. When a mixture is treated in a VLM for more than 4 minutes, the presence of unhydrated lime grains is not observed, which is consistent with the results of the authors [14].

4. Conclusions

1. It was established that when quartz sand is treated in the VLM for 3–5 minutes, the average particle size decreases from $D_{50} = 235$ to 6–7 μm , and the maximum – from $D_{98} = 498$ to 81–77 μm . A similar quartz powder particles distribution can be obtained by means of treatments in spring and centrifugal mills for 45–117 minutes. That being said, the specific surface area of the quartz powder, determined by the BET method, increases significantly (by 1.14–1.5 times).

2. The peculiarity of VLM treatments is that when quartz sand particles are being ground, separation occurs along individual conglomerates, and not along cleavage planes, as compared to ball and centrifugal mills.

3. It was found that only for quartz powder treated in a VLM, an increase in solubility is observed more intensively as compared with an increase in the total powder surface. This allows us to conclude that the quartz sand treatment in a VLM leads to its mechanical activation, i.e., a nonlinear increase in the physiochemical property (in this case, solubility) with an increase in the interface phase is observed.

4. The building lime VLM treatment leads to a reduction of the lime slaking time from 2.75 minutes to 1.75 minutes, which naturally decreases with increasing treatment time in the VLM. In this case, there is a significant increase in the maximum hydration temperature, which illustrates an increase in the reactive capacity of building lime.

5. The kinetics of the lime-sand mixtures strength gain depending on the VLM treatment was established. The rational treatment time in the VLM was determined. It was found that when a VLM treatment lasts more than 5 minutes, the compressive strength of the lime-sand compound at the age of 28 days increases by 209 %, and the bending strength – by 172 %, as compared with the control composition. Moreover, there is a decrease in the porosity of the compound by 24 %. An increase in the VLM treatment time for more than 5 minutes does not lead to significant changes in the physiochemical parameters of the studied compounds.

5. Acknowledgements

This research was supported by the President of Russia's Grant for Young Scientists (No. 14Z56.18/1643–MK).

References

1. Kachaev, A., Chmerichko, G. The dynamics of the interruptual flows in the wet grinding disintegrators. Bulletin of Belgorod State Technological University named after. V.G. Shukhov. 2017. 7. Pp. 106–110. DOI: 10.12737/article_5940f019cc2835.33982345
2. Liu, J., Wang, D. Influence of steel slag-silica fume composite mineral admixture on the properties of concrete. Powder Technology. 2017. 320. Pp. 230–238. DOI: 10.1016/j.powtec.2017.07.052
3. Sedira, N., Castro-Gomes, J. Effect of activators on hybrid alkaline binder based on tungsten mining waste and ground granulated blast furnace slag. Construction and Building Materials. 2020. 232. DOI: 10.1016/j.conbuildmat.2019.117176
4. Fediuk, R., Smoliakov, A., Muraviov, A. Mechanical properties of fiber-reinforced concrete using composite binders. Advances in Materials Science and Engineering. 2017. 1. Pp. 1–13. DOI: 10.1155/2017/2316347
5. Fediuk, R.S., Mochalov, A.V., Bituev, A.V., Zayakhanov, M.E. Structuring Behavior of Composite Materials Based on Cement, Limestone, and Acidic Ash. Inorganic Materials. 2019. 55(10). Pp. 1079–1085. DOI: 10.1134/S0020168519100042
6. Grishina, A.N., Korolev, E.V. Influence of nanoscale barium hydrosilicates on composition of cement stone. Key Engineering Materials. 2016. 683. Pp. 90–94.
7. Khair, EM, M., Faried, M. Preliminary Evaluation of Silica Sand in Sudan with Respect to Fracture Sand. Journal of Petroleum & Environmental Biotechnology. 2016. 7(3). Pp. 1–4. DOI: 10.4172/2157-7463.1000276
8. Hůšťavová, J., Černý, V., Drochytka, R. Influence of the specific area of quartz sand on the character of an autoclaved calcium silicate composite. Materiali in Tehnologije. 2019. 53(1). Pp. 39–47. DOI: 10.17222/MIT.2018.168
9. Ibragimov, R.A., Korolev, E.V., Deberdeev, T.R., Leksin, V.V. Optimal Parameters and Pattern of Magnetic Field of Working Chamber in Apparatus with Vortex Layer. Stroitel'nye Materialy. 2018. 761(7). Pp. 64–67. DOI: 10.31659/0585-430x-2018-761-7-64-67
10. Ibragimov, R.A., Korolev, E.V., Kayumov, R.A., Deberdeev, T.R., Leksin, V.V., Sprince, A. Efficiency of activation of mineral binders in vortex-layer devices. Magazine of Civil Engineering. 2018. 82(6). Pp. 191–198. DOI:10.18720/MCE.82.17
11. Rakhimova, N.R., Rakhimov, R.Z. Reaction products, structure and properties of alkali-activated metakaolin cements incorporated with supplementary materials – a review. Journal of Materials Research and Technology. 2019. 8(1). Pp. 1522–1531. DOI: 10.1016/j.jmrt.2018.07.006
12. Islam, G.M.S., Rahman, M.H., Kazi, N. Waste glass powder as partial replacement of cement for sustainable concrete practice. International Journal of Sustainable Built Environment. 2017. 6(1). Pp. 37–44. DOI: 10.1016/j.ijsbe.2016.10.005

13. Ibragimov, R.A., Korolev, E.V., Deberdeev, T.R., Leksin, V.V. Efficient complex activation of Portland cement through processing it in the vortex layer machine. *Structural Concrete*. 2019. 20(2). Pp. 851–859. DOI: 10.1002/suco.201800008
14. Ibragimov, R.A., Korolev, E.V. Technical properties of activated gypsum. *IOP Conference Series: Materials Science and Engineering*. 2018. 451(1). Pp. 1–6. DOI: 10.1088/1757-899X/451/1/012028
15. Smirnova, O.M. Evaluation of superplasticizer effect in mineral disperse systems based on quarry dust. *International Journal of Civil Engineering and Technology*. 2018. 8(9). Pp. 1733–1740.
16. Loganina, V.I., Petukhova, N.A., Fediuk, R.S., Timokhin, R.A. Polystyrene paint with reduced contents of volatile compounds. *Magazine of Civil Engineering*. 2019. 88(4). Pp. 25–41. DOI: 10.18720/MCE.88.3
17. Trejbal, J. Mechanical properties of lime-based mortars reinforced with plasma treated glass fibers. *Construction and Building Materials*. 2018. 190. Pp. 929–938. DOI: 10.1016/j.conbuildmat.2018.09.175
18. Kang, S.H., Kwon, Y.H., Hong, S.G., Chun, S., Moon, J. Hydrated lime activation on byproducts for eco-friendly production of structural mortars. *Journal of Cleaner Production*. 2019. 231. Pp. 1389–1398. DOI: 10.1016/j.jclepro.2019.05.313
19. Arizzi, A., Cultrone, G. Comparing the pozzolanic activity of aerial lime mortars made with metakaolin and fluid catalytic cracking catalyst residue: A petrographic and physical-mechanical study. *Construction and Building Materials*. 2018. 184. Pp. 382–390. DOI: 10.1016/j.conbuildmat.2018.07.002
20. Şahin, M., Mahyar, M., Erdoğan, S.T. Mutual activation of blast furnace slag and a high-calcium fly ash rich in free lime and sulfates. *Construction and Building Materials*. 2016. 126. Pp. 466–475. DOI: 10.1016/j.conbuildmat.2016.09.064

Contacts:

Ruslan Ibragimov, rusmag007@yandex.ru

Evgeny Korolev, korolev@nocnt.ru

Timur Deberdeev, deberdeev@mail.ru

© Ibragimov, R.A., Korolev, E.V., Deberdeev, T.R., 2020



DOI: 10.18720/MCE.98.5

Effect of multicomponent modifier on the properties of cement pastes formulated from self-compacting concrete

Q.S.R. Marshdi^a, Z.H.A. Al-Sallami^a, N.M. Zaichenko^{b*}

^a Al-Qasim Green University, Babylon, Iraq

^b Donbas National Academy of Civil Engineering and Architecture, Makiyivka, Ukraine

* E-mail: zaichenko_nikola@mail.ru

Keywords: self-compacting-concrete, cement paste, superplasticizer, ground granulated blast-furnace slag, shrinkage reducing admixture, set accelerator, rheological properties

Abstract. The article presents the results of studies of the influence of multicomponent modifier on the properties of cement pastes and self-compacting concretes. To reduce the cost of self-compacting concretes as well as to enhance their properties in fresh and hardened state the multicomponent modifier has been developed. It consists of ground granulated blast furnace slag, superplasticizer on the base of sulphonated naphthalene formaldehyde condensate, shrinkage-reducing admixture based on the polypropylene glycol derivative, and sodium sulphate set accelerator. The workability of SCC mixtures is considered from the rheological properties of cement pastes formulated from self-compacting concrete. The properties of fresh SCC have been tested according to EFNARC Committee's suggestions. A partial replacement of Portland cement with granulated blast-furnace slag decreases hydration activity of the cementitious material resulting in contributing to higher flowability of cement paste. Shrinkage-reducing admixture in a combination with superplasticizer provide the effect of decreasing apparent viscosity of Portland cement-slag pastes. Sodium sulphate set accelerator coupled with superplasticizer and shrinkage-reducing admixture increase both the apparent viscosity of cement-slag paste and slump retention of SCC mixture. The multicomponent modifier provides an improvement of the properties of fresh (increased slump flow and slump retention) and hardened (28-day compressive strength comparable to control sample and decreased drying shrinkage) SCCs.

1. Introduction

Self-compacting concrete (SCC) is a high performance material which is able to flow under its own weight and completely fill formwork, while maintaining homogeneity even in the presence of congested reinforcement, then consolidating without any vibration and achieving full compaction [1–3]. The cement paste composition as well as paste volume have a predominant effect on fresh concrete properties as compared with water or powder content individually (for a given combination of aggregates) [4]. In order to achieve SCC of high fluidity and to prevent the segregation and bleeding during transportation and placing, the formulators employ high Portland cement (PC) content and use superplasticizers (SPs) and viscosity modifying admixtures. However, cost of such concretes remarkably increases associated with the use of high volume of Portland cement and chemical admixtures [5, 6]. It is one of the disadvantages of SCC responsible for key problems of modern materials science, which are very topical today.

The use of mineral additions in particular ground granulated blast furnace slag (GGBFS) reduces the material cost of SCCs and improves the properties of fresh and hardened concretes [5, 7]. Apart from the economical, technical and technological benefits, the use of waste materials such as GGBFS as a partial replacement of the Portland cement can result in a more sustainable concrete [8]. This problem has recently attracted an increased attention [9]. Besides, it must be taken into consideration that partial replacement of Portland cement by mineral additions affects the required dosage of superplasticizer [10, 11]. For instance, when SP was added with GGBFS concrete mixture became more flowable [12]. Furthermore, an increased content of ground granulated blast-furnace slag decreases the dosage of superplasticizers to achieve the desired workability [13]. This effect corresponds to usual practice of the cost-effective production of SCCs because synthetic superplasticizers are the most expensive components of concretes.

Marshdi, Q.S.R., Al-Sallami, Z.H.A., Zaichenko, N.M. Effect of multicomponent modifier on the properties of cement pastes formulated from self-compacting concrete. Magazine of Civil Engineering. 2020. 98(6). Article No. 9805
DOI: 10.18720/MCE.98.5



This work is licensed under a CC BY-NC 4.0

A variety of superplasticizers from different basic groups is available at the construction market. Traditional sulphonated naphthalene formaldehyde (SNF) condensates can be inexpensive amongst available admixtures; but they are not capable of addressing to the issues of high-performance concrete, where long workability is required without affecting the strength. SPs based on polycarboxylate (PC) polymers are more effective for water reducing capability and for preventing slump loss, for they can disperse cement particles not only by electrostatic repulsions, but also by strong steric hindrance effects [14]. On the other hand, although PC SPs could maintain the workability of concrete for a long period, their application in preparing flowing concrete is limited due to economic reasons. In other words, SNF is still the main SP used instead of PC polymers because of the relatively low cost. However, care must be taken to prevent rapid slump loss of concrete mixture when SNF SPs are used [15].

The results reported by S. Chandra and J. Björnström [16] indicate that slump loss of concrete mixture with SNF SP is associated with the relatively large adsorption of SP by the aluminate phase of cement. There is a competition between SO_4^{2-} ions and molecules of SP for adsorption on the cement particles. It has been observed that the addition of alkali sulphates (e.g., Na_2SO_4) can lead to improvements in the rheological properties of cement paste. On the other hand, the sodium sulphate could play the role of a multifunctional admixture of SCC. In recent years, scientific work has focused on improving properties of binders (e.g., long setting time, low early strength etc.) containing large quantity of mineral additions [17]. The effect of GGBFS on the setting time is more pronounced at high level replacement in binders [18]. To avoid the risk of segregation of SCC associated with the aforementioned effect the sodium sulphate can be used as a set accelerator. The use of GGBFS must be considered also with respect to its possible effect on plastic shrinkage cracking, especially when concreting under hot weather condition [19]. Thus, shrinkage-reducing admixture (SRA) can be used to mitigate the risk of cracking. This kind of admixtures provides a reduction of drying shrinkage by reducing the surface tension of capillary water. Moreover, SRA can reduce the water diffusivity in concrete in order to achieve an enhanced durability [20]. On the other hand, the incorporation of SRA resulted in slight increase in the workability of fresh concrete [21].

Thus, as mentioned in [22] superplasticizers may play the role of a peculiar center for the formation of multicomponent complex modifier that provides any concrete needs, in particular SCC [23]. The aim of this investigation was to assess the effect of the developed cost-effective multicomponent modifier containing sulphonated naphthalene formaldehyde superplasticizer, ground granulated blast furnace slag, shrinkage-reducing admixture, and sodium sulphate set accelerator on the properties of cement pastes and self-compacting concretes, which has not yet been investigated. The key factor for a successful formulation of SCC is clear understanding the role of various constituents in concrete mixture and their effect on the fresh and hardened concrete properties [24]. The objectives of the study included: i) rheological properties (apparent viscosity and yield stress of cement pastes), ii) setting time and compressive strength of binders, iii) properties of self-compacting concretes with or without the multicomponent complex modifier.

2. Materials and Methods

2.1. Materials

Commercial Ordinary Portland cement type I OPC (Taslooj Cement Factory, Iraqi Specifications Limits I.Q.S. No.5/1984) and ground granulated blast furnace slag with specific area of $414 \text{ m}^2/\text{kg}$ and specific gravity of 1.91 g/cm^3 were used as cementitious materials. The chemical composition and physical properties of cementitious materials are given in Table 1 and Table 2, respectively.

Table 1. Chemical composition of the cementitious materials used.

Compound composition	Abbreviation	Percentage by weight	
		OPC	GGBFS
Silica	SiO_2	20.21	35.11
Lime	CaO	64.69	40.09
Alumina	Al_2O_3	2.93	13.52
Iron oxide	Fe_2O_3	3.23	0.75
Sulfate	SO_3	2.41	0.35
Magnesium	MgO	1.79	6.57
Loss On Ignition	L.O.I	3.11	3.61
Lime Saturation Factor	L.S.F	0.97	—
Insoluble Residue	I.R	0.66	—

Table 2. Physical properties of ordinary Portland cement.

Properties	Units	Limits I.O.S No.5 1984	Test result
Specific Surface Area (Blaine method)	m^2/kg	≥ 230	315

Setting time	min		
Initial setting (Vicat)	min	≥ 45	125
Final setting (Vicat)	min	≤ 600	270
Compressive strength	MPa		
3 days		≥ 15	18.2
7 days		≥ 23	24.8
28 days		—	44.3

A normal weight sand (fine aggregate FA) of 4.75 mm maximum size and 2.65 specific gravity as well as normal weight coarse aggregate (CA) of 9.5 mm maximum size and 2.6 specific gravity were used for producing normal weight concrete. Table 3 illustrates the grading of fine and coarse aggregates used respectively. The grading is conformed to the limits of Iraqi specifications I.Q.S. No.45/1984 and ASTM C330.

Table 3. Sieve analysis of aggregates.

Sieve size, mm	Selected aggregate grading, %			
	Test result		Limits of	
	fine	coarse	I.Q.S. No.45/1984	ASTM C330
12.5	—	100	—	100
9.5	—	84.6	—	80–100
4.75	100	30.6	90–100	5–40
2.36	90.8	4.5	85–100	0–20
1.18	81.5	0	75–100	0–10
0.6	62.3	—	60–79	—
0.3	25.8	—	12–40	—
0.15	8.4	—	0–10	—

Two types of chemical admixtures: polypropylene glycol based shrinkage-reducing admixture (Mapecure SRA-25, Mapei) and sulphonated naphthalene formaldehyde-based superplasticizer (Conmix SP1B) were used. The properties of chemical admixtures are the follows: Conmix SP1B – solids content 35 %, pH-value 9, specific gravity 1.20, recommended dosage 0.8–2.0 % liquid and 0.3–0.8 % dry, Mapecure SRA-25 – pH-value 8.5, specific gravity 0.99, recommended dosage 1.0–2.0 % liquid.

The proportions of cement pastes with the multicomponent modifier formulated from self-compacting concrete are summarized in Table 4. The water demand (w/b ratio) was changed for preparing a standard consistency of cement pastes (Vicat test). The SP dosage (liquid) has been limited to the saturation value. Beyond this value, an increase in the SP dosage does not significantly affect the standard consistency of cement pastes at given water/binder ratio.

Table 4. The proportions of cement pastes.

Cement paste	OPC, %	GGBFS, %	SP, %*	SRA, %	Sodium sulphate, %	w/b
CP-1	100	—	—	—	—	0.260
CP-2	65	35	1.0	—	—	0.208
CP-3	65	35	1.0	1.5	—	0.190
CP-4	65	35	1.0	1.5	1.5	0.210

*weight of SP (35 wt. % solution SNF), a dosage of 1 % of liquid SP is comparable to a dosage of 0.35 % of a SP in a solid form.

2.2. Test Procedures

Vicat apparatus mold was used to determine the standard consistency of cement paste as per ASTM 187–11 “Standard Test Method for Amount of Water Required for Normal Consistency of Hydraulic Cement Paste”. The paste should be of normal consistency when the plunger of the Vicat apparatus penetrates into the paste 5 mm to 7 mm above the bottom of the mold in 30 s after being released. Consistency was determined by taking an average of three tests. After the standard consistency had been established, the setting time was determined (as per ASTM 191–08 “Standard Test Method for Time of Setting of Hydraulic Cement by Vicat Needle”).

Recently, many researchers have investigated SCC from the rheological point of view and specifically focused on the paste rheology [25]. The rheological behaviour of a fluid such as cement paste, mortar or

concrete mixture is most often characterized by at least two parameters, τ_0 and μ , as defined by Bingham equation [26]:

$$\tau = \tau_0 + \mu\dot{\gamma} \quad (1)$$

where τ is the shear stress applied to material (Pa), τ_0 is the yield stress (Pa), μ is the plastic viscosity (Pa·s), and $\dot{\gamma}$ is the shear strain rate (s⁻¹).

Shear stress values, as well as plastic viscosity and yield stress of cement pastes at different shear rates were obtained using rheometer RHEOTEST® RN 4.1 (RHEOTEST Medingen GmbH) with cone-and-plate measuring system according to DIN 53018-1 "Viscometry; Measurement of the Dynamic Viscosity of Newtonian Fluids with Rotational Viscometers; Principles". The technical characteristics of the cone-and-plate measuring systems are the following: plate P1 Ø 38, viscosity rang 100–10⁸ mPa s, cone K1 Ø 38/0.3°, viscosity rang 100–10⁶ mPa s, shear rate 2–20000 s⁻¹. The cement paste was mixed manually for 5 minutes in a porcelain crucible and poured into the viscometer.

The proportions of self-compacting concrete are summarized in Table 5. A constant water/binder ratio (w/b = 0.38) was used at all SCC to compare the mixtures and to evaluate the effect of admixtures on the properties of fresh SCC. The following mixing procedure was used to prepare SCC mixture: well-stirring aggregates with Portland cement and ground granulated blast furnace slag together for a minute, adding 70 % of necessary water and mixing during 2 min, then adding the remaining 30 % of water containing superplasticizer, shrinkage-reducing admixture and set-accelerator. The mixing procedure was continued for another 5 min.

Table 5. The proportions of self-compacting concrete.

Component	Units	SCC-1	SCC-2	SCC-3
OPC	kg/m ³	440	286	286
GGBFS	kg/m ³	–	154	154
Fine aggregate	kg/m ³	885	885	880
Coarse aggregate	kg/m ³	796	796	796
SP	l/m ³	9.2	9.2	9.2
SRA	l/m ³	–	36.7	36.7
Sodium sulphate	kg/m ³	–	–	6.6
Water	l/m ³	158	121.3	121.3
w/c	–	0.38	0.58	0.58
w/b	–	0.38	0.38	0.38

The properties of SCC were tested according to EFNARC Committee's suggestions [2] and ASTM C1610/C1610M-10 "Standard Test Method for Static Segregation of Self-Consolidating Concrete Using Column Technique". The slump-flow SF and T₅₀₀ time tests were used to assess the flowability and the flow rate of self-compacting concrete in the absence of obstructions. A standard slump cone was used for the test and the concrete was poured into the cone without consolidation. Slump flow value represented the mean diameter (measured in two perpendicular directions) of concrete mixture after lifting the standard slump cone. When the cone is withdrawn upwards the time from commencing upward movement of the cone to when the concrete has flowed to a diameter of 500 mm is measured; this is the T₅₀₀ time. Slump flow value of SCC was also measured after 45 min of mixing to evaluate the slump loss.

The L-box test was used to assess the passing ability of self-compacting concrete to flow through tight openings including spaces between three reinforcing bars and other obstructions without segregation or blocking. The filling hopper of the L-box was poured with concrete. After 60 ± 10 s the gate of hopper was raised so that the concrete flowed into the horizontal section of the box. When movement has ceased, the vertical distance, at the end of the horizontal section of the L-box, between the top of the concrete and the top of the horizontal section of the box at three positions equally spaced across the width of the box was measured. By difference with the height of the horizontal section of the box, these three measurements are used to calculate the mean depth of concrete as H₂ mm. The same procedure is used to calculate the depth of concrete immediately behind the gate as H₁ mm. The passing ability PA is calculated from the following equation: PA = H₂/H₁.

Cubes 50 mm × 50 mm × 50 mm and 100 mm × 100 mm × 100 mm were used to evaluate the compressive strength of cement paste and concrete, respectively. Tests were conducted at different test age: 3, 7, and 28 days. All experiments were performed on three specimen replicates. The average values are brought in the discussion of the test results. All specimens remained in a humidity chamber (90 % < RH < 95 %) until the time of testing, for 28 days.

Prisms (three specimen) 100 mm × 100 mm × 400 mm were used to evaluate the drying shrinkage of concrete. The specimens were cured for 24 h at 20 °C and 100 % relative humidity and then were demoulded. Then, the specimens were exposed to drying in a humidity chamber at 23 ± 2 °C and 50 ± 5 % relative humidity as per ASTM C157/C157M "Standard Test Method for Length Change of Hardened Hydraulic-Cement Mortar and Concrete" for 90 days.

3. Results and Discussion

3.1. Rheological Properties of Cement Pastes

Fig. 1 represents the behaviour of the steady state effective viscosity of the cement pastes as a function of shear rate throughout the 30–270 s^{-1} rate interval. For very low shear rate of 30 s^{-1} cement pastes show high dynamic (apparent) viscosity, which continuously reduces with increasing shear rate. The reference cement paste without GGBFS and any admixtures (CP-1) with $w/b = 0.26$ has the highest value of the apparent viscosity at the low shear rate of 30 s^{-1} . When the superplasticizer is added and a part of Portland cement is replaced by ground granulated blast furnace slag, the water requirement of the cement paste of standard consistency (CP-2) decreases up to $w/b = 0.208$. In comparison with the reference cement paste, the value of the apparent viscosity at the low shear rate of 30 s^{-1} reduces to 36 %. The electrostatic attractive forces, existing among cement particles and causing agglomeration, are neutralized by the adsorption of the anionic polymer negatively charged, such as SNF SP [27].

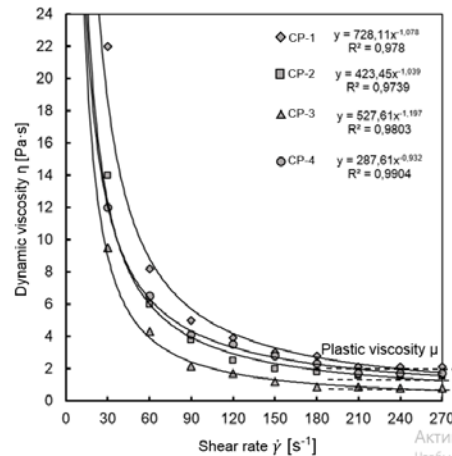


Figure 1. Rheological behaviour of cement pastes as a function of the shear rate.

Beyond a certain shear rate value – 240 s^{-1} , in the case of the reference cement paste the latter one behaves as a power-law shear thinning fluid. The power-law rheological behaviour is followed by a Newtonian plateau, where the apparent viscosity approaches a final value, the so-called plastic viscosity. The plastic viscosity is virtually independent of shear rate. In accordance with [6] the shear thinning part of the rheogram can be attributed to shear-induced dispersion of cement aggregates. The higher the shear rate, the finer the aggregates at equilibrium between shear breakdown and Brownian activated rebuilding (along with hydration) are. For a given solid volume fraction, the viscosity will decrease when the aggregate size decreases. The smallest value of the apparent viscosity over the whole range of shear rate has the cement paste with addition of the ground granulated blast furnace slag, superplasticizer and shrinkage-reducing admixture (CP-3). J. Mora-Ruacho et al. [28] reported that the incorporation of the SRA resulted in increasing the workability of fresh concrete. In a combination with SNF superplasticizer, this effect is stronger. Besides, ground granulated blast furnace slag also makes a contribution to decreasing the apparent viscosity. It is in a good agreement with the results reported in [24].

On the other hand, it must be emphasized that the surface area of GGBFS is higher (414 m^2/kg) as compared with cement (315 m^2/kg), so GGBFS has the higher fine fraction content. Nevertheless, the effect of superplasticizer on the rheological properties of cement paste with granulated blast furnace slag corresponds to the data [29] relating to the effectiveness of superplasticizers to the growing percentage of finest fraction. The finest particles improve the fluidity of cement paste with superplasticizer. In accordance with [30] the GGBFS acts as a good flowability aid up to 30 wt. % in OPC–GGBFS system. The GGBFS has a high specific surface area and roughly spherical particles which fill into the spaces made by larger particles of cement and decrease frictional forces of this material. In addition, the replacement of OPC with GGBFS decreases hydration activity of the sample resulting in contributing to high flowability of this system.

The plastic viscosity of the CP-3 sample is the smallest among the investigated cement pastes and reaches the value 0.7 $\text{Pa}\cdot\text{s}$ when the shear rate is above 200 s^{-1} . However, when the set-accelerator of sodium sulphate (Na_2SO_4) is added (CP-4), the water requirement slightly increases up to $w/b = 0.21$. On the other

hand, the values of the apparent and plastic viscosity are higher as compared with the cement paste without set-accelerator (CP-3).

It should be noted that the cement pastes possess also a yield stress. However no significant effect of GGBFS and chemical admixtures (SP and SRA) on the values of yield stress of cement pastes has been identified (CP-1: $\tau_0 = 58.4$ Pa, CP-2: $\tau_0 = 56.5$ Pa, CP-3: $\tau_0 = 56.0$ Pa, CP-4: $\tau_0 = 57.3$ Pa). This fact must be taken into account because it is necessary for all SCCs to have relatively low yield stress values in order to self-consolidate.

3.2. Setting time and compressive strength of binders

The original formulation of cement paste (CP-1) has the following values of setting time – the initial 125 min and the final 270 min. Experiments demonstrate that due to the addition of SP and GGBFS (CP-2) the hydration process takes longer and retards the initial setting time up to 142 min (13 %). However, it does not affect the final setting time so much. The addition of GGBFS in a combination with SP and SRA (CP-3) retards the hydration process more significantly: the initial setting time increases up to 185 min (48 %) and the final setting time increases up to 420 min (56 %). On the other hand, the addition of sodium sulphate (CP-4) significantly decreases the initial setting time up to 154 min (23 %) and the final setting time up to 315 min (17 %).

The compressive strength of the cement paste specimens at the age of hardening 3, 7, and 28 days is presented in Table 6. The values of the compressive strength of every formulation increase with increasing their age. However, it was found that all values of early compressive strength (3 and 7 days) of cement pastes with GGBFS and admixtures (CP-2, CP-3, and CP-4) are smaller as compared with the control sample (CP-1). Primarily, it is due to the effect of dilution of binder by the granulated blast furnace slag that confirms the slower initial rate of hydration of cement containing GGBFS as a cement replacement as opposed to the reference OPC. Besides, the formulation CP-3 contains shrinkage-reducing admixture, which retards the hydration process of ordinary Portland cement pastes as well as alkali-activated slag systems [31]. This effect is more pronounced at the early stages of hydration.

Table 6. Compressive strength of cement pastes.

Sample	Compressive strength, MPa (%)		
	3d	7d	28d
CP-1	27.8 (100)	42.4 (100)	68.4 (100)
CP-2	24.6 (88.5)	41.3 (97.4)	74.3 (108.6)
CP-3	19.7 (70.9)	30.4 (71.7)	66.8 (97.7)
CP-4	26.2 (94.2)	39.6 (93.4)	72.1 (105.4)

At the age of 28 days of hardening, the value of compressive strength is practically identical with those of the reference formulation. Furthermore, the results show that the compressive strength of CP-4 in the presence of 1.0 wt. (%) Na_2SO_4 is 5.4 % higher than CP-1 sample. It is in a good agreement with obtained data [32] that indicate the beneficiating effect of 0.8 wt. (%) Na_2SO_4 on the mechanical properties of concrete. This occurs probably due to the activating effect of the sodium sulphate set accelerator on hydraulic and pozzolanic properties of granulated blast furnace slag to yield adhesive and cementitious compounds [33, 34].

3.3. Properties of self-compacting concretes

In accordance with [2] all tested concrete formulations (SCC-1, SCC-2, and SCC-3) refer to the following classes: slump-flow SF-1, viscosity VS1/VF1, passing ability PA2, segregation resistance SR-2 (Table 7). In the case, when the value of initial slump flow of SCC-1 is 552 mm, these results for SCC-2 and SCC-3 under the constant water/binder ratio and superplasticizer content are 4.5 and 2.4 % higher, respectively. Several factors could increase the workability parameters: i) higher volume fraction of cement paste at a constant water/binder ratio due to the lower specific gravity of granulated blast-furnace slag; ii) higher specific surface area of GGBFS improves the particle packing, reduces the inter-particle spacing, and decreases frictional forces between cement and slag particles; iii) the availability of the shrinkage-reducing admixture. At this point, the effect of SRA on the concrete mixture rheology was taken as secondary and not evaluated individually in this study. For example, cases occurred where the addition of SRA in High Performance SCC had little influence on the rheological behaviour of the mixtures over time [35]. Thus, the use of mineral addition of GGBFS with increased specific area was likely the dominant factor in increasing the slump flow of SCC-2(3). This hypothesis is proved by the data indicated an improvement of the properties of fresh and hardened SCCs having a constant water/binder ratio of 0.44 and total binder content of 450 kg/m^3 and including only ordinary Portland cement as the binder as well as binary (OPC + GGBFS) cementitious blends. The replacement levels for GGBFS were 20, 40, and 60 % [5].

The admixtures of SRA (SCC-2) as well as SRA + sodium sulphate (SCC-3) improve the slump retention of concrete mixtures in terms of 45 minutes after mixing (61 % for SCC-1, 75 % SCC-2, and 89 % SCC-3). As for the SCC-2 mixture the slump retention of 75 % appears due to the retardation effect of the shrinkage-reducing admixture SRA-25. As for the SCC-3 mixture apart of the mentioned effect of SRA, the addition of inorganic alkali salt, in particular, the sodium sulphate contributes the improvements in the rheological properties of cement paste (concrete mixture) as well as slump retention, especially when superplasticizer on the base of naphthalene formaldehyde condensate was used. This is due to the concurrent adsorption of sodium sulphate ions and superplasticizer on the surface of cement and mineral addition particles [36]. Whereas the results obtained may not be generalized, they are consistent with the concepts of SO_4^{2-} /SP competition. The presence of SO_4^{2-} ions leads to decreasing adsorption of the superplasticizer, leaving more of the latter available in the solution phase for paste fluidification; the fluidity of cement paste increases, accordingly, with the amount of sodium sulphate Na_2SO_4 added [16].

Table 7. The properties of self-compacting concrete.

Properties	Units	SCC-1	SCC-2	SCC-3
Initial slump flow	mm	552	577	565
Slump flow after 45 minutes	mm	337	433	503
Viscosity T_{500}	s	2.0	1.8	2.0
Passing ability (L-box test)	H_2/H_1	0.87	0.89	0.86
Segregation resistance	%	13.2	14.0	9.6
Compressive strength at	MPa			
3 days		22.4	12.8	17.8
7 days		31.7	21.7	26.5
28 days		45.8	34.4	38.8
Drying shrinkage	micro strain	-302	-225	-207

Compressive strength of SCCs at the early (3 and 7 days) and at the design (28 days) age of hardening coupled with drying shrinkage were determined to evaluate the hardened concrete properties. A similar data reported in [7], related to the influence of partial replacement of Portland cement with ground granulated blast-furnace slag (SCC-2 and SCC-3) on the values of early compressive strength have been obtained. The test results show that the compressive strength of the reference SCC-1 is higher by 75 % (3 days) and 20.5 % (7 days) as compared with SCC-2, by 31.5 % (3 days) and 16.4 % (7 days) as compared with SCC-3, respectively. This means that the hydraulic and pozzolanic activity of GGBFS in concrete formulations was not sufficient to enhance compressive strength at the early age. At the age of 28 days of hardening SCC-2 and SCC-3 still demonstrate the lower values of compressive strength as compared with the reference SCC-1 (by 25 and 15 %, respectively) but not to the degree that occurred at the early age. Besides, it is necessary to mention the effect of sodium sulphate admixture on the activity of GGBFS and concrete compressive strength.

One of the most visible effects of using the shrinkage-reducing admixture in the formulations of SCC-2 and SCC-3 is a decreased early compressive strength of concrete. However, the reduction in strength can be compensated, probably, by the lowering water/binder ratio without compromising the workability of concrete mixture, because as mentioned above SRA slightly improves the rheological properties of cement paste (w/b ratio of cement paste CP-3 is the lowest amongst the investigated cement pastes of standard consistency). Therefore, the value of compressive strength of CP-3 at the age of 28 days essentially corresponds to the reference formulation CP-1. The value of compressive strength of the cement paste CP-4, however, which contains the multicomponent modifier is 5.4 % higher as compared with CP-1.

It has been found also that SRA provides decreasing drying shrinkage of SCC-2 and SCC-3 concretes by 25–31 %.

4. Conclusions

The following conclusions can be reached regarding the expected influence of the multicomponent modifier consisting of ground granulated blast furnace slag, the sulphonated naphthalene formaldehyde-based superplasticizer, shrinkage-reducing admixture based on a polypropylene glycol derivative, and sodium sulphate set accelerator on the rheological properties and hardening process of cement pastes formulated from self-compacting concretes.

1. The cement-slag paste (partial replacement of OPC with 35 wt. % GGBFS) with addition of superplasticizer and shrinkage-reducing admixture has the smallest value of the apparent and plastic viscosity over the whole range of shear rate.

2. No significant effect of GGBFS and chemical admixtures on the values of yield stress of all four OPC-GGBFS pastes has been determined.

3. GGBFS, SNF SP, and SRA affect the strength development rate of OPC-GGBFS pastes. Shrinkage-reducing admixture retards the hydration process of OPC-GGBFS cementitious blend (the initial and final setting time increases, early compressive strength decreases). However, when the sodium sulphate set accelerator is used there is no retardation effect due to the presence of sulfates ions increasing the hydraulic and pozzolanic activity of GGBFS.

4. The chemical admixtures of SRA and SRA + sodium sulphate improve the slump retention of SCC in terms of 45 minutes after mixing. The obtained results are consistent with the concepts of SO_4^{2-} /SP competition. The presence of SO_4^{2-} ions (from Na_2SO_4) leads to decreasing adsorption of the superplasticizer, leaving more of the latter available in the solution phase for paste fluidification.

5. The use of shrinkage-reducing admixture in the formulations of SCC-2 and SCC-3 decreases early compressive strength of concrete. However, the reduction in strength could be compensated, probably, by the lowering water/binder ratio without compromising the workability of concrete mixture, because SRA slightly improves the rheological properties of cement paste.

6. SRA provides decreasing the drying shrinkage of SCC-2 and SCC-3 concretes by 25–31 %.

References

- Ahmad, S., Arshad, U. Characterization of self-compacting concrete. *Procedia Engineering*. 2017. 173. Pp. 814–821. DOI: 10.1016/j.proeng.2016.12.108
- The European guidelines for self-compacting concrete: specification, production and use. SCC European Project Group, 2005. 68 p.
- Benyamina, S., Menadi, B., Bernard, S.K., Kenai, S. Performance of self-compacting concrete with manufactured crushed sand. *Advances in Concrete Construction*. 2019. 7(2). Pp. 87–96. DOI: 10.12989/acc.2019.7.2.087
- Nanthagopalan, P., Santhanam, M. Experimental investigations on the influence of paste composition and content on the properties of Self-Compacting Concrete. *Construction and Building Materials*. 2009. 23(11). Pp. 3443–3449. DOI: 10.1016/j.conbuildmat.2009.06.029
- Gesoğlu, M., Güneyisi, E., Özbay, E. Properties of self-compacting concretes made with binary, ternary, and quaternary cementitious blends of fly ash, blast furnace slag, and silica fume. *Construction and Building Materials*. 2009. 23(5). Pp. 1847–1854. DOI: 10.1016/j.conbuildmat.2008.09.015
- Phan, T.H., Chaouche, M., Moranville, M. Influence of organic admixtures on the rheological behaviour of cement pastes. *Cement and Concrete Research*. 2006. 36(10). Pp. 1807–1813. DOI: 10.1016/j.cemconres.2006.05.028
- Uysal, M., Yilmaz, K., Ipek, M. The effect of mineral admixtures on mechanical properties, chloride ion permeability and impermeability of self-compacting concrete. *Construction and Building Materials*. 2012. 27(1). Pp. 263–270. DOI: 10.1016/j.conbuildmat.2011.07.049
- Scrivener, K.L., John, V.M., Gartner, E.M. Eco-efficient cements: Potential economically viable solutions for low- CO_2 cement-based materials industry. *Cement and Concrete Research*. 2018. 114. Pp. 2–26. DOI: 10.1016/j.cemconres.2018.03.015
- Larsen, L.O., Naruts, V.V. Self-compacting concrete with limestone powder for transport infrastructure. *Magazine of Civil Engineering*. 2016. No. 8. Pp. 76–85. DOI: 10.5862/MCE.68.8
- Thulasi, M., Abin Thomas, C.A. Compatibility study of superplasticizers with cement partially replaced with brick powder. *International Research Journal of Engineering and Technology*. 2017. 04(08). Pp. 878–883.
- Barabanshchikov, Yu.G., Belyaeva, S.V., Arkhipov, I.E., Antonova, M.V., Shkol'nikova, A.A., Lebedeva, K.S. Influence of superplasticizers on the concrete mix properties. *Magazine of Civil Engineering*. 2017. No. 6. Pp. 140–146. DOI: 10.18720/MCE.74.11
- Abdel-Mohti, A., Shen, H., Khodair, Y. Characteristics of self-consolidating concrete with RAP and SCM. *Construction and Building Materials*. 2016. 102(Part 1). Pp. 564–573. DOI: 10.1016/j.conbuildmat.2015.11.007
- Yakobu, F.K., Ravichandran, P.T., Sudha, C., Rajkumar, P. Influence of GGBS on rheology of cement paste and concrete with SNF and PCE based superplasticizers. *Indian Journal of Science and Technology*. 2015. 8(36). Pp. 1–7. DOI: 10.17485/ijst/2015/v8i36/87539
- Bauchkar, S.D., Chore, H.S. Effect of PCE superplasticizers on rheological and strength properties of high strength self-consolidating concrete. *Advances in Concrete Construction*. 2018. 6(6). Pp. 561–583. DOI: 10.12989/acc.2018.6.6.561561
- Liao, T.S., Hwang, C.L., Ye, Y.S., Hsu, K.C. Effect of carboxylic/sulfonic acid copolymer on the material properties of cementitious materials. *Cement and Concrete Research*. 2006. 36(4). Pp. 650–655. DOI: 10.1016/j.cemconres.2005.10.005
- Chandra, S., Björnström, J. Influence of superplasticizer type and dosage on the slump loss of Portland cement mortars – Part II. *Cement and Concrete Research*. 2002. 32(10). Pp. 1613–1619. DOI: 10.1016/S0008-8846(02)00838-4
- Giergiczny, Z. Fly ash and slag. *Cement and Concrete Research*. 2019. 124. 105826. DOI: 10.1016/j.cemconres.2019.105826
- Dave, N., Misra, A.K., Srivastava, A., Kaushik, S.K. Setting time and standard consistency of quaternary binders: The influence of cementitious material addition and mixing. *International Journal of Sustainable Built Environment*. 2017. 6(1). Pp. 30–36. DOI: 10.1016/j.ijse.2016.10.004
- Al-Martini, S., Nehdi, M. Coupled effects of time and high temperature on rheological properties of cement pastes incorporating various superplasticizers. *Journal of Materials in Civil Engineering*. 2009. 21(8). Pp. 14–29. DOI: 10.1061/(ASCE)0899-1561-(2009)21:8(392)
- Qin, R., Hao, H., Rousakis, T., Lau, D. Effect of shrinkage reducing admixture on new-to-old concrete interface. *Composites Part B: Engineering*. 2019. 167. Pp. 346–355. DOI: 10.1016/j.compositesb.2018.11.087
- Zaichenko, M., Nazarova, A., Qusay Al-Marshdi. Effect of expansive agent and shrinkage-reducing admixture in shrinkage-compensating concrete under hot-dry curing environment. *TEKA. Commission of Motorization and Energetics in Agriculture*. Lublin, 2014. 14(2). Pp. 170–178.
- Sebök, T., Krejčí, J., Musil, A., Šimoník, J. A contribution to the explanation of the action principles of organic plasticizers. *Cement and Concrete Research*. 2005. 35(8). Pp. 1551–1554. DOI: 10.1016/j.cemconres.2004.07.014

23. Bogdanov, R.R., Ibragimov, R.A. Process of hydration and structure formation of the modified self-compacting concrete. Magazine of Civil Engineering. 2017. No. 5. Pp. 14–24. DOI: 10.18720/MCE.73.2
24. Boukendakdji, O., El-Hadj Kadri, Kenai, S. Effects of granulated blast furnace slag and superplasticizer type on the fresh properties and compressive strength of self-compacting concrete. Cement and Concrete Composites. 2012. 34(4). Pp. 583–590. DOI: 10.1016/j.cemconcomp.2011.08.013
25. Nie, D., An, X. Optimization of SCC mix at paste level by using numerical method based on a paste rheological threshold theory. Construction and Building Materials. 2016. 102(Part 1). Pp. 428–434. DOI: 10.1016/j.conbuildmat.2015.10.195
26. Ling, G., Shui, Z., Sun, T., Gao, X., Wang, Y., Sun, Y., Wang, G., Li, Z. Rheological behavior and microstructure characteristics of SCC incorporating metakaolin and silica fume. Materials. 2018. 11. 2576. DOI: 10.3390/ma11122576
27. Collepardi, M. Chemical admixtures today. Proceedings of the Second International symposium on concrete technology for sustainable February – development with emphasis on infrastructure. Hyderabad, India. 2005. Pp. 527–541.
28. Mora-Ruacho, J., Gettu, R., Aguado, A. Influence of shrinkage-reducing admixtures on the reduction of plastic shrinkage cracking in concrete. Cement and Concrete Research. 2009. 39(3). Pp. 141–146. DOI: 10.1016/j.cemconres.2008.11.011
29. Grzeszczyk, S., Janowska-Renkas, E. The influence of small particle on the fluidity of blast furnace slag cement paste containing superplasticizers. Construction and Building Materials. 2012. 26(1). Pp. 411–415. DOI: 10.1016/j.conbuildmat.2010.11.06.040.
30. Park, C.K., Nohb, M.H., Park, T.H. Rheological properties of cementitious materials containing mineral admixtures. Cement and Concrete Research. 2005. 35(5). Pp. 842–849. DOI: 10.1016/j.cemconres.2004.11.002
31. Bílek, V., Kalina, L., Novotný, R., Tkacz, J., Parízek, L. Some issues of shrinkage-reducing admixtures application in alkali-activated slag systems. Materials. 2016. 9. 462. DOI: 10.3390/ma9060462
32. Cyr, M., Patapy, C. Synergic effects of activation routes of ground granulated blast-furnace slag (GGBS) used in the precast industry. 2016. hal-01344929.
33. Dai, J., Wang, Q., Xie, C., Xue, Y., Duan, Y., Cui, X. The effect of fineness on the hydration activity index of ground granulated blast furnace slag. Materials. 2019. 12(18). 2984. DOI: 10.3390/ma12182984
34. Singh, N., Sarita, R., Singh, N.B. Effect of sodium sulphate on the hydration of granulated blast furnace slag blended portland cement. Indian Journal of Engineering and Materials Sciences. 2001. 8. Pp. 110–113.
35. Pilar, R., Ferron, R.D., Repette, W.L. Fresh properties of HPSCC containing SRA and expansive admixtures. Revista Matéria. 2018. 23(3). DOI: 10.1590/S1517-707620180003.0484
36. Zaichenko, N.M., Khalyushev, A.K., Sakshoshko, E.V. High-strength fine-grained concretes with modified mineral admixtures of fly ash and milled slag of power station. Proceedings of the International conference on alkali activated materials – research, production, utilization. Prague, Czech R. 2007. Pp. 745–756.

Contacts:

Qosai Marshdi, qusaymarshdi@gmail.com

Zainab Al-Sallami, z198995@yahoo.com

Nikolai Zaichenko, zaichenko_nikola@mail.ru

© Marshdi, Q.S.R., Al-Sallami, Z.H.A., Zaichenko, N.M., 2020



Cement slurry from electro-phosphoric slag

A. Shaikhezhan^a, A.D. Anuarova^{a*}, V. Antonovic^b

^a Karaganda State Technical University, Karaganda, Republic of Kazakhstan

^b Vilnius Gediminas Technical University, Vilnius, Lithuania

* E-mail: anuarova_ayaulym@mail.ru

Keywords: Portland cement, phosphoric slag, limestone, rheology, alite

Abstract. Possibility to obtain high alite Portland cement of alternative raw materials was established by complete replacement of clay component with electro-phosphoric (EPS) slag. This technology allowed disposal of considerable volume of slag with production of high grade cement and reduction of CO₂ emissions. Fuel saving was about 15 % increase in productivity of kiln was 10–15 %. It was detected after industrial tests that some rheological properties of slag were unknown. We studied properties of limestone-residual slag, aimed at production of clinker with alite content 69.6 and 65.4 %. EPS slag was weak structuring element at the initial stage of coagulative structuring. An increase in the volume concentration of solid phases led to an increase in viscosity, dynamic shear stress, and plastic strength. With an increase in concentration by 3 % from 35 to 38 %, fluidity decreased by 20 mm, and mobility by 1.3 times. Increase of bulk concentration of solid phases led to increase in viscosity, dynamic stress viscosity, and plastic strength. With the increase in concentration by 3 % from 35 to 38 %, fluidity had been decreased by 20 mm, and mobility by 1.3 times. Further growth of concentration led to reduction of these indicators by an order. Coarse limestone-residual slag with moisture content 37 % preserved its mobility during 26 days. Under static conditions, critical structural strength (100 g.cm²) of slag was achieved during 24 days. In case of proper mixing, duration of slags' mobility shall be increased. Therefore 37 % can be recommended for lower limit of slag moisture.

1. Introduction

The industrial program of the Government of the Republic of Kazakhstan defines the task of stimulating the investment flow of the country's economy, which requires improving the quality of construction, in which the development of technology for the production of binders continues to play a leading role. The problem of improving the quality, reducing energy intensity, finding more productive and economical methods for the production of Portland cement remains relevant. An effective way to solve the problem is to increase the alite content in cement, accelerating the rate of reaction of its formation, but not increasing the clinker calcination temperature, for which purpose a new type of raw material, granulated electro-phosphoric slags (EPS) slags, instead of the traditional clay component of the Portland cement raw material mixture, was investigated. The use of granular phosphoric slag in a Portland cement mixture as a complete clay substitute for the production of high alumina Portland cement has shown the promise of this direction. In this role, this material has not been previously investigated. By the beginning of this work, it was known that the addition of EPS slag to the limestone-clay mixture has a mineralizing effect on the clinker formation process. Phosphate-containing composites are distinguished by high construction and operational properties of concrete [1]. Recently, this direction has been intensively developed in China and other countries [2, 3]. In connection with the use of EPS slags as a raw material component in the production of cement by the wet method, it becomes necessary to study the stability of sludge prepared from such raw mixes. The wet method of cement production, widespread in Russia, Kazakhstan, and other CIS countries, has many edges over the dry one [4].

EPS slag is characterized by relatively low melting and softening temperature (1050–1100°C), and on 90 % consists of lime and silica, and molar ratio is close to monocalcium silicate; contains admixtures of phosphoric anhydride and calcium fluoride. The first is stabilizer of β -C₂S, and the second is effective mineralizer of silication. EPS slag has following variation limits of chemical composition, mass. %: CaO = 44.1 ÷ 50.6 (47.1); SiO₂ = 39.3 ÷ 43.0 (42.0); Al₂O₃ = 1.9 ÷ 3.0 (2.3); Fe₂O₃ = 0.4 ÷ 2.3 (1.0);



MgO = $2.2 \div 4.1$ (3.2); P_2O_5 = $0.2 \div 4.0$ (1.8) and F = $1.7 \div 3.4$ (2.5) (average contents, derived by statistical processing of the results of chemical analyses, which were carried out during 4 years, are given in brackets).

Using EPS slags as primary component in production of cement, it is necessary to study stability of slags, prepared from such primary mixtures.

Task on production of cement with given features and structure is of great importance, sludge with desired properties and structure. It is known, that kinetic stability of limestone-clay slag depends on dispersion and concentration of solid phases, and energy state of particles surface. Slags on the basis of granular blast furnace slags have increased settleability versus to limestone-clay. This is related to higher density of slags and low content of colloidal size particles. Raw slags on the basis of phosphorus slag also have higher sedimentation. Increase of slag content in raw mixture from 14 to 45 % leads to increase in rate of sedimentation of raw slag by 4–8 %.

Established, that tixotropy is peculiar to structure formation of limestone-clay slag and coagulation structure is easily broken by system stirring. Raw mixes from belite component contain 35–55 % of dicalcium silicate, depending on quality and quantity of initial raw materials, which means that slags are not only got thicker, but set. Systems, including granular blast-furnace slags or microsilica [5], are characterized by similar feature.

Performing pilot testing of new technology, we knew that slags demonstrate solidification during long-term storage. Works, devoted to cement raw slags, containing slags of phosphorus production, are small-scale and related to partial clay replacement. Alternative works [6–19] do not contain information on behavior of slag. The study [20, 21] is related only to rheology of activated phosphorus slag. Stated circumstances determined necessity to study structural and mechanical properties of slags of limestone and EPS slag (their stability, viscosity structural strength, dynamic and static shear stresses).

The aim of the article is to evaluate and find out possibility and conditions in order to obtain stable slimes of contained limestone and phosphoric industrial slag. At the same time stability means possibility of slime to preserve solid-state phases in suspension.

2. Methods

2.1. Raw materials

Raw materials were limestone from the Astahov deposit of the Karaganda Cement Plant (Central Kazakhstan) and granular slag from the Taraz phosphate plant (South Kazakhstan). Chemical composition of raw materials is given in Table 1.

Table 1. Chemical composition of limestone and granular electro-phosphoric slags, mass.

Raw material	CaO	SiO ₂	Al ₂ O ₃	Fe ₂ O ₃	MgO	MnO	R ₂ O	F	P ₂ O ₅	TiO ₂	S	loss of ignition*
Limestone	53.62	1.98	1.16	0.52	0.53	0.46	no	0.23	0.03	traces	0.05	42.00
Slag	45.70	41.50	2.32	0.61	4.00	0.58	0.38	1.95	1.97	traces	0.35	0.47
Clay	7.92	55.20	12.11	6.15	2.77	–	2.91	–	–	–	0.10	11.99

*ignition losses.

The density of slag was 2.92 and that of limestone 2.71. The density of clay was about 2.60–2.65. Limestone excels in purity and has the titer 95.75 %. Comparison of data from the table with the abovementioned bulk composition demonstrated that slag sample is chemically representative. Potable water is used for preparation of raw slug.

2.2. Research methods

Limestone – slag slime was studied by the Nurse method [22] for high alit clinker. Saturation coefficient (SC) was taken 0.93 and 0.97 which correspond to 69.6 % and 65.4 % alit content.

The density was determined by pycnometer (bottle) method at 20° C in toluene. Particle-size distribution was determined by sedimentation analysis of pipette method. Grain shape was evaluated by using of microscope NU-2. The features of interaction between the studied objects aggregates with water were estimated on the electronic microscope UEMV-100K.

The specific surface was determined by a standard surface meter T-3 based on the principle of air permeability of powder materials. Suspension was prepared by means of the LE-305 type mixer.

According to fluidity slime moisture content was determined by its flow and optimal diameter was about 70 mm. Fluidity was defined using fluidity meter TN-2 (of the RHTU n.a. D. Mendeleyev system). Slime thickening (decreasing of fluidity) during a time was tested in static conditions.

Assessment of sedimentation was accompanied by establishment of sedimentation volume, its moisture capacity and changes over time. Observation continued till achievement of constancy of sedimentation volume. Rotary viscosimeter "Rheotest – 2" (Germany), Waler-Rehbinder device and Rehbinder cone-and-plate rheometer (modified device of VNIINGP, Russia) were used during study of structural-mechanical properties of primary cement slurries. Calculating formulas were adjusted depending on development of system structure.

2.3. Samples preparation

Raw materials were grinded by laboratory tumbling mill with using of standard grinding balls loading. There were prepared two samples. The first sample had the remainder on the 008 sieve 8 %, the second sample 14 %.

Limestone slime, slag slime, two component mixed slime and to compare slime from horizontal stank of Karaganda cement plant (KCP) were studied. The control slime was stored in a hermetically sealed vessel and was subjected to numerous and careful hashing. All this could improve its sedimentation stability and other indicators.

Experimental slimes were tested in a freshly prepared form, i.e. in more adverse conditions in comparison with the control slime. It gives more reliable relative results of supervision.

Two tests were carried out at different dispersion. The first test was carried out at 8 % remainder on 008 sieve. The second test was carried out at 14 % remainder on 008 sieve. Such sifting was the same with low and high limits of grinded material in plants. Controlling plant slime has residual on 008 sieve 14.4 %. Limestone-slag slime was tested at 37 % of moisture content that was typical for industrial slime. KCP slime that was used in tests had 39.5 % and 37 % moisture content.

3. Results and Discussion

3.1. Sludge of a mixture of limestone and granulated phosphoric slag

Materials dispersion. The data of the dispersion are shown in Table 2.

Table 2. Specific surface and results of sedimentation analysis of the powders.

Sample	Specific surface, m ² .kg	Remainder, mass. %.		Content, mass. %				
		on the sieve		Fractions, mm				
		0.2	0.08	> 0.06	0.06 – 0.01	0.01 – 0.005	0.005 – 0.001	0.001
Granulated phosphoric slag								
S – 1	2325	0.6	14.0	33.34	55.06	5.95	4.55	1.10
S – 2	2908	0.4	8.0	14.75	72.50	6.30	4.30	2.15
Limestone								
L – 1	4563	0.6	14.0	14.83	80.77	1.20	2.72	0.48
L – 2	5278	0.7	8.0	13.20	82.10	0.70	2.15	1.85

The data presented in Table 2 show that the granulated slag of phosphoric production in comparison with limestone is more coarse-dispersed when crushed. In case of slag the bulk (about 90 %) of particles has the size more than 10 mc. The raised grinding subtleties by means of decreasing the remainder from 14 to 8 % increase the 0.06–0.01 mm fraction yield at the expense of fraction that is larger than 0.06 mm. At this the number of fractions less than 10 mc remains almost without change.

In limestone there are more fractions that are smaller than 60 mc and their yield grows with increasing the general fineness of grinding i.e. with reducing the quantity of particles that are larger than 80 mc from 14 to 8 %.

According to the content of fraction that is smaller than 60 mcm the specific surface of materials changes. With the remainder of 8 % the specific surface of limestone exceeds that of slag 1.8 times and with the remainder of 14 % – almost twice.

Form of grains. Viewing the powders under the microscope showed that particles of slag have a flat-limited detrital form with acute corners and twisting sides. Configuration of grains in most cases is irregular. There are met grains of the extended form.

Limestone units are more isometric in comparison with slag grains, but they also have an irregular shape with twisting outlines.

Sedimentation of slimes. Sedimentation was studied with the use of slimes which component compositions are presented in Table 3.

The solid phase of the KCP slimes contains to 80 % of limestone and 3–5 % of scale. The other part is presented by clay slate.

Table 3. Component composition and technological indicators of slimes.

Slime	Composition of the mix, mass. %				Slime humidity, %	Slime fluidity, mm	Volume concentration of dispersed phases, %
	S – 1	S – 2	L – 1	L – 2			
1	100	–	–	–	29.0	70.0	45.60
2	–	100	–	–	30.0	70.0	44.41
3	–	–	100	–	30.0	63.0	46.27
4	–	–	–	100	30.0	61.0	46.27
5	41.4	–	58.6	–	30.0	69.0	45.54
6	41.4	–	58.6	–	37.0	97.0	37.90
7	–	41.4	–	58.6	30.0	70.0	45.54
8	–	41.4	–	58.6	37.0	92.0	37.90
KCP slime					39.5	68.0	35.94

Note: S – slime, L – limestone

In limestone-slag slimes the content of limestone is reduced to 60 % but in spite of this it is the prevailing component. In addition, it is necessary to consider the developed specific surface of limestone.

The total surface of limestone and limestone-slag slimes exceeds the slag surface about three times. In this regard it would be possible to expect the decisive effect of limestone on the properties of slimes. In reality there is not observed such a picture.

For example, fluidity of limestone-slag slimes (Table 3, slimes 5 and 7) coincides with fluidity slag (1 and 2) but not with calcareous (3 and 4) suspensions. Similarly, the KCP slime fluidity is strongly affected by humidity of the clay component.

Limestone-slag slimes in a freshly prepared state in comparison with the KCP slime of identical fluidity show water requirement nearly 10 % less. It is entirely connected with the feature of interaction of phosphoric slag with water. As there were tested only freshly prepared slimes, it must be kept in mind the initial stage of water interaction here.

Comparing concrete figures, it is possible to note that slag suspensions are characterized by the smallest values of the lower limit of humidity (29–30 %). These suspensions with identical humidity surpass in fluidity the calcareous ones. The reason is probably in the coarse dispersion of slag suspensions and their smaller a little volume concentration.

Calcareous suspensions with humidity of 30 % show rather high fluidity, too.

In sedimentation duration experimental slimes, as well as the KCP slime don't practically differ from each other. The bulk of the disperse phase in them sediments already in 20 min. despite all distinctions in humidity, fluidity, specific surface and volume concentration spoken above.

Initial moisture capacity of the sediment. Sedimentation volume after 20 min. in Limestone-slag slimes (Table 4, slimes 5 and 8) does not depend on the fineness of grinding the furnace charge at all and is mainly defined by their humidity. Slimes 6 and 8 of high humidity (37 %) forms sediments with moisture capacity of 61.32 % whereas the same slimes (5 and 7) at 30 % humidity allocate sediments with moisture capacity only about 54 %.

Sediments of Limestone-slag slimes and the KCP slimes with identical humidity has almost equal moisture capacities.

However, Limestone-slag slimes of equal fluidity sediment with allocation of a denser deposit in comparison with the KCP slime.

The smallest moisture capacity belongs to the deposit of slag suspension prepared from the powder of the remainder on the 0.08–14 % sieve. However, the low moisture capacity of sediments is not characteristic of slag suspensions. The moisture capacity of their sediments raises with increasing the fineness of grinding. So, for example, moisture capacity of slime sediment twice surpasses moisture capacity of calcareous suspensions sediments, though the specific surface of slag flour is less than the of calcareous 1.6–1.8 times.

Table 4. Moisture capacity of slime sediments.

Slime	Initial moisture capacity after 20 min., %	Final moisture capacity, %	Initial and final moisture capacities ratio, %	Sedimentation volume to slime volume ratio, %
1	48.97	48.97	100.00	89.37
2	54.77	52.16	95.23	98.21
3	53.46	51.52	96.97	99.40
4	53.54	52.27	97.63	99.59
5	53.80	52.01	96.67	98.57
6	61.32	54.67	89.16	98.00
7	53.89	51.85	96.21	98.80
8	61.32	55.93	91.21	98.00
KCP	63.66	58.80	92.37	98.93

Final moisture capacity of the sediment, i.e. the stabilized sedimentation volume of the KCP slime is 57.7 % less than in calcareous and slag slimes. But the deposit of plant slime is condensed very slowly: within 11 days and in experimental ones this consolidation comes to the end in one day.

The final moisture capacity of Limestone-slag slimes sediments still depends on their humidity, though to a lesser extent than in case of the initial moisture capacity.

In values of the final moisture capacity Limestone-slag slimes sediments do not significantly differ from the KCP slime after a daily storage if their humidity coincides.

Suspensions 2, 3 and 4 are almost identical by the final moisture capacity.

Changing sedimentation volume of slime in time (Table 5). The largest duration belongs to changing sedimentation volume of the KCP slime, i.e. 11 days.

Table 5. Sedimentation characteristics of slimes.

Slime	Time of count from the experiment beginning, min.						
	20	40	60	80	100	120	140
	Sedimentation volume changing, %						
1	100.00	100.00	100.00	100.00	100.00	100.00	100.00
2	100.00	97.16	95.14	94.53	94.53	94.53	94.53
3	100.00	99.00	99.00	99.00	98.60	98.20	96.00
4	100.00	99.38	98.97	98.77	98.56	98.36	97.33
5	100.00	98.96	98.34	97.52	97.10	96.69	96.28
6	100.00	98.70	97.30	95.90	94.50	93.20	85.30
7	100.00	98.98	98.58	97.97	97.37	96.56	95.75
8	100.00	98.70	97.70	96.50	95.50	95.50	87.70
KCP	100.00	99.35	98.88	98.35	97.83	97.66	91.63

The time of sedimentation volume stabilization of limestone-slag slimes makes 24 hours. The same is observed for calcareous suspensions.

Coarse-dispersion slag suspension (Table 5, slime 1) gives a compact deposit right after sedimentation and its volume does not decrease later on. The duration of changing sedimentation volume in the second slag suspension is equal to 80 min.

Viscoplastic properties of slimes. In these experiments initial materials and furnace charges were the same as were described above. Humidity of slimes covered the lower and top limits of admissibility for each type and include one intermediate point.

Slag and calcareous suspensions are tested at limit temperatures, Limestone-slag slimes at 40 and 60 °C; such temperatures are most probable industrially.

The curve of slime currents is given in Fig. 1–4. As it should be expected, they did not pass through the beginning of coordinates.

For limestone (Fig. 1) at humidity 40 and 43 % the relation between the shearing effort and the gradient of speed remains almost linear. At 28 % humidity a straight line is bent when approaching the axes of shear stresses.

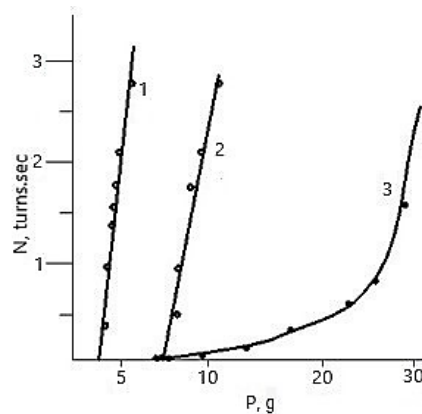


Figure 1. Curves of limestone suspensions currents depending on the speed of rotation (N , turns.sec.) of the mobile internal cylinder of the viscometer, on loading (P , g) rotating the cylinder:
 1 – the remainder on the sieve 0.08 – 8 %, humidity – 40 %. temperature 10 °C;
 2 – the remainder on the sieve 0.08 – 14 %, humidity – 43 %, temperature 60 °C;
 3 – the remainder on the sieve 0.08 – 14 %, humidity – 28 %, temperature 60 °C.

Rectilinear nature of the considered dependence remains also for slag at humidity 37 and 43 %. In case of 28 % humidity the relation is complicated-stepped (Fig. 2) and the initial character of the relation between the shearing effort and the gradient of speed reminds a system having a fragile failure.

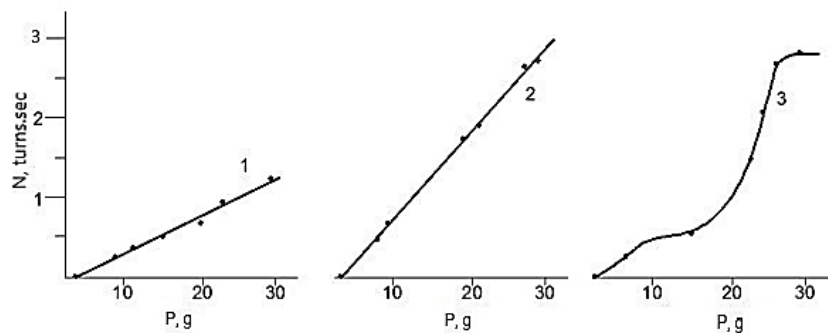


Figure 2. Curve of slag suspensions currents depending on the speed of rotation of the mobile internal cylinder (N , turns.sec.) of the viscometer, on loading (P , g) rotating the cylinder:
 1 – the remainder on the sieve 0.08 – 14 %, humidity – 37 %. temperature 10 °C;
 2 – the remainder on the sieve 0.08 – 8 %, humidity – 43 %, temperature 80 °C;
 3 – the remainder on the sieve 0.08 – 8 %, humidity – 28 %, temperature 80 °C.

The bends of curves of the Limestone-slag slimes currents are sharp at 40 and 46 % humidity (Fig. 3). The LCPZ slime has a similar dependence at all tested temperatures (Fig. 4).

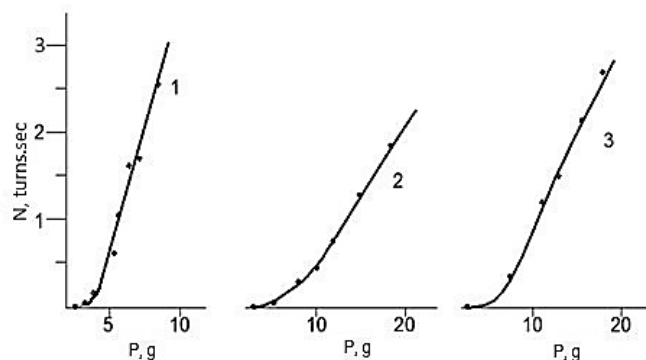


Figure 3. Curve of limestone-slag slimes depending on the speed (N , turns.sec.) of rotation of the mobile internal cylinder of the viscometer, on loading (P , g) rotating the cylinder:
 1 – the remainder on the sieve 0.08 – 14 %, humidity – 40 %, temperature 40 °C;
 2 – the remainder on the sieve 0.08–8 %, humidity – 31 %, temperature 60 °C;
 3 – the remainder on the sieve 0.08 – 8 %, humidity – 46 %, temperature 60 °C.

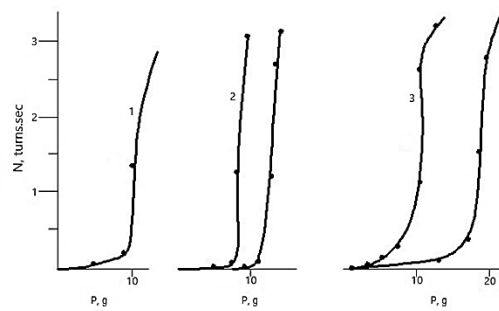


Figure 4. Curve of the KCP slime currents depending on the speed of rotation of the mobile internal cylinder (N, turns.sec.) of the viscometer, on loading (P, g). rotating the cylinder:

**1 – 10 °C; 2 – 20 °C; 3 – 40 °C; 4 – 60 °C;
5 – 80 °C (the remainder on the sieve 0.08 – 14 %, humidity – 37 %)**

The curve of the calcareous and slag slime current at 31 % humidity has a flatter initial bend.

Viscoplastic properties of slimes are presented in Table 6.

Table 6. Viscoplastic properties of slimes.

Slime	Humidity, %	Volume concentration of dispersed phases, %	Temperature, °C	Largest plastic viscosity, (η_o), poise	Smallest plastic viscosity, (η_m), poise	Static shear stress (θ_s), dn.cm ²	Dynamic shear stress (θ_d), dn.cm ²
1	37	36.8	10	23.9	9.5	51	51
2	28	46.8	80	not defined	7.6	107	107
	43	31.2		30.0	3.6	28	28
3	28	48.7	60	67.3	0.9	28	305
	43	32.8		35.4	0.7	32	32
4	40	35.6	10	53.6	0.4	42	42
5	40	35.0	40	82.8	1.1	34	43
7	31	44.3	60	122.6	3.4	31	88
	46	29.6		20.6	2.8	35	45
			10	117.4	0.4	46	195
			20	95.7	0.8	28	175
KCP	37	38.4	40	74.2	0.5	31	131
			60	34.4	0.7	28	173
			80	27.5	0.6	33	157

The difference $\theta_d - \theta_s$ is not large in limestone-slag slimes (Table 6, slimes 5 and 7).

In the KCP slime $\theta_d > \theta_s$ is 4–6 times as large.

In slag and limestone suspensions $\theta_d = \theta_s$, excluding coarse-dispersion limestone suspension with 28 % humidity and 60 °C temperature that has $\theta_s = 28$, and $\theta_d = 305$ dn.cm².

Static shear stress. Slimes differ from each other but little in this indicator. Slag suspensions do not enter here.

In general, in slag suspensions θ_s significantly depends on their humidity: the lower is humidity, the larger is θ_s . For example, at 28 % humidity slag suspension has $\theta_s = 107$ dn.cm².

Dynamic shear stress. It is high when humidity of slimes is low. Those are suspensions: a slag one with 28 % humidity ($\theta_d = 107$ dn.cm²); a calcareous one with 28 % humidity ($\theta_d = 305$ dn.cm²); and a calcareous, and slag slime with 31 % humidity ($\theta_d = 88$ dn.cm²).

Limestone-slag slimes in comparison with the plant slimes can have θ_d 2-4 times less.

Structural (effective) viscosity of slimes is not given here. It is changeable in the limits between η_o and η_m depending on the applied loading. Therefore below there are considered the values η_o and η_m that are constants under existing conditions.

The largest plastic viscosity of limestone-slag slimes at 40–60 °C depends on their humidity. It is high at low humidity 31 % ($\eta_o = 122.6$ poise). Then there are coarse-dispersion slimes.

In the KCO slime η_o falls with temperature increase. There is an impression that this slime in η_o has no essential advantage before limestone-slag slimes.

At 10 °C a slag suspension in comparison with the plant slime shows by 5 times smaller viscosity η_o , but at 80 °C it is slightly larger in a slag suspension.

Calcareous suspensions 0 °C have a smaller η_o than in the KCP slime. But at 60 °C and 28 % humidity this suspension in this indicator is worse than the plant slime.

The smallest plastic viscosity of the completely destroyed structure in limestone-slag slimes in comparison with the production slime will be higher in connection with the presence of slag in them which suspension has always an increased value. Calcareous suspensions and KCP slime have almost identical viscosity η_m independent of the temperature (Table 6).

The difference $\eta_o - \eta_m$ in the KCP slime is much larger than in calcareous and slag slime. In the small difference $\eta_o - \eta_m$ of the latter there appeared the influence of the slag component.

Slime thickening. For the purpose of studying slimes thickening there were prepared slimes which component composition and technological indicators are presented in Table 7. Changing slimes fluidity in dependence of their storage duration is shown in Table 8.

Table 7. Component composition and technological indicators of slimes.

Slime	Mix composition, mass. %				Remainder on the sieve, %	Specific surface, m ² .kg	Humidity, %	Volume concentration of dispersed phases, %	Fluidity, mm
	S-1	S-2	L-1	L-2					
A	100	–	–	–	14	196.1	31	43.25	100.5
B	–	100	–	–	8	226.5	34	39.93	107.0
C	–	–	100	–	14	456.3	31	45.09	65.0
D	–	–	–	100	8	527.8	34	41.75	70.5
E	41.4	–	58.6	–	14	342.1	31	44.73	69.0
F	41.4	–	58.6	–	14	342.1	37	37.89	97.0
G	–	41.4	–	58.6	8	364.2	34	41.03	98.0
H	–	41.4	–	58.6	8	364.2	37	37.90	100.5

Note: S – slime, L – limestone

The property to get thick is inherent in all slimes their specificity is shown only in the process duration which, except the nature of materials, significantly depends on humidity of slimes.

Among coarse-dispersion (remainder on the sieve 0.08–14 %) suspensions with 31 % humidity and prepared from separate components, the suspension of the granulated slag (5 days) is quickly getting thick and limestone – within 8 days.

The increase in humidity to 34 % did not affect the behavior of calcareous suspension but led to increasing the duration of jelling to 11 days for the granulated slag characterized by the remainder on the sieve 0.08–8 %.

The most coarse-dispersion calcareous and slag slime (it is designated by Z) containing granulated slag but having humidity 37 % kept the mobility within 26 days. This fact shows that in the phenomenon of jelling of Limestone-slag slimes their humidity is of great importance.

The structural durability was determined at the temperature of 25 ± 1 °C and humidity of slimes 37 %. When assessing the time of preservation of grouting cements mobility its structural durability is accepted as the limit of their pumpability equal to 100 g.cm². From this point of view calcareous suspensions (Fig. 5) are mobile within a very long period of time. Calcareous suspensions gain durability slowly. After 36 days their structural durability makes only 14 and 16 g.cm².

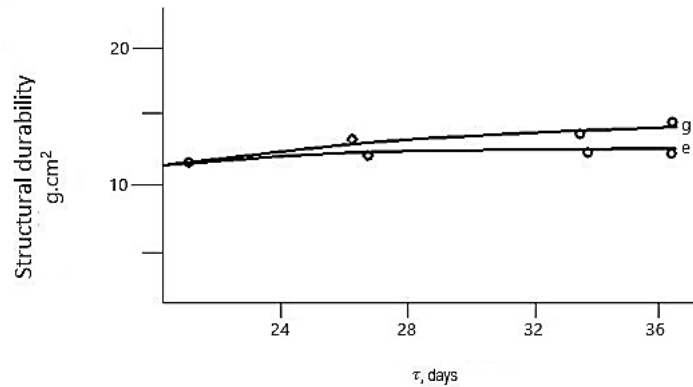


**Figure 5. Changing structural durability of limestone suspensions (humidity – 37 %):
a – the remainder on the sieve 0.08 – 14 %, b – 8 %.**

Table 8. Changing slimes fluidity depending on the storage duration.

Designation	Fluidity, mm									
	Period of slime storage, days									
	0	1	2	3	4	5	6	7	8	9
a	100.5	100.5	103.0	93.0	62.0			thickened		
b	107.0	112.5	113.0	114.0	111.5	104.5	104.5	98.0	90.5	75.5
c	65.0	65.0	63.0	61.0	56.5	48.0	42.0	40.0	thickened	
d	70.5	70.5	70.5	65.0	63.5	57.0	54.0	42.5	thickened	
e	69.0	74.0	70.5	66.5	63.0	53.0	46.5	40.0	thickened	
f	97.0	102.0	105.5	106.0	94.5	101.0	95.0	99.5	99.5	-
g	98.0	96.5	90.0	84.0	81.0	77.5	71.0	62.0	50.0	43.0
h	100.5	108.0	104.0	102.0	-	100.0	96.0	92.0	85.5	80.0

The limit of pumpability of a more coarse-dispersion suspension of the granulated slag is reached in 15 and 23 days respectively for powders, 14 and 8 % of which are characterized by the remainder on the sieve 008 (Fig. 6). In suspensions of the granulated slags structural durability after two-day storage reaches 13 and 17 g.cm². Then it grows rather slowly depending on dispersion of powders till 22 and 14 days. On expiration of the specified terms the growth rates of durability sharply increase, especially for a powder from the remainder on the sieve 008–8 % which suspension after 27 days of storage has durability about 1400 g.cm². The curve of structural durability coarse-dispersion suspension growth has a step character, the rate of increasing durability is slow till 14 days, in the range from 14 to 22 days it is accelerated, then becomes again smooth; after 22 days there comes the second stage of sharp hardening.

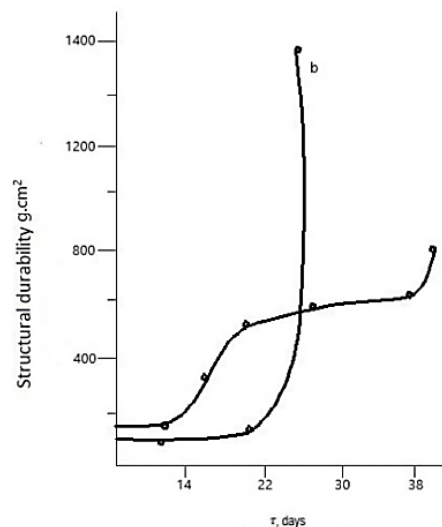


**Figure 6. Changing structural durability of slag suspensions (humidity – 37 %):
a – granulated slag, the remainder on the sieve 0.08 – 14 %, b – the same, 8 %.**

Thus, a suspension of granulated slag considerably loses its pumpability. However, mobility of calcareous and slag slime is larger when using granulated slag that is seen in Fig. 7. Critical structural durability of slimes with granulated slag was reached in 24 days.

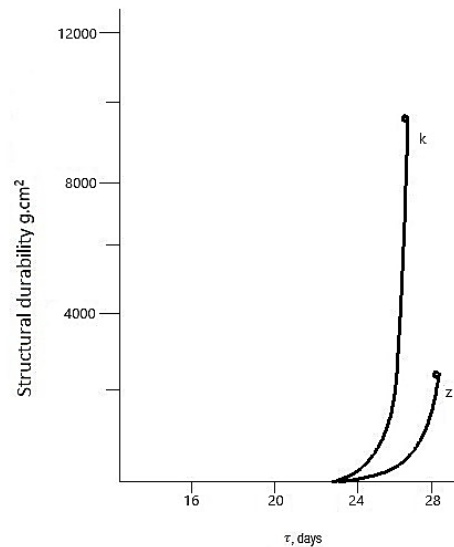


**Figure 7. Changing structural durability of limestone – slag slimes (humidity – 37 %):
a – slime with granulated slag, the remainder on the sieve 0.08 – 14 %, b – the same, 8 %.**

Limestone-slag slimes before achieving the critical structural durability are strengthened gradually, then the growth rates of durability increase sharply.

Summarizing, we can say that thickening is due to the dispergation of slag particles, and setting is due to the formation of calcium hydrosilicates. This is confirmed by the bands established by the IR method at 3450 and 1650–1640 cm^{-1} , according to Nakamoto, K and Lazarev, A.N. [23] which relate to crystallization water, part of calcium hydrosilicates.

General observations permitted to establish the following facts:

1. Phosphoric industrial slags have a higher density than clay.
2. Limestone-slag slime has a low water requirement ability. This slime flow in 70 mm was reached at 30 % of moisture content when KCP slime at 39–40 %.
3. Limestone-slag slime as KCP slime is kinetically unstable. Time of sedimentation is not higher than 20 minutes.
4. Initial water-absorbing capacity of sedimentation volume in two slimes was equal at the same moisture content. But at the same fluidity limestone-slag slime made denser settlement.
5. Limestone – slag slime compacted (reducing of sedimentation volume) in 24 hours. KCP slime in 11 days. Final water – absorbing capacity of limestone – slag and KCP slimes after 24 hours were not very different.
6. Values of static shear stress of slimes were almost equal.
7. Limestone – slag slime's dynamic shear stress was almost in 4 times at the same moisture content and in 2 times at the same fluidity higher than KCP slag's.
8. The difference between dynamic and static shear stresses of limestone – slag slime was not so big. At the same time KCP slime's dynamic shear stress value was in 4-6 times higher than static.
9. Limestone – slag slime had high plastic viscosity of unbroken structure at the same fluidity with KCP slime. But at the same moisture contents these viscosities were almost similar.
10. Completely broken structure's viscosity of limestone – slag slime was in 2–3 times higher than KCP slime's. Also it increased in higher temperature whereas KCP slime's viscosity was not.
11. In KCP slime the difference between viscosities of unbroken and broken structures was higher than this difference in limestone – slag slime.
12. Moisture content strongly affects the thickening of limestone – slag slime. At 37 % moisture content low dispersion slime (008 sieve residual was 14 %) contained granular slag thickened in 26 days. The using of molten slime instead of granular did not improve fluidity of limestone – slag slime.

13. Limestone – slag slime included molten slime set more quickly. Such slime lost its fluidity in 20 days while slime contained granular slag in 24 days.

All described states are useful for recent prepared slimes at testing in static conditions. In case of thorough stirring duration of fluidity keeping must increase.

Described high density of blast-furnace granular slag is considered by researchers as decreasing factor of kinetic stability of cement raw slimes contained that slag. This statement also applies to phosphate slag.

Coefficient of equal falling (e) of phosphate slag and clay can be calculated by:

$$e = \frac{d_c}{d_s} = \frac{\sqrt{\delta_s - 1}}{\sqrt{\delta_c - 1}}, \quad (1)$$

Where δ_s and δ_c is slag and clay density, d_c and d_s is diameter of their particles.

The density of granular slag was 2.92. $d_s = 2.60$ were used. So after calculations equal falling coefficient of slag and clay particles was equal to 1.1. In other words, to obtain slag suspension with the same kinetic stability with clay's it is necessary to increase. At other same conditions dispersion degree of slag almost to 10 % in compare with clay.

Clay is grinded easy. Furthermore, clay can provide considerable product with colloidal size of fraction.

Granular phosphoric industrial slag at typical grinding provides small amount of colloidal size fraction. Increasing of grinding fineness by decreasing of residual on 008 sieve from 14 % to 8 % results in growth of 60–10 mkm fraction.

Therefore, the variant to increase of grinding fineness of granular phosphate slag to 10 % in compare with clay for kinetic stability is not possible.

This statement is based on results of slag tests on laboratory grinding mill. The grinding of limestone was not done there. At the same residuals on 008 sieve limestone powder had considerably higher fineness. Therefore, low dispersion of grinding represents in granular phosphate slag. But it does not mean that such material cannot be grinded more finely. For increasing grinding fineness loading components of grinding mill must be changed.

Cement raw slime is kinetically unstable at all. For example, KCP slime settled in 20 minutes. Almost the same situation was observed in limestone – slag slime. Therefore, there is no necessarily to achieve kinetic stability of limestone – slag slime by increasing of grinding fineness. Consequently, grinding fineness that is used in plants (8–14 % remainder on the 008 sieve) recommended. Slime stability can be carried as usual by mechanical stirring.

Moisture content of cement raw slime is important operation property. Low limit of moisture content commonly is determined by its fluidity on fluidity – meter device.

At the determination of low limit moisture content of limestone – slag slime contained phosphate industrial slag other properties should be taken into account. Properties are such as initial water – absorbing capacity of sedimentation volume, dynamic shear stress and thickening.

There is an opinion that kinetic stability also depends on moisture content. But this dependence is not used in research work because cement raw slime is kinetically unstable.

According to fluidity and shear stress value for limestone – slag slime 30 % of moisture content would be enough. But this moisture content was too low taking into account water – ability capacity of sedimentation volume and thickening of slime.

Water – ability capacity of sedimentation volume of dispersion system is defined by shape of particles and distribution of dispersion composition. Structure formation in system increases its sedimentation volume.

Structure formation at the same time is defined by chemical compositions of solid phases entered into dispersion system and their interaction with dispersion system. Mechanism of structure formation in limestone – slag slime is serious and big issue that is not considered in this research work.

Grinded granular phosphate slime generally contains narrow fraction and its grains are anisodiametrical. It has good effect on increasing of limestone – slag slime water – absorbing capacity of sedimentation volume. But initial water – absorbing capacity of settlement is considerably higher at 37 % moisture content than at 30 %.

Thickening of slime also depends on its moisture content. At 30 % moisture content slime thickens rather quickly. And at 37 % moisture content slime mobility maintains for 26 days.

In accordance with these cases low limit of moisture content for limestone – slag slime can be recommended as 37 %.

Results of that research work show that structure formation of limestone – slag slime occurs from commencement. It reveals because slime viscosity does not obey Einstein's law fluidity curve does not intersect coordinate origin, slime has resilient – plastic properties, etc.

The difference $\eta_o - \eta_d$ in KCP slime is higher than in limestone – slag slime. So its structuring is higher. At the same time resilient is clearer in limestone – slag slime because θ_s and θ_d are close.

At higher moisture content sedimentation volume increasing in limestone – slag slime can be explained by decreasing influence of volume concentration of dispersed phases on structure formation.

Apparently at limestone – slag slime kept in quiescence structure formation should be divided into three stages: initial stage, thickening and gelling accompanied with sharp hardening. And only because of last structure formation stage some doubts appears about the possibility of limestone – slag slime using at cement production. But the fact that slime sets only in quiescence conditions during a long time is omitted. At industrial conditions slag slime does not set and can be used at cement production with moist preparation of raw materials.

Experimental – industrial tests at KCP showed that there was no any property abnormality of limestone – slag slime in horizontal stank. Slime can settle also in vertical stank if it is not mixed. But it cannot be permitted.

According to P.I. Bazhenov, in Russian the Pykalev and Achinsk plants used nepheline slime as a raw component that indicates the possibility of phosphoric slag using in cement production with moist preparation. Nepheline slime generally consists of two calcium silicate that has high hydraulic activity.

3.2. Physical and mechanical properties of lime-slag sludge cement

Based on the carbonate-slag mixtures sludge the strength properties of cement were studied.

There were studied 5 mixtures (Table 9) of CaCO_3 and granulated phosphoric slag I (mixtures 1 and 2) and II (the rest). Mixtures 1 and 3 were composed on the basis of production of a belite clinker, 2 and 4 – an alite, and the mixture 5 – a clinker with the 60 % content of alite ($\text{SC} = 0.67; 1.00$ and 0.87). In the last two, the amount of limestone is 20–25% less than in clay mixtures.

Table 9. Mixtures composition, % by weight.

Component	Mixture				
	1	2	3	4	5
Phosphoric slag	57.47	39.22	61.42	41.40	46.88
CaCO_3	42.53	60.78	38.76	58.60	53.12

The studies show for obtaining an alite clinker the lime-slag mixture with $\text{SC} = 1.00$ can be burned at 1400°C , in which lime is absorbed with reasonably practicable completeness ($\text{CaO}_{\text{free}} = 0.70\%$) for 10 minutes (slag contains $\text{CaF}_2 = 5.13\%$).

The product consists of the C_3S phase with small inclusions of the C_2S phases and fluorite. When calculating the amount of alite, it was assumed that at temperatures starting from 1300°C and above, MgO (2.07 %), Al_2O_3 (1.70 %) are dissolved in the C_3S in the form of tricalcium aluminate, $\text{Fe}_2\text{O}_3 = 0.15\%$ and $\text{P}_2\text{O}_5 = 0.26\%$; the C_2S phase dissolves the C_3P . Dicalcium silicate is being formed at 1100°C after 3 minutes; at 1200°C and above – from the first minute of heating. The beginning of the C_3S formation coincides with the end of calcite decarbonization process and slag transformation into the C_2S . According to X-ray photographs *a*, *b*, *c* (according to the Fig. 8) and *d* (according to the Fig. 9) in the citric acid draw sediments, there fluorite and wollastonite are present.

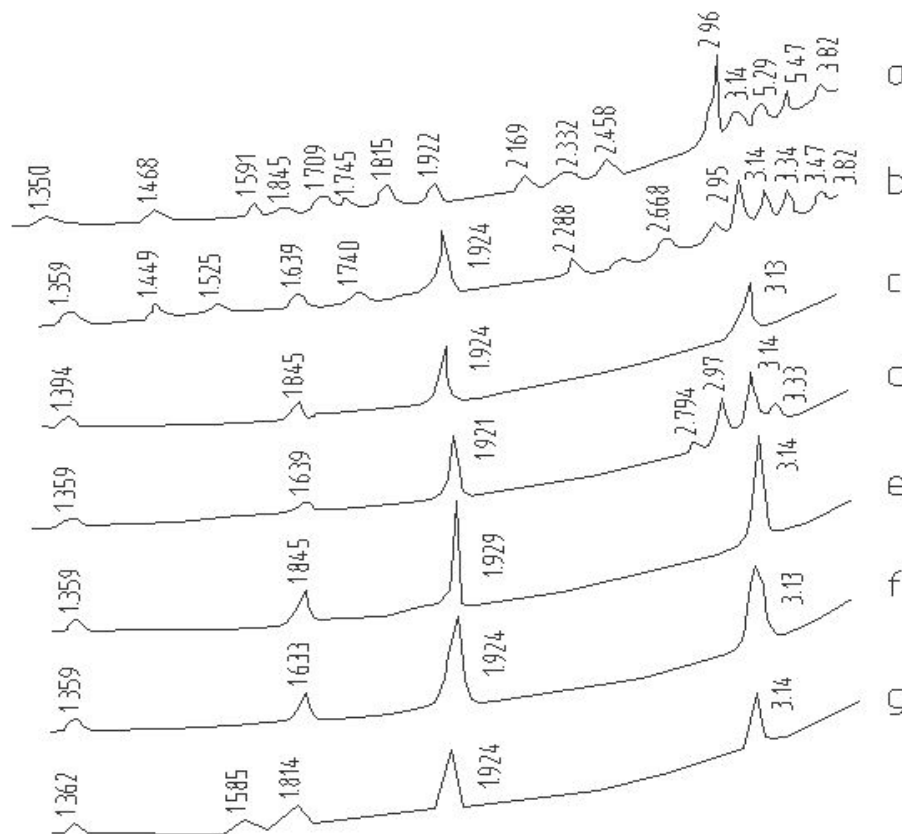


Figure 8. The citric acid draw sediments X-ray photographs
a – 1100 °C, 5 min; b – 1100 °C, 10 min; c – 1100 °C, 25 min; d – 1200 °C, 5 min;
e – 1200 °C, 10 min; f – 1200 °C, 20 min; g – 1200 °C, 25 min.

The amount of free fluorite above 1200°C decreases with increasing the temperature and duration of burning. According to the Fig. 9, g at 1500°C after 20 minutes there remains a tiny amount of the substance. Therefore, the bulk of fluorine was dissolved in calcium silicates.

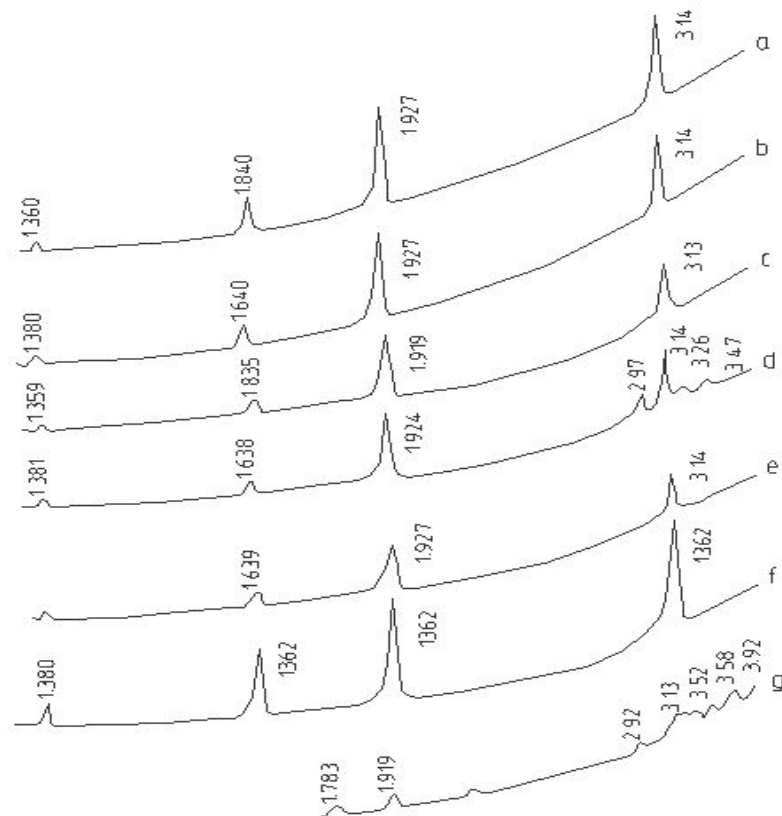


Figure 9. The citric acid draw sediments X-ray photographs
a, b, c – 1100 °C, 5, 10, 25 min; d, e, f, g – 1200 °C, 5, 10, 20, 25 min.

In the mixture 2, after adding 2 % of the CaF_2 into it and burning at 1400°C for 30 and 60 min., there are formed large alite crystals with smoothed angles (according to the Fig. 10). The further increase in burning duration at the given temperature or its increase up to 1500°C leads to a decrease in crystal size to $5\text{ }\mu\text{m}$.

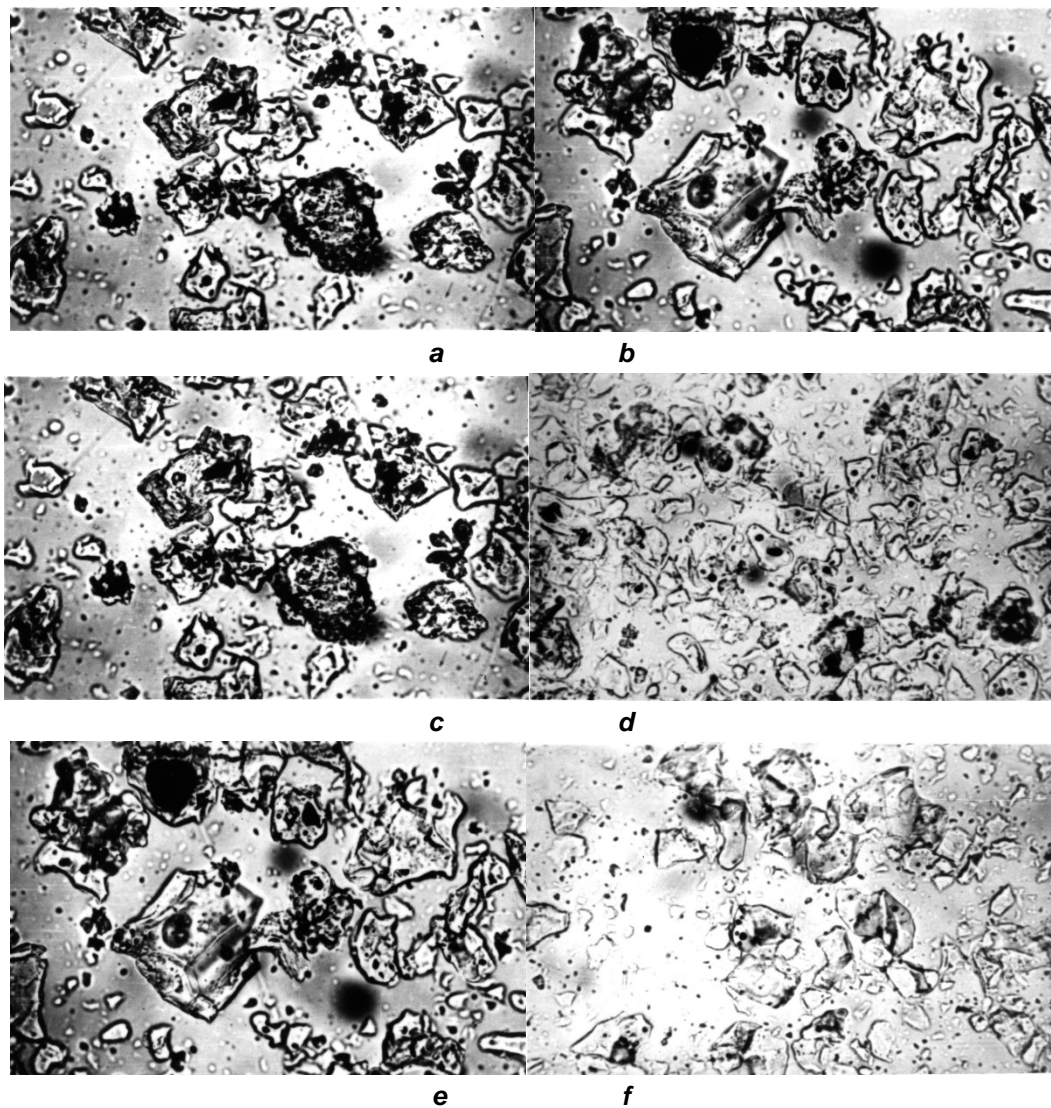


Figure 10. Photomicrographs roasted mixture 2 for C_3Sc 2% CaF_2 , x240.
a – 1400°C , 30 min; b – 1400°C , 60 min; c – 1400°C , 120 min; d – 1500°C , 30 min;
e – 1500°C , 60 min; f – 1500°C , 120 min

The mixture 5 with $\text{SC} = 0.87$ shall be also roasted at 1400°C within 20 minutes (Table 10), i.e. it has no advantage over the mixture with $\text{SC} = 1.0$. The samples roasted at 1300 , 1400 and 1500°C within 60, 20 and 10 minutes consist of alite and belite (according to the Fig. 11). Dicalcium silicate is formed from the first minute of heating. The C_3S lines (alite) appear on the X-ray radiograph of the cakes roasted for 10, 5, and 3 min at 1200 , 1300 , and 1400°C .

Table 10. Free calcium oxide of the mixture 5, % by weight.

Temperature $^\circ\text{C}$	Burning duration, min									
	1	3	5	10	15	20	25	30	60	120
1200	5.82	14.29	14.38	7.27	4.57	4.38	4.00	3.21	3.14	1.75
1300	9.11	17.37	9.10	4.80	3.10	1.36	1.50	1.91	0.47	0.13
1400	11.66	17.82	7.11	3.28	1.13	0.33	0.29	0.23	0.13	no
1500	15.82	8.50	2.24	0.41	0.09	no	–	–	–	–

With slow burning, the formation of belite and alite clinkers ends with a practical acceptable completeness at 1000 and 1400°C . Under slow burning conditions, as in the case of an abrupt one, reactions in the mixture 4 ($\text{KN} = 1.0$) proceed better than in the mixture 5. At 1100°C , there are formed as much alite as at 1200°C in case of abrupt burning. In the final roasted product of the mixture 4, only the alite lines are preserved. Cuspidine, as an intermediate formation, disappears at 1200°C .

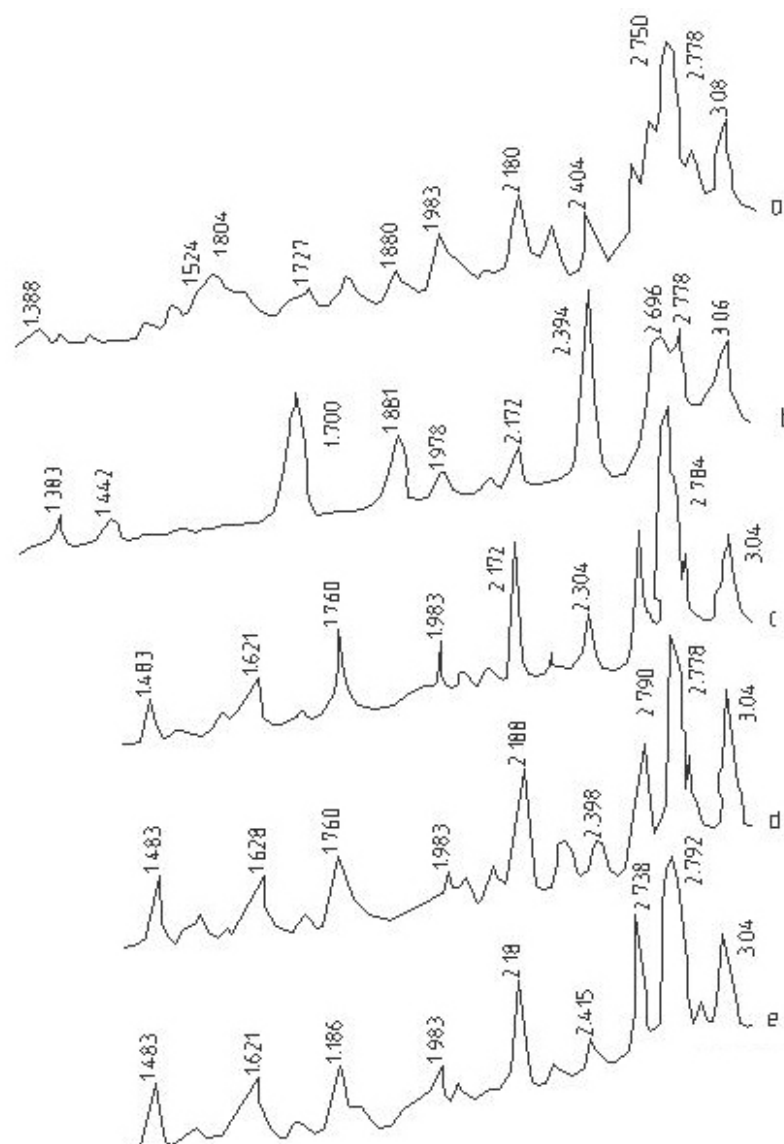


Figure 11. The roasted cakes X-ray photographs
a – C₂S, 1200 °C; b, c, d, e – 60% C₃S, 900, 1300, 1400 and 1500 °C

Mixtures for producing high-alumite clinker were tested at the pilot plant of the Cement Research Institute. A differential characteristic of the obtained clinkers, to be detected microscopically, is their high porosity. It leads to easy grinding.

3.2.1. Physical and mechanical properties of cement based on phosphoric slag and fuel consumption assessment for clinkers

Standard grid cement obtained with adding 3 % gypsum from clinkers 2-7, high-strength (Table 11). The most strength is the cement 6 with SC = 1.00 and containing the maximum alite amount, the least – cement 2 with SC = 0.95. However, the cement strength can be defined not only with the SC value.

Table 11. Cement test results (Water.cement = 0.4).

Cement	Density standard, %	Setting time, h-min		Cone flow diameter, mm	Breaking stress, MP					
		beginning	end		under bending, after			under compression, after		
					3 days	7 days	28 days	3 days	7 days	28 days
2	25.0	2-40	5-00	109	6.5	7.0	7.0	36.7	50.5	50.9
3	23.5	0-50	1-20	109	5.6	6.9	7.9	30.9	47.1	59.3
4	23.5	0-50	2-40	108	4.2	6.7	7.1	38.4	48.5	59.0
5	24.5	0-30	3-10	110	5.3	6.7	7.3	30.9	41.4	57.3
6	24.5	1-20	3-40	108	6.9	6.6	7.6	34.4	48.4	61.8
7	24.0	1-50	4-00	110	5.9	6.7	7.2	34.8	49.7	58.8

There was made an attempt to determine the effect of sulfur content in cinders and the iron amount (Table 12) on cement quality obtained from limestone-slag raw materials with additives.

Table 12. The content of basic oxides in clinkers, % by weight.

Clinker	CaO	SiO ₂	Al ₂ O ₃	Fe ₂ O ₃	P ₂ O ₅	SC	n	p
Used the cinder with the 2.5 % content of SO ₃								
1	66.65	22.00	2.19	3.75	0.92	0.95	3.70	0.58
2	66.53	23.65	2.24	3.95	1.04	0.91	3.82	0.57
3	67.24	21.65	2.24	4.80	1.00	0.99	3.08	0.47
4	65.34	21.40	2.19	4.83	0.90	0.94	3.05	0.45
5	66.53	22.35	2.35	5.05	1.07	0.95	3.02	0.46
6	66.89	21.50	2.49	5.11	0.97	0.99	3.26	0.49
7	67.24	20.70	2.30	5.20	1.15	1.00	2.76	0.44
8	65.83	20.70	2.78	6.62	1.04	0.96	2.20	0.42
Used the cinder with the 12.80 % content of SO ₃								
1	67.81	22.51	1.90	3.80	1.04	0.98	3.95	0.50
2	67.24	22.46	1.97	4.20	1.04	0.97	3.64	0.47
3	66.25	21.85	2.00	4.53	1.02	0.98	3.35	0.44
4	67.24	22.20	2.00	4.73	1.01	0.98	3.30	0.42
5	66.11	21.80	1.92	4.95	1.00	0.97	3.18	0.39
6	67.24	21.75	1.88	5.19	1.00	0.99	3.08	0.36

The data of the table 13 show the following:

Table 13. Cement test results (water.cement = 0.4; gypsum 5 %).

Cement	Density standard, %	Setting time, h-min		Cone flow diameter, mm	Breaking stress, MP					
		beginning	end		under bending, after			under compression, after		
					3 days	7 days	28 days	3 days	7 days	28 days
SO ₃ in cinder with 2.52 %										
1	22.25	0-45	6-32	107.0	5.1	5.4	7.1	37.0	43.8	53.4
2	23.85	0-40	6-45	108.0	4.9	5.4	6.5	35.4	42.0	48.2
3	23.38	2-07	7-27	107.0	4.8	5.2	6.6	35.5	47.5	60.0
4	24.50	0-37	6-47	116.5	4.6	5.5	6.2	30.5	37.7	52.6
5	22.75	1-05	6-35	108.0	4.7	5.4	6.4	30.5	40.0	51.7
6	25.00	2-45	7-05	110	4.8	5.6	6.9	32.5	44.2	49.1
7	22.50	1-20	7-35	110.5	4.1	5.3	6.0	27.1	40.1	48.6
8	23.75	1-12	9-15	110	4.1	4.5	5.9	23.3	31.7	37.3
SO ₃ in cinder with 12.80 %										
1	20.50	0-57	5-55	115.5	4.9	5.9	6.9	24.5	42.6	55.2
2	21.25	1-40	10-20	106.5	3.7	4.8	5.8	19.0	32.7	46.2
3	21.75	1-00	10-53	105.0	3.8	4.9	5.9	20.9	33.4	47.1
4	21.75	0-56	9-20	110.0	4.4	4.7	5.3	20.9	34.6	47.5
5	22.00	0-30	9-45	109.0	4.0	4.8	5.9	22.4	31.0	42.4
6	21.75	0-22	6-17	110.0	3.9	5.1	5.6	23.3	35.5	46.7

– sulfur in cinder and iron oxides in clinker have a significant effect on cements properties. In limestone-slag mixtures the low-sulfur cinders should be used;

– when using low-sulfur cinders the cement of 500 rank can be obtained from the clinker with SC = 0.94 and higher. At the same time, the Fe₂O₃ content in clinker can be brought up to 5 %. Further increase in the Fe₂O₃ amount reduces the cement rank despite its high SC (cements 6–8);

– with polysulphide cinders the cement of 500 rank can be obtained from a clinker with SC of at least 0.97 and the Fe₂O₃ content of not more than 3.80 %.

If the last limit is exceeded, cements do not meet the setting time standard requirements. The reason for this is, obviously, the high content of magnetite in polysulphide cinders. Clinker mixtures were made of limestone and slag with introducing cinders. The content of P_2O_5 was varied by adding tricalcium phosphate in the 3–6 mixture. The SO_3 content in the mixture ranged from 0.67–1.25 %.

Mixtures in the form of bars of 110×110×20 mm were roasted at 1400 °C for 4 hours in a laboratory furnace. The temperature was raised to 1400°C for 10 hours. As a result of prolonged burning the sulfur in cinders burned out, the SO_3 content in clinkers was leveled out. With an increase in phosphorus content the residual sulfur slightly increases in clinkers; it is comparatively larger in the case of using a polysulphide cinder.

Clinker 1. SC = 0.96; n = 3.75; p = 0.77. Alite – 75; C_4AF – 10 and $C_{12}A_7$ – 1%. Alite grains have irregular, angular, often with a rounded shape; there are also tabular or prismatic grains in splices with each other; grains size in cross-section is 0.05–0.2 mm; color is dark gray.

The intermediate phase fills small cavities between alite grains; irregular excriting shape, the borders are wavy, clear; color is light gray to grayish white; dimensions 0.1 mm in cross-section. Clinker porosity is 25–30 %.

Clinker 3. SC = 1.00; n = 3.34; p = 0.73, alite – 80; C_4AF – 11; $C_{12}A_7$ – 1 %. Alite crystals have irregular, isometric, rounded shape, tightly adjacent to each other, form almost continuous drainage aggregate; in some areas, the aggregate is so tight that its grain structure cannot be practically differed, and grain boundaries are difficult to be determined; grains size in cross-section is 0.05–0.25 mm. The intermediate phase fills cavities between the alite grains; with dimensions of 0.01–0.2 mm in cross-section. Clinker porosity is 15–25.

Clinker 5. SC = 0.96; n = 3.81; p = 0.63; Alite – 78; C_4AF – 11 %. Alite grains have irregular, isometric shape, less commonly slightly elongated, and are also tightly against each other; sizes of 0.01–0.3 mm with a predominance of grains of 0.1 mm. The crystals size of the intermediate phase is 0.01–0.1 mm in cross-section. Clinker porosity is 35–40 %.

The clinker crystallization rate using the 8-point Hyprocement system is estimated as average (4 points) with the exception for the 3rd (3.5 points).

The clinkers obtained using a high-sulfur cinder are distinguished by a denser structure and better alite crystallization.

Clinker 2. SC = 0.97; n = 4.24; p = 0.76. Alite – 77; C_4AF – 9; $C_{12}A_7$ – 1 %. Alite grains have irregular, isometric or slightly elongated shape with different sizes; there are also well-formed tabular or short-prismatic grains with slightly rounded peaks; with dimensions of 0.05–0.4 mm in cross-section. The intermediate phase is located in the alite grains interstitial tissue, repeating outlines of the latter; with dimensions of 0.01–0.15 mm in cross-section. Clinker porosity is 10–15 %.

Clinker 4. SC = 1.00; n = 4.12; p = 0.63. Alite – 82; C_4AF – 10 %. Alite grains, except in very rare exceptions, fill cavities without gaps; with dimensions of 0.01–0.2 mm. Clinker porosity is 10–15 %.

Clinker 6. SC = 0.96; n = 3.68; p = 0.58. Alite – 72; C_4AF – 10; C_2F – 1 %. Alite grains have irregular, isometric or elongated shape, are also tightly against each other. A nonequigranular grain structure is characteristic: along with the widely-spread grains of 0.01–0.3 mm, there are areas that sharply stand out against the general background with grains size up to 0.5–1.0 mm in cross-section. In such areas, the intermediate phase content is sharply reduced.

In general, clinkers have a glomeroblastic structure with a crystallization degree of 2 and 6 clinkers equal to four points, and the clinker 4 – three points. Cements from these clinkers were milled at the same duration (1 h 50 min). The fineness of cement grinding is almost the same, about 300 m².kg. The data in the table 6 show the following:

Table 14. Mechanical and physical testing results of clinker cements.

Cement	SO_3 content, %	008 sieve residue, %	Density standard, %	Setting time, h-min		Water. cement	Cone flow diameter, m	Breaking stress, MP					
								under bending, after			under compression, after		
				begin- ning	end			3 days	7 days	8 days	3 days	7 days	28 days
1	2.08	5.5	23.25	1-10	5-20	0.39	111	5.6	7.2	8.5	36	54	71
2	1.60	5.8	23.25	1-10	6-55	0.38	109	5.2	5.7	7.4	23	39	63
3	2.00	6.3	23.25	2-35	7-20	0.35	107	6.5	6.9	9.1	32	59	82
4	1.76	5.2	23.50	1-45	6-45	0.37	106	6.0	7.8	9.0	37	57	77
5	2.16	5.6	23.75	3-50	7-50	0.37	107	6.2	7.8	8.2	44	58	72
6	2.08	6.8	23.50	3-25	8-10	0.38	110	5.1	6.6	7.8	31	46	66

– cements are with high strength; among them the cement 2 of furnace blend with a high-sulfur cinder has the minimum strength (63 MPa), and the maximum – with a low-sulfur one (cement 3, SC = 1.00; 82 MPa). In general, when using a high-sulfur cinder instead of a low-sulfur, the cements rank with a high SC decreases by 5–8 MPa. There is no pronounced dependence of cements strength against its phosphorus pentoxide content in the range of 1.00–2.23 %. In terms of three-day strength, cements are referred to the quick-hardening category;

– cements water demand is relatively low. This feature of high alite cement from phosphoric slag we mention above;

– in terms of setting time, cements meet the Russian State Standard GOST 10178-85 requirements. The data in the table 15 show the following:

a) cements grindability is slightly improved with SC increase;

b) cements are characterized by relatively low water demand (water.cement = 0.36–0.37);

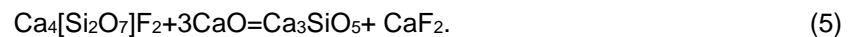
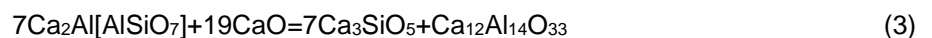
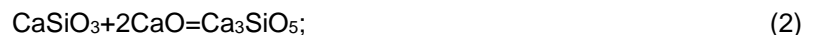
c) cements show a slow initial setting (from 3 h 25 min to 4 h 20 min);

g) cements activity increases from 44.6 to 59.3 MPa, depending on the value of SC = 0.92–0.98.

Table 15. Physical and mechanical parameters.

Cement	SO ₃ content, %	008 sieve residue, %	Density standard, %	Setting time, h-min		Water. cement	Cone flow diameter, mm	Breaking stress, MP					
								under bending, after			under compression, after		
				beginning	end			3 days	7 days	8 days	3 days	7 days	28 days
1	0.4	9.6	22.75	4-20	9-09	0.36	108	4.7	5.2	5.9	22.3	33.3	44.6
2	0.4	9.2	22.50	3-25	7-59	0.37	106	5.1	5.1	6.1	24.5	36.1	50.7
3	0.4	8.0	22.50	3-25	8-09	0.37	108	5.8	5.6	6.4	33.5	43.5	59.3

Theoretical fuel consumption for alite clinker is determined by the total reactions.



Due to reduction in release of the reaction gaseous products, the total consumption of raw materials decreases by at least 1.13 times. The theoretical fuel consumption calculated using the data of the Karaganda Cement Plant for clinker formation in an alite mixture is 2.246.588 kJ.t versus 3.059.315 kJ.t based on carbonate, i.e. it decreases by 1.3 times.

4. Conclusions

1. Study of impact of concentration of dispersion phase on rheological and elastic-plastic-viscous properties of slug of charge materials, consisting of limestone and phosphorus slag, firstly applied for production of high alite Portland cement, demonstrated ability of slag to preserve solid phases of charge materials in suspension.

2. Slags of phosphoric plants can be applied for cement production by wet method of raw materials preparation. Granular slag is preferable to molten as cement raw component.

3. It is recommended to control fineness of grinding of residual slag by quantity of rest on sieves 02 and 008. Rest on a sieve 008 shall be within 8–14 %. Rest on a sieve 02 shall not be more than existing norms.

4. It is recommended that lower limit of slag moisture was 37 %.

5. Stability of residual slag is achieved by the existing methods of slags blending.

6. Blending mode in vertical mixing basins shall be developed taking into account specific features of residual slag.

7. The more strength activity of cements from limestone-slag mixture is, the more the SC is. With the same SC value with a relatively high strength of cement one can achieve controlling the content of C₄AF in it. Of great importance for the strength of cements is also the crystallization degree of clinkers. High alite clinkers with an intermediate content of not more than 20 % have a crystallization degree of not more than 4 points according to the Giprocement system. At this crystallization degree, a clinker with

SC = 1.00 obtained using a low-sulfur cinder provides cement with an activity of 82 MPa with a standard grinding fineness; when using a polysulphide magnetite cinder, the strength of the cement is reduced to 77 MPa.

8. Equivalent fuel consumption, for burning 1 ton of Portland cement clinker from the phosphoric slag mixtures compared to the limestone-clay mixture of the Karaganda Cement Plant with a wet production method is reduced by at least 15 %, which is confirmed by a pilot-plant test performed at the plant.

References

1. Wang, H., He, Y., Pan, Y., Yu, G. Mechanical properties of magnesium potassium phosphate cement. Magazine of Civil Engineering. 2019. 87(3). Pp. 59–65. DOI: 10.18720/MCE.87.5
2. Li, D., Shen, J., Mao, L., Wu, X. Influence of admixtures on the properties of phosphorous slag cement. Cement and Concrete Research. 2000. 30(7). Pp. 1169–1173. DOI: 10.1016/S0008-8846(00)00291-X
3. Ifka, T., Palou, M., Baráček, J., Šoukal, F., Boháč, M. Evaluation of P₂O₅ distribution inside the main clinker minerals by the application of EPMA method. Cement and Concrete Research. 2014. 59. Pp. 147–154. DOI: 10.1016/j.cemconres.2014.02.010 URL: <https://linkinghub.elsevier.com/retrieve/pii/S000888461400060X> (date of application: 1.12.2019).
4. Khvostenkov, S.I. Comparative technical and economic indexes of dry and wet methods of manufacturing the portland cement. Stroitel'nye Materialy. 2005. (5). Pp. 16–20.
5. Goberis, S., Antonovich, V., Pundene, I., Stonis, R. Effect of the quality of microsilica on the flow properties of cement slurry and characteristics of low-cement refractory concrete on a chamotte filler. Refractories and Industrial Ceramics. 2007. 48(2). Pp. 123–127. DOI: 10.1007/s11148-007-0042-4
6. Guo, C., Zhu, J., Zhou, W., Sun, Z., Chen, W. Effect of phosphorus and fluorine on hydration process of tricalcium silicate and tricalcium aluminate. Journal Wuhan University of Technology, Materials Science Edition. 2012. 27(2). Pp. 333–336. DOI: 10.1007/s11595-012-0462-y
7. Guan, Z., Chen, Y., Qin, S. Effect of phosphor on the formation of alite-rich portland clinker: Proceedings of the 12th International Congress on the Chemistry of Cement. Montreal Canada. 2007. Pp. 40.
8. Le Coustumer, P., et al. Effect of clinker phosphorus on the microstructure and physico-chemical properties of cement. Cement and its Applications. 2010. 2. Pp. 96–100.
9. Boughanmi, S., Labidi, I., Megriche, A., Tiss, H., Nonat, A. Does phosphorus affect the industrial Portland cement reactivity? Construction and Building Materials. 2018. 188. Pp. 599–606. DOI: 10.1016/j.conbuildmat.2018.08.060
10. De Noirfontaine, M.N., Tusseau-Nenez, S., Signes-Frehel, M., Gasecki, G., Girod-Labianca, C. Effect of phosphorus impurity on tricalcium silicate T 1: From synthesis to structural characterization. Journal of the American Ceramic Society. 2009. 92(10). Pp. 2337–2344. DOI: 10.1111/j.1551-2916.2009.03092.x
11. Hökfors, B., Boström, D., Viggh, E., Backman, R. On the phase chemistry of Portland cement clinker. Advances in Cement Research. 2015. 27(1). Pp. 50–60. DOI:10.1680/adcr.13.00071.
12. Hu, Y., Li, W., Ma, S., Wang, Q., Zou, H., Shen, X. The composition and performance of alite-ye'elinite clinker produced at 1300 °C. Cement and Concrete Research. 2018. 107. Pp. 41–48. DOI: 10.1016/j.cemconres.2018.02.009
13. Ma, S., Ge, D., Li, W., Hu, Y., Xu, Z., Shen, X. Reaction of Portland cement clinker with gaseous SO₂ to form alite-ye'elinite clinker. Cement and Concrete Research. 2019. 116. Pp. 299–308. DOI: 10.1016/j.cemconres.2018.11.021
14. Staněk, T., Sulovský, P. The influence of phosphorous pentoxide on the phase composition and formation of Portland clinker. Materials Characterization. 2009. 60(7). Pp. 749–755. DOI: 10.1016/j.matchar.2008.11.013
15. Staněk, T., Sulovský, P., Boháč, M. Berlinite substitution in the cement clinker. Cement and Concrete Research. 2017. 92. Pp. 21–28. DOI: 10.1016/j.cemconres.2016.11.007
16. Yin, C., Lu, L., Wang, S. Effect of P₂O₅ on the properties of alite-calcium strontium sulphoaluminate cement. Advanced Materials Research. 306–307/2011. Pp. 961–965.
17. Kuz'min, M.P., Larionov, L.M., Kondratiev, V.V., Kuz'mina, M.Yu., Grigoriev, V.G., Kuz'mina, A.S. Burnt rock of the coal deposits in the concrete products manufacturing. Magazine of Civil Engineering. 2017. 8. Pp. 169–180. DOI: 10.18720/MCE.76.15
18. Kuzmin, M.P., Larionov, L.M. and other. Industrial uses of fluorogypsum. Proceedings of Universities. Investment. Construction. Real estate. 2019. 9 (2). Pp. 324–333.
19. Maghsoodloord, H., Allahverdi, A. Developing low-cost activators for alkali-activated phosphorus slag-based binders. Journal of Materials in Civil Engineering. 2017. 29(6). DOI: 10.1061/(ASCE)MT.1943-5533.0001806
20. Mehdizadeh, H., Najafi Kani, E. Rheology and apparent activation energy of alkali activated phosphorous slag. Construction and Building Materials. 2018. 171. Pp. 197–204. DOI: 10.1016/j.conbuildmat.2018.03.130
21. Mehdizadeh, H., Najafi Kani, E., Palomo Sanchez, A., Fernandez-Jimenez, A. Rheology of activated phosphorus slag with lime and alkaline salts. Cement and Concrete Research. 2018. 113. Pp. 121–129. DOI: 10.1016/j.cemconres.2018.07.010
22. Nurse, R.W. The effect of phosphate on the constitution and hardening of Portland cement. J. Appl. Chem. 1952. 2(12). Pp. 708–716.
23. Nakamoto, K. Infrared and Raman Spectra of Inorganic and Coordination Compounds: Part A: Theory and Applications in Inorganic Chemistry: Sixth Edition. John Wiley and Sons, 2008. 419 p.

Contacts:

Amankeldi Shaikezhana, shikg_a@mail.ru

Ayaulym Anuarova, anuarova_ayaulym@mail.ru

Valentin Antonovic, Valentin.antonovic@mail.ru



Antiskid prediction model for cement pavements in seasonal frost regions

Q.Q. Zhao^a, H.T. Zhang^{*b}, R.S. Fediuk^c, J.W. Wang^d

^a Northeast Agricultural University, Harbin, Heilongjiang, China

^b Northeast Forestry University, Harbin, Heilongjiang, China

^c Far Eastern Federal University, Vladivostok, Russia

^d Harbin Dongan Automobile Engine Manufacturing Co., Harbin, Heilongjiang, China

* E-mail: 2586762756@qq.com

Keywords: concrete, pavement, numerical model, temperature, optimization

Abstract. The antiskid performance of the cement concrete pavement in the seasonal frost regions is an important factor determining the safety of road use. However, due to the low efficiency and high cost of on-site detection, it is very important to reasonably predict it. Five key factors such as ice film thickness, tire pressure, tire load, driving speed, and structural depth were determined. The response surface test was performed to determine the corresponding range of the five factors when the model was optimally predicted. A prediction model of antiskid performance for cement concrete pavement in the seasonal frost regions was created, the goodness of model fitting and the normal distribution of the model were tested, and the applicability of the model was verified. The results show that when the thickness of the ice film is 1.5 mm ~ 3 mm, the tire pressure is 180 kPa ~ 240 kPa, the driving speed is 40 km/h ~ 80 km/h, the structural depth is 0.24 mm ~ 0.62 mm and the tire load is 3250 N ~ 4000 N, the prediction level of the model is the best; SRI can be interpreted by the model accounting for 98.5 %, and the regression model has a high degree of fit, which meets the assumption of normal distribution; the model's SRI predicted value fits the field measured SRI value to 0.995, and the degree of fit is high. The prediction model of antiskid performance is of great significance to prolong the service life of cement concrete pavement in seasonal frost regions.

1. Introduction

The antiskid performances of the cement concrete pavement in the seasonal frost regions have a great influence on the performance of the pavement. The area of China's seasonal frost regions is 5.137 million square kilometers, accounting for 53.5 % of the total land area, and the area of seasonal frost regions and short-term frost regions in the world accounts for 25 % of the total land area. Therefore, the establishment of a scientific prediction model of the antiskid performance of the cement concrete pavement in the seasonal frost regions can reasonably predict the antiskid performance of the pavement, monitor the damaged state of the cement concrete pavement [1], carry out safety warning for the highway traffic, and extend the service life of the cement concrete pavement [2, 3], which is of great significance for timely pavement maintenance.

The research on antiskid performance prediction at internal and abroad mostly focuses on the qualitative analysis of antiskid performance factors, the review of evaluation methods of antiskid performance level and the influence of single factor antiskid performance [4–6]. It does not establish the relationship between antiskid performance and influencing factors, so it can not quantify the anti-slip performance. In a few models predicting antiskid performance, PIARC model [7] uses the relationship between speed constant and standard friction number to detect the antiskid performance in any speed range, but the influencing factors are single, which is not enough to comprehensively predict the sliding performance. Paper [8] integrated the statistical results of mixture gradation, aggregate structure and traffic level to establish the prediction model of antiskid performance. Usanova et al [9] established a model for estimation of polished stone value to study the influence of aggregate on antiskid performance, and ignored the change of anti-skid performance when the climate factor acts on the pavement aggregate. Dong Zheng [10] established a prediction model of long-term antiskid performance based on the optimized GA-BP neural network method, which has the limitation of

Zhao, Q.Q., Zhang, H.T., Fediuk, R.S., Wang, J.W. Antiskid prediction model for cement pavements in seasonal frost regions. Magazine of Civil Engineering. 2020. 98(6). Article No. 9807 DOI: 10.18720/MCE.98.7



This work is licensed under a CC BY-NC 4.0

pavement service time and has a low prediction level for the overall antiskid performance of the pavement. Kane et al [11–14] according to the decomposition process of the pavement structure, it is confirmed that there is a certain relationship between the antiskid performance and the structure of the pavement, but the pavement structure can only be used as a part of the internal influence, and the research on the integrity of the antiskid performance is limited. Scientists [15, 16] established a model of antiskid performance and time, the model can stably predict the situation that the traffic volume tends to zero. Papers [17, 18] collected the accumulated traffic data of the road surface, established the soil volume reduction model, which can predict the antiskid performance of the road surface in different periods, but the prediction accuracy of the above models are low because the seasonal effect is not considered. Aliha et al [19] has carried out the braking test under different water film thickness, simulated the friction process of the tire rubber braking on the road, which has guiding significance for the tread pattern design that can improve the antiskid performance. The prediction model established by Xing et al [20] based on factors such as driving speed and water film thickness is more practical, but the influence of climate factors on antiskid performance is not considered. The antiskid performance of the cement concrete pavement in the seasonal frost regions is an important factor determining the safety of road use. However, due to the low efficiency and high cost of on-site detection, it is very important to reasonably predict it.

2. Methods

2.1. Screening of influencing factors for antiskid

In the selection of factors affecting the antiskid performance of cement concrete pavement, domestic and foreign experts have conducted relevant research. Dołycki and Jaskuła [21] applied the heat machine friction model to study the effect of temperature on the friction between the tire and the road surface. It was found that the high temperature would reduce the hysteresis friction of the road surface and negatively correlated with the antiskid performance level of the road surface. Abirami et al [5] model tire and road confirmed that the contact stress between tire and road surface is large when tire load is too heavy and tire inflation pressure is insufficient, which has a positive impact on road antiskid. Guo et al [8] tested the antiskid of cement concrete specimen under different environmental conditions, and the results showed that the antiskid performance of the pavement is reduced under the environmental conditions such as water accumulation, oil stain, tire scrap and soil. Taryma [22] proposed tire type and tire pressure factors such as tread pattern and tread wear are important external factors affecting the antiskid performance of cement concrete pavement. Papers [23–32] has carried out the test of large vehicles acting on the road surface, evaluated the morphology change state of the aggregate on the road surface, and considered that the structural depth, material polishing degree and driving speed are the main factors controlling the antiskid performance. According to the investigation results of the actual traffic conditions of the road, Plati [33, 34] proposed that the pavement structure has a significant impact on the antiskid performance. Based on the research results of the above literature, the factors such as tire type, tire pressure, tread pattern, tread wear, structural depth, material polish, oil, soil and other road pollution, temperature, tire load, water film thickness and driving speed are obtained can affect the antiskid performance of cement concrete pavement.

In order to further verify whether the climatic factors can be used as important indicators to influence the antiskid performance, under the same environmental conditions that ensure the above-mentioned influencing factors, the antiskid performance of three sections with similar completion year, same investigation year, similar traffic flow, respectively in the seasonal frost regions, the short-term frost regions and the non-frost regions is tested, as shown in Fig. 1. The non-frost regions select the Longzhou Highway section of Guangdong Province, China, the short-term frost regions select the Kaiyang Expressway section of Jiangsu Province, China, and the seasonal frost regions selects the Zhaozhao Highway section of Heilongjiang Province, China. Each of the 3 sections has 15 piles, with the pile numbers ranging from K117 to K131. In Fig. 1, the horizontal coordinate is the pile number K117 ~ K131, the ordinate is the antiskid Index (SRI). According to China's standard for evaluation of highway technical conditions (JTGH20-2007), the calculation equation of SRI is as follows:

$$SRI = \frac{100 - SRI_{\min}}{1 + a_1 e^{\frac{a_2 SFC}{2}}} + SRI_{\min}, \quad (1)$$

where: SRI is the antiskid index; SRI_{\min} is the limit value of antiskid performance, taken as 35; SFC is the lateral force coefficient; a_1 is the calibration coefficient, taken as 28.6; a_2 is the calibration coefficient, taken as - 0.105;

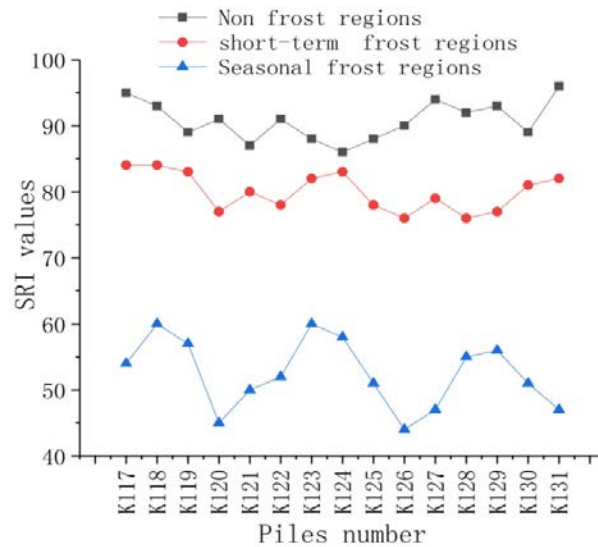


Figure 1. SRI values for different areas.

In Fig. 1, the SRI values corresponding to different stations in three different regions are different. For example, at K126, the SRI ratio of the non- frost regions to the seasonal frost regions is 2.09, and the ratio of the short-term frost regions to the seasonal frost regions is 1.79, which indicates that the SRI value of the seasonal frost regions is significantly lower than that of the short-term frost and the decrease of the SRI value in the short-term permafrost area is significantly higher than that in the non-frost regions. In Fig. 1, the SRI value of the non-frost regions is mostly between 90 and 100, and the antiskid performance is excellent. The SRI value of 15 stations in the short-term permafrost area varies from 75 to 90, the reason is that on the cement concrete pavement in the short-term frost soil area, the tire contacts with ice particles, water and road aggregate at the same time. The friction between the tire and the pavement is mainly composed of adhesion between the micro convex body of the friction pair surface and fluid shear. In this case, the SRI value of the pavement antiskid index is slightly lower than that of the non-frost soil pavement. Compared with the other two highways, the SRI value of the pavement in the seasonal frost regions is significantly lower, because the rain and snow on the cement concrete pavement in the seasonal frost regions will freeze to form ice film under the influence of the severe cold climate, and the pavement is covered by ice film, so that the friction between the pavement and the tire only depends on the interface adhesion and the deformation of the tire surface, and the SRI value is significantly lower than that in the short-term frost regions and non- frost regions. At the same time, there are usually 3 to 5 grades of northwest wind in the seasonal frost regions. Due to the wind force, the snow cover on the road is unevenly distributed and the thickness of the ice film is uneven, resulting in a significant difference in the SRI values of individual stations in the seasonal frost regions. For example, the SRI value of K120 is 21 % lower than that of K119.

In summary, the climatic factors have a significant impact on the antiskid performance of the pavement. In order to accurately predict the antiskid performance of cement concrete pavement in the seasonal frost regions, climate parameters that reflect the characteristics of the seasonal frost regions must be added to the prediction model. It is concluded from the above that the ice film thickness has a great influence on the antiskid performance index of the cement concrete pavement in the seasonal frost regions. Therefore, the ice film thickness factor is added to the antiskid performance prediction model for analysis. Combined with the previous research results, 12 influencing factors were extracted to screen the parameters of the model. Number 12 influencing factors, $F_1 - F_{12}$, as shown in Table 1.

Table 1. Influencing factors categories and numbers.

Number	Tire characteristic factors	Number	Road surface structure and medium factors	Number	Climate and traffic factors
F_1	Tire type	F_5	Structure depth	F_9	Temperature
F_2	Tire pressure	F_6	Material polishing degree	F_{10}	Driving speed
F_3	Tread pattern	F_7	Water film thickness	F_{11}	Tire load
F_4	Tread wear	F_8	Surface fouling, soil and other pollution	F_{12}	Ice film thickness

2.2. Identification of key factors

Based on the measured SRI data of Zhaozhao highway in Heilongjiang Province of China, the group analysis of the above 12 influencing factors is carried out, and the key factors influencing the model prediction

are screened out. The Euclidean distance method is used to calculate the group distance between the 12 factors. The factors with relatively small group distance are divided into the same group. Then the group distance between the groups is calculated by the Group Average Linkage method, and the two groups with the smallest group distance are rejoined into a group, and the number of the most reasonable groups determined by calculating the Silhouette index is 5, and the group distribution map is drawn by Statistical Package for Social Sciences (SPSS) software. The factors in the distribution map that affect the SRI value and the relatively large impact range can be identified as the key factors. The group classification and distribution are shown in Fig. 2.

In Fig. 2, the abscissa is the influence range standard value Z (RIV), and the ordinate is the influence degree standard value Z (SDV). The factors influencing the larger Z (RIV) and Z (SDV) values are the F_2 (tire pressure), F_5 (structural depth), F_{11} (tire load) in group 2, and F_{10} (driving speed) and F_{12} (ice film thickness) in group 3. It shows that the five factors in these two groups have a wide range of influence on antiskid performance, so these five factors are the main factors. The other three groups contain seven factors which are less influential than the five factors in group 2 and group 3, so they are secondary factors. After analyzing the grouping distribution results of 12 influencing factors, five factors including tire pressure, structural depth, driving speed, tire load and ice film thickness were identified as the key factors affecting the SRI value. They can be used as a parameter of the prediction model of the antiskid of the cement concrete pavement in the seasonal frost regions.

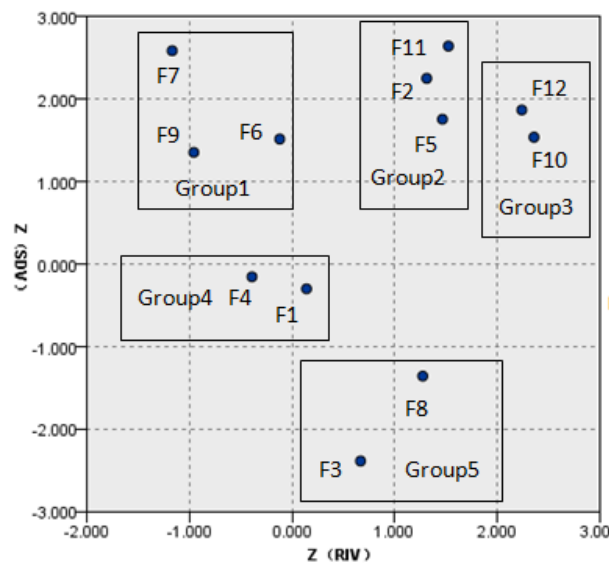


Figure 2. Grouping map.

2.3. Determination of model parameter value range

The antiskid performance prediction model of cement concrete pavement in the seasonal frost regions is constructed by using five parameters such as tire pressure, tire load, ice film thickness, driving speed and structural depth. It is necessary to determine the range of parameters. The parameters are denoted by symbols as follows: TP , TL , H , V and TD .

The range of 5 parameters should be reasonable and suitable for the characteristics of seasonal frost regions. If the TP value is too low or too high, the safety factor and driving comfort will be reduced. Therefore, the range of TP is selected within 180 kPa to 300 kPa. The TD range is obtained by calculating the ratio of groove depth and groove width multiplied by groove spacing. The groove width, groove depth and groove spacing commonly used in cement concrete pavement are 3–5 mm, 2–4 mm and 15–25 mm. The range of V is at highway speed 40 km/h ~ 120 km/h within the maximum and minimum limit value of degree. Too high TL value will cause damage to the road surface, so the common load value of 2500 ~ 4000 N is selected for TL range. According to the classification of road surface icing conditions studied by Smirnova et al [35], the ice film thickness is less than 1 mm when the ice layer is initially formed, and the driving condition is slightly slippery; the ice film thickness is 1 ~ 2 mm when partially frosted, and the driving conditions are smooth; all frost When the ice film thickness is greater than 3 mm, the driving conditions are very smooth, and the road surface should not continue to drive, so the highest value of H does not exceed 3 mm.

2.4. Determination of the optimal prediction space of the model

According to the above five parameters, the response surface test is designed to determine the optimal prediction space for the antiskid performance prediction model of cement concrete pavement in the seasonal

frost zone. In order to facilitate the drawing of test records, the codes of TP , TL , H , V and TD in response surface test are A, B, C, D, and E. According to the number and range of parameters, five factors and three levels of response surface test were selected. The coding level and value are shown in Table 2.

Due to the positive relationship between SRI and friction coefficient in the research results of Highway Technical Status Assessment Standard (JTGH20-2007) and Smirnova [35], in order to simplify TP , TL , H , V and TD pairs SRI response surface drawing process, the ordinate of the response surface is set as the friction coefficient value, the abscissa is the factor value, and the degree of change of the friction coefficient value is the degree of change of the SRI value. Therefore, in the response surface analysis below, the change of ordinate value is still explained by the change of SRI value.

Table 2. 5 factor coding level and value.

Coding level	A(TP /kPa)	B(TL /N)	C(H /mm)	D(V /km/h)	E(TD /mm)
- 1	180	2500	1	40	0.24
0	240	3250	2	80	0.62
1	300	4000	3	120	1

In the case where the coding levels of T , V , and TD are 0, the response surface of the design H (mm) and TP (kPa) to the SRI value is as shown in Fig. 3(a). When H was between 1 mm and 1.5 mm, the SRI value increased slightly, because the initial ice sheet was crushed and the edges of the crushed ice were convex and the cutting and furrow functions between the sharp corners and the tires increased the SRI value while increasing the lagging resistance; when H is increased from 1.5 mm to 3 mm, the inclination of the response surface is significantly increased from 1 mm to 1.5 mm. The reason is that the 3 mm ice film is compact and flat. Under the action of vehicle driving friction, the completely frost ice film surface will produce only a few molecular thick water films and enter into the boundary lubrication state. The adhesion friction between tire and ice surface drops sharply, and the SRI value drops the most. At this time, the SRI is the most sensitive to the change of H and has the highest response. Observe the surface change of TP in Fig. 3(a). As the TP increases, the contact area between the tire and the road surface decreases, and the SRI value decreases. When the TP is 180 kPa to 240 kPa, the slope of the surface is larger than that of 240 kPa to 300 kPa, and the SRI value is significantly reduced. The reason is that the deformation of the tire is the most serious in this interval and the contact area with the road surface changes most obviously, therefore, in the range of 180 KPa to 240 kPa, SRI has the highest response to TP .

In the case where the coding levels of TP , V , and H are 0, the response surface of the design TL (N) and TD (mm) to the SRI value is as shown in Fig. 3(b). After the TD exceeds 0.62 mm, the response surface gradually flattens. The reason is that when the structural depth of the groove reaches 0.62 mm, although reducing the slot spacing, increasing the slot depth or increasing the slot width can increase the TD value, the SRI value will not increase with it. At this time, the response of SRI to TD change is the lowest. Observe the surface change of TL in Fig. 3(b). When the TL exceeds 3250 N and close to 4000 N, the slope of the response surface increases obviously compared with 2500 N to 3250 N. The reason is that the road surface is pressed into the tire with heavy load, and the contact area between the tire and the road surface is from the tire. The center area is turned to the sides of the tire, and the grounding compressive stress becomes significantly larger as the tire sinks, so that the SRI value is significantly increased compared with the light load, indicating that the SRI has a higher responsiveness to the TL range above 3250 N.

In the case where the TL , TP , and H coding levels are zero, the response surface of the design V (km/h) and TD (mm) to the SRI value is as shown in Fig. 3(c). When V gradually increases from 80 km/h to 120 km/h, the inclination of the response surface is less than 40 km/h to 80 km/h, because the tire can be in full contact with the macroscopic structure of the road surface at low speed, and the higher the V , the smaller the actual contact area, the actual contact area between the tire and the road surface is gradually constant after the V exceeds 80 km/h, so the variation of the SRI value tends to be flat, indicating that the SRI has a lower response to V when the V range is above 80 km/h.

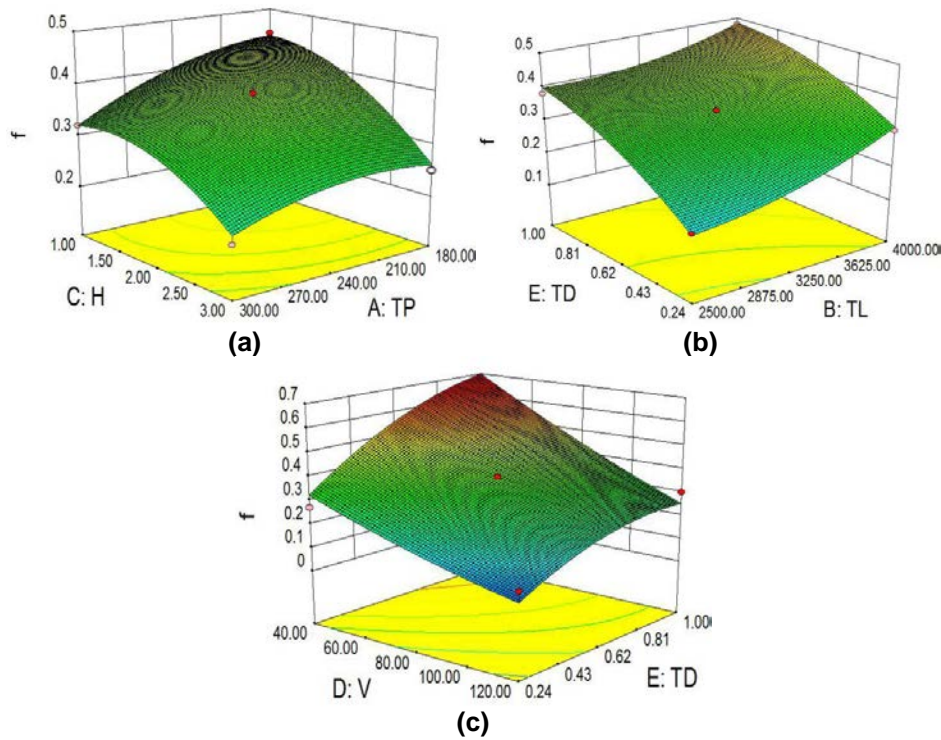


Figure 3. Response surface of five parameters to SRI:
(a) TP and H response surface to SRI values (b) TL
and TD response surface to SRI values (c) V and TD response surface to SRI values.

Combined with the above analysis of the response surface, if the response surface approaches the gradual, it means that the SRI value cannot change synchronously with the parameter value within the range of parameters corresponding to the surface, and the SRI responds to the change of parameters is low, at this time, the prediction accuracy of the antiskid performance prediction model of cement concrete pavement is low. If the slope of the response surface is large, the SRI value changes significantly, and the corresponding parameter range is more suitable for model prediction. According to the results of response surface analysis, the parameters of H value is 1.5 mm ~ 3 mm, TP value is 180 kPa ~ 240 kPa, TL value is 3250 N ~ 4000 N, TD value is 0.24 mm ~ 0.62 mm, V value is 40 km/h ~ 80 km/h, the range of values is the optimal prediction space of the model. When the five parameters are in the optimal prediction space, the prediction level of the model is the best.

3. Results and Discussion

3.1. Establishment of Model Relationship

By analyzing the variance of the response surface test results, the primary and secondary influence degree values of each parameter on the SRI value can be obtained, thereby integrating the parameters and establishing the relationship between the SRI and the parameters. After removing the source of variation with a small F value, the results of the variance analysis of 5 parameters were retained, and are shown in Table 3.

Table 3. Variance analysis of parameters.

Source	Sum of Squares	df	Mean Square	F	P
Model	0.35	5	0.07	52.994	< 0.001
TP	0.005	1	0.005	8.287	0.026
TL	0.007	1	0.007	13.750	0.009
H	0.036	1	0.036	66.065	< 0.001
V	0.034	1	0.034	43.750	< 0.001
TD	0.021	1	0.021	39.676	< 0.001
Residual	0.003	19	0.000	—	—
Lack of fit	0.001	14	0.000	0.368	0.9573
Pure Error	0.001	5	0.000	—	—
Total	0.353	24	—	—	—

In Table 3, the ratio of the squared sum of the regressions of the factors to the degrees of freedom (the mean square) is much higher than the mean square of the residuals, and the pure error term is close to 0, indicating that the experimental error is small. The significance value p of each factor is less than 0.05; the p value of the lack of fit is 0.9573, which is close to 1, indicating that the five parameters have a significant effect on the SRI. The higher the F value, the greater the degree of influence, the F value of ice film thickness is 66.065, which is the largest F value compared with the other four parameters. The F value of driving speed and structural depth is relatively close and the size is middle, respectively 43.750 and 39.676. The F values of tire load and tire pressure are similar to the other three parameters, which are 13.750 and 8.287, respectively. After the above analysis, the effect of ice film thickness on SRI value is most significant, followed by driving speed and structural depth, and finally tire load and tire pressure. Therefore, when establishing the relationship between parameters and SRI, the ice film thickness is listed as a separate indicator, and the driving speed and structural depth, tire load and tire pressure are respectively integrated into a comprehensive index. With reference to the prediction model of antiskid performance in the form of exponential function established by parameters such as water film thickness of Xing [20], the relationship between SRI and ice film thickness, tire pressure, tire load, driving speed and structural depth is established as follows:

$$SRI = \lambda \cdot (TP/TL)^{\lambda_1} \cdot H^{\lambda_2} \cdot \exp \lambda_3 \cdot [(60-V)/TD] \quad (2)$$

where SRI is the antiskid index; TP is the tire inflation pressure (kPa); TL is the load applied to the tire (N); H is the ice film thickness on the road surface (mm); V is between the road surface and the tire Relative slip speed (km/h); TD is the pavement structure depth (mm); $\lambda, \lambda_1, \lambda_2$ and λ_3 are regression coefficients.

Since equation (2) is a nonlinear equation, in order to simplify the method and steps of nonlinear equations in regression analysis, a logarithmic function method is used to linearly transform the equation. To find the natural logarithm of both sides of the equation, the equation turned into:

$$\ln SRI = \ln \lambda + \lambda_1 \ln(TP/TL) + \lambda_2 \ln H + \lambda_3 (60-V)/TD \quad (3)$$

$$\text{Let } \ln SRI = y, \ln \lambda = \lambda_0, \ln(TP/TL) = x_1, \ln H = x_2, (60-V)/TD = x_3.$$

Then equation (3) can be converted into:

$$y = \lambda_0 + \lambda_1 x_1 + \lambda_2 x_2 + \lambda_3 x_3 \quad (4)$$

The original nonlinear equation can be transformed into a linear equation for solving.

3.2. Significance test of regression equation

From the typical section of the seasonal frost regions, the field survey data of 20 sections of the three roads of Zhaozhao Highway, Heda Expressway and Hazhao Highway are selected for regression analysis. According to equation (4), the SRI value of the on-site survey is set to correspond to the transformation y as the dependent variable, TP and TL correspond to the transformed x_1 , H corresponding transformed x_2 , V and TD corresponding transformed x_3 as independent variables, and the model is linearly tested. In Table 4, the regression sum of the dependent variables is 60.544, and the ratio of the squared regression to the mean square is 20.181, which is much higher than the mean square of the residual 0.071. The ratio of the mean regression squared to the sum of the squared mean residuals (F) is 274.339, the value is large, and indicating that the change of the dependent variable is caused by the change of the independent variable rather than the experimental error, and the independent variable has a high explanatory force for the dependent variable. The significance value is 0, less than 0.05, the model linear regression significant. It is shown that in the F test, the linear regression of the equation is obvious, and a linear model can be established between the dependent variable and the independent variable.

Table 4. Regression model of ANOVAs.

model		Sum of Squares	df	Mean Square	F	Sig.
1	Regression	60.544	3	20.181	274.339	0
	Residual	0.786	11	0.071	–	–
	Total	61.330	14	–	–	–

3.3. Significance test of regression coefficient

After the F test shows that the linear model can be established, it is necessary to determine whether the influence of the independent variable on the dependent variable is significant. Therefore, the regression coefficient should be tested for significance. In Table 5, the partial regression coefficient represents the weight of each index. The absolute value of the standardized partial regression coefficient indicates the degree of influence of each variable on the dependent variable. The absolute value of the standardized partial regression coefficient of x_2 is the largest among the three indicators, indicating the parameter H corresponding to x_2 has

the greatest influence on SRI value, the x_3 corresponding parameter V and TD influence degree is second, and the relatively small degree of influence is the x_1 corresponding parameter TP and TL . This is consistent with the analysis of variance when determining the relationship between parameters and SRI. The standard error of the partial regression coefficient of each parameter is small, the Sig. significance value is less than 0.05, and the absolute value of the bilateral test threshold t is all greater than the significance level, indicating that the independent variable has significant influence, and the independent variable is retained in the model.

Table 5. Coefficient of regression model.

Parameter	Partial regression coefficient	Partial regression coefficient standard error	Standardized partial regression coefficient	t	Sig.
Constant	2.808	0.216	-	15.048	0.003
x_1	-0.513	0.041	-0.224	-6.575	0.012
x_2	-0.199	0.117	-0.811	-24.328	0.005
x_3	0.005	0.001	0.652	17.338	0.009

Bring the results of the above regression analysis into equation (4), the model is expressed as:

$$y = 2.808 - 0.513x_1 - 0.199x_2 + 0.005x_3 \quad (5)$$

Reconverted to a nonlinear equation:

$$SRI = 16.58(TP/TL)^{-0.513} H^{-0.199} \exp[0.005(60-V)/TD] \quad (6)$$

where SRI is the antiskid index; TP is the tire inflation pressure (kPa); TL is the load applied to the tire (N); H is the ice film thickness on the road surface (mm), $H \leq 3$ mm; V is between the road surface and the tire Relative slip speed (km/h); TD is the pavement structure depth (mm).

3.4. Model goodness of fit test

After the antiskid performance prediction model of cement concrete pavement in the seasonal frost regions is established, the goodness of fit between the independent variable and the dependent variable should be tested to ensure that the dependent variable can be interpreted by the model. In Table 6, R^2 is the deterministic coefficient between the dependent variable and the independent variable. Adjusting R^2 is the mean square error ratio that eliminates the influence of the number of independent variables. The closer R^2 and the adjusted R^2 are to 1, the better the fitting effect of the regression equation. The regression equation has an adjustment of R^2 of 0.985, which is close to 1, and the standard estimation error is only 0.113, indicating that the model has a good goodness of fit, and the dependent variable can be accounted for 98.5 % by the model interpretation.

Table 6. Summary of regression models.

R^2	Adjust R^2	Standard estimated error
0.992	0.985	0.113

3.5. Model normal distribution test

In order to verify the applicability of the prediction model of the antiskid performance of the cement concrete pavement in the seasonal frost regions, the normal distribution test was carried out for the model. Observing the residual histogram and the normal distribution curve of Fig. 4, the sample size is large enough and the residual distribution conforms to the normal distribution, which proves the correctness of the prediction model. Observe the residual P-P graph of Fig. 5, the residual distribution curve changes around the pre-set diagonal and diagonal directions. The two are close to coincide, and the regression model satisfies the normal distribution hypothesis. In summary, the SRI prediction model established by using TP , TL , H , V and TD as parameters has passed various tests, and the regression effect is remarkable, and the goodness of fitting is high.

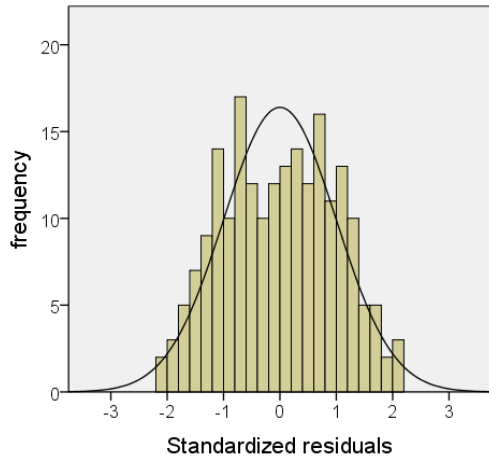


Figure 4. Residual histogram.

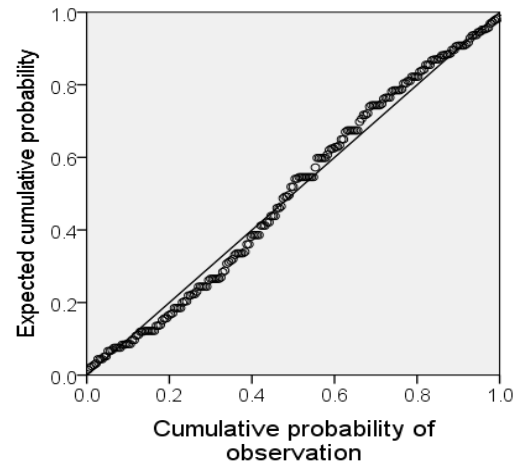


Figure 5. Residual regression P-P diagram.

3.6. Model verification

In order to verify the practicability of the antiskid performance prediction model of cement concrete pavement in the seasonal frost regions, the measured value of SRI and the predicted value of the model in a section of Zhaozhao highway in the past 9 years are selected for verification. The predicted value of SRI of the prediction model and PIARC model [7] are respectively matched with the measured value of SRI by SPSS software. In Fig. 6, the abscissa is the SRI measured value k_m , the ordinate is the SRI predicted value k_p , the deterministic coefficient R^2 of the PIARC model SRI predicted value and the measured value is 0.852, and the deterministic coefficient R^2 of the predicted model SRI predicted value and the measured value is fitted, it is 0.995, which proves that the prediction model has a higher degree of fit.

The test points for model verification on a highway section may lack randomness and result in deviation of results. Therefore, the measured SRI data of the six roads of the three roads of Zhaozhao Highway, Heda Expressway and Hazhao Highway are verified again in the same year. As shown in Fig. 7, the abscissa is the numerical number of 6 road segments in turn, and the ordinate is the SRI value, and the SRI value curve under different road segments is drawn. Since the ice film thickness of each of the six sections is not completely the same, according to the above response surface analysis results, when the ice film thickness of the road section is in the best prediction space of 1.5 mm to 3 mm, the SRI prediction value of the model will be close to or lower than the actual measurement Value, the SRI prediction value in other prediction space will be higher than the measured value, so the SRI prediction value of different road sections has higher or lower difference than the measured value. At the same time, it can be observed that the predicted model SRI predictive value curve is closer to the SRI measured value curve than the PIARC model SRI predicted value curve, which proves that the predictive model predicts the SRI value better, and the predictive model has good practicability.

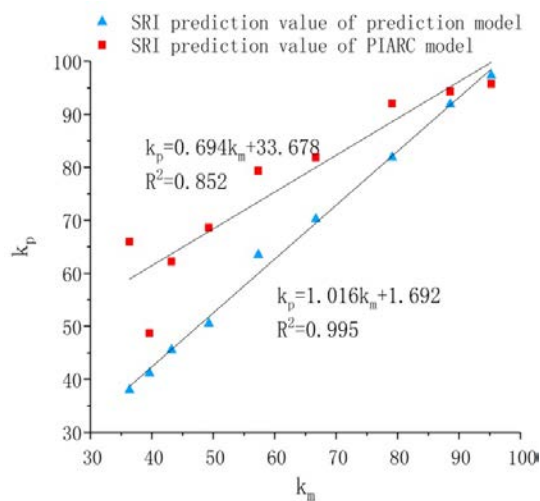


Figure 6. SRI predicts the correlation between the measured value and the measured value.

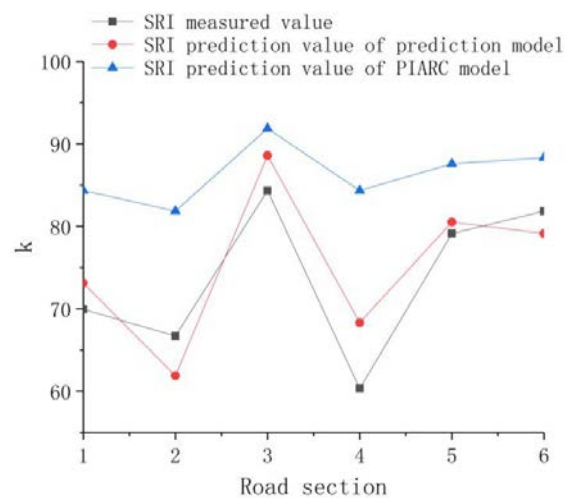


Figure 7. SRI prediction effect of prediction model.

4. Conclusions

1. The climatic factors have a significant impact on the antiskid performance of cement concrete pavement. The key factors affecting the antiskid performance of cement concrete pavement in the seasonal frost regions are ice film thickness, tire pressure, tire load, driving speed and structural depth. The test statistic value (F) of each factor is larger, which means that the influence degree of factor on antiskid performance is higher. The F value of the ice film thickness is 66.065, the F value of the driving speed is 43.750, the F value of the construction depth is 39.676, the F value of the tire load is 13.750, and the F value of the tire pressure is 8.287. It shows that the effect of ice film thickness on SRI value is most significant, followed by driving speed and construction depth, and finally tire load and tire pressure.

2. When the ice film thickness ranges from 1.5 mm to 3 mm, the tire pressure is between 180 kPa and 240 kPa, the driving speed is between 40 km/h and 80 km/h, the structural depth is between 0.24 mm and 0.62 mm, and the tire load is between 3250 N and 4000 N, the SRI's responsiveness to parameter changes is higher than other parameter values, which is the optimal prediction space of the model. At this time, the model's prediction level is optimal.

3. Using the five parameters of ice film thickness, tire pressure, tire load, driving speed and structural depth, the SRI value of the antiskid performance index of the cement concrete pavement in the seasonal frost regions can be predicted, and the ice film thickness in the prediction model is a separate indicator. Tire pressure and tire load, driving speed and structural depth are combined into a comprehensive index. The function forms of the index are exponential functions, and the coefficients after regression are -0.513, -0.199 and 0.005. The predictive model has a decisive coefficient R^2 of 0.985 and a significance level of 0. The model has a high degree of fit and significant regression, indicating that the predictive model has statistical applicability.

4. The prediction model and the PIARC model are verified in the same period of different sections and different sections of the same section. The R^2 of the prediction model is 0.995, the R^2 of the PIARC model is 0.852, and compared with the PIARC model, the SRI value predicted by the prediction model is closer to the measured value of SRI. It indicates that the prediction model of the antiskid performance of cement concrete pavement in the seasonal frost regions has a high prediction level and is highly practical.

5. Acknowledgements

Project Support: Youth Talent Project of Northeast Agricultural University (54978412).

References

- Gao, J., Wang, H., Chen, J., Meng, X., You, Z. Laboratory evaluation on comprehensive performance of polyurethane rubber particle mixture. *Construction and Building Materials*. 2019. 224. Pp. 29–39.
- Ueckermann, A., Wang, D., Oeser, M., Steinauer, B. A contribution to non-contact skid resistance measurement. *International Journal of Pavement Engineering*. 2015. 16(7). Pp. 646–659.
- Zhao, Q., Cheng, P., Wang, J., Wei, Y. Damage prediction model for concrete pavements in seasonal frost regions. *Magazine of Civil Engineering*. 2018. 84(8). Pp. 57–66. doi: 10.18720/MCE.84.6.
- De Larrard, F., Martinez-Castillo, R., Sedran, T., Hauza, P., Poirier, J.E. Cementitious artificial aggregate particles for high-skid resistance pavements. *Road Materials and Pavement Design*. 2012. 13(2). Pp. 376–384.
- Abirami, T., Loganaganandan, M., Murali G., Fediuk, R., Vickhram Sreekrishna, R., Vignesh, T., Janupriya, G., Karthikeyan K. Experimental research on impact response of novel steel fibrous concretes under falling mass impact. *Construction and Building Materials*. 2019. 222. Pp. 447–457.
- Klyuev, S.V., Klyuev, A.V., Vatin, N.I. Fiber concrete for the construction industry. *Magazine of Civil Engineering*. 2018. 84(8). Pp. 41–47. doi: 10.18720/MCE.84.4.
- Denisova, Yu.V. Additive technology in construction. *Construction Materials and Products*. 2018. 1(3). Pp. 33 – 42.
- Guo, R., Nian, T., Li, P., Fu, J., Guo, H. Anti-erosion performance of asphalt pavement with a sub-base of cement-treated mixtures. *Construction and Building Materials*. 2019. 223. Pp. 278–287.
- Usanova, K., Rybakov, V., Udalova, V., Kovylkov, A. Examination of Quality and Operational Properties of Vibropressed Paving Elements. *MATEC Web of Conferences*. 2016. 73. 040131.
- Zheng, D., Qian, Z., Liu, Y., Liu, C. Prediction and sensitivity analysis of long-term skid resistance of epoxy asphalt mixture based on GA-BP neural network. *Construction and Building Materials*. 2018. 158. Pp. 614–623. <https://doi.org/10.1016/j.conbuildmat.2017.10.056>.
- Kane, M., Rado, Z., Timmons, A. Exploring the texture-friction relationship: From texture empirical decomposition to pavement friction. *International Journal of Pavement Engineering*. 2015. 16(10). Pp. 919–928.
- Lin, C., Tongjing, W. Effect of fine aggregate angularity on skid-resistance of asphalt pavement using accelerated pavement testing. *Construction and Building Materials*. 2018. 168. Pp. 41–46. URL: <https://doi.org/10.1016/j.conbuildmat.2018.01.171>.
- Fediuk, R., Smoliakov, A., Muraviov, A. Mechanical Properties of Fiber-Reinforced Concrete Using Composite Binders. *Advances in Materials Science and Engineering*. 2017. Pp.1–13. <https://doi.org/10.1155/2017/2316347>
- Klyuev, S.V., Klyuev, A.V., Vatin, N.I. Fine-grained concrete with combined reinforcement by different types of fibers. *MATEC Web of Conferences*. 2018. No. 245, 03006.
- Fediuk, R.S., Lesovik, V.S., Liseitsev, Yu.L., Timokhin, R.A., Bituyev, A.V., Zaiakhanov, M.Ye., Mochalov, A.V. Composite binders for concretes with improved shock resistance. *Magazine of Civil Engineering*. 2019. 85(1). Pp. 28–38. DOI: 10.18720/MCE.85.3.

Zhao, Q.Q., Zhang, H.T., Fediuk, R.S., Wang, J.W.

16. Nelyubova, V.V., Babayev, V.B., Alfimova, N.I., Usikov, S.A., Masanin, O.O. Improving the efficiency of fibre concrete production. *Construction Materials and Products*. 2019. 2 (2). Pp. 4-9.
17. Yong-hong, Y., Yuan-hao, J., Xuan-cang, W. Pavement Performance Prediction Methods and Maintenance Cost Based on the Structure Load. *Procedia Engineering*. 2016. 137. Pp. 41–48.
18. Horníček, L., Rakowski, Z. Mechanical Stabilization of Intermediate Granular Layers in Pavement Structures – Laboratory Study *Procedia Engineering*. 2017. 189. Pp. 174–180.
19. Aliha, M.R.M., Bahmani, A., Akhondi, Sh. A novel test specimen for investigating the mixed mode I+III fracture toughness of hot mix asphalt composites – Experimental and theoretical study. *International Journal of Solids and Structures*. 2016. 90, Pp. 167–177.
20. Xing, B., Fan, W., Zhuang, C., Qian, C., Lv, X. Effects of the morphological characteristics of mineral powder fillers on the rheological properties of asphalt mastics at high and medium temperatures. *Powder Technology*. 2019. 348. Pp. 33–42.
21. Dołżycki, B., Jaskuła, P. Review and evaluation of cold recycling with bitumen emulsion and cement for rehabilitation of old pavements. *Journal of Traffic and Transportation Engineering (English Edition)*. 2019. 6(4). Pp. 311–323.
22. Taryma, T., Ejsmont, J.A., Ronowski, G., Swieczko-Zurek, B., Mioduszeński, P., Drywa, M., Woźniak, R. Road Texture Influence on Tire Rolling Resistance. *Key Engineering Materials*. 2013. 597. Pp. 193–198.
23. Guan, B., Wu, J., Xie, C., Fang, J., Zheng, H., Chen, H. Influence of macrotexture and microtexture on the skid resistance of aggregates. *Advances in Materials Science and Engineering*. 2018. Pp. 1–9.
24. Mengue, E., Mroueh, H., Lancelot, L., Medjo Eko, R. Design and parametric study of a pavement foundation layer made of cement-treated fine-grained lateritic soil. *Soils and Foundations*, 2018. 58(3). Pp. 666–677.
25. Shi, X., Mukhopadhyay, A., Zollinger, D. Sustainability assessment for portland cement concrete pavement containing reclaimed asphalt pavement aggregates. *Journal of Cleaner Production*. 2018. 192. Pp. 569–581.
26. Rezaei, A., Masad, E. Experimental-based model for predicting the skid resistance of asphalt pavements. *International Journal of Pavement Engineering*. 2013. 14(1). Pp. 24–35.
27. Farhan, A.H., Dawson, A.R., Thom, N.H., Adam, S., Smith, M.J. Flexural characteristics of rubberized cement-stabilized crushed aggregate for pavement structure. *Materials & Design*. 2015. 88. Pp. 897–905.
28. Qian, Z., Meng, L. Study on micro-texture and skid resistance of aggregate during polishing. *Frontiers of Structural and Civil Engineering*. 2017. 11(3). Pp. 346–352.
29. Huang, B., Shu, X., Li, G. Laboratory investigation of portland cement concrete containing recycled asphalt pavements. *Cement and Concrete Research*. 2005. 35(10). Pp. 2008–2013.
30. Chindapasirt, P., Sujumnongtokul, P., Posi, P. Durability and Mechanical Properties of Pavement Concrete Containing Bagasse Ash. *Materials Today: Proceedings*. 2019. 17(4). Pp. 1612–1626.
31. Alenezi, T., Norambuena-Contreras, J., Dawson, A., Garcia, A. A novel type cold mix pavement material made with calcium-alginate and aggregates. *Journal of Cleaner Production*. 2019. 212. Pp. 37–45.
32. Gupta, T., Sachdeva, S.N. Laboratory investigation and modeling of concrete pavements containing AOD steel slag. *Cement and Concrete Research*. 2019. 124. 105808.
33. Plati, C., Pomoni, M. Impact of Traffic Volume on Pavement Macrotexture and Skid Resistance Long-Term Performance. *Transportation Research Record*. 2019. 2673(2). Pp. 314–322.
34. Plati, C., Pomoni, M., Stergiou, T. Development of a mean profile depth to mean texture depth shift factor for asphalt pavements. *Transportation Research Record*. 2017. 2641(1). Pp. 156–163.
35. Smirnova, O., Kharitonov, A., Belentsov, Y. Influence of polyolefin fibers on the strength and deformability properties of road pavement concrete. *Journal of Traffic and Transportation Engineering (English Edition)*. 2019. 6(4). Pp. 407–417.

Contacts:

Qianqian Zhao, 492954791@qq.com
Hetong Zhang, 2586762756@qq.com
Roman Fediuk, roman44@yandex.ru
Jianwu Wang, nihaone@163.com

© Zhao, Q.Q., Zhang, H.T., Fediuk, R.S., Wang, J.W., 2020



Stress-strain state of Insulated Glass Unit in structural glazing systems

E. Gerasimova^a, A. Galyamichev^b, S. Dogru^c

^a NIUPC «Mezhregional'nyj institut okonnyh i fasadnyh konstrukcij», St. Petersburg, Russia

^b Peter the Great St. Petersburg Polytechnic University, St. Petersburg, Russia

^c Istanbul Okan University, Istanbul, Turkey

* E-mail: katyageras17@gmail.com

Keywords: glass, structural optimization, finite element method, stiffness, stress-strain state, Limit State Design

Abstract. Article presents the analysis of classical and structural ways of fastening of the glass unit subjected to uniformly distributed wind load under the various conditions: modification of the fixing step in horizontal and vertical direction, change of gas-filled gap and glass panel thicknesses. Calculation is performed in FEM-based SJ Mepla software for three most common types of glass units of the size of 1200×1200 mm, 2400×1200 mm and 3600×1200 mm. On the basis of obtained results, it is possible to conclude that modification of the fixing step in horizontal direction and glass panel thickness have a significant influence on the stress and deformation values; in contradistinction, modification in vertical direction and gas filling thickness do not noticeably impact stress-strain state of a plate. Default fixing step between two adjacent supports, which is often adopted by manufactures of IGUs without preliminary calculation for actual applied load, has to be verified in each case in terms of deformation in order to satisfy the conditions of SLS. The table of recommended values of maximum distance between supports is presented.

1. Introduction

Glass facades are nowadays an indispensable part of modern structures [1–3]. However, besides numerous advantages of glass units' application the design of IGU may face challenges of both aesthetics and performance character [4–6]. Translucent facade structures are exposed to various combinations of mechanical and climatic loads throughout the whole lifecycle of the building [7]. Existing researches [8, 9] indicate an increased risk of glass damage and destruction due to the effect of “thermal shock”. The experimental studies devoted to the analysis of the stress-strain state of glass panels under the climatic load, including those associated with extreme difference of temperature [10], are of a particular interest. However, conducting of such tests is technically complex and expensive [11]. It causes the necessity in other methods, such as computer modelling, which could produce sufficiently accurate results. The authors of [11] compare experimental and finite element modeling data obtained for similar facade systems in order to verify the use of Finite Element Method (FEM) for the calculation of systems subjected to thermally induced climatic load.

One of the main problems regarding aesthetics aspect is an appearance of optical distortion. Article [12] examines available engineering approaches and proposes a new way for mitigation of this effect. The new method is based on the partial rarefaction inside the IGU and performed by installation of additional pointed or linear support. The causes of optical distortion, also known as a «lens effect» in construction practice, are described in [13, 14].

Due to increased requirements for the reduction of thermal heat losses [15, 16] in buildings, parameters of IGUs are actively reconsidered what leads to change in their structural scheme. In order to minimize thermal transmittance, the thickness of gas-filled gaps tends to be increased, causing the higher weight of the structure, which can be partially eliminated by reducing the thickness of glass panes. The influence of IGU thickness on the values of deflections and stresses occurring in the glass panes is analyzed in [17]. The article presents a static calculation of the unit under various thicknesses of gas-filled gap and glass panes for 2-, 3- and 4-glazed IGUs.



Article [18] contains the analysis of load sharing in IGUs by determination of the pressure of a cavity air. Cavity pressure is a complex function of different parameters including panel stiffness, which in its turn depends on edge sealant behavior among other factors. The research on edge seal spacers and their impact on overall performance of IGU is presented in [19]. The article covers an analysis of specific mechanical characteristics, which are not comprehensively stated in existing regulatory documents.

Among different factors which should be taken into account while designing the glazing system, the choice of fixing method of a significant importance [20]. Behavior of bolted and adhesive connections under static loads are investigated in [21]. Common IGUs are characterized by 4-side continuous supports (classical scheme), however novel methods such a point-fixings (structural scheme) and 2-side continuous supports are increasingly used in construction practice [22]. In [22], the specific case of IGUs with 2-side continuous supports subjected to both compression and combined action of compression and bending is investigated by Analytical and Finite Element (FE) numerical studies for the purpose of determining the IGUs' buckling resistance. Embedded laminated connections explored via FE modeling and validated towards past full-scale experimental test results are analyzed in [23].

Current research partially refers to the determination of an optimal option. Some of the optimization problems are defined and analyzed in [24]. The investigation of strategies which lead to the optimization though the use of generic algorithms is presented in [25]. These algorithms are characterized by providing exact satisfying of existing limitations with high stability and convergence rate.

The analysis carried out in this article shows difference between classic and structural ways of fixing under the various conditions. Ultimate Limit State (ULS) and Serviceability Limit State (SLS) define the requirements for considered IGUs. The application of different formulations in ULS in for glass elements and in particular IGUs are studied in [26].

Classical (continuous) fixing of the facade filling the substructure is a system, which includes a decorative cover of any shape, installed in the grooves of the clamping bar, which is mechanically fixed by self-tapping screws to the mullion or transom façade [5].

Structural way is a type of glazing, in which the external filling element forms a single plane of the facade, hiding the fastening elements by means of a facade sealant. For this type of fixing, it is necessary to use special glass units with edge enameling and embedded profiles for hidden fixation from the end surface of the filling [5].

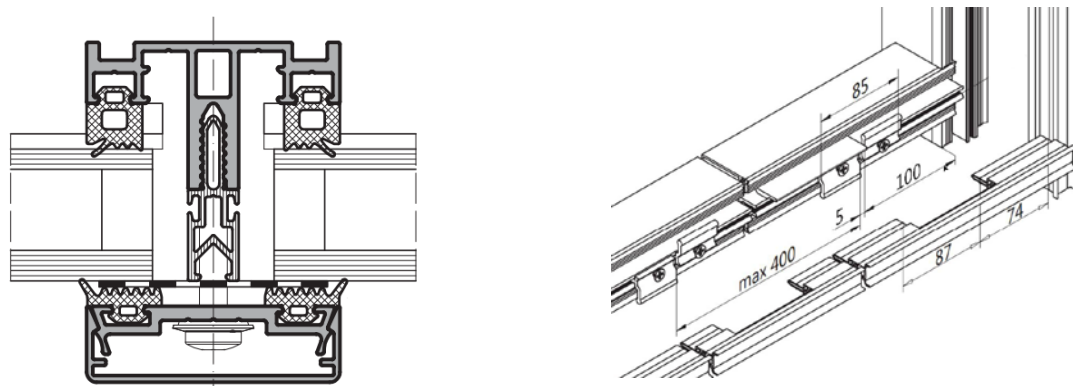


Figure 1. Left – classical scheme, right – structural scheme of IGU's fixing.

Nowadays design of both façade systems is based on the same technical algorithm without taking into account the discreteness of fixing placement. On the other hand, some manufacturers of the structural glass façades assume the distance between supports equal to 400 mm by default (Fig. 1, right). These factors lead to subsequent problems of the entire glazing system.

The object of the study is an insulating glass unit of the most common types: 1200×1200 mm, 2400×1200 mm, 3600×1200 mm, where first dimension is height of the fire barrier and second dimension is the width of the unit. Chosen values are justified on the one hand by the necessity of performing a study on the samples with different ratio of the vertical and horizontal dimensions, and on the other hand the equality of the vertical dimension to the height of interfloor fire belt.

Within this study, the authors intend to verify the correctness of fixing step value stated by manufacturers in case of structural scheme of façade and analyze the possibilities of usage of both structural and classical schemes.

Following tasks were carried out in order to find their influence on the stress-strain state of the glass plates under various boundary conditions:

1. Modification of the fixing step in horizontal direction

2. Modification of the fixing step in vertical direction
3. Change of gas filling thickness
4. Change of glass panel thickness

With the SJ MEPLA software, it is possible to perform a static calculation and determine which fixing scheme will work more efficiently.

2. Methods

Calculation of the stresses arising in the glass plate was based on the finite element method, which is widely used for analysis of glass elements under various conditions [4, 6, 25, 26], is realized within Mepla SJ software (version 4). The mesh of the plate was formed by a free meshing algorithm and controlled via the defined minimum value of an element size. Main concepts about the calculation and mathematic modeling for the complex systems containing polyvinyl chloride based profiles are considered in [29].

The methods described in [30] demonstrate the approach to the determination of a stress-strain state due to nonlinear distribution of a temperature field. Nonlinear problem of unsteady thermal conductivity and a problem of mechanical statics applied to the plane deformation are defined and solved. The general conclusions regarding the theoretical base of the performed calculations were as well adapted in the current research.

2.1. Element building

All considered glass unit were composed of three layers with determined parameters of Young's modulus, thickness and Poisson's ratio: two 6 (8) mm thick decking plates of toughened glass enclosing 20 mm thick gas volume filled with Argon in between them (Fig. 2, left).

The glass elements had following characteristics:

- Density:

$$\rho = 2500 \frac{\text{kg}}{\text{m}^3}$$

- Young's modulus:

$$E = 70000 \text{ MPa}$$

- Poisson's ratio:

$$\nu = 0.2$$

- Thickness of glass panes:

$$t_1 = 6 \text{ mm}; t_2 = 8 \text{ mm}$$

- Argon-filled gap:

$$d = 20 \text{ mm}$$

The metal frame of the considered facade consisted of horizontal and vertical bars (transoms and mullions) with predetermined cross-sections shown in Fig. 2, right. Profiles were chosen due to necessity of accounting the geometrical characteristics of metal frame surrounding glass units for the purpose of investigation of its contribution to overall system performance.

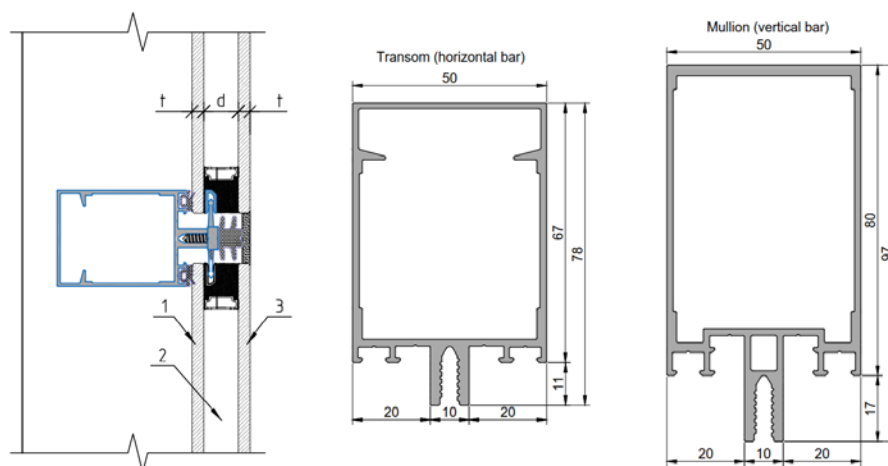


Figure 2. Left – glass unit composition (1, 3 – inner and outer glass panels respectively, 2 – gas-filled gap), right – cross-sections of the horizontal and vertical profiles of the metal frame.

2.2. Supports

Continuous way of fixing was implemented by edge hinged (pinned) supports, acting on the entire plate border and providing adequate stiffness with the defined number of freedom degrees:

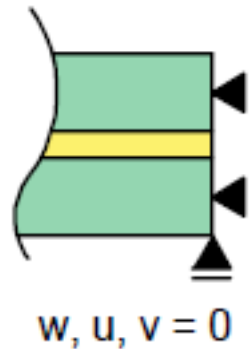


Figure 3. Scheme of the hinged support (SJ Mepla).

Structural variant of fixing was realized by using spring supports: each of them imitated a local embedded part. Each fixing limited linear movement along the z-axis (Fig. 4) and rotation about x- and y-axes. The bottom supports prevented the glass unit from moving in the plane of the facade under the action of gravity load (along the y-axis).

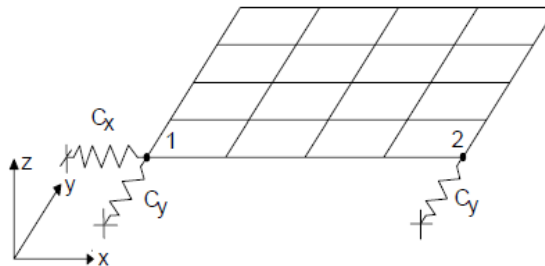


Figure 4. Scheme of the spring support.

The value of rigidity in x-direction refers to the characteristics of aluminum profiles (Fig. 2, right), which bound together create a frame of façade system. The total deflection of insulated glass unit within the system consists of deflections of both glass panes and profile (Fig. 8). Current regulations set the formulas for the maximum allowable deformations of the filling separately from the frame system, therefore two models were developed and analyzed in this study: in the first one spring rigidities c_z were taken as nearly infinite, so only deflection of panes itself was considered. In the second one rigidities c_z were calculated for each case in respect with the profile's structural response to the load distributed on the plate and further transferred to the horizontal and vertical profiles. The scheme of load distribution to the frame for each insulated glass unit is shown in Fig. 5, in accordance with [31]. The model consisted of two components, which allowed obtaining deflections in the location of embedded part and corresponding support reactions when embedded part was imitated. These values enabled the calculation of spring rigidity.

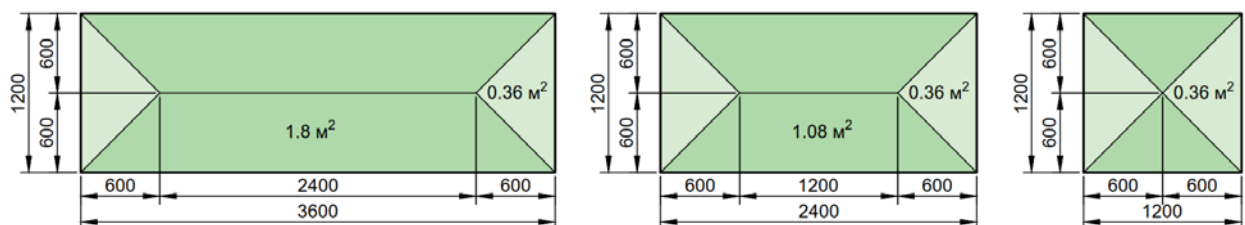


Figure 5. Area of the load transferred to the profiles of the systems for different glass unit sizes.

Two approaches are illustrated by Fig. 6, which contains the schemes of the horizontal profile with fixing step of 340 mm between supports and its rigidity assigned as nearly infinite in the first case and obtained through a static calculation by Finite Element Method (FEM) applied to continuous beam in the second case.

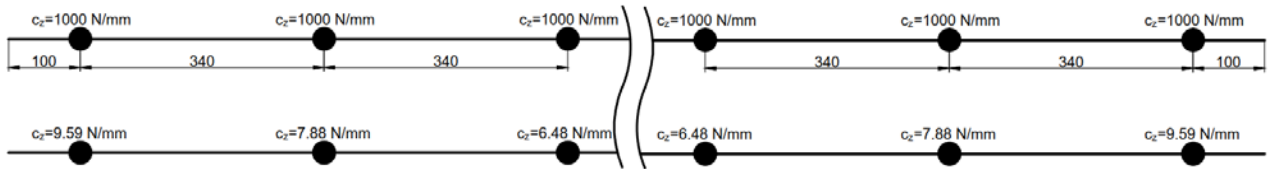


Figure 6. Spring rigidity assigned as nearly infinite and obtained through the calculation incorporating structural behavior of the profile.

2.3. Principal stresses

For each layer of stresses on the top and bottom surfaces σ_{xx} , σ_{yy} , σ_{xy} of each panel were calculated. The principal stresses were obtained through the following formulas:

Major principal stress

$$\sigma = \frac{\sigma_{xx} + \sigma_{yy}}{2} + \sqrt{\left(\frac{\sigma_{xx} - \sigma_{yy}}{2}\right)^2 + \sigma_{xy}^2}$$

Minor principal stress

$$\sigma = \frac{\sigma_{xx} + \sigma_{yy}}{2} - \sqrt{\left(\frac{\sigma_{xx} - \sigma_{yy}}{2}\right)^2 + \sigma_{xy}^2}$$

where σ_{xx} is a component of stress in x-direction; σ_{yy} is a component of stress in y-direction; σ_{xy} is a component of stress in shear stress plane.

The values of maximum principal stresses were used for structural analysis of glass plates.

2.4. Loading approach

Plates were studied under the action of uniformly distributed face load, which simulated an action of a peak wind load. The minimum value of the load applied was 0.45 kN/m^2 , the maximum was 1.45 kN/m^2 .

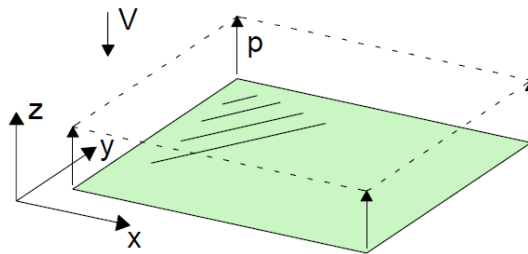


Figure 7. Scheme of load application.

2.5. Screening and selection of values

Obtained values of the principal stresses and deformations were compared for the same layer in case of each glass unit. For structural way of fixing maximum values of the stresses appeared around the springs, while for the classical way they arose in the corners of the plate. Character of horizontal deformation pattern remained same for both design schemes therefore values in the plate's center were taken.

2.6. Ultimate Limit State

Requirements for the maximum values of bearing capacity of the glass unit derived from the Ultimate Limit State specify the limit value equal to 120 MPa in case of toughened glass in accordance with Russian State Standard GOST 30698-2014 "Tempered glass".

2.7. Serviceability Limit State

According to Russian State Standard GOST 30698-2014 "Tempered glass", maximum allowable deformation is determined by the following equation:

$$w_{\text{lim}} = \frac{1}{250} \cdot a$$

where a is the shortest side of the element (1200 mm in the case of considered glass units). Therefore,

$$w_{\text{lim}} = 4.8 \text{ mm}$$

3. Results and Discussion

Results of the static calculation performed on the glass units with two different approaches applied to the rigidity determination showed that for the purpose of estimation of the glass filling deflection the spring rigidity can be assumed as nearly infinite. Difference between deflection values of glass panes within glass units represents profile deformation, while regulations set the maximum allowable values for the deflection of the filling apart from the frame.

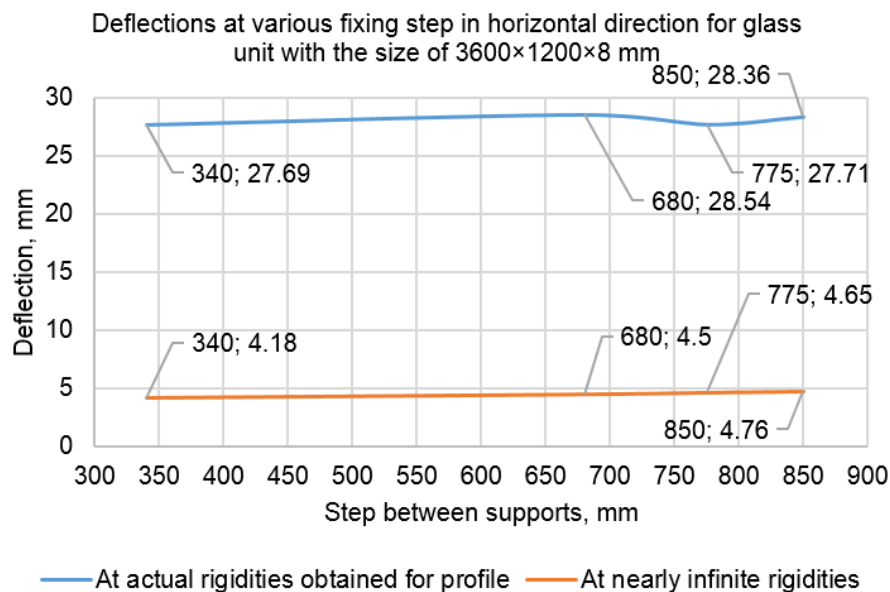


Figure 8. The deflections obtained at various boundary conditions.

The stresses arising in the glass pane of 3600×1200 mm were around 1.5 times higher when actual boundary conditions were accounted. The difference in character of stress distribution is shown in Fig. 9.

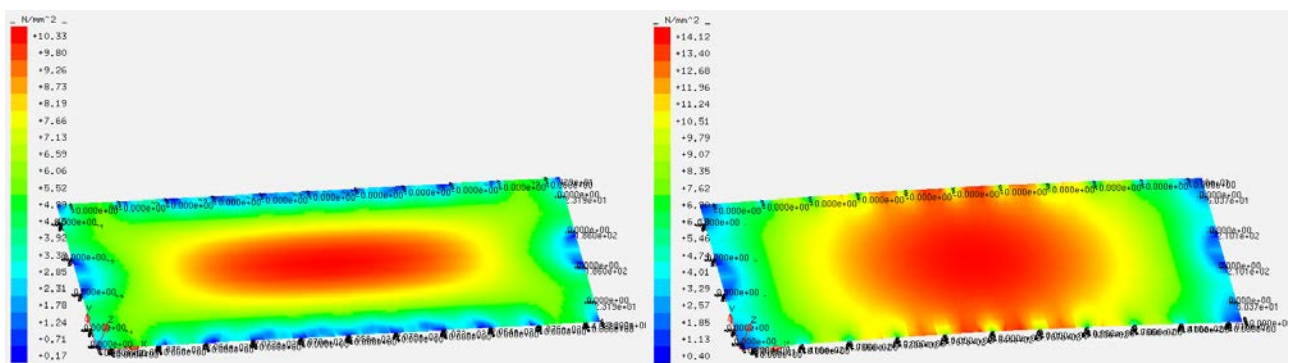


Figure 9. Stress distribution at various boundary conditions.
Left – nearly infinite rigidity, right – actual profile's rigidity.

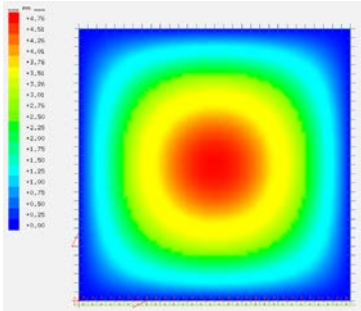
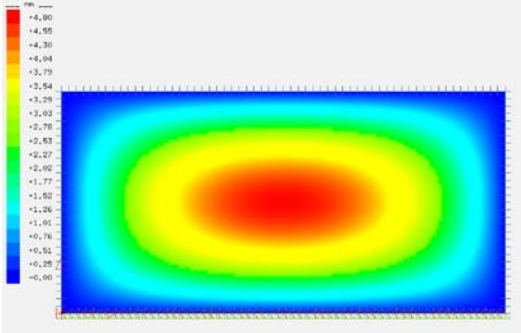
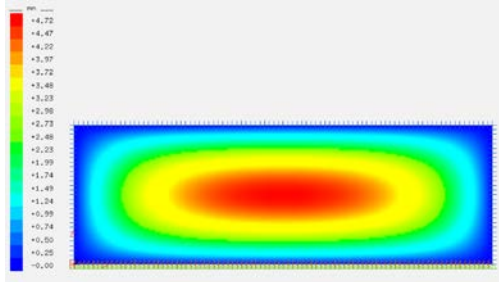
For the smaller glass units stress values as well as the distribution pattern did not differ significantly. For the further analysis of the structural response of the glass pane itself without taking into account profile's behavior spring rigidities in the direction out of the glass plane were assumed nearly infinite.

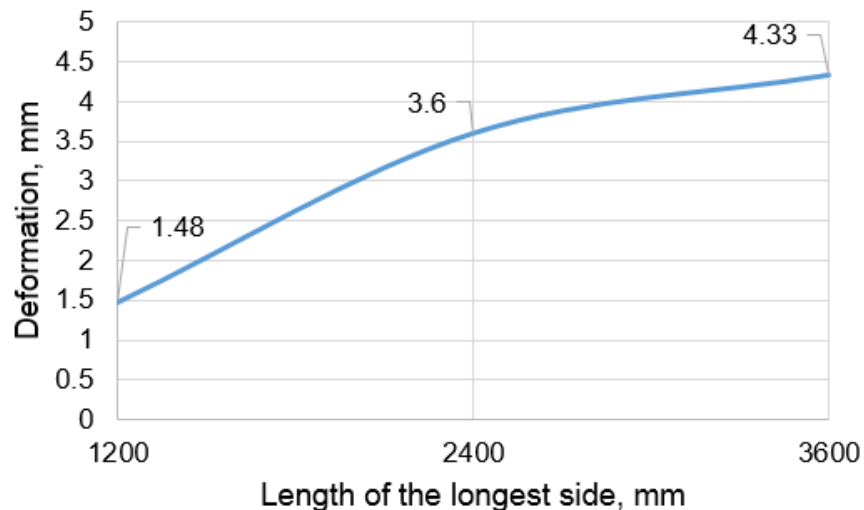
3.1. Classical scheme

Glass units with the dimensions of 1200×1200 mm, 2400×1200 mm, 3600×1200 mm were subjected to uniformly distributed load; glass unit formula:

Toughened glass 6 mm + Argon 20 mm + Toughened glass 6 mm.

Table 1. Values of the maximum load applied before reaching the limit deformation value.

Calculation scheme	Graphic surface	Load, kN/m^2	Max deformation, mm
1200×1200		1.45	4.76
2400×1200		0.6	4.8
3600×1200		0.5	4.72

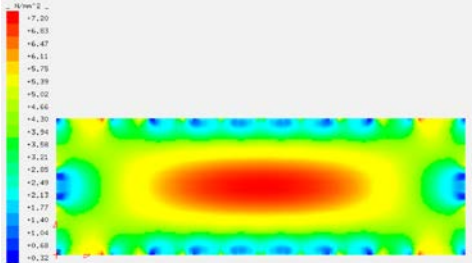
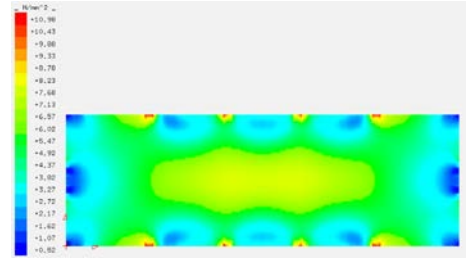
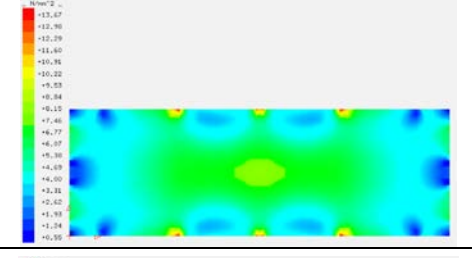
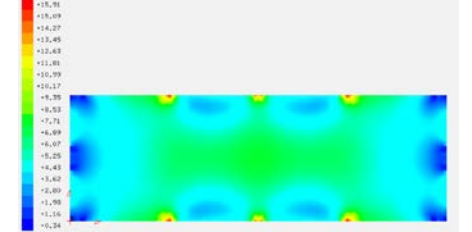
**Figure 10. Deformations obtained under the uniform load $P = 0.45 \text{ kN/m}^2$.**

Glass units of all considered sizes with the formula *Toughened glass 6 mm + Argon 20 mm + Toughened glass 6 mm* fastened in the classical way satisfy conditions of ULS and SLS, therefore it can be concluded that this type of fixing is more rigid in comparison with point fixing. Structural behavior remains constant regardless the ratio between unit's sides: the center of the plate has a maximal deflection. Among three considered schemes the unit with the dimensions of 3600×1200 mm is characterized by maximal stresses and deformations under a similar face load. The size of the panel contributes to the overall unit stiffness as well as the fixing type.

3.2. Structural scheme

Glass unit with the dimensions of 3600×1200 mm was subjected to uniformly distributed load $P = 0.5 \text{ kN/m}^2$; glass unit formula: *Toughened glass 8 mm + Argon 20 mm + Toughened glass 8 mm*.

Table 2. Dependence of the stress distribution on various support steps in horizontal direction.

Support step in horizontal direction, mm	Graphic surface	Max stress, MPa
340		7.2
680		10.98
775		13.67
850		15.91

Deformation values are obtained for different width between supports under the uniform load $P = 0.5 \text{ kN/m}^2$ on the scheme 3600×1200 mm.

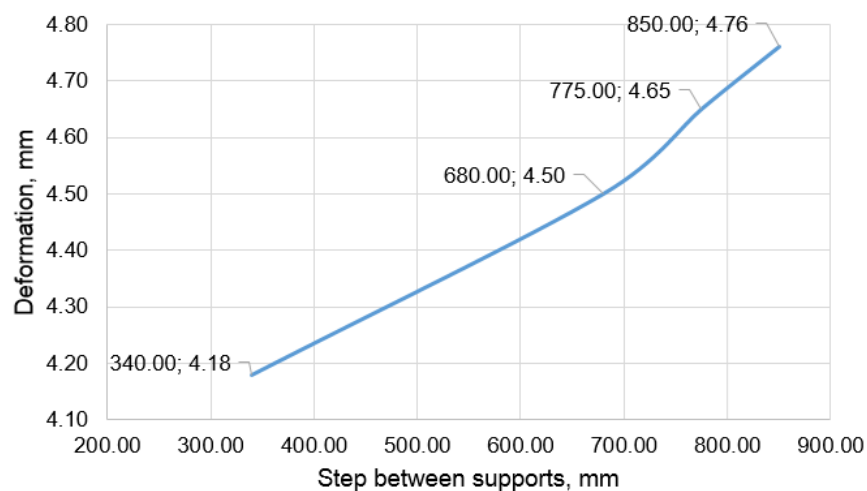


Figure 11. Dependence of the deformation values on various support steps.

As it can be seen from Fig. 12 and Fig. 13, value of the step between horizontal supports in structural scheme has a significant influence on the stress and deformation values, but not on their distribution character. Maximum value of deformation grows exponentially with the increase of the step in horizontal direction.

For a glass unit of the size 3600×1200 mm with the support step of 340 mm maximum value of deformation exceeds the limit value determined by SLS, therefore it can be concluded that step of 400 mm which is often adopted by manufactures without further checking has to be calculated in terms of deformation in order to satisfy the conditions of SLS.

Glass unit with the dimensions of 2400×1200 mm was subjected to uniformly distributed load $P = 0.3 \text{ kN/m}^2$; glass unit formula: *Toughened glass 6 mm + Argon 20 mm + Toughened glass 6 mm*.

Table 3. Dependence of the deformation values on various support steps vertical direction.

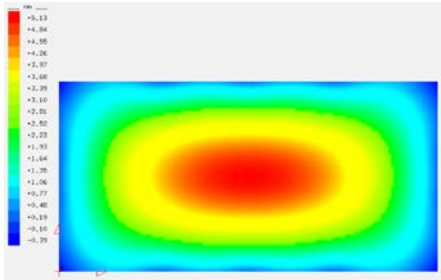
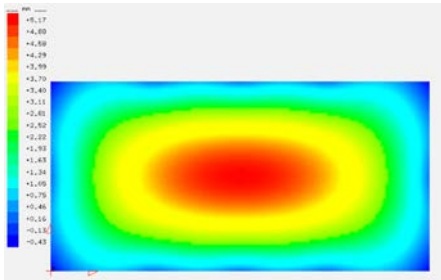
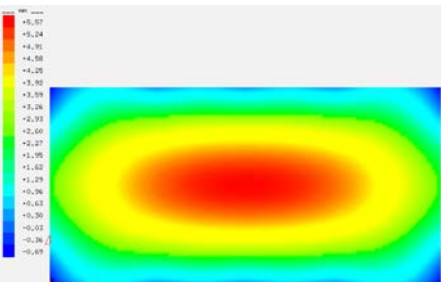
Support step in vertical direction, mm	Graphic surface	Max deformation, mm
293		5.13
440		5.17
880		5.57

Fig. 14 shows that increase of number of the supports placed on the short side (in vertical direction) do not essentially influence the maximum values of the deformations; however, increase of number of the supports placed on the long side and increase of glass thickness provide pursuance of the conditions stated by SLS.

Thickness of glass panel has a significant influence on the deformation values. Glass unit of the size of 3600×1200 mm requires increase of the thickness from 6 mm to 8 mm for all the variations of structural way of fixing, and glass unit of the size of 2400×1200 mm requires increase of the thickness from 6 mm to 8 mm for some variations of structural way.

Calculations carried out for different values of the gas filling shows that its modification does not significantly impact the values of stresses and deformation, therefore its influence on the maximum stresses and deformations can be neglected.

Recommended values of the maximum distance between supports and glass unit composition in order to fulfil the conditions of SLS are presented in Fig. 15.

Figure 15. Dependence of distances between supports on the value of face load and unit composition.

Glass unit size; panel thickness, mm	Maximum value of support step, mm		
	Face load, kN/m ²		
	0.4	0.5	0.6
1200×1200; 6	880	440	290
2400×1200; 8	950	770	475
3600×1200; 8	850	680	340

Existing researches, which were found and analyzed by authors within this study, did not have comprehensive information regarding stress-strain state of considered element under consimilar parameters and therefore final results could not be compared, however the methods and main principles of calculation in accordance with Limit State design remain analogous.

4. Conclusions

Within this study, three types of IGUs representing different ratios of width height were modelled in order to verify correctness of a default fixing step value given by manufacturers of structural glazing and find out the dependence of the main changeable parameters of IGU on its overall performance.

The model incorporating profile's contribution to the total deflections and stresses of system through rigidity characteristics was developed, and its influence on glass unit's performance under the action of uniformly distributed load was described. Evaluation of pane's stress-strain state was performed separately from the frame in accordance with current regulations.

On the basis of obtained results, it is possible to make the following conclusions:

1. Modification of the fixing step in horizontal direction (along larger side) and glass panel thickness have a significant influence on the stress and deformation values;
2. In contradistinction, modification in vertical direction (along shorter side) and gas filling thickness do not noticeably impact stress-strain state of a plate;
3. Default fixing step between two adjacent supports, which is often adopted by manufactures of IGUs without preliminary calculation for actual applied load, has to be verified in each case in terms of deformation in order to satisfy the conditions of SLS.

Recommended maximum values of support steps and glass unit composition are proposed in accordance with the value of the face load acting on the plate surface and parameters of IGUs.

References

1. Hachem-Vermette, C. Multistory building envelope: Creative design and enhanced performance. *Solar Energy*. 2018. No. 159. Pp. 710–721. DOI: 10.1016/j.solener.2017.11.012
2. Kozlovskaya, M., Mackova, D., Spisakova, M. Knowledge database of modern methods of construction. *Proceedings of the 2nd International Conference on Engineering Sciences and Technologies, ESaT. Tatranské Matliare, 2017*. Pp. 489–494.
3. Leśniak, A., Górka, M. Analysis of the cost structure of aluminum and glass facades. *Proceedings of the 3rd International Conference on Engineering Sciences and Technologies. Tatranské Matliare, 2019*. Pp. 445–450.
4. Bernard, F., Daudeville, L. Point fixings in annealed and tempered glass structures: Modeling and optimization of bolted connections. *Engineering Structures*. 2009. 31(4). Pp. 946–955. DOI: 10.1016/j.engstruct.2008.12.004
5. Galyamichev, A.V. Comparative analysis of the classical and structural ways of fastening the glazing to the aluminium facade substructure. *Svetoprozrachnye konstrukcii*. 2017. No. 3. Pp. 44–51. URL: https://www.researchgate.net/publication/323199607_Comparative_analysis_of_the_classical_and_structural_ways_of_fastening_the_glazing_to_the_aluminium_facade_substructure (rus)
6. Stratiij, P.V., Luchkin, E.A. Snizhenie iskazhayushchej krivizny steklopaketov za schet chastichnogo razrezheniya vnutrennego vozduha [Reduction of a distorting curvature of double-glazed windows due to partial rarefaction of internal air]. *Promyshlennoe i grazhdanskoe stroitel'stvo*. 2016. No. 4. Pp. 54–58. (rus)
7. Bedon, C., Zhang, X., Santos, F., Honfi, D., Kozłowski, M., Arrigoni, M., Figuli, L., Lange, D. Performance of structural glass facades under extreme loads – Design methods, existing research, current issues and trends. *Construction and Building Materials*. 2018. No. 163. Pp. 921–937. DOI: 10.1016/j.conbuildmat.2017.12.153
8. Luible, A., Haldimann, M., Overend, M. *Structural use of Glass*. International Association for Bridge and Structural Engineering. Zürich, 2008. 215 p.
9. Wüest, T., Luible, A. Increased thermal induced climatic load in insulated glass units. *Journal of Facade Design and Engineering*. 2017. 4(3–4). Pp. 91–113. DOI: 10.3233/FDE-161146
10. Tofilo, P., Delichatsios, M. Thermally induced stresses in glazing systems. *Journal of Fire Protection Engineering*. 2010. 20(2). Pp. 101–116. DOI: 10.1177/1042391509344243
11. Bedon, C., Kozłowski, M., Honfi, D. Thermal assessment of glass façade panels under radiant heating: Experimental and preliminary numerical studies. *Journal of Facade Design and Engineering*. 2018. 6(3). Pp. 49–64. DOI: 10.7480/jfde.2018.3.2477

12. Plotnikov, A.A. Partial Rarefaction as Way to Reduce Distortion Curve of double-glazed unit. Proceedings of IOP Conference Series: Earth and Environmental Science. Khabarovsk, 2017. 90(1). DOI: 10.1088/1755-1315/90/1/012127
13. Stratij, P.V. Metodika rascheta progibov stekol v sostave steklopaketa pod klimaticheskoy nagruzkoy [Calculation methods for glass plates deflections in a double-glazed unit under climatic load]. Moscow State University of Civil Engineering, 2013. PhD dissertation. 168 p. (rus)
14. Plotnikov, A.A., Stratij, P.V. Chislenno-analiticheskaya metodika rascheta progibov stekol germetichnogo steklopaketa ot klimaticheskoy (vnutrennej) nagruзки [Numerical and analytical method for calculating the deflections of glass plates in a double-glazed unit under climatic (internal) load]. Vestnik MGSU. 2014. 12(9). Pp. 70–76. DOI: 10.22227/1997-0935.2014.12.70-76. (rus)
15. Gorshkov, A.S., Vatin, N.I., Rymkevich, P.P., Kydrevich, O.O. Payback period of investments in energy saving. Magazine of Civil Engineering. 2018. 78(2). Pp. 65–75. DOI: 10.18720/MCE.78.5
16. Gorshkov, A., Vatin, N., Nemova, D., Shabaldin, A., Melnikova, L., Kirill, P. Using life-cycle analysis to assess energy savings delivered by building insulation. Procedia Engineering. 2015. 117(1). Pp. 1080–1089.
17. Respondek, Z. Influence of insulated glass units thickness and weight reduction on their functional properties. Open Engineering. 2018. 8(1). Pp. 455–462. DOI: 10.1515/eng-2018-0056
18. Huveners, E.M.P., Herwijnen van, F., Soetens, F. Load sharing in insulated double glass units : determination of the air pressure in the cavity due to mechanical and thermo-mechanical loads. Heron. 2003. 48(2). Pp. 99–122.
19. Hagl, A. Experimental and numerical analysis of edge seal spacers of insulated glass units for structural sealant glazing applications. Proceedings of Challenging Glass 3: Conference on Architectural and Structural Applications of Glass. Delft, 2012. Pp. 221–234.
20. Cwyl, M., Michalczyk, R., Grzegorzewska, N., Garbacz, A. Predicting performance of aluminum - Glass composite facade systems based on mechanical properties of the connection. Periodica Polytechnica Civil Engineering. 2018. 62(1). Pp. 259–266. DOI: 10.3311/PPci.9988
21. Katsivalis, I., Thomsen, O.T., Feih, S., Achintha, M. Strength evaluation and failure prediction of bolted and adhesive glass/steel joints. Glass Structures and Engineering. 2018. 3(2). Pp. 183–196. DOI: 10.1007/s40940-018-0070-0
22. Bedon, C., Amadio, C. Buckling analysis and design proposal for 2-side supported double Insulated Glass Units (IGUs) in compression. Engineering Structures. 2018. No. 168. Pp. 23–34. DOI: 10.1016/j.engstruct.2018.04.055.
23. Bedon, C., Santarsiero, M. Laminated glass beams with thick embedded connections – Numerical analysis of full-scale specimens during cracking regime. Composite Structures. 2018. No. 195. Pp. 308–324. DOI: 10.1016/j.compstruct.2018.04.083
24. Alekseytsev, A.V., Al Ali, M. Optimization of hybrid I-beams using modified particle swarm method. Magazine of Civil Engineering. 2018. 7(83). Pp. 175–185. DOI: 10.18720/MCE.83.16
25. Serpik, I.N., Alekseytsev, A.V., Balabin, P.Y. Mixed Approaches to Handle Limitations and Execute Mutation in the Genetic Algorithm for Truss Size, Shape and Topology Optimization. Periodica Polytechnica Civil Engineering. 2017. 3(61). Pp. 471–482. DOI: 10.3311/PPci.8125
26. Bedon, C., Amadio, C. A linear formulation for the ULS design of glass elements under combined loads: application to IGUs. Glass Structures & Engineering. 2018. 3(2). Pp. 289–301. DOI: 10.1007/s40940-018-0060-2
27. Pourmoghaddam, N., Schneider, J. Finite-element analysis of the residual stresses in tempered glass plates with holes or cut-outs. Glass Structures & Engineering. 2018. 3(1). Pp. 17–37. DOI: 10.1007/s40940-018-0055-z
28. Pourmoghaddam, N., Nielsen, J., Schneider, J. Numerical simulation of residual stresses at holes near edges and corners in tempered glass: A parametric study. Proceedings of Engineered Transparency Conference. Düsseldorf, 2016. Pp. 513–525.
29. Sesysus, S.G., Eldashov, Y.A. Primenenie metodov matematicheskogo modelirovaniya dlya kompleksnogo resheniya zadach strukturnogo analiza konstrukcij iz PVH pri dejstvii na nih ekspluatacionnyh nagruzk [The use of mathematical modeling methods for the complex solution of the problems of structural analysis of PVC structures under the action of operational loads]. Svetoprozrachnye konstrukcii. 2006. No. 5. Pp. 20–25. (rus)
30. Sesysus, S.G., Eldashov, Y.A. Modelirovanie sopryazhennoj zadachi termouprugosti na primere variantov konstruktivnogo oformleniya okonnogo bloka zdaniy [Modeling the coupled problem of thermoelasticity on the example of the design options for the window unit]. Svetoprozrachnye konstrukcii. 2005. No. 4. Pp. 35–38. (rus)
31. Galyamichev, A.V., Nefedova, A.V., Fidrikova, A.S., Bykova, YU.V. Analiz dejstviya vetrovoj nagruзки na alyuminievye svetoprozrachnye vitrazhnye konstrukcii na primere zdaniya «Gidrokopus-2» SPbPU Petra Velikogo [Analysis of the effect of wind load on aluminum transparent facade structures (on the example of the building "Gidrokopus-2" of Peter the Great St. Petersburg Polytechnic University)]. Svetoprozrachnye konstrukcii. 2017. No. 2. Pp. 24–29. (rus)

Contacts:

Ekaterina Gerasimova, katyageras17@gmail.com

Alexander Galyamichev, gav@spbstu.ru

Selcuk Dogru, seltrue@hotmail.com

© Gerasimova, E., Galyamichev, A., Dogru, S., 2020



DOI: 10.18720/MCE.98.9

Behavior of heat treated self-compacting mortar cured in seawater

R. Derabla^{a, b}, F. Sajedi^c

^a Department of Civil Engineering, University of 20 august 1955, Skikda, Algeria

^b Laboratory of Civil Engineering and Hydraulic (LGCH), University of 8 May 1945, Guelma, Algeria

^c Department of Civil Engineering, Ahvaz Branch, Islamic Azad University, Ahvaz, Iran

* E-mail: rderabla@gmail.com

Keywords: GGBFS, limestone, mortar, heat treatment, mechanical properties, seawater

Abstract. The acceleration of the hardening of self-compacting concrete (SCC) using the process of heat treatment is widely used in the field of prefabrication. Because mortar serves as the basis for the workability properties of SCC, these properties could be assessed by self-compacting mortars (SCMs). This paper has the purpose to study the behavior of heat-treated SCM based on two different mineral additions in marine environment. The additions are used as micronized powder to substitute 20 % and 40 % of cement. They are as ground granulated blast furnace slag (GGBFS) and limestone filler (LF). The cycle regime of heat treatment process used achieves a temperature of 60 °C and total duration of 24 hours. The research was conducted through the study of the physical and mechanical properties of elaborated SCMs under two curing regimes as freshwater and seawater. The obtained results indicate that the incorporation of LF seemed more effective in standard treatment process but it is advisable to limit its use to levels of less than or equal to 20 % as it develops resistance levels lower than those obtained by GGBFS. The incorporation of GGBFS especially with high amount of 40 % is very beneficial to improve physical-mechanical properties of heat-treated SCMs and it has many advantageous for obtaining stable and resistant SCMs against aggressive environment.

1. Introduction

According to the experimental researches, concrete subjected to high temperatures at early ages attains higher early-age mechanical strengths but has lower later-age mechanical strengths than concrete subjected to normal temperatures. This is because the higher curing temperatures which affect the physical characteristics of the cementitious system by altering the dormant period of hydration process. Many laboratory studies carried out on pastes, mortars or concretes under controlled conditions have shown that expansion does not occur if the material has not been subjected to a temperature above 70 °C [1, 2].

The use of some mineral admixtures in concretes has several interests. It can diminish the final cost of the production by reducing the cement content which is the most expensive component in the concrete, it can reduce the emission of CO₂ generated in the production of ordinary Portland cement and it is inevitable to improve concrete fresh and hardened properties and to enhance concrete durability [3].

The quality of the normal concrete (NC) and self-compacting concrete (SCC) elaborated with mineral admixtures e.g. silica fume (SF), fly ash (FA), pozzolans (PZ), limestone fillers (LF) and ground granulated blast furnace slag (GGBFS), is higher than that of the concrete made with pure cement [4–6]. When the hardening of the concrete is accelerated by heat treatment (HT), the researches [7–9] have proven the effectiveness of these additives. Under the heat curing, the high temperature will strongly enhance the reactivity of FA and GGBFS in NC and SCC and therefore the hydration action of mineral additions [10].

On the other hand, it is suitable that the building materials are as durable as resistant and economic to allow their use in aggressive environments such as marine environment. In seawater, there are large amount of chloride and sulfates where the reinforced concrete structures are often found to be deteriorated by corrosion. The chloride causes the Friedels Salt and the sulfate reacts with calcium hydroxide and calcium aluminate hydrate to form gypsum and secondary ettringite that are more voluminous than the initial reactants [11]. It can affect the long-term durability of concrete structures, and leads to expansion, cracking, and deterioration of concrete specimens.



Among of the mineral admixtures, the GGBFS has been widely used as successful replacement material with OPC in making durable concrete for improving some properties of concrete in marine environments and for achieving environmental and economic benefits since the beginning of 20th century [12]. GGBFS can effectively fill the pores of concrete which are very much helpful for reducing the permeability and then restricts the penetration of seawater inside the concrete. It has been observed that GGBFS can be effectively used to reduce the pore sizes and cumulative pore volume considerably leading to more durable and impermeable concrete and therefore increases the durability of concrete in seawater environments [13]. Although, the strength development of concrete made with GGBFS is remarkably reduced at early ages due to its low initial rate of hydration especially if it will be activated thermally as the case of precast [14]. Although low heat of hydration of slag, the structural benefit is that the decrease of the thermal cracking of mass concrete is significant and it is seen to be lower than ordinary Portland cement [15]. Concerning the LF, its use to replace cement has a positive effect on the development of mortar strength [16]. It confers flow-ability, viscosity and stability; however, it does not present pozzolanic or hydraulic properties [17]. According to [18–20], LF accelerates the hydration of C_3S and thereby increases the early compressive strength of the mortar. Medjigbodo et al. [21] explain this early acceleration by the chemical reaction between the calcium carbonate of LF and the aluminate supplied by cement.

Since the mortar serves as the basis for the workability properties of SCC, these properties could be assessed by SCM. The SCMs are especially preferred for the rehabilitation and repair of reinforced concrete structures. Several works have been studied the behavior of SCMs under different conditions. The authors [22] have determined that the production of SCM with good rheological and strength properties could be successfully assessed using LF. The researchers [23, 24] have concluded that FA and LF powder increased significantly the workability and had an improved overall response on SCMs.

The characteristics of heat-treated SCC could also be assessed by the characteristics of heat-treated SCM. Safi et al. [25] showed that heat-cured SCMs (temperature of 60 °C) containing calcined silt of dams and ground brick waste (BW) have permitted to obtain a strength gains compared to reference SCM. Other authors have studied the heat curing of normal mortars. Famy et al. [26] showed that the heat curing at 90 °C lead to dimensional changes of mortars due to the formation of the expansive ettringite. Sajedi and Hashim [27] are found that 50 % level of slag with heat curing of 60 °C in duration of 20 hours is the optimum regime for compressive strength of cement-slag mortars studied. It has been proved as reported in our previous paper [28] that it is possible to produce a heat-treated-concrete (at 60 °C for duration of 9 hours) resistant to chlorides and sulphates existing in the marine environment by either combining 20 % of slag, with the use of water reducing plasticizer admixture and W/C rate limited to 0.35 or by the use of 40 % of slag, without admixture and a W/C slightly higher and equal to 0.5. Erdogdu [29] has been found that the type of cement and the preheating duration have an important influence on the flexural strength of heat-treated mortar. Thus, the fineness of the cementitious materials is a very interesting parameter to obtain high level of resistance of the elaborated materials, whether in standard treatment conditions or in thermal treatment conditions [30].

The durability of mortars in seawater environment has been also studied. Moinul et al. [31] have been revealed that GGBFS cement-mortar having mix ratio 70:30 with water binder ratios of 0.46 has better resistance against strength deterioration at different ages and all curing conditions. So, it was concluded by Boufenara et al. [32] that the cements with high content of GGBFS offer good chemical resistance against the aggression of sodium sulfate solution and seawater.

Following this short introduction and on the basis of our bibliographic research, few works that have been interested of the durability of elaborated concrete or mortar in seawater environments; but there is almost no work which studied the behavior of heat-treated concrete or mortar based on mineral admixtures in aggressive environments.

This paper investigates the effect of local mineral additions as GGBFS and LF on the physical and mechanical properties of SCMs in seawater environment. For this, the SCMs have been prepared with water to binder ratio of 0.42 for all binder mixtures which are based on various levels of mineral additions as 20 % and 40 %. The physical and mechanical tests were conducted on prismatic samples (4×4×16in) of SCMs subject to HT process at 60 °C and kept after demoulding in seawater medium (SW). The results of these tests were compared with those obtained with standard treatment process (ST) at 20 °C and kept in freshwater medium (FW).

2. Materials and Methods

2.1. Materials

The cement used is a Portland cement compound, CPJ CEM II 42.5, the limestone filler (LF) is a calcium carbonate powder ($CaCO_3 = 98\%$) and the GGBFS is obtained after grinding of blast furnaces slag to obtain a fine powder similar to that of common cements.

The chemical composition of the various cementitious materials is given in Table 1. The chemical composition of LF indicate that is inert product and that of GGBFS is near to that of the cement which indicate that is reactive product and its activity index ($A_{GGBFS} = 0.96$) indicates that it is basic [33].

The physical characteristics of the admixtures: absolute density, specific surface of Blaine (SSB) (EN 196-6), and specific surface by laser diffraction (SSDL) (NF X11-666), are shown in Table 2 and their particle size distribution is illustrated in Fig. 1.

The superplasticizer (SP) used is MEDAPLAST SP 40 which is a high water reducer for ready-mix concrete according to EN 934-2.

Two types of sand were used: Siliceous sand 0/1 (noted S1) and Crushed limestone sand 0/4 (noted S2) of fineness modulus of 1.66 and 3.51, apparent densities of 1.46 and 1.49 and absolute densities of 2.50 and 2.56 respectively. The chemical analyses of sands are given in Table 1.

2.2. Methods

2.2.1. Experimental program

The heat treatment cycle used in this study (Fig. 2) take into account the specifications of the norm NF EN13369 [34]. The characteristics of the adopted cycle of heat-treatment are near to the cycles used in precast concrete industry. Also, The T^{re} of treatment of 60 °C was adopted to avoid the formation of delayed ettringite (DEF) which can be effected by the instability of ettringite crystals when they are exposed to temperatures above 65 °C, phenomenon which causes internal damage and expansive behavior in concrete samples [35]. The cycle starts after 3 hours of the mixing and takes a total duration of 24 hours. It includes 3 hours of pretreatment (pre-setting at 20°C), a phase of temperature rise of 2.5 hours before stabilizing at 60 °C for a period of 16 hours (isothermal stage) and finally a natural cooling phase of 2.5 hours. The demoulding of the SCM specimens was carried out just at the end of the cooling phase. The specimens were placed in two different curing regimes, i.e. the freshwater (FW) and the seawater (SW).

The characteristics of the heat-treated SCMs are compared to the characteristics of that of the control SCMs (without addition and/or standard treatment at 20 °C).

The effect of the amount of GGBFS and LF as 20 % and 40 % to substitute the cement is well studied by its effect on the characteristics of the elaborated SCMs in both fresh and hardened states. The amounts of GGBFS and LF of 20 and 40 selected in this work are within the actual rates usually adopted in the manufacture of Algerian composite cements: such as CPJ-CEM II/A (6–20 % of mineral additives) and CPJ-CEM II/B (21–35 % of mineral additives).

The tests realized are the bulk density (ρ_{bulk}), the slump flow (S_f) and the occluded air (O_a) at the fresh state. In hardened state they are as:

- The porosity (P) at the age of 28 days calculated as the ratio of the difference of the masses of specimen (saturated and dried) to the total volume of the specimen according to standard NBN B 15-215 [36].
- The shrinkage and the swelling at the age of 28 days calculated as described in the standard NF P15-433 [37].
- The compressive strength at the age of 1, 7, 28 and 180 days according to the standard NF EN 196-1 [38].

2.2.2. Mortar mixes-design

The composition of the SCMs given in Table 2 is that of the mortar which composes the SCC that formulated based on the recommendations of the AFGC [39]. The mixing and the preparation of SCMs specimens were carried out according to EN 196-1.

- Ratio Water to Binder W/B as 0.42 for all SCMs,
- Type of treatment: standard treatment (ST) (or untreated) and heat treatment (HT),
- Level of substitution of cement by the GGBFS and LF are as 20% and 40 %,
- Curing regimes are as freshwater (FW) and seawater (SW). The mineral composition of seawater is given in Table 3.

For the elaborated SCMs which W/B = 0.42, the parameters are as:

- Volume of the paste: Cement (C) + Water (W) + Admixture (A) + Occluded air = 397 liters,
- Volume of the sand equal to 42 % compared to the volume of the mortar,
- Ratio S1/S2 = 1 by volume and S1/S2= 0.97 by mass,
- Dosage of SP adopted which corresponds to the saturation dosage (SP_{sat}),
- Ambient air curing regime for the shrinkage test.

Table 1. Chemical composition of raw materials.

Oxides (%)	CaO	SiO ₂	Al ₂ O ₃	Fe ₂ O ₃	MgO	K ₂ O	Na ₂ O	SO ₃	Loss on ignition
C	59–62	22–24	5.3–6.0	3.0–4.0	1.5–1.8	< 0.9	< 0.7	1.8–2.2	na
GGBFS	42.77	41.23	7.89	1.38	4.60	0.94	0.00	0.34	na
LF	56.18	0.43	0.08	0.09	0.26	0.01	0.07	0.03	42.85
S1	0.62	95.21	1.12	0.55	0.04	0.46	0.10	00	na
S2	56.73	3.71	0.23	0.20	1.18	0.02	0.07	0.09	37.77

Table 2. Composition of elaborated SCMs.

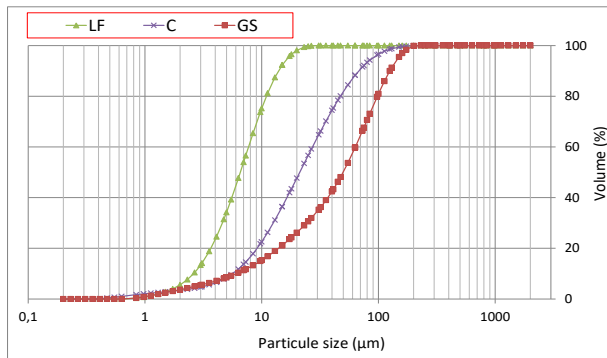
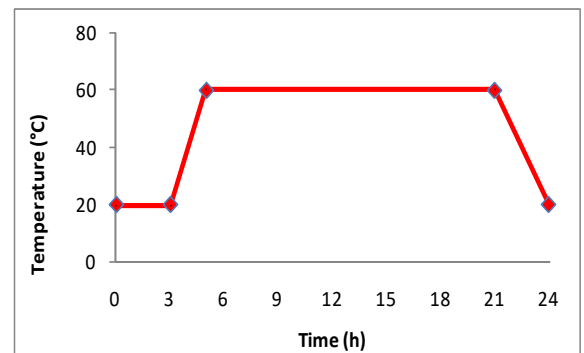
Mix type	C (kg)	A (kg)	W (kg)	S1 (kg)	S2 (kg)	W/C (%)	W/B (%)	SPsat (%)
SCM-R	530	0	220	360	369	0.42	0.42	1.85
SCM20GGBFS	440	88	220	360	369	0.50	0.42	1.60
SCM40GGBFS	377	151	220	360	369	0.58	0.42	1.70
SCM20LF	430	86	215	360	369	0.50	0.42	1.70
SCM40LF	362	145	211	360	369	0.58	0.42	2.00

SCM-R: Reference SCM
SCM20GGBFS: SCM having 20% of GGBFS
SCM40GGBFS: SCM having 40% of GGBFS
SCM20LF: SCM having 20% of LF
SCM40LF: SCM having 40% of LF

Table 3. Mineral composition of seawater [40].

T(°C)	S(‰)	pH	O ₂ (%)	O ₂ (mg/l)	rH (mV)	Condi (μS/cm)
20.2	37.1	7.7	66.1	6.1	- 38.6	55846

T: Temperature (°C) S: Salinity (‰)
pH: hydrogen potential (°), O₂: oxygen saturation rate (%),
O₂: dissolved oxygen (mg / l), rH: reducing power (mV)
Condi: conductivity (μS / cm)

**Figure 1. Particle Size Distribution of cement, GGBFS and LF.****Figure 2. Heat treatment cycle.**

3. Results and Discussion

The results of the tests carried out for the characterization of the SCMs in the fresh state are given in Table 4 and that of the hardened state are shown in Fig. 3 to 17.

It can be said that, in the fresh state, the incorporation of the GGBFS and LF causes a decrease of the measured values of the physical properties of SCMs. The increase in the content of the GGBFS is associated to a decrease of slump flow and an increase of occluded air. The opposite is observed in the case of LF for both characteristics.

The LF confers flow-ability due to the considerable fineness compared to that of cement which allows a good filling of the voids and a better understanding of the paste particles. Thus it does not present pozzolanic or hydraulic properties which allows to water to be free and this helps to minimize occluded air bubbles. The

GGBFS is characterized by its reactivity and its considerable absorption of water which needs a larger amount of water than is required by the cement. These characteristics of GGBFS lead to decrease the amount of Occluded air and to reduce the fluidity of the SCM paste and consequently its flow.

Table 4. Characteristics of SCMs in fresh state.

Mix type	SCM-R	SCM20GGBFS	SCM40GGBFS	SCM20LF	SCM40LF
ρ_{bulk} (kg/m ³)	2100	2103	2080	2217	2105
Oa (%)	6.0	4.0	5.9	4.4	3.7
S _f (cm)	32.5	29.0	27.5	31.5	32.5

3.1. Porosity

The porosities at the age of 28 days of the studied SCMs are presented in Fig. 3. Overall, the least porous SCMs are:

- In terms of nature and dosage of admixture, SCMs based on 20 % of GGBFS in FW medium and SCMs based on 20 % LF in SW medium,
- In terms of treatment process, heat treated SCMs based on GGBFS and untreated SCMs based on LF.

These results confirm the advantage of the incorporation of the mineral admixtures to reduce the porosity of SCMs. Also, the dosage of 20 % showed better yield than that of 40 % for both mineral admixtures used. The SCM20GGBFS which has a limited amount of air occluded (by 4 %) is also less porous than the reference mortar SCM-R. This is almost which has been reached by [41] where they found that at the age of 1 year, slag concrete with slag substitution ratio 20% has the least pore size. This benefit has been obtained by Pal et al. [42] who observed that slag can be effectively used to reduce the pore sizes and cumulative pore volume considerably leading to more durable and impermeable concrete. The slag is reactive and has a latent hydraulic power, which need to an activator as temperature to can be reactivated and then to have the ability to properly fill the space and existing voids. In seawater, the presence of slag gives birth to some expansive hydrates (aragonite, calcite and gypsum) which decrease size of the pores and the capillary absorption coefficient. The SCM20LF is very beneficial in standard treatment and seawater curing regime. The limestone filler is inert and finer than the cement, which allows a good filling of the voids and a better understanding of the paste particles. The amount of 40 % of LF is useless and it is even harmful, for that we must limit the incorporation of this admixture to levels a little lower.

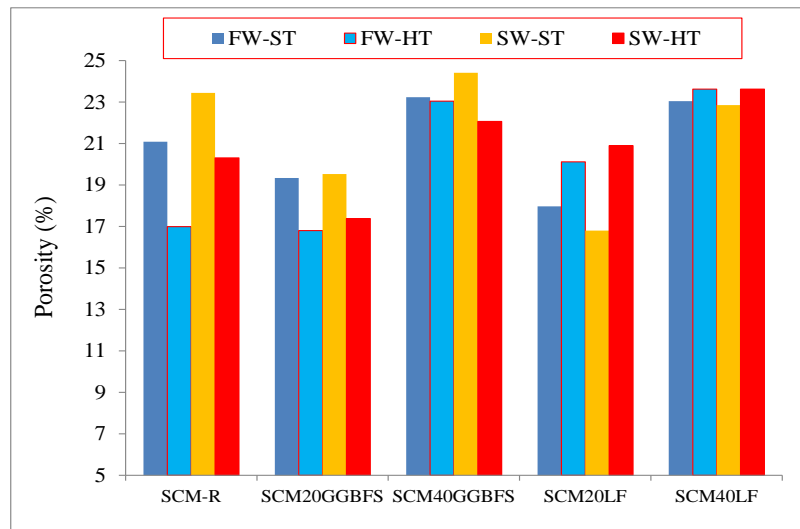


Figure 3. Porosity of SCMs.

3.2. Shrinkage and swelling

Regarding the test results of shrinkage (Fig. 4) and swelling (Fig. 5), the following comments can be given:

The HT process caused an increase in the shrinkage of elaborated Slag-SCM specimens and a decrease in that of LF-SCMs. The level of substitution of cement by 40 % of the additions is more advantageous, in both treatment cases. The SCM40LF is the less shrinking one among the others SCMs.

For the swelling test with both treatment process and compared to all studied SCMs, the SCM20GGBFS and SCM40GGBFS are that which give the lower swelling in FW and SW mediums respectively. With 40 % of LF, heat-treated SCMs are very advantageous than of 20 % in both curing regimes. These results prove that

using GGBFS or LF could help to obtain stable heat-treated mortars against swelling in aggressive medium as marine environment especially with high replacement level ($\geq 40\%$).

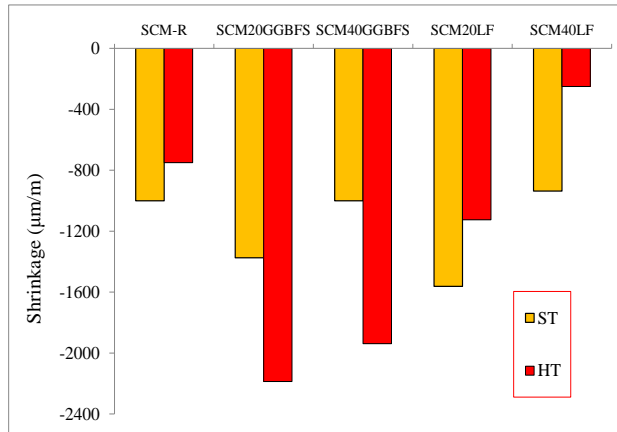


Figure 4. Shrinkage of SCMs.

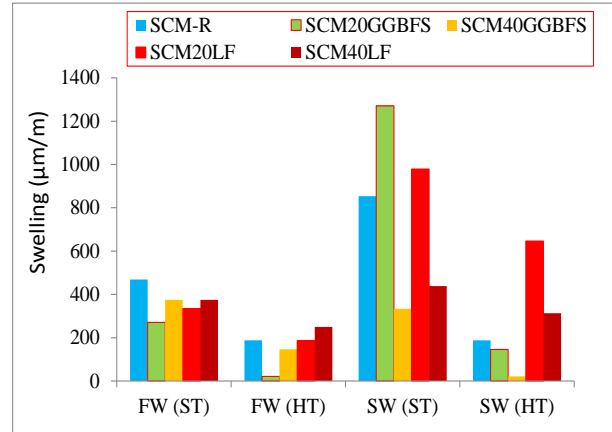


Figure 5. Swelling of SCMs.

3.3. Compressive strengths

The results of compressive strengths are schematized in Fig. 6 to 17.

3.3.1. Effect of the nature of the mineral addition

a. Dosage of 20 %

In fresh water (Fig. 6), LF and GGBFS allowed to obtain very close resistances in the first days. Beyond, GGBFS preponderates a little and shows its advantage due to its inherent hydraulic power and its distinctive reactivity at long-term. Thus, the SCM20GGBFS could be even more resistant than the SCM-R in HT process. In the SW medium (Fig. 7), the ST elaborated SCMs are more resistant than SCM-R but only heat treated SCM20GGBFS which predominates at the age of 180 days. These benefit results prove the advantage of GGBFS in the aggressive marine environment especially at very long term (180 days). Therefore, a good durability is ensured for the structures or the elements built with this eco-sustainable-product.

b. Dosage of 40 %

In both mediums, FW (Fig. 8) and SW (Fig. 9), the GGBFS is very beneficial while the LF is very harmful. We can notice here that GGBFS shows always its positive performance especially in SW environment and offers the possibility to have SCMs more resistant and more durable than those without GGBFS. This positive result using GGBFS remains valid for this level of substitution and even for levels above 40 %. Its according to the search results of Binici et al. [43] which came to conclude that the durability of concrete depending on the types and amount of additives and he was found that between (40 %, 60 % and 80 %) of GGBFS, the specimen based on high level of GGBFS (80 %) have the higher seawater attack resistance than that of the reference concrete.

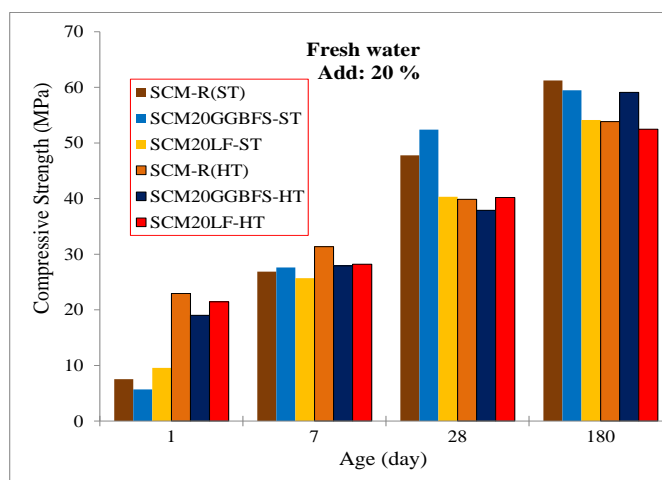


Figure 6. Effect of the nature of the mineral addition (20 %) on compressive strength of SCMs in freshwater.

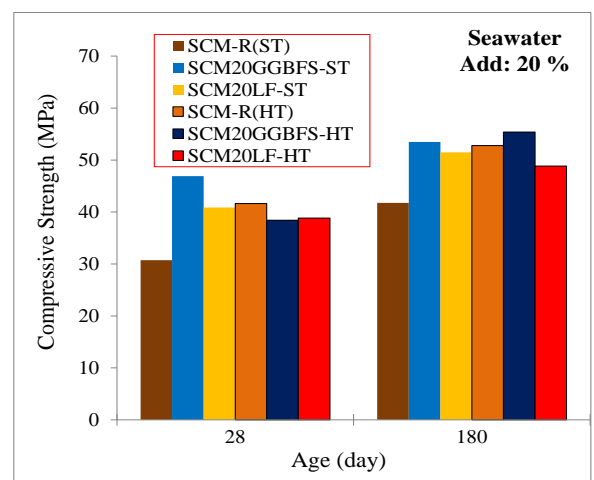


Figure 7. Effect of the nature of the mineral addition (20 %) on compressive strength of SCMs in seawater.

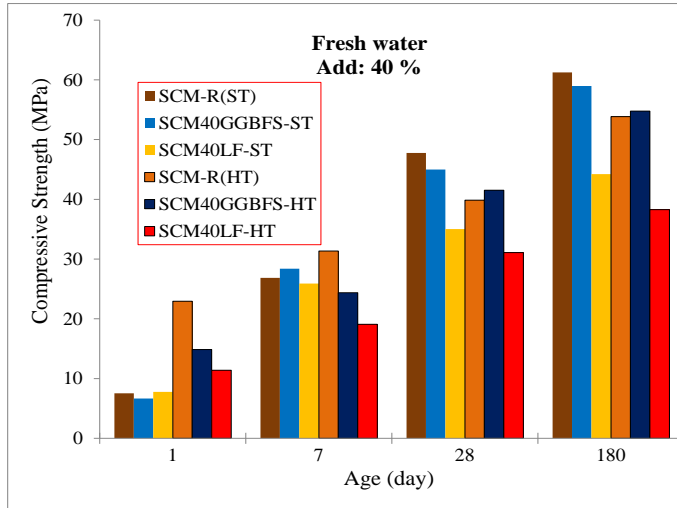


Figure 8. Effect of nature of the mineral addition (40 %) on compressive strength of SCMs in freshwater.

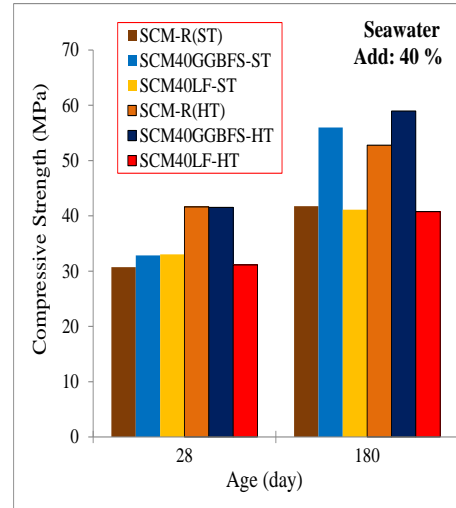


Figure 9. Effect of the nature of the mineral addition (40 %) on compressive strength of SCMs in seawater.

3.3.2. Effect of the dosage of the mineral addition

a. GGBFS

In fresh water (Fig. 10), the two dosages of admixture have allowed to have almost the same level of resistance except at the age of 28 days where the untreated SCM20GGBFS where could even preponderate the SCM-R.

In sea water (Fig. 11), except at the age of 28 days where the SCM20GGBFS has reached a resistance level higher than that of the SCM-R, it is very clear that SCM based on 40 % of GGBFS is very beneficial than that based on 20 %. This allows to consider that SCM40GGBFS as a stable material and thus more durable in the marine environment.

b. Limestone Filler

In fresh water (Fig. 12), except at early age (1 and 7 days) where the untreated SCM40LF has reached a level resistance almost the same of that of SCM-R and SCM20LF, the dosage of 40 % of LF is very harmful in all cases compared to that of 20 %. The same observations remain valid for SCMs cured in the SW medium (Fig. 13).

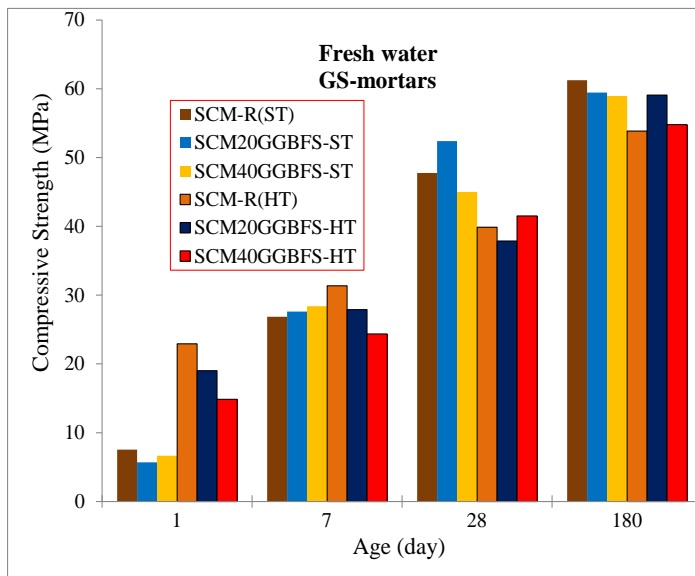


Figure 10. Effect of treatment process on compressive strength of Slag-SCMs in freshwater.

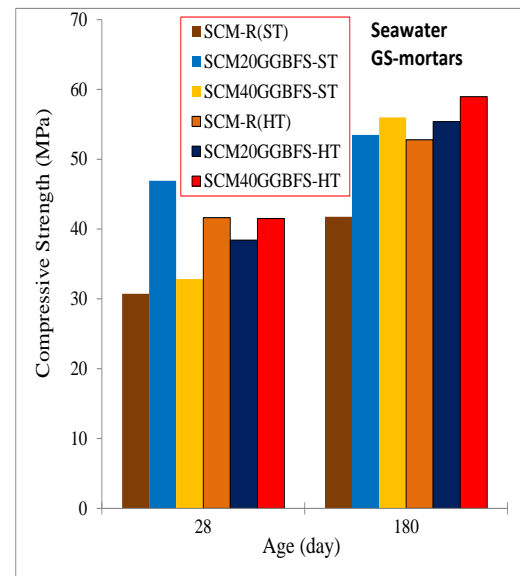


Figure 11. Effect of treatment process on compressive strength Slag-SCMs in seawater.

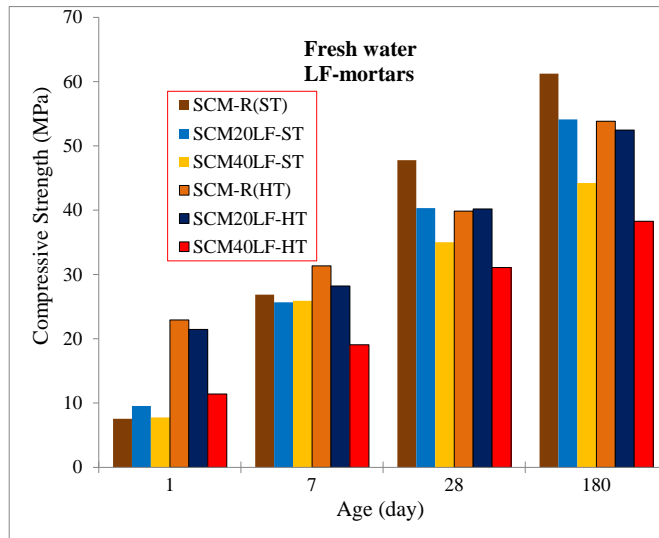


Figure 12. Effect of treatment process on compressive strength of LF-SCMs in freshwater.

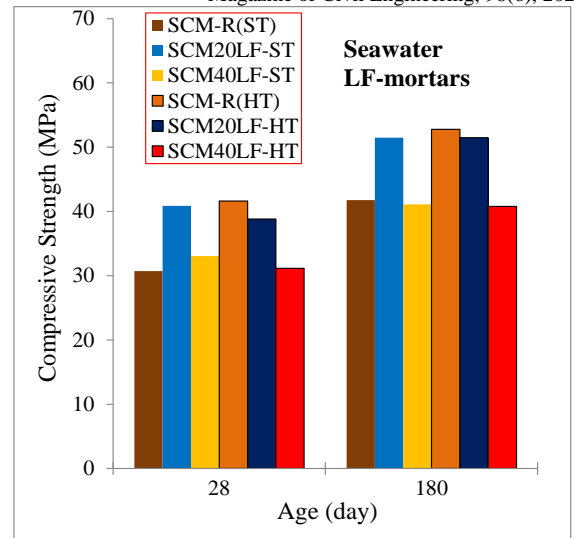


Figure 13. Effect of treatment process on compressive strength LF-SCMs in seawater.

3.3.3. Effect of treatment process

a. Using GGBFS

In fresh water (Fig. 10), at early age (1 day) all heat treated SCMs have higher strengths compared to untreated SCMs. The early age strengths of heat-treated mortars (SCM20GGBFS and SCM40GGBFS) achieved respectively, as 234 % and 123 % compared to their heat-treated strengths at 1 day, and reached respectively as 50 % and 36 % compared to their heat treated strengths at 28 days and attain respectively as 36 % and 33 % compared to their heat treated strengths 28 days.

At the age of 7 days, the resistances are nearly equal.

Beyond 28 days, the phenomenon reversed and the untreated SCFs had the high compressive strengths except for SCM20GGBFS where the results of the strengths are almost equal. Compared to the strength of heat-treated SCM-R at 28 days, SCM20GGBFS marks a loss of 5 % and SCM40GGBFS offers a gain of 4 %. Compared to the strength of untreated SCM-R at 28 days, the strengths of heat-treated mortars (SCM20GGBFS and SCM40GGBFS) at 28 days have respectively the losses as 21 % and 13 %.

At the age of 180 days, the elaborate SCMs have higher resistant compared to the heat-treated control mortar (SCM-R). Compared to the strength of heat-treated SCM-R at 180 days, heat treated SCMs (SCM20GGBFS and SCM40GGBFS) mark losses of 1 % and 7 % respectively. Compared to the strength of untreated SCM-R at 180 days, the strengths of heat-treated mortars (SCM20GGBFS and SCM40GGBFS) at 180 days have respectively the losses as 4 % and 11 %.

In sea water (Fig. 11), at the age of 28 days, the HT process leads to an increase of the strength of SCM40GGBFS (26 %), but a decrease for SCM20GGBFS (18 %). At very long-term (180 days), all heat-treated SCMs had the highest strengths compared to those of untreated SCMs. The slag-SCMs have higher resistant compared to the SCM made without slag. They are about 4 % and 5 % for SCM20GGBFS and SCM40GGBFS respectively.

b. Using LF

In fresh water (Fig. 12), at early age (1 day) all heat treated SCMs have higher strengths compared to untreated SCMs. The early age strengths of heat-treated mortars (SCM20LF and SCM40LF) achieved respectively, as 125 % and 47 % compared to their heat-treated strengths at 28 days and reached, respectively as 53 % and 37 % compared to their heat treated strengths at 28 days and attain respectively as 53 % and 33 % compared to their HT strengths at 28 days.

At the age of 7 days, the resistances are nearly equal.

Beyond 28 days, the phenomenon reversed and the untreated SCMs had the high compressive strengths except for SCM20LF where the results of the strengths are almost equal. Compared to the strength of heat-treated SCM-R at 28 days, SCM20LF offers a gain of 1 % and SCM40LF marks a loss of 22 %. Compared to the strength of untreated SCM-R at 28 days, the strengths of heat-treated mortars (SCM20LF and SCM40LF) at 28 days have respectively the losses of 16 % and 35 %.

At the age of 180 days, the elaborate SCMs have higher resistant compared to the heat-treated control mortar (SCM-R). Compared to their untreated at 180 days, SCM20LF and SCM40LF mark losses of 3 % and 13 % respectively. Compared to the strength of untreated SCM-R at 180 days, the strengths of heat-treated mortars (SCM20GGBFS and SCM40GGBFS) at 180 days have respectively the losses as 14 % and 38 %.

In sea water (Fig. 13), at the age of 28 days, the heat treatment process always leads to a decrease of the strength of SCM20LF and SCM40LF (5 % and 6 %). At very long-term (180 days), the HT process slightly influenced the strength of the elaborated SCMs and they have losses of about (5 % and 1 %).

The HT process leads to obtain promising early age strengths. These results allow demoulding concrete elements quickly (after some hours) and then a gain of time, money and high productivity. So, it is very important in the precast industry and has many advantages for arid regions to overcome curing of concrete structures. Beyond 28 days (long term), the HT process leads to losses in CS of all SCMs without SCM40GGBFS which offers a gain in CS of about 5 %. This confirms that the temperature supplied by HT process in our study was able to reactivate the GGBFS and consequently to increase its hydraulic power as obtained with other researches. Battagin [44] observed that the slag hydration increased systematically with temperature. This acquired property contributes to increase the CS of the developed SCM.

3.3.4. Effect of curing regime

From the results obtained for CS of untreated SCMs (Fig. 14), all SCMs kept in FW medium have higher resistant compared to those kept in SW medium. In the case of HT regime (Fig. 15), only SCM based on 40 % of GGBFS has the best result in SW compared to that stored in FW. With 20 % of GGBFS is even interesting in both process treatment (ST and HT). The same observations that have been made in the case of the use of GGBFS remain valid and right here with LF either with HT regime (Fig. 16) or with ST regime (Fig. 17). But the level of CS developed with GGBFS is superior to that obtained with LF and the amount of 20 % is much better compared to 40 %.

These results show the effectiveness of the incorporation of mineral additions into SCMs to enhance their resistance to seawater aggressively. It is clear that the increase of the substitution rate of the cement by GGBFS ensures a good durability of the SCM in SW medium. This finding has been confirmed by the researchers [31, 32] who concluded that the cements with high content of GGBFS offer good chemical resistance against the aggression of seawater. But the opposite using LF where it is preferable to limit its incorporation to levels less than or equal to 20 % and/or or if it is combined with other additions as MK.

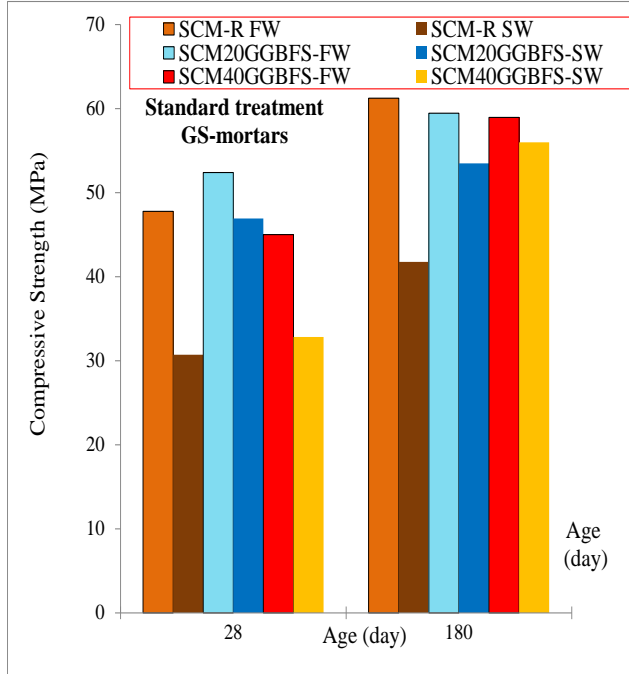


Figure 14. Effect of curing regime on the compressive strength of untreated Slag-SCMs.

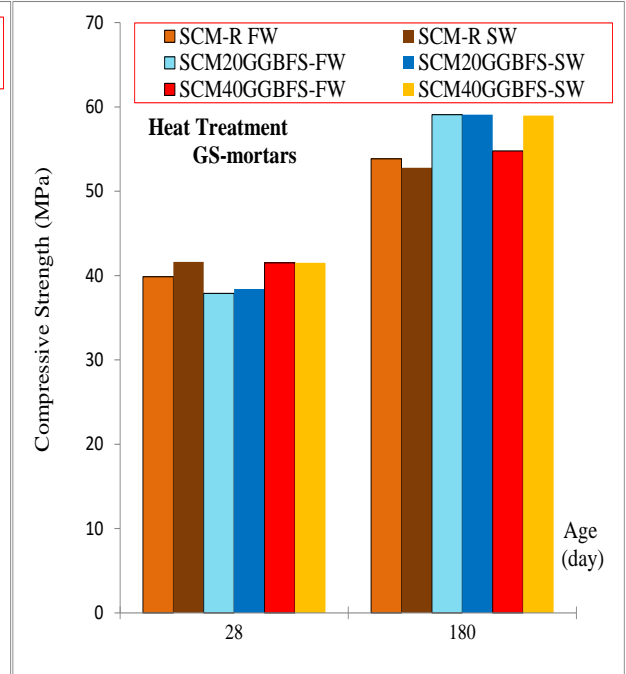


Figure 15. Effect of curing regime on the compressive strength of heat-treated Slag-SCMs.

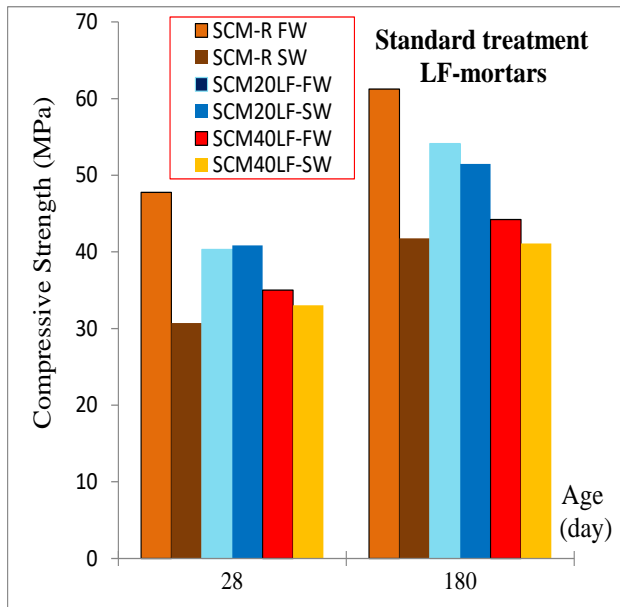


Figure 16. Effect of curing regime on the compressive strength of untreated LF-SCMs.

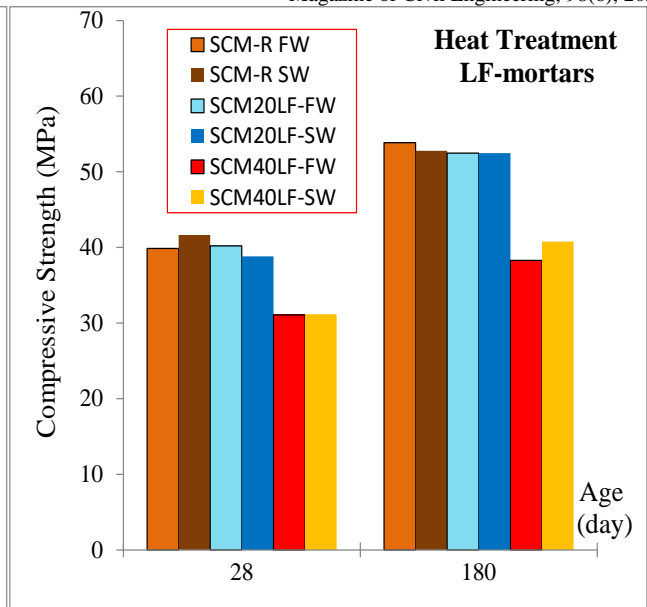


Figure 17. Effect of curing regime on the compressive strength of heat-treated LF-SCMs.

4. Conclusions

The main results derived from this study are as follows:

1. The heat treatment method has many advantages especially at early ages where all the heat-treated SCMs could develop higher strengths than those of SCMs matured in normal conditions.
2. The incorporation of the mineral admixtures is very advantageous to improve physical-mechanical properties of heat-treated SCMs and almost to enhance its durability;
3. The nature and the dosage of the mineral admixture have significant impact on the behavior of SCMs with both HT and ST process and in both FW and SW mediums;
4. The dosage of 20 % LF seemed more effective than that with 40 %, so it is advisable to limit its use to levels of less than or equal to 20 %.
5. The incorporation of GGBFS has played a very important role in improving the behavior of SCM in the marine environment especially in the case of HT process where it could be reactivated by temperature and was able to show its long-term power.
6. The 40 % GGBFS dosage is more profitable than that of 20 % to provide a more stable SCM HT in the face of seawater aggression.

References

1. Heinz, D., Ludwig, U. Delayed ettringite formation in heat-treated mortars and concretes. *Concr. Precast. Plant Technol.* 1996. 55 (11). Pp. 56–61. [http://dx.doi.org/10.1016/0958-9465\(96\)00012-1](http://dx.doi.org/10.1016/0958-9465(96)00012-1)
2. Odler, Y., Chen, Y. On the delayed expansion of heat cured Portland cement pastes and concretes. *Cem. Comp. Res.* 1996. No. 18. Pp. 181–185. [http://dx.doi.org/10.1016/0958-9465\(95\)00014-3](http://dx.doi.org/10.1016/0958-9465(95)00014-3)
3. Victor, T. Effect of Mineral and Chemical Admixtures on Durability of Cementitious Systems. Graduate Theses and Dissertations, University of South Florida. 2015. <http://scholarcommons.usf.edu/etd/6040>
4. Gonen, S., Yazici, O., Gonen, T., Yazicioglu, S. The influence of mineral admixtures on the short and long-term performance of concrete. *Building and Environment.* 2007. No. 42. Pp. 3080–3085. <http://dx.doi.org/10.1016/j.buildenv.2006.10.019>
5. Tasdemir, C. Combined effects of mineral admixtures and curing conditions on the sorptivity coefficient of concrete. *Cem. & Conc. Res.* 2003. No. 33. Pp. 1637–1642. [http://dx.doi.org/10.1016/S0008-8846\(03\)00112-1](http://dx.doi.org/10.1016/S0008-8846(03)00112-1)
6. Uysal, M., Yilmaz, K. Effect of mineral admixtures on properties of self-compacting concrete. *Cem. & Conc. Comp.* 2011. No. 33. Pp. 771–776. <http://dx.doi.org/10.1016/j.cemconcomp.2011.04.005>
7. Liu, B., Xie, Y., Li, J. Influence of steam curing on the compressive strength of concrete containing supplementary cementing materials. *Cem. & Conc. Res.* 2005. No. 35. Pp. 994–998. <http://dx.doi.org/10.1016/j.cemconres.2004.05.044>
8. Jacquemot, F., Rougeau, P., Flahault, N. Acceleration of hardening kinetics of SCC, Design, production and placement of self-consolidating concrete. *RILEM Book series.* 2010. No. 1. Pp. 307–316.
9. Felekoglu, B. Utilization of high volumes of limestone quarry wastes in concrete industry (self-compacting concrete case). *Resources Conservation and Recycling.* 2007. No. 51. Pp. 770–791. <http://dx.doi.org/10.1016/j.resconrec.2006.12.004>
10. Zhimin, H., Junzhe, L., Kangwu, Z. Influence of Mineral Admixtures on the Short and Long-term Performance of Steam-cured Concrete. *Energy Procedia.* 2012. No. 16. Pp. 836–841. <http://dx.doi.org/10.1016/j.egypro.2012.01.134>
11. Hooton, R.D. Influence of silica fume replacement of cement on physical properties and resistance to sulfate attack, freezing and thawing, and alkali silica reactivity, *ACI Mater. J.* 1993. 90(2). Pp. 143–151.

12. Eascalante, J.I., Gomez, L.Y., Johal, K.K., Mendoza, G., Mancha, H., Mendez, J. Reactivity of blast-furnace slag in Portland cement blends hydrated under different conditions. *ACI Material Journal*. 2001. 31(10). Pp. 1403–1409. [http://dx.doi.org/10.1016/S0008-8846\(01\)00587-7](http://dx.doi.org/10.1016/S0008-8846(01)00587-7)
13. Pal, S.C., Mukherjee, A., Pathak, S.R. Corrosion Behavior of Reinforcement in Slag Concrete. *ACI Material Journal*. 2002. 99(6). Pp. 521–527. <http://dx.doi.org/10.1016/j.cemconres.2003.12.029>
14. Takashi, M., Iwaki, I., Strength Development of Concrete Incorporation High Levels of Ground Granulated Blast-Furnace Slag at Low Temperatures. *ACI Material Journal*. 2000. 97(1). Pp. 66–70.
15. Sajedi, F., Hashim, A.R. Thermal activation of ordinary Portland cement–slag mortars. *Materials and Design*. 2010. No. 31. Pp. 4522–4527. <http://dx.doi.org/10.1016/j.matdes.2010.04.011>
16. Antoni, M., Rossen, J., Martirena, F., Scrivener, K. Cement substitution by a combination of metakaolin and limestone. *Cem. Concr. Res.* 2012. 42(12). Pp. 1579–1589. <https://doi.org/10.1016/j.cemconres.2012.09.006>
17. Ye, G., Liu, X., De Schutter, G., Poppe, A. M., Taerwe, L. Influence of limestone powder used as filler in SCC on hydration and microstructure of cement pastes. *Cem. & Con. Com.* 2007. No. 29. Pp. 94–102. <https://doi.org/10.1016/j.cemconcomp.2006.09.003>
18. Vuk, T., Tinta, V., Gabrovšek, R., Kaucic, V. The effects of limestone addition, clinker type and fineness on properties of Portland cement. *Cem. Concr. Res.* 2001. 31 (1). Pp. 135–139. [https://doi.org/10.1016/S0008-8846\(00\)00427-0](https://doi.org/10.1016/S0008-8846(00)00427-0)
19. Liu, S.H., Wang, L. Influence of limestone powder on hydration properties of complex binders, *Mater. Res. Innov.* 2014. 18(2). Pp. S2–186–S2–190. <https://doi.org/10.1179/1432891714Z.0000000000624>
20. Qi, L., Liu, J., Liu, Q. Compound effect of CaCO_3 and $\text{CaSO}_4 \cdot 2\text{H}_2\text{O}$ on the strength of steel slag-cement binding materials, *Mater. Res.* 2016. No. 19(scio). Pp. 269–275. <http://dx.doi.org/10.1590/1980-5373-MR-2015-0387>
21. Medjigbodo, G., Rozière, E., Charrier, K., Izoret, L., Loukili, A. Hydration, shrinkage, and durability of ternary binders containing Portland cement, limestone filler and metakaolin. *Con. & Buil. Mat.* 2018. No. 183. Pp. 114–126. <https://doi.org/10.1016/j.conbuildmat.2018.06.138>
22. Benchaa, B., Kadri, H., Azzouz, L., Kenai, S. Properties of self-compacting mortar made with various types of sand. *Cem. & Con. Com.* 2012. No. 34, Pp. 1167–1173. <http://dx.doi.org/10.1016/j.cemconcomp.2012.07.007>
23. Sahmaran, M., Heru, A.C., Yaman, I.O., The effect of chemical admixtures and mineral additives on the properties of self-compacting mortars. *Cem. & Con. Com.* 2006. No. 28, Pp. 432–440. <http://dx.doi.org/10.1016/j.cemconcomp.2005.12.003>
24. Rizwan, S.A., Bier, A.T. Blends of limestone powder and fly-ash enhance the response of self-compacting mortars. *Con. & Buil. Mat.* 2012. No. 27, Pp. 398–403, <http://dx.doi.org/10.1016/j.conbuildmat.2011.07.030>
25. Safi, B., Ghernouti, Y., Rabehi, B., Aboutaleb, D. Effect of Heat Curing on Strength Development of Self-compacting Mortars Containing Calcined Silt of Dams and Ground Brick Waste. *Mat. Res.* 2013. No. 16, Pp. 1058–1064. <http://dx.doi.org/10.1590/S1516-14392013005000094>
26. Famy, C., Scrivener, K.L., Atkinson, A., Brough, A.R. Influence of the storage conditions on the dimensional changes of heat-cored mortars. *Cem. & Con. Res.* 2001. No. 31, Pp. 795–803. [https://doi.org/10.1016/S0008-8846\(01\)00480-X](https://doi.org/10.1016/S0008-8846(01)00480-X)
27. Hashim, A.R., Sajedi, F. The effect of heat treatment on the compressive strength of cement-slag mortars. *Mat. and Des.* 2011. No. 32 Pp. 4618–4628. <http://dx.doi.org/10.1016/j.matdes.2011.04.038>
28. Derabla, R., Benmalek, M.L., Sajedi, F. Effect of Steam Curing on the Properties of Slag-Cement Concrete in Seawater Environment. 10th International Congress on Advances in Civil Engineering (ACE), METU, Ankara – Turkey, 17–19 October. 2012. 161 p.
29. Erdogdu, S., Kurbetci, S. Influence of cement composition on the early age flexural strength of heat-treated mortar prisms. *Cem. & Con. Com.* 2005. No. 27. Pp. 818–822. <http://dx.doi.org/10.1016/j.cemconcomp.2005.03.006>
30. Sajedi, F., Hashim, A.R. Effects of curing regimes and cement fineness on the compressive strength of ordinary Portland cement mortars. *Con. and Buil. Mat.* 2011. No. 25. Pp. 2036–2045. <http://dx.doi.org/10.1016/j.conbuildmat.2010.11.043>
31. Moïnul, I.M., Saiful, I.M., Bipul, C. M., Amrita, D. Strength behavior of mortar using slag with cement in sea water environment. *Journal of Civil Engineering (IEB)*. 2010. 38(2). Pp. 129–140.
32. Boufenara, K., Guetteche, M.N., Mezhoud, S. Durabilité des mortiers à base des laitiers de haut fourneau. Colloque CMEDIMAT, Oran – Algeria, 6–7 December. 2005.
33. Dreux, G., Festa, J. New guide of concrete and its constituents. Edition Eyrolles. 1998.
34. Common rules for precast concrete products, NF EN 13369. 2004.
35. Scrivener, K.L., Damidot, D., Famy, C. Possible Mechanisms of Expansion of Concrete Exposed to Elevated Temperatures During Curing (Also Known as DEF) and Implications for Avoidance of Field Problems. *Cement, Concrete, and Aggregates. CCAGDP*. 1999. 21(1). Pp. 93–101.
36. Concrete testing - Absorption of water by immersion. NBN B 15-215, Brussels: IBN. 1989.
37. NF P 15-433 Methods of testing cement. Determination of shrinkage and swelling. – Méthodes d'essais des ciments. Février 1994.
38. NF EN 196-1 Méthodes d'essais des ciments – Partie 1 : détermination des résistances – Méthodes d'essais des ciments – Partie 1: Détermination des résistances. Septembre 2016.
39. French Association of Civil Engineering AFGC. Recommendations for the use of self-compacting concrete. January, 2008. P. 63. <http://www.afgc.asso.fr/images/stories/pub/Recommandations-SCC-AFGC-version-anglaise.pdf>
40. Mezedjri, L. Modélisation de l'Impact de la Pollution Industrielle Hydrique dans le Golfe de Skikda (Littoral Est algérien). Thèse de doctorat, University Badji Mokhtar Annaba. 2008. <http://dx.doi.org/10.13140/RG.2.2.11990.91204>
41. Jau, W.C., Tsay, D.S. Study of the basic engineering properties of slag cement concrete and its resistance to seawater corrosion. *Cement and Concrete Research*. 1998. No. 28. Pp. 1363–1371. [https://doi.org/10.1016/S0008-8846\(98\)00117-3](https://doi.org/10.1016/S0008-8846(98)00117-3)
42. Pal, S.C., Mukherjee, A., Pathak, S.R. Corrosion Behavior of Reinforcement in Slag Concrete. *ACI Material Journal*. 2002. 99(6). Pp. 521–527.
43. Binici, H., Aksogan, O., Bahsude, E., Kaplan, H., Bodur, M.N. Performance of ground blast furnace slag and ground basaltic pumice concrete against seawater attack. *Cons. and Buil. Mat.* 2008. 22. Pp. 1515–1526. <https://doi.org/10.1016/j.conbuildmat.2007.03.024>
44. Battagin, A.F. Influence of degree of hydration of slag on slag cements. *Proceeding GGBFS of the 9th ICCG, National Council for Cement and Building Materials*, vol. III. New Delhi, India. 1992. Pp. 166–172.

Contacts:

Riad Derabla, rderabla@gmail.com

Fathollah Sajedi, sajedi@iauhvaz.ac.ir



DOI: 10.18720/MCE.98.10

The shear behavior of CFRP strengthened RC beams

R. Al-Rousan

Jordan University of Science and Technology, Irbid, Jordan

E-mail: rzalrousan@just.edu.jo

Keywords: reinforced concrete, structural strength, shear, flexural strength, fiber reinforced polymer, nonlinear, finite element analysis

Abstract. The primary objective of this paper is to study the effectiveness of using externally applied CFRP composites as a method of shear strengthening. The parameters investigated in this study included CFRP amount and distribution (i.e., sheet versus strips), bonded surface (i.e., web sheet versus U-wrap), and fiber orientation (i.e., 90° fiber direction versus 45° fiber direction). Firstly, a novel Nonlinear Finite Element Analysis (NLFEA) model is created and validated. Then, five RC beams (150×225×1500 mm) have been constructed. The overall behavior of the NLFEA beams loaded up to failure, the onset of the cracking, and crack development with increased load and ductility were described. The NLFEA results showed that externally bonded CFRP increased the shear capacity of the strengthened RC beams significantly depending on the variables investigated. The beams strengthened with 90° CFRP U-wrap sheet provided a large increase in the ultimate load carrying capacity compared to beams strengthened with 90° CFRP web strips of 50 mm width. Decreasing the spacing between the strips is also efficient, while using 45° strips rather than 90° strips does not produce a remarkable increase in the shear capacity. The externally bonded CFRP can increase the shear capacity of the beam significantly by 34–62 % than that of the control beams, depending on the variables investigated. The inclination of the primary shear crack influenced the shear strength contribution of the external strengthening. Finally, an inclusive assessment of the NLFEA results, as well as three other well-known shear strength models, is conducted using a large test database. It is shown that the proposed shear strength, Chen and Teng, and the Chen et al. models give consistently good correlation with test data with an acceptable coefficient of variation as well as ACI Model shows unsatisfactory performance probably owing to its empirical nature and the use of an inappropriate model for the effective FRP bond length.

1. Introduction

A significant portion of the infrastructure in the world is in urgent need of strengthening and rehabilitation. Rehabilitation of either structural members or whole structures is applied when increasing live load is essential or in order to treat a structural or environmental defects. Public funds for infrastructure rebuilding are extremely limited. Therefore, engineers have been looking for innovative solutions that reduce the costs associated with traditional methods. The strengthening should be designed with consideration to minimize the maintenance and repair needs. Due to the different advantages and drawbacks of existing methods, designers must closely evaluate all of the alternatives including the possibility that strengthening may not be the best choice. Finally, it is not only the economical and structural aspects that should form the basis for decisions of strengthening and choice of strengthening method, but environmental and aesthetic aspects must also be considered. In design, the consequences from loss of strengthening effectiveness by fire, vandalism, collision should be considered as a main parameter in the external strengthening of damaged structures.

Upgrading of design standards, deterioration of the infrastructures coupled with the damage caused by natural disasters, and increased safety requirements, necessitate the need for effective construction materials for repair and strengthening of existing structure. Therefore, externally bonded carbon fiber reinforced polymer (CFRP) composites become a commonly used technique, allowing simple repair or reinforcement of structural elements, damage or otherwise structurally inadequate for verity of reasons [1–20]. The use of CFRP composites in rehabilitating structures can greatly reduce maintenance requirements, increase life safety, and increase service life of concrete structures. So far, the majority of research and applications carried out, using CFRP as strengthening material, has be devoted to use for flexural strengthening. A reinforced concrete beam



must be designed to develop its full flexural strength to insure a ductile flexural failure mode under extreme loading. Hence, a beam must have a safety margin against other types of failure that are more dangerous and less predictable than flexural failure. Shear failure of reinforced concrete beam is a type of failure mode which has a catastrophic effect, should it occur. If reinforced concrete beam deficient in shear strength is overloaded, shear failure may occur suddenly without advance warning of distress; while a flexural failure occurs gradually (if the beam is under reinforced), with large deflections and cracking giving ample warning. Also, shear failure reduces the strength of structural elements below the flexural capacity and considerably reduces the ductility of the elements. Therefore, reinforced concrete beams must have sufficient protection, strengthened, in shear zone to insure ductile flexural failure. Among FRP types, CFRP has the advantage of exhibiting relatively higher tensile strength and excellent fatigue properties. FRP reinforcement is essential for strengthening members subjected to bending, shear and can provide confinement to compression members. Structural deficiencies in reinforced concrete (RC) members can be either flexural or shear; however, shear deficiencies are inherently more dangerous because shear failures can occur suddenly and with no possibility for redistribution of internal forces. Therefore, this can be eliminated by promoting flexural failure to increase the probability of ductile flexural failure rather than brittle shear failure. Shear problems exist from insufficient design, reduction in shear reinforcement (RFT) due to corrosion or due to increase in live loads. It was evident that externally bonded FRP reinforcement can increase shear capacity in such situations [21–25]. It is evident that the ultimate resistance of FRP strengthened RC beams depends basically on the tensile strength of FRP material, FRP shear reinforcement ratio, the configuration of FRP materials and its relation to shear cracks inclinations, the compressive strength of concrete, the yield strength of shear reinforcement, the yield strength of main bars and its tensile reinforcement ratio. The shear reinforcement of strengthened RC structures by externally bonded FRP has been reported in a number of studies [26–28]. Until now, there have been a number of analytical models that describe the shear behavior of strengthened RC beams [29–34]. In general, ultimate shear capacity of strengthened RC beams proposed by these models was based on a combination of three basic elements. The first is the contribution of concrete strength, the second is the contribution of shear steel reinforcement and the third is the contribution of FRP reinforcement materials.

Although there is a tremendous effort considering the experimental works for testing RC beams strengthened with FRP sheets [1–3], there are a fewer experimental takes into account the effect of different strengthening configurations and parameters. Shbeeb et al. [35] studied the effectiveness of using externally bonded carbon-fiber-reinforced polymer composite sheets as a method of increasing the shear strength of reinforced concrete beams. The investigated parameters were the amount and distribution of the composite, the bonded surface and fiber orientation. The overall behavior of the test beams up to failure, the onset of cracking and crack development with increased load and ductility were recorded. Thus, the shear behavior of an RC beam in practice is more complex and difficult to understand than its behavior in flexural, although much more research has been carried out on the shear mode of failure. Therefore, Nonlinear Finite Element analysis (NLFEA) work was firstly validated against the experimental load deflection behavior and mode of failure and then the objective of this study expanded to investigate the effect of studied parameters (CFRP amount and distribution, bonded surface, and fiber orientation) on crack inclination, crack opening behavior, concrete compressive strain, and steel tensile strain.

2. Methods

NLFEA is an important and effective tool in the analysis of complex structures. The main benefits that NLFEA provided include: 1) substantial savings in the cost, time, and effort compared with the fabrication and experimental testing of structure elements; 2) allows to change any parameter of interest to evaluate its influence on the structure, such as the compressive strength of concrete; 3) allows to see the stress, strain, and displacement values at any location and at any load level; 4) the ability to change any parameter of interest, and the capability of demonstrating any interesting behavior at any load value and at any location in the system. Six full-scale models strengthened using CFRP are developed to carry out different investigated parameters.

2.1. Beam Description

The validation process of the finite element model is based on the experimental work performed by Shbeeb et al. [35]. Six rectangular reinforced concrete beams, 150 mm (width)×225 mm (depth) with a total length of 1500 mm, were cast with the reinforcement of 2×8 bars at the top and 3×15 bars. Stirrups were placed at 250 mm center to center to allow easier positioning of flexural reinforcement and to provide improved confinement of concrete along the entire beam length as shown in Fig. 1. The design choices were made to ensure that shear failure would occur in the beams. One beam was tested as control beams without strengthening and five beams were strengthened with different schemes with CFRP strips and sheets (Fig. 1). Fig. 1 shows the reinforcement and the CFRP sheet and strips configurations for all the beams specimens. All specimens were tested as simply supported in a special designed built-up rigid steel frame. A hydraulic jack was used to apply a concentrated load through a hydraulic cylinder on a spread steel beam to produce two-

point loading condition to generate a constant moment region at mid-span. Table 1 shows the failure load from the tested [35] and NLFEA.

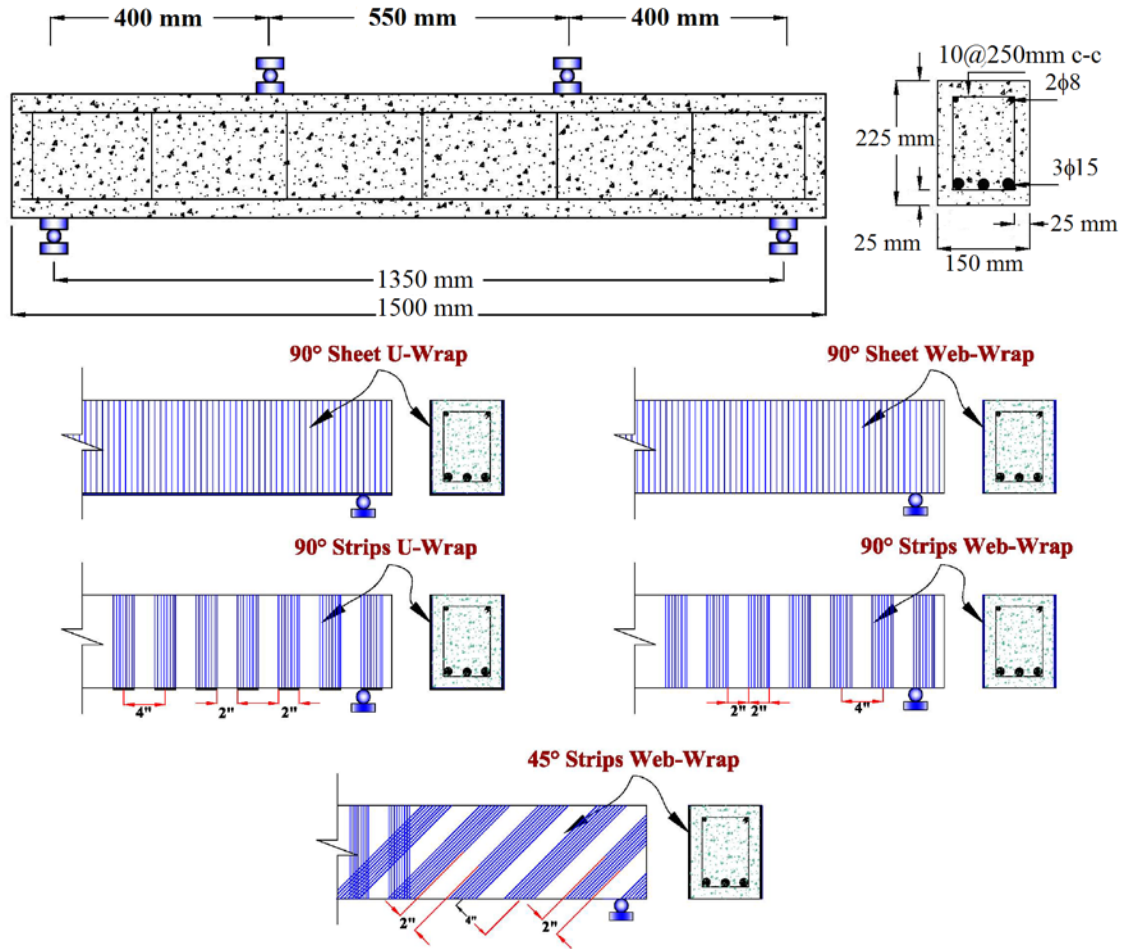


Figure 1. Setup and reinforcement details of the beams [35].

Table 1. NLFEA results.

Beam Designation	Type of strengthening	NLFEA Ultimate load, kN	Experimental. Ultimate load, kN	Percentage of increase with respect to control beam (%)
B2.2N0	Without	180.2	181.3	0
B2.2U90SH1	CFRP 90o Sheet U-Wrap	289.8	293.1	62
B2.2W90SH1	CFRP 90o Sheet Web-Wrap	261.9	264.2	46
B2.2U90ST1	CFRP 90o Strips U-Wrap	266.6	268.7	48
B2.2W90ST1	CFRP 90o Strips Web-Wrap	241.1	243.8	34
B2.2W45ST1	CFRP 45o Strips Web-Wrap	252.3	254.0	40

2.2. Description of Non-linear Finite Element Analysis (NLFEA)

Concrete is a quasi-brittle material and has different behavior in compression and tension. SOLID65 element is capable of predicting the nonlinear behavior of concrete materials using a smeared crack approach. The model is capable of predicting failure for concrete materials and accounts for both cracking and crushing failures. The two input strength parameters, ultimate uniaxial tensile and compressive strengths, are needed to define a failure surface for the concrete. Consequently, a criterion for failure of the concrete due to a multiaxial stress state can be calculated. Poisson's ratio of 0.2 was used for all beams. The shear transfer coefficient (β_t) represents the conditions at the crack face. The value of β_t ranges from 0.0 to 1.0, with 0.0 representing a smooth crack (complete loss of shear transfer) and 1.0 representing a rough crack (no loss of shear transfer). The value of β_t was used in many studies of reinforced concrete structures; however, it varied

between 0.05 and 0.25. Therefore, a value of 0.2 for β_t was used in this study. The concrete properties include concrete compressive strength of 55 MPa, initial young's modulus (E_c) of 35063 MPa. In tension, the stress-strain curve for concrete is assumed to be linearly elastic up to the ultimate tensile strength. After this point, the concrete cracks and the strength decreases to zero (Fig. 2(a)).

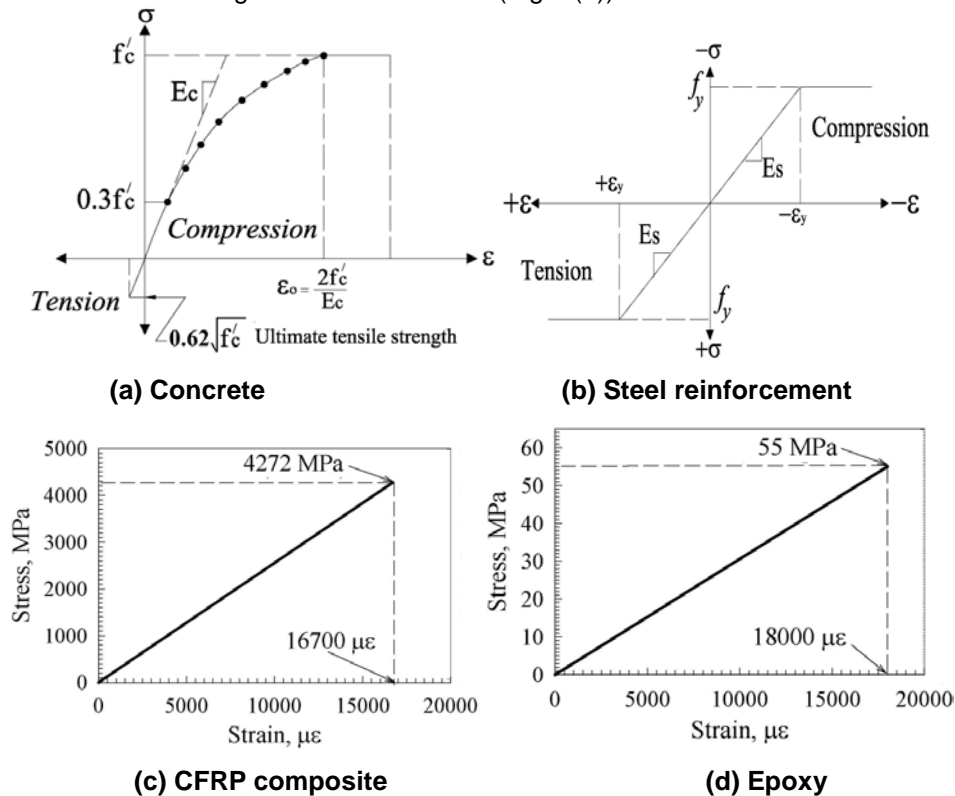


Figure 2. Stress-strain curves [35].

Fig. 2 shows the stress-strain relationships that are used in this study. The steel for the finite element models was assumed to be an elastic-perfectly plastic material and identical in tension and compression. Poisson's ratio and yield stress of 0.3 and 413 MPa respectively were used for the steel reinforcement. Fig. 2(b) shows the stress-strain relationship for steel reinforcement. Steel plates were added at both ends of the beams to provide a more even stress distribution over the support areas. The steel plates were assumed to be linear elastic materials with an elastic modulus equal to 200 GPa (29,000 ksi) and Poisson's ratio of 0.3. The CFRP composite and epoxy are modeled by a layered solid element, SOLID46. The CFRP is assumed to be an orthotropic material of 0.165 mm thick, tensile strength of 3790 MPa, elastic modulus of 228 GPa, and ultimate tensile strain of 0.017 mm/mm. The epoxy used is 0.343 mm thick, ultimate tensile strength 55 MPa, elastic modulus of 30 GPa, and ultimate tensile strain of 0.018 mm/mm. In the other directions perpendicular to the fiber direction, the elastic modulus of CFRP was assumed to be 10^{-6} times that of the main direction. Linear elastic properties were assumed for both CFRP composites and epoxy.

The total load applied was divided into a series of load increments or load steps. Newton – Raphson equilibrium iterations provide convergence at the end of each load increment within tolerance limits equal to 0.001. Load step sizes were automated by ANSYS program for the maximum and minimum load step sizes. In a concrete element, cracking occurs when the principal tensile stress in any direction lies outside the failure surface. After cracking, the elastic modulus of the concrete element is set to zero in the direction parallel to the principal tensile stress direction. Crushing occurs when all principal stresses are compressive and lies outside the failure surface; subsequently, the elastic modulus is set to zero in all directions, and the element effectively disappears. The finite element model fails impulsively when the crushing capability of the concrete is turned on. Crushing of the concrete started to develop in elements located directly under the loads. Afterward, adjacent concrete elements crushed within several load steps as well, significantly reducing the local stiffness. Finally, the model showed a large displacement, and the solution diverged. Therefore, the crushing capability was turned off and cracking of the concrete controlled the failure of the finite element models. During concrete cracking and ultimate load stages in which large number of cracks occurred, the loads were applied gradually with smaller load increments. Failure for each model was identified when the solution for 0.0045 kN load increment was not converging.

CONTA174 element was used to model the layer between the concrete and epoxy layer. This element is an 8-node element that is intended for general rigid-flexible and flexible-flexible contact analysis. In a general contact analysis, the area of contact between two (or more) bodies is generally not known in advance. Also, CONTA174 element is applicable to 3-D geometries. It may be applied for contact between solid bodies or

shells. One of the most accurate bond stress slip models that can be incorporated into a finite element analysis is that proposed by Lu et al. [36]. The mechanical behavior of the FRP/concrete interface is represented by a relationship between the local shear stress, τ , and the relative displacement, s , between the FRP composites and the concrete. Three different bond slip relations have been suggested by these authors; these are classified according to their level of sophistication and are referred to as the precise, the simplified, and the bilinear models. In the current study, the simplified model, as shown in Fig. 3, is adopted for its simplicity.

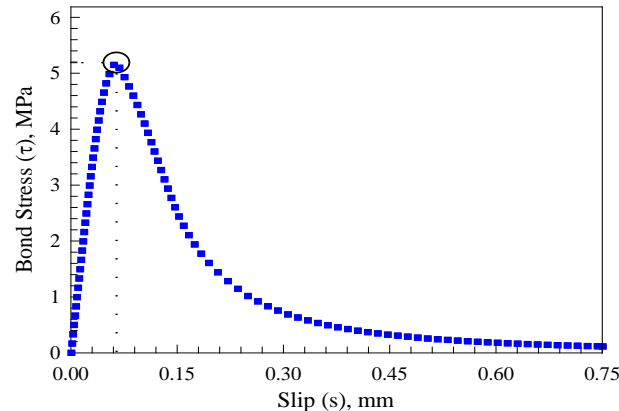


Figure 3. CFRP to concrete bond slip model [36].

Square and rectangular elements were created for the rectangular volumes (concrete, CFRP, epoxy, and steel plates) using the volume-mapped command. This properly sets the width and length of the steel reinforcement elements to be consistent with the elements and nodes of the concrete. A convergence study was carried out to determine the appropriate mesh density as shown in Fig. 4. The meshing of the reinforcement was a special case and the individual elements were created in the modeling process. However, the necessary mesh attributes for the concrete were set before each section of the reinforcement was created. SOLID46 elements for epoxy and CFRP layers had the same meshing as SOLID65 elements for concrete to allocate the node over the node of each element. The command merge item was used to merge separate entities that have the same location into single entities. To ensure proper modeling, displacement boundary conditions were applied at the planes of symmetry. The symmetry boundary conditions were set first. Nodes defining a plane through the beam cross section at the center of the beam define one plane of symmetry. The support was modeled as a roller and hinge that allows the beam to rotate at the support. The applied force was applied across the entire centerline of the steel plate. The beams were analyzed simulating 4-point loading case with the distance between the 2-point of loading is 550 mm. The total applied load was divided into a series of small load increments, each 0.45 kN, and the Modified Newton–Raphson equilibrium iterations were used to check the convergence at the end of each load increment within a tolerance value of 0.001. The static analysis type was utilized to obtain the behavior of the beams. The model failure was identified when the solution of 0.0045 kN load increment was not converging.

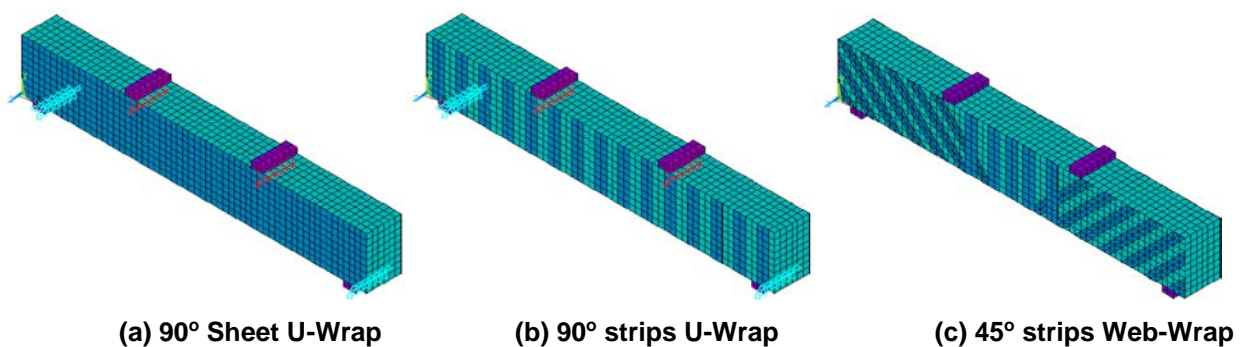


Figure 4. Typical finite element meshing of the beams.

2.3. Validation Process

Fig. 5 shows the load deflection behavior of experimental and NLFEA results. Inspection of Fig. 5 reveals that the load deflection curve can be divided into two stages: stage one represents the pre-cracking stage (creation of the first flexural crack) in which the behavior almost linear and stage two represents the after-cracking stage in which the behavior is nonlinear due to nonlinearity of concrete. With further load increase, the beams strengthened with web CFRP strips or sheet failed in shear due to debond of CFRP strips or sheet before reaching ultimate flexural capacity. The post-cracking stage was clear only for beams strengthened with CFRP 90° strips and sheet U-Wrap sloped upward indicating that the CFRP composites have a significant influence on the post-peak behavior of the strengthened beams. This could be due to the crack arresting mechanism provided by anchoring of the web strips with the tension sides of the beam.

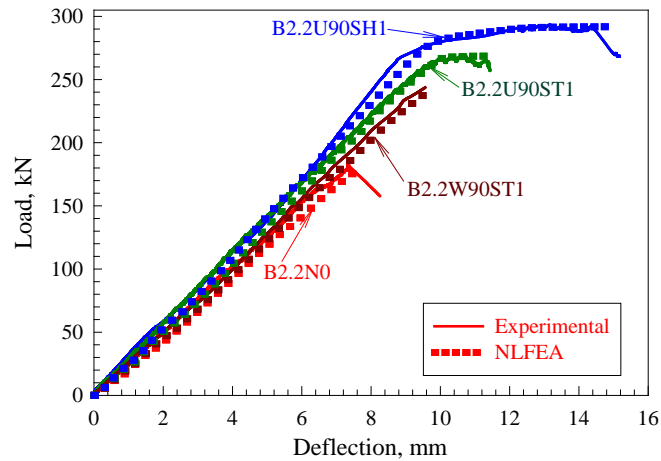


Figure 5. Experimental [35] and NLFEA load-deflection curves.

The experimental results for the tested beams are presented in Table 1. The numerical values of the ultimate strengths and the corresponding percentage increase in the ultimate shear strength of the strengthened beams over the control beam indicated that the performance of the shear deficient beams is enhanced due to the use of CFRP composites. Table 1 and Fig. 5 show that the NLFEA results correlates well with the experimental data at ultimate load capacity. Fig. 6 shows typical stress contours of the control and strengthened beams.

3. Results and Discussion

3.1. Failure Mode

Each specimen without shear reinforcement exhibited an initial flexural crack at the center of the specimen and subsequent flexural cracks away from that section. As the applied load was increased, one of the flexural cracks extended into a diagonal crack near one of the supports, or a diagonal crack formed abruptly at the mid height of the beam within the shear span area. After the formation of the diagonal crack, failure occurred by splitting along the tension reinforcement. A representative cracking pattern is shown in Fig. 6. The load carrying capacity and the mode of failure of shear reinforced concrete beams are summarized in Table 1.

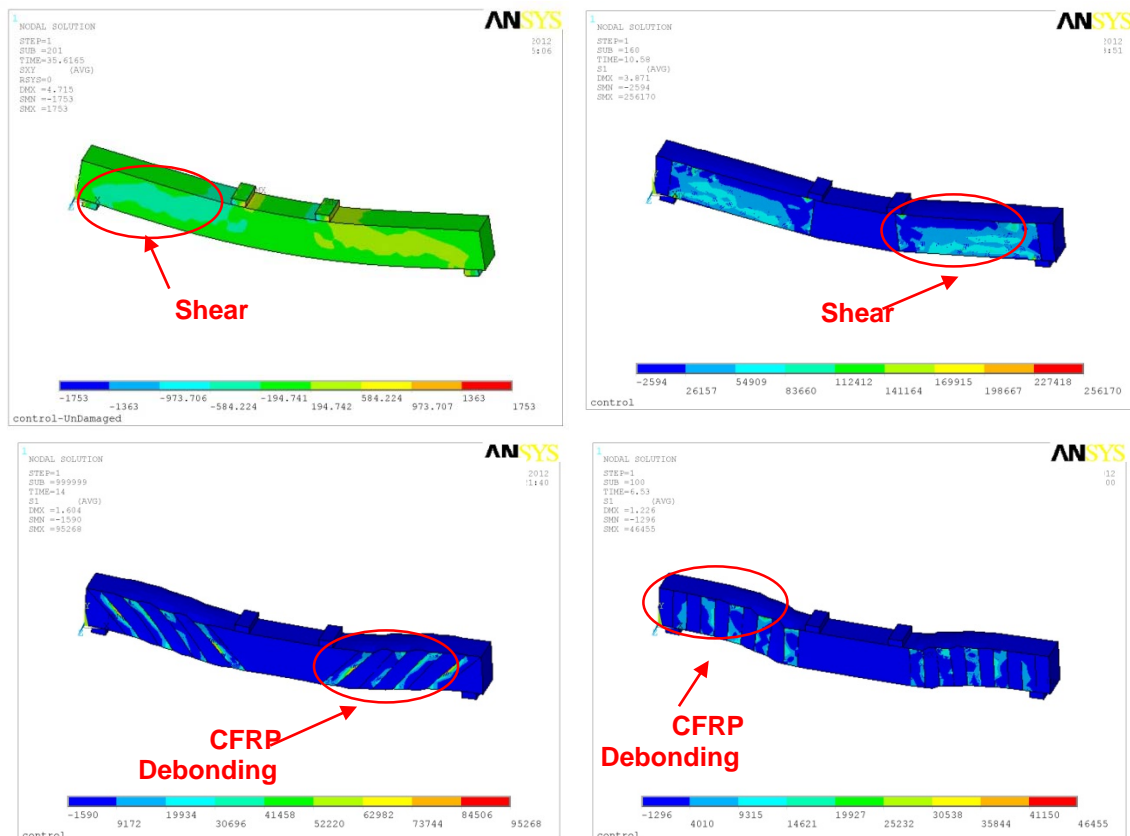


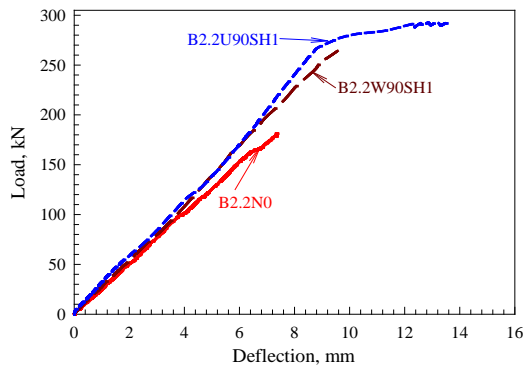
Figure 6. Typical NLFEA stress contours of NLFEA beams.

Table 2 shows the first flexural cracking load, the diagonal shear crack load, and modes of failure. The first flexural crack created within the constant moment region at a load of P_{cr} as shown in Table 2. Beyond this load, cracks extended toward the top fiber. Additional flexural cracking was developed throughout the beam length. At V_{cr} (diagonal shear crack load), a diagonal shear crack formed along a line joining the support and the load point. The crack initiated at the middle of the shear span and extended both towards the support and the load point (Table 2). All beams exhibited shear failure except CFRP 90° Sheet U-Wrap beam exhibited a ductile flexural failure and failed at a load of V_u (Table 1) as shown in Fig. 6. Finally, the shear strength increases with the increase of (1) bonded surface area (34 % for CFRP 90° Strips Web-Wrap, 40 % for CFRP 45° Strips Web-Wrap, 46 % for CFRP 90° Sheet Web-Wrap, 48 % for CFRP 90° Strips Web-Wrap, and 62 % for CFRP 90° Sheet U-Wrap); (2) CFRP distribution (48 % for CFRP 90° Strips Web-Wrap and 62% for CFRP 90° Sheet U-Wrap); and (3) CFRP orientation angle (40% for CFRP 45° Strips Web-Wrap, 46 % for CFRP 90° Sheet Web-Wrap and 48 % for CFRP 90° Strips Web-Wrap).

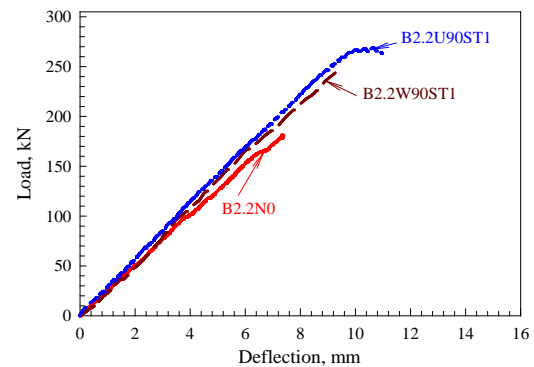
Table 2. Failure load and modes of failure.

Beam Designation	P_{cr} , kN	V_{cr} , kN	V_u , kN	Elastic Stiffness, kN/mm	Cracking stiffness, kN/mm	Failure mode
B2.2N0	32.9	115.6	180.2	27.1	20.9	Shear failure followed by 45° diagonal crack
B2.2U90SH1	34.7	133.4	289.8	28.0	25.8	Flexural failure followed by crushing of concrete in compression zone
B2.2W90SH1	34.1	211.3	261.9	25.8	23.8	Shear failure followed by 44° diagonal crack, debonding of CFRP sheets, and ripping of concrete
B2.2U90ST1	34.3	124.5	266.6	26.8	25.3	Shear failure followed by 37° diagonal crack and debonding of CFRP sheets
B2.2W90ST1	33.6	116.8	241.1	25.2	23.1	Shear failure followed by 41° diagonal crack and debonding of CFRP sheets
B2.2W45ST1	33.8	118.7	252.3	26.1	25.8	Shear failure followed by 44° diagonal crack, debonding of CFRP sheets, and ripping of concrete

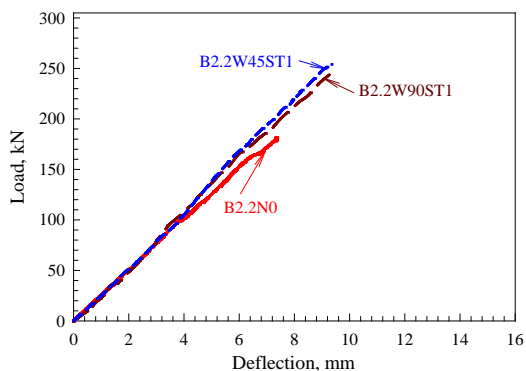
Note: P_{cr} : the first flexural cracking load, V_{cr} : the diagonal shear crack load, V_u : the ultimate shear load



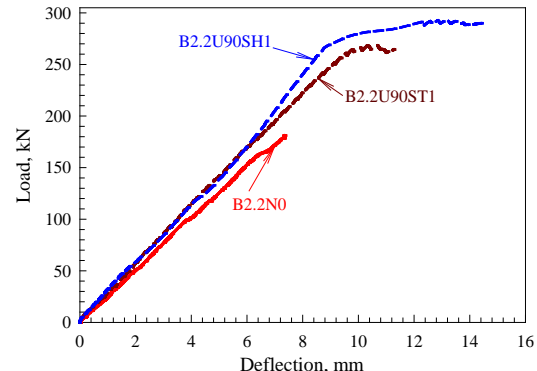
(a) Effect of bond surface (CFRP sheet)



(b) Effect of bond surface (CFRP Strips)



(c) Effect of CFRP orientation



(d) Effect of CFRP distribution

Figure 7. NLFEA load-deflection curve curves.

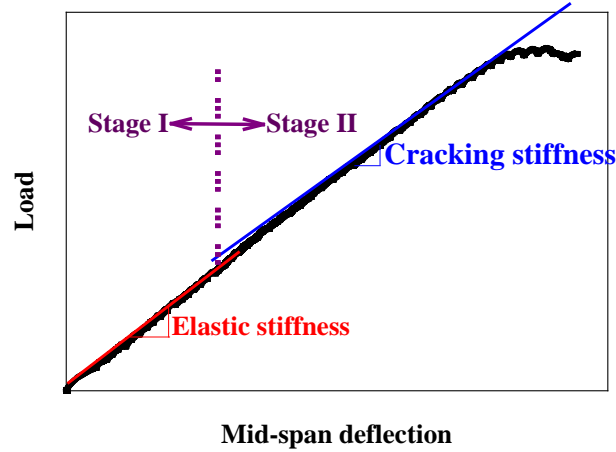
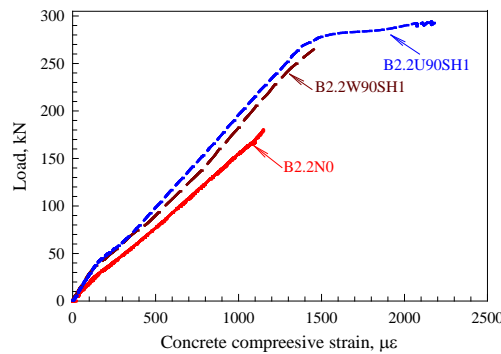


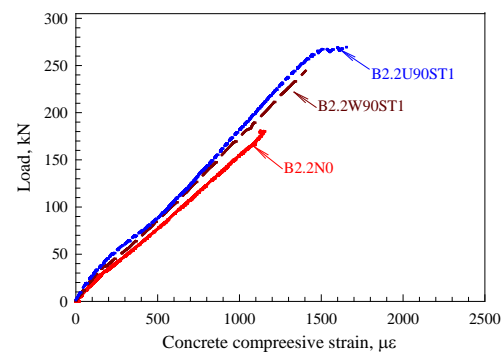
Figure 8. Stages and characteristics of load deflection behavior.

3.2. Load-deflection behavior

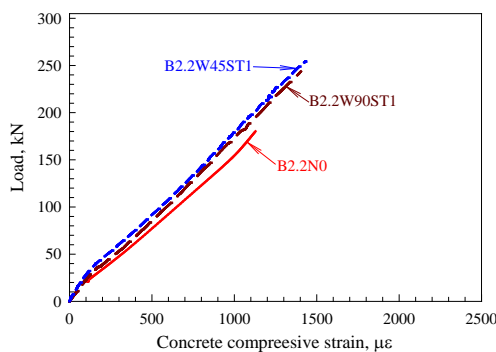
Fig. 7 shows the load deflection curves for NLFEA beams which exhibited almost linear behavior up to the load creation of the first flexural crack (P_{cr}) as shown in Table 2. The slope of the first stage of the load-deflection curve before initiation of the first main flexural crack represents the elastic stiffness while the slope of the second stage represents the cracking stiffness. This indicates that the stiffness of the beam decreased with the increase of load in which the elastic stiffness of the curve before creation of the first flexural crack is larger than the cracking stiffness as shown in Fig. 8. In addition, the increase in elastic stiffness can be observed from the angle of the diagonal shear crack (Table 2) of the elastic stage curve of the NLFEA beams in which the relationship between them is reverse. Also, the angle of the diagonal shear crack decreases with the increase of CFRP sheet bond strength area (Table 2). The load displacement curves have the same conclusion where all beams had sudden drop in load after peak load while CFRP 90° Sheet U-Wrap had ductile behavior. This indicates that an increase in the ultimate deflection can be confirmed by the use of U-wrap which give the structure behavior more ductility, and the ultimate deflection is higher than others. Inspection of Table 2 reveals that the angle of the diagonal shear crack decreases with the increase of bond surface, CFRP distribution, and CFRP sheet orientation.



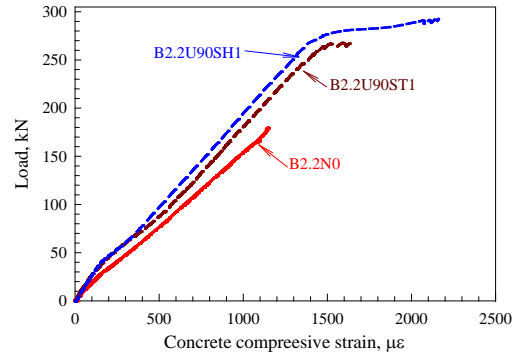
(a) Effect of bond surface (CFRP sheet)



(b) Effect of bond surface (CFRP Strips)



(c) Effect of CFRP orientation



(d) Effect of CFRP distribution

Figure 9. NLFEA load-concrete compressive strain curves.

3.3. Concrete compressive strain

Fig. 9 shows the relationship between the load and concrete compressive strain all tested beams. Inspection of Fig. 9 reveals that the compression strain increased with increasing the load as well as the concrete compressive strain in the concrete decreases with the increase of bond surface, CFRP distribution, and CFRP sheet orientation. After the yielding of steel reinforcement of B2.2U90SH1, the compression strain in concrete increased at a higher rate. The strengthened reinforced concrete beam with the U-shape CFRP sheet obtained the highest strain without occurring huge damage at the compression zone due to the confinement of the concrete.

3.4. Steel tensile strain

Fig. 10 shows the relationship between the load and strain at the level of steel for all tested beams. The load strain curve followed the same trend for all the beams before the cracking. After cracking the slope of the curve was reduced as a result of reduction in stiffness. Inspection of Fig. 10 reveals that the steel tensile strain followed the same trend and behavior as the concrete compressive strain which increased with increasing the load as well as the steel tensile strain in the concrete decreases with the increase of bond surface, CFRP distribution, and CFRP sheet orientation. B2.2U90SH1 are the only beams reached the yielding point as well as the steel reinforcement in U-shaped strengthened beam experienced highest tensile strain development than that of other beams at ultimate load.

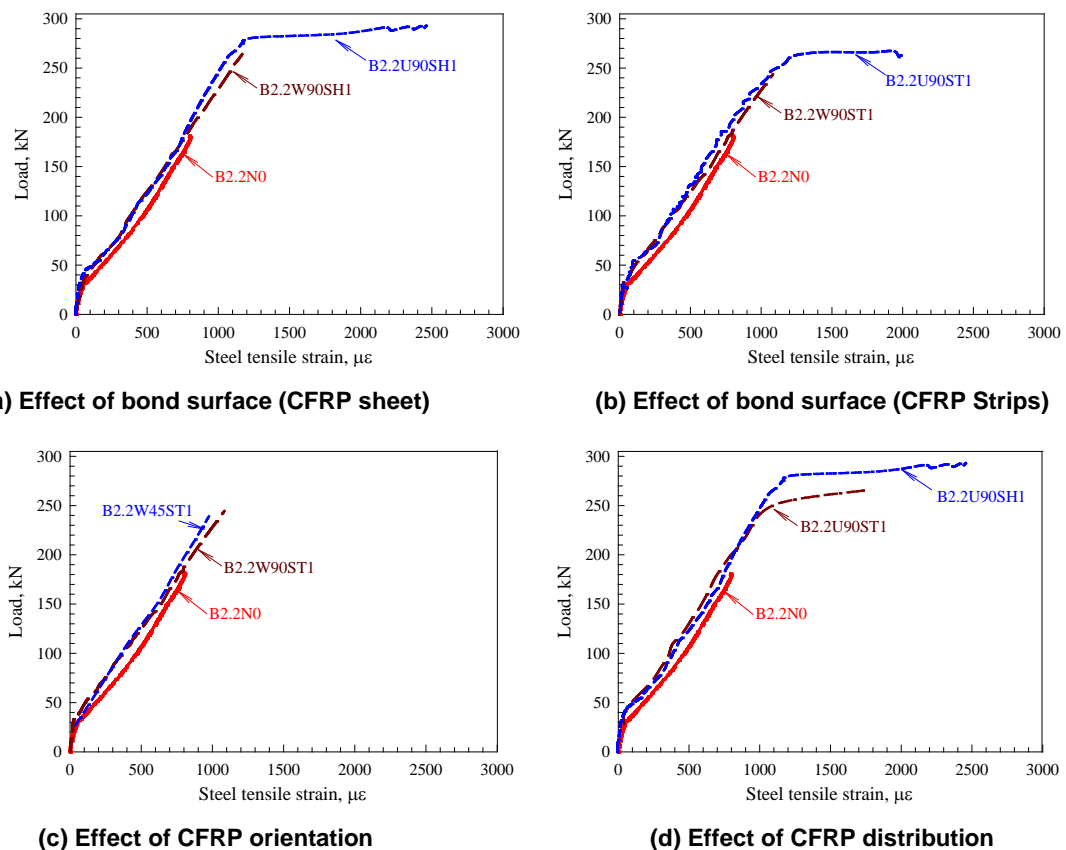
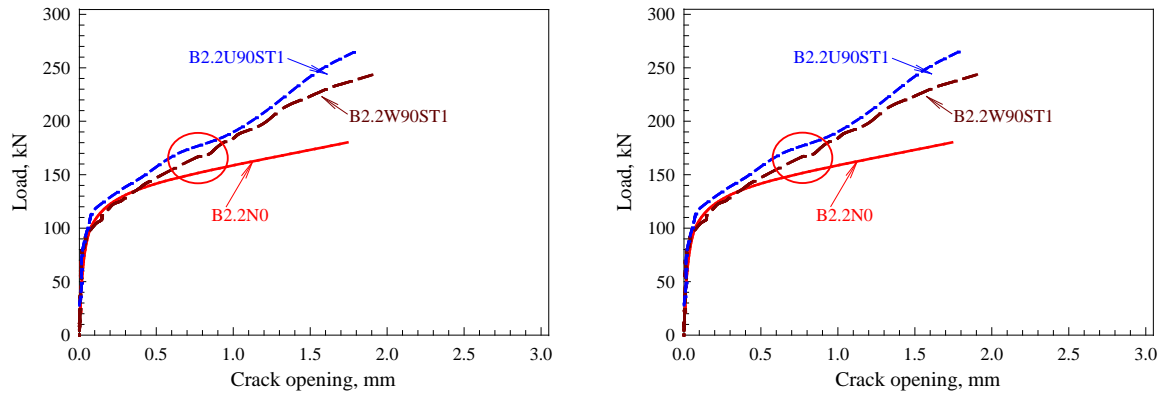


Figure 10. NLFEA load- steel tensile strain curves.

3.5. Crack opening behavior

Fig. 11 shows the relationship between the load and crack opening for beams with different CFRP strips bond surface. According to Fig. 11(a), crack opening width was initiated at load 115.7 kN and 124.5 kN for B2.2W90ST1 and B2.2U90ST1, respectively, after the formulation of diagonal shear crack. Fig. 11 shows also that the development of crack width also becomes sluggish around 0.8 mm for B2.2N0, B2.2W90ST1 and B2.2U90ST1. In addition, the crack width of B2.2N0 started to develop at 115.7 kN follows by the B2.2W90ST1 while the crack width of B2.2U90ST1 started around the load of 124.5 kN. It can be observed that the crack developed at a slower as the bond area decreases. At ultimate load, the ultimate crack width is 2.89, 1.93 and 1.82 mm for B2.2N0, B2.2W90ST1, and B2.2U90ST1, respectively. Therefore, the U-shape strengthened beam showed less crack width for the same load than the other beams. Figure 11(b) shows the relationship between the load and crack opening for beams with different CFRP orientation. According to Fig. 11(b), the development of crack width also becomes sluggish around 0.25 mm in B2.2N0, B2.2W90ST1 and B2.2W45ST1. It can be observed the crack developed at a slower rate as the CFRP orientation angle is decrease. At ultimate load, the ultimate crack width is 2.89, 1.93 and 1.07 mm for B2.2N0, B2.2W90ST1, and

B2.2W45ST1 respectively. Therefore, the 45° strips strengthened beam showed less crack width for the same load than the other beams.



(a) Effect of bond surface (CFRP Strips)

(b) Effect of CFRP orientation

Figure 11. NLFEA load-crack opening curves.

3.6. Comparison of NLFEA with theoretical models

The first step in each theoretical modeling should be adequately validated to confirm its reliability and its predictive ability against a large number of experimental of the beams with a wide range of geometrical and mechanical characteristics. These beams differ in terms of geometry, concrete strength, and amount and strength of internal and external reinforcement. The proposed model has been applied to NLFEA results as well as the literature test results. For purposes of comparison, the NLFEA results are compared with those of the Chen and Teng model [37], Chen et al. model [38], and ACI model [39]. The comparison between NLFEA and analytical results based on the proposed structural model is shown in Table 3.

Note that the ACI model was calibrated for CFRP should be used with caution for other types of composites as shown in Table 3. The overall predictions by ACI model does not appear to be equally satisfactory with a mean $V_{f,exp}/V_{f,ACI}$ value of 2.122 and a COV of 96 %. In the ACI model, the general design guidance is derived from the NLFEA data and they are only applicable to external FRP reinforcement. Based on Table 3, the proposed, Chen and Teng [37] and Chen et al. [38] models give a better prediction of NLFEA data. Therefore, Chen and Teng [37] and Chen et al. [38] models are thus applicable to all externally bonded beams irrespective of whether the bonded reinforcement is made of steel or CFRP.

Table 3. Comparison of results obtained with different models.

Beam Designation	NLFEA Ultimate load, kN	Chen and Teng model [37] $\left(\frac{V_{f,NLFEA}}{V_{f,mod}}\right)$	Chen et al. model [38] $\left(\frac{V_{f,NLFEA}}{V_{f,mod}}\right)$	ACI 440.2R model [39] $\left(\frac{V_{f,NLFEA}}{V_{f,mod}}\right)$
B2.2N0	180.2	0.941	0.951	2.078
B2.2U90SH1	289.8	0.932	0.942	2.058
B2.2W90SH1	261.9	0.980	0.990	2.163
B2.2U90ST1	266.6	0.990	1.000	2.186
B2.2W90ST1	241.1	1.000	1.010	2.208
B2.2W45ST1	252.3	0.923	0.933	2.038
Average	----	0.961	0.970	2.122
CoV (%)	----	39	39	96

4. Conclusions

1. The inclination of the primary shear crack influenced the shear strength contribution of the external strengthening.

2. The use of CFRP composites is an effective technique to enhance the shear capacity of RC beams. The externally bonded CFRP can increase the shear capacity of the beam significantly by 34 (CFRP 90° Strips Web-Wrap) to 62 % (CFRP 90° Sheet U-Wrap) than that the control beams, depending on the variables investigated.

3. Using of 45° strips rather than 90° strips does not produce a remarkable increase in the shear capacity.
4. The concrete compressive and steel tensile strain decrease with the increase of bond surface, CFRP distribution, and CFRP sheet orientation.
5. The strengthened reinforced concrete beam with the U-shape CFRP sheet obtained the highest strain without occurring huge damage at the compression zone due to the confinement of the concrete.
6. It is shown that the proposed, Chen and Teng [37] and Chen et al. [38] models give consistently good correlation with test data with an acceptable COV that can be expected for the behavior of RC beams. Therefore, Chen and Teng [37] and Chen et al. [38] models are thus applicable to all externally bonded beams irrespective of whether the bonded reinforcement is made of steel or CFRP.

References

1. Ahmed, A., Kodur, V. The experimental behavior of FRP-strengthened RC beams subjected to design fire exposure. *Engineering Structures*. 2011. 33(1). Pp. 2201–2211. DOI: 10.1016/j.engstruct.2011.03.010
2. Kodur, V.K.R., Agrawal, A. An approach for evaluating residual capacity of reinforced concrete beams exposed to fire. *Engineering Structures*. 2016. 110(1). Pp. 293–306. DOI: 10.1016/j.engstruct.2015.11.047
3. Al-Ostaz, A., Irshidat, M., Tenkhoff, B., Ponnappalli, P.S. Deterioration of bond integrity between repair material and concrete due to thermal and mechanical incompatibilities. *Journal of Materials in Civil Engineering*. 2010. 22(2). Pp. 136–144. DOI: 10.1061/(ASCE)0899-1561(2010) 22:2(136)
4. Petkova, D., Donchev, T., Wen, J. Experimental study of the performance of CFRP strengthened small scale beams after heating to high temperatures. *Construction and Building Materials*. 2014. 68(1). Pp. 55–61. DOI: 10.1016/j.conbuildmat.2014.06.014
5. Ji, G., Li, G., Alaywan, W. A new fire resistant FRP for externally bonded concrete repair. *Construction and Building Materials*. 2013. 42(1). Pp. 87–96. DOI: 10.1016/j.conbuildmat.2013.01.008
6. Trentin, C., Casas, J.R. Safety factors for CFRP strengthening in bending of reinforced concrete bridges. *Composite Structures*. 2015. 128(1). Pp. 188–198. DOI: 10.1016/j.compstruct.2015.03.048
7. Ferrari, V.J., de Hanai, J.B., de Souza, R.A. Flexural strengthening of reinforcement concrete beams using high performance fiber reinforcement cement-based composite (HPFRCC) and carbon fiber reinforced polymers (CFRP). *Construction and Building Materials*. 2013. 48(1). Pp. 485–498. DOI: 10.1016/j.conbuildmat.2013.07.026
8. Attari, N., Amziane, S., Chemrouk, M. Flexural strengthening of concrete beams using CFRP, GFRP and hybrid FRP sheets. *Construction and Building Materials*. 2012. 37(1). Pp. 746–757. DOI: 10.1016/j.conbuildmat.2012.07.052
9. Kara, I.F., Ashour, A.F., Köroğlu, M.A. Flexural behavior of hybrid FRP/steel reinforced concrete beams. *Composite Structures*. 2015. 129(1). Pp. 111–121. DOI: 10.1016/j.compstruct.2015.03.073
10. Alver, N., Tanarlan, H.M., Sülün, Ö.Y., Ercan, E., Karcılı, M., Selman, E., Ohno, K. Effect of CFRP-spacing on fracture mechanism of CFRP-strengthened reinforced concrete beam identified by AE-SiGMA. *Construction and Building Materials*. 2014. 67(1). Pp. 146–156. DOI: 10.1016/j.conbuildmat.2014.05.017
11. Khan, A. ur R., Fareed, S. Behaviour of reinforced concrete beams strengthened by CFRP wraps with and without end anchorages. *Procedia Engineering*. 2014. 77(1). Pp. 123–130. DOI: 10.1016/j.proeng.2014.07.011
12. Hawileh, R.A., Rasheed, H.A., Abdalla, J.A., Al-Tamimi, A.K. Behavior of reinforced concrete beams strengthened with externally bonded hybrid fiber reinforced polymer systems. *Mater. Des.* 2014. 53(1). Pp. 972–982. DOI: 10.1016/j.matdes.2013.07.087
13. You, Y.-C., Choi, K.-S., Kim, J. An experimental investigation on flexural behavior of RC beams strengthened with prestressed CFRP strips using a durable anchorage system. *Composites Part B: Engineering*. 2012. 43(1). Pp. 3026–3036. DOI: 10.1016/j.compositesb.2012.05.030
14. Al-Rousan, R., Abo-Msamh, I. Bending and Torsion Behaviour of CFRP Strengthened RC Beams. *Magazine of Civil Engineering*. 2019. 92(8). Pp. 62–71. DOI: 10.18720/MCE.92.8
15. Kiyaneets, A.V. Concrete with recycled polyethylene terephthalate fiber. *Magazine of Civil Engineering*. 2018. 84(8). Pp. 109–118. DOI: 10.18720/MCE.84.11
16. Kolchunov, V.I., Dem'yanov, A.I. The modeling method of discrete cracks in reinforced concrete under the torsion with bending. *Magazine of Civil Engineering*. 2018. 81(5). Pp. 160–173. DOI: 10.18720/MCE.81.16
17. Travush, V.I., Konin, D.V., Krylov, A.S. Strength of reinforced concrete beams of high-performance concrete and fiber reinforced concrete. *Magazine of Civil Engineering*. 2018. No. 77(1). Pp. 90–100. DOI: 10.18720/MCE.77.8
18. Al-Rousan, R. Behavior of two-way slabs subjected to drop-weight. *Magazine of Civil Engineering*. 2019. 90(6). Pp. 62–71. DOI: 10.18720/MCE.90.6
19. Al-Rousan, R. The impact of cable spacing on the behavior of cable-stayed bridges. *Magazine of Civil Engineering*. 2019. 91(7). Pp. 49–59. DOI: 10.18720/MCE.91.5
20. Yu, B., Kodur, V.K.R. Fire behavior of concrete T-beams strengthened with nearsurface mounted FRP reinforcement. *Engineering Structures*. 2014. 80(1). Pp. 350–361. DOI: 10.1016/j.engstruct.2014.09.003
21. Triantafyllou, T.C., Antonopoulos, C.P. Design of concrete flexural members strengthened in shear with FRP. *J Compos Constr.* 2000. 4(4). Pp.198–205. DOI: 10.1061/(ASCE)1090-0268(2000)4:4(198)
22. Bousselham, A., Chaallal, O. Shear strengthening reinforced concrete beams with fiber-reinforced polymer: assessment of influencing parameters and required research. *ACI Struct J.* 2004. 101(2). Pp. 219–227. DOI: 10.14359/13019
23. Belarbi, A., Bae, S., Brancaccio, A. Behavior of full-scale RC T-beams strengthened in shear with externally bonded FRP sheets. *Constr Build Mater.* 2012. 32(1). Pp. 27–40. DOI: 10.1016/j.conbuildmat.2010.11.102
24. Khalifa, A., Nanni, A. Improving shear capacity of existing RC T-section beams using CFRP composites. *Cem Concr Compos.* 2000. 22(1). Pp. 165–174. DOI: 10.1016/S0958-9465(99)00051-7
25. Mosallam, A., Banerjee, S. Shear enhancement of reinforced concrete beams strengthened with FRP composite laminates. *Composites: Part B.* 2007. 38(1). Pp. 781–93. DOI: 10.1016/j.compositesb.2006.10.002

26. Ashrafuddin, M., Baluch, M.H., Sharif, A., Al-Sulaimani, G.J., Azad, A.K., Khan, A. Peeling and diagonal tension failures in steel plated R/C beams. *Constr Build Mater.* 1999. 13(1). Pp. 459–467. DOI: 10.1016/S0950-0618(99)00044-6
27. Rangan, B.V. Shear design of reinforced concrete beams, slabs and walls. *Cem Concr Compos.* 1998. 20(1). Pp. 455–464. DOI: 10.1016/S0958-9465(98)00027-4
28. Spadea, G., Bencardino, F., Swamy, R.N. Optimizing the performance characteristics of beams strengthened with bonded CFRP laminates. *Mater Struct.* 2000. 33(1). Pp. 1119–1126. DOI: 10.1007/BF02484166
29. Malek, A.M., Saadatmanesh, H. Ultimate shear capacity of reinforced concrete beams strengthened with web-bonded fiber-reinforced plastic plates. *ACI Struct J.* 1998. 95(4). Pp. 391–399. DOI: 10.14359/555
30. Triantafillou, T.C. Shear strengthening of reinforced concrete beams using epoxy-bonded FRP composites. *ACI Struct J.* 1998. 95(2). Pp. 107–115. DOI: 10.14359/531
31. Khalifa, A., Nanni, A. Improving shear capacity of existing RC T-section beams using CFRP composites. *J Cem Concr Compos.* 2000. 22(2). Pp. 165–174. DOI: 10.1016/S0958-9465(99)00051-7
32. Hutchinson, R.L., Rizkalla, S.H. Shear strengthening of AASHTO bridge girders using carbon fiber reinforced polymer sheets. *ACI Special Publications (SP-188).* 1999. 188(1). Pp. 945–958. DOI: 10.14359/5692
33. Zhang, Z., Hsu, C.T. Shear strengthening of reinforced concrete beams using carbon-fiber-reinforced polymer laminates. *J Compos Constr.* 2005. 9(2). Pp. 158–169. DOI: 10.1061/(ASCE)1090-0268(2005)9:2(158)
34. Monti, G., Liotta, M.A. Tests and design equations for FRP-strengthening in shear. *Constr Build Mater.* 2007. 21(24). Pp. 799–809. DOI: 10.1016/j.conbuildmat.2006.06.023
35. Shbeeb, N.I., Al-Rousan, R., Issa, M.A., Al-Salman, H. Impact of bonded carbon fibre composite on the shear strength of reinforced concrete beams. *Proceedings of the Institution of Civil Engineers: Structures and Buildings.* 2018. 171(5). Pp. 364–379. DOI: 10.1680/jstbu.16.00145
36. Lu, X.Z., Teng, J.G., Ye, L.P., Jiang, J.J. Bond-slip models for FRP sheets/plates bonded to concrete. *Engineering Structures Journal.* 2005. 27(1). Pp. 920–937. DOI: 10.1016/j.engstruct.2005.01.014
37. Chen, J.F., Teng, J.G. Shear capacity of FRP strengthened RC beams: FRP debonding. *Construction and Building Materials.* 2003b. 17(1). Pp. 27–41. DOI: 10.1016/S0950-0618(02)00091-0
38. Chen, G.M., Teng, J.G., Chen, J.F. Shear strength model for FRP-strengthened RC beams with adverse FRP-steel interaction. *Journal of Composites for Construction, ASCE.* 2013. 17(1). Pp. 50–66. DOI: 10.1061/(ASCE)CC.1943-5614.0000313
39. ACI Committee 440. Design and Construction of Externally Bonded FRP Systems for strengthening Concrete Structures. *ACI440.2R-02. 2002. American Concrete Institute, Farmington Hills, Mich.: 45 pp. DOI: 10.1061/40753(171)159

Contacts:

Rajai Al-Rousan, rzalrousan@just.edu.jo



DOI: 10.18720/MCE.98.11

The mechanical properties of the expandable polyurethane resin based on its volumetric expansion nature

M.M. Sabri^a, K.G. Shashkin^b

^a *Peter the Great St. Petersburg Polytechnic University, St. Petersburg, Russia*

^b *PI "Georeconstruction", St. Petersburg, Russia*

* *E-mail: mohanad.m.sabri@gmail.com*

Keywords: soil injection technology, expandable polyurethane resin, mechanical properties, soil compaction, foundation lifting, foundation settlement, resin expansion nature

Abstract. The expandable polyurethane resin is an innovative material used in the field of soil stabilization and foundation restoration. The injection technology using the expandable polyurethane resin is an effective way that raises the foundations rapidly, strengthening the soil beneath. Nevertheless, different technical aspects have not been studied yet, which might affect the lifting and stabilization process, such as the density of the resin formed in the massive of the injected soils. The density of the resin formed in the massive of the injected soils during the injection process is varied due to the expansion nature of the resin when mixed proportionally controlled by the amount of the injected resin, the injection pressure, the injection temperature, and other factors. Obviously, the differences in resin densities lead to a variation of the resin mechanical properties; consequently, it affects the desired lifting and strengthening results gained. The article demonstrates the results of a laboratory experiment that has been conducted to investigate the mechanical properties of an expandable polyurethane resin consists of two components based on its volumetric expansion ratios controlled by the amount of the injectable resin. The density of the resin gained for each expansion ratio has been obtained and given in this article. The stress-strain diagrams of the resin for various densities and expanding ratios are incorporated. The results were interpreted, and the strength-density relationship of the resin has been established and introduced.

1. Introduction

The expandable polyurethane resin is an expansive material consists of two-liquid components which can be injected into the soil massive using a hydraulic system. Component A represents a polyol, while component B is mainly isocyanates. However, each component contains additives in its composition according to the manufacturers of the material [1–10]. When the resin is injected into the soil massive under high pressure, it expands and propagates in the hydrofracturing mode, leading to compact the surrounding soil, altering its properties. Thus, it leads to strengthening the injected soil, increasing its bearing capacity, besides the rapid lifting of the foundations gained through the propagation and expansion process of the resin [1–3, 11, 12].

The main uses of the expandable polyurethane resin are foundation lifting and soil compaction. However, it is also used for extruding the undesired water from the soil cavities and as injectable barriers to control the groundwater level [1, 2, 15, 16, 3, 4, 6–8, 11, 13, 14].

This resin is capable of expanding up to 30 times its original volume in non-restricted volumes due to the chemical reaction of the mixing components. When the resin is injected into the soil massive, it forms in various densities based on its mixing amount when combined in volumetrically established proportions. Several factors affect the actual density formed in the injected soil's massive, such as the amount of the injected resin, the injection pressure, the injection temperature, and the type of the injected soil itself. The exothermic reaction between its components produces the expansion process of the resin [1, 17, 18].

During the injection process, the volumetric expansion of its mixture occurs due to the chemical reaction between the resin's components, which produces a large amount of carbon dioxide, leading to form a porous structure. The water is required to fulfill the production of carbon dioxide as it reacts with the isocyanates

Sabri, M.M., Shashkin, K.G. The mechanical properties of the expandable polyurethane resin based on its volumetric expansion nature. Magazine of Civil Engineering. 2020. 98(6). Article No. 9811. DOI: 10.18720/MCE.98.11



This work is licensed under a CC BY-NC 4.0

group. In the absence of water, a chemically inert swelling agent with a low boiling point is used, which is a vaporized consuming part of the polymerization heat [1–3, 10, 19–21].

The resin mixture changes from a liquid to the solid-state and hardens in the soil massive within several seconds. The reaction time, which depends on the amount of the injected resin and the catalysts used, is influenced by the mixing temperature of the components and the controlled injection pressure in the hydraulic system. In practice, controlling the mixing temperature, lead to speed up or slow down the reaction time, while, the injection pressure lead to ease the flow of the material in the soil massive [1–3].

The low viscosity and liquidity of the resin ensure easy penetration into any soil type, when hardened, compact the surrounded soils, and displacing water without a negative impact on the structure and the stability of the injected resin properties [1–3].

2. Methods and Materials

2.1. The aim of the experiment

A laboratory experiment was conducted to investigate the strength-density relationship of an expandable polyurethane resin consists of two components for various densities, formed based on its volumetric expansion nature controlled by the amount of the injectable resin. Resin samples of different densities have been prepared based on the injected weight of the resin, considering its volumetric expansion, determined the density, and the stress-strain state of the resin using the uniaxial compression test. Thereby the relationship between the strength characteristics and the density of the resin formed according to prespecified volumetric expansion ratios was established. The investigated resin in the experiment is called (MC-Montan Injekt LE) produced by the company MC-Baucheime.

2.2. Samples preparation

Seven PVC cylindrical tubes with a special valve were used to model the resin samples of various densities in the laboratory environment. The valves were pre-welded to each tube to prevent the resin's overflowing during the injection process, as shown in Fig. 1. The volumes of the tubes used are constant, as given in Table 1.

Table 1. The dimensions of the tubes used.

Tube length	900 mm
Inner tube diameter	42 mm
Tube volume	1246898.124 mm ³



Figure 1. The injection process during the laboratory investigations.

The resin was injected into each tube using a particular injection pistol according to the mixing ratio (2:1) of both A and B components, respectively. Extraneous external pressure was not used to ensure resin supply to the tubes. That is, the injection process was carried out through the pressure arising as a result of a chemical reaction during the expansion of the composite components, which is a natural property of the material used.

The resin was introduced into each tube according to a sequential decrease in the weight of its components, which led to forming different densities samples by occupying the full fixed volume of the tube, due to volume expansion of the substances.

After the formation of the resin in the tubes, the resin remained in the tubes to fulfill the hardening process, allowing the resin to gain its maximum mechanical properties. Further, each tube was cut to five cylindrical samples of approximate fixed sizes (Diameter = 4.25 cm, Length = 10 cm).

The prespecified resin expansion ratios and the mixing weights of its components are given in Table 2.

Table 2. The resin expansion ratios and the mixing weights of its components used.

The expansion ratios of the resin	Number of samples tested	The total amount of resin used, Gramm	Amount of component A, Gramm	Amount of component B, Gramm	Reaction time, Seconds
3	5	416	277	139	4
4	5	312	208	104	4
6	5	208	139	69	5
8	5	156	104	52	6
10	5	125	83	42	8
12.5	3	100	67	33	12
15	5	84	56	28	29

The reaction time of the injected resin increases in direct proportion to the weight of the components used; however, this relationship is nonlinear, as shown in Fig. 2. The volumetric expansion of the injected resin decreases in direct proportion to its weight; however, this dependence is also non-linear, as shown in Fig. 3.

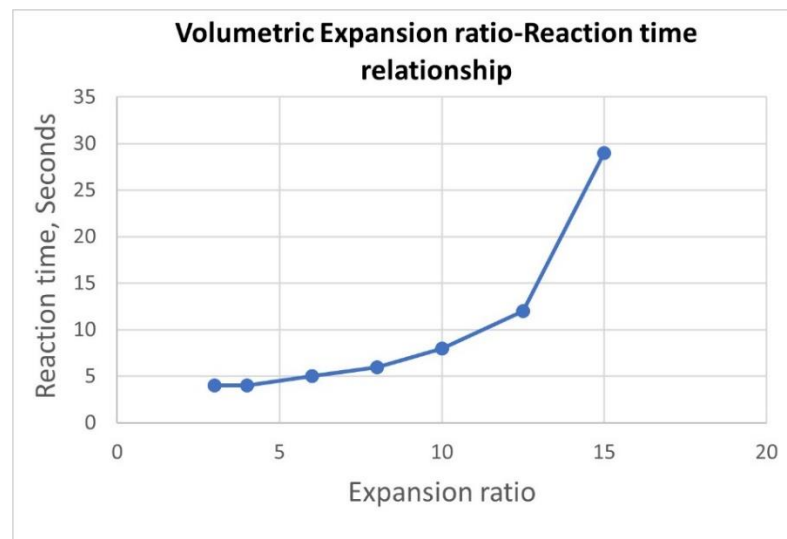


Figure 2. The relationship between the chemical reaction time and the volumetric expansion ratio.

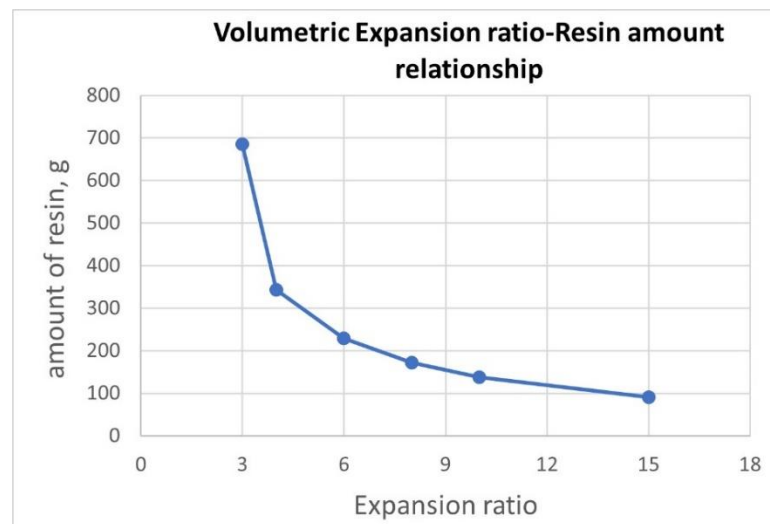


Figure 3. The relationship between the resin's amount used and its expansion ratio.

2.3. Determination of the resin densities

The density of the resin in the liquid state is equal to 1.1 g/cm³. However, the density of the resin changes due to its expansion properties, and the amount of the injected resin plays a significant role in its resulting density. For a constant volume, the injection of a different amount of resin leads to the formation of different densities compared to its initial density in the liquid state.

After the preparation, the obtained samples were divided into seven groups according to the values of their density obtained by their prespecified volumetric expansion ratios, as shown in Fig. 4.



Figure 4. The prepared resin's samples of different densities.

The actual density of each obtained sample was determined according to the following formula:

$$\rho = m / V$$

where ρ is the density of the sample, m is the measured weight of the sample, V is the sample's volume.

In this manner, the average density was calculated for each expansion ratio, as shown in the Table 3. The weight measurement process of each sample is shown in Fig. 5.

Table 3. The values of the average density of the resin and expansion coefficients obtained.

The resin's expansion ratios	The actual resin's density obtained, g/cm ³
3	0.349
4	0.255
6	0.184
8	0.128
10	0.088
12.5	0.066
15	0.056



Figure 5. The weight measurement process of each obtained sample.

2.4. Samples testing using the uniaxial compression test

At this step, samples were tested using the uniaxial compression test under a laboratory environment, as shown in Fig. 6, to determine the mechanical properties of the resin for each obtained density. The test has been conducted at x % deformation (yield strain %).



Figure 6. Some of the resin samples during the uniaxial compression tests. (a) The sample during the compression test; (b) The sample at the end of the compression process; (c) The sample after the release of the uniaxial forces

It was observed that the resin has fully returned to its initial state after the release of the uniaxial force.

According to [22–26], The expandable polyurethane resins have three stages of stress-strain response when subjected to the unconfined compression test. The first stage is the so-called initial linear elastic phase leading to the yield strength followed by a post-yield protracted plateau of either (elastic or plastic) based on the type of the solid foam and a final sharp rise, which called densification.

Moreover, Gibson [26] has revealed that there are three different kinds of the stress-strain curve of solid foam under compressive loading: elastomeric foam, elastic-plastic foam, and elastic-brittle foam as shown in Fig. 7. Polyurethane foams have an elongated stress-strain plateau after yield, making them different from the standard behavior of solid materials, which generally do not.

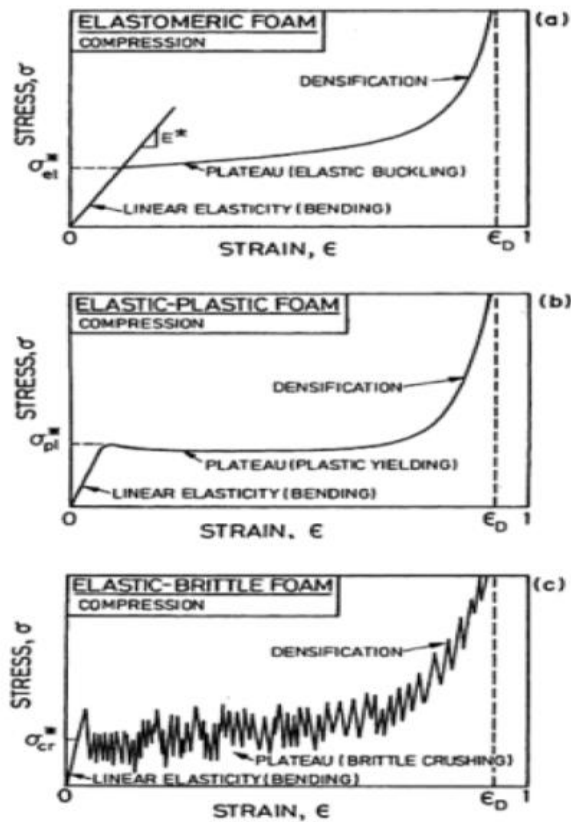


Figure 7. The patterns of the stress-strain state of polyurethane foams under compression loading, according to Gibson [26].

Furthermore, the failure point differs at which noticed in standard deformed solid materials. At the densification part of the polyurethane foams, the cellular structure "cells" of the foam are subjected to so-called "localization deformation" due to the nature of the material [22–26].

3. Results and Discussion

The stress-strain state of the investigated resin, according to its expansion ratios are obtained, as shown in Fig. 8–13.

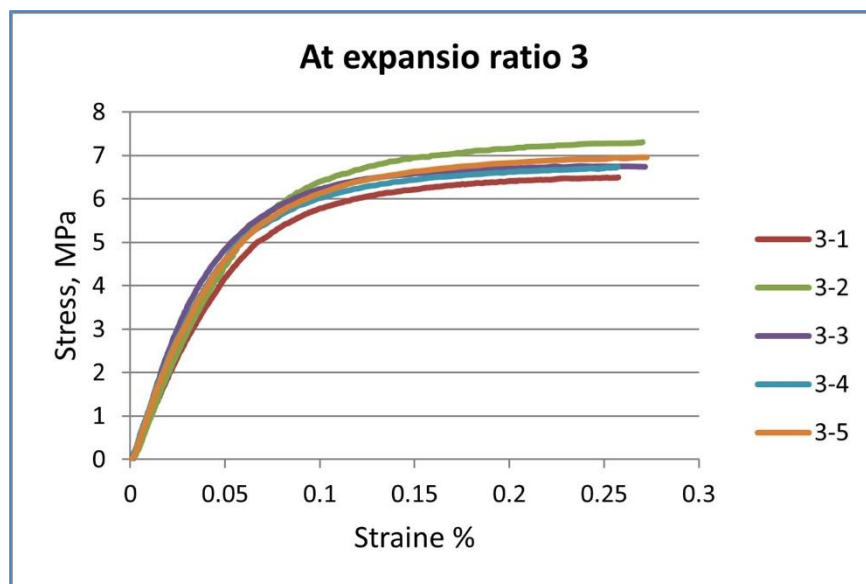


Figure 8. The stress-strain state of the resin at volumetric expansion ratio 3.

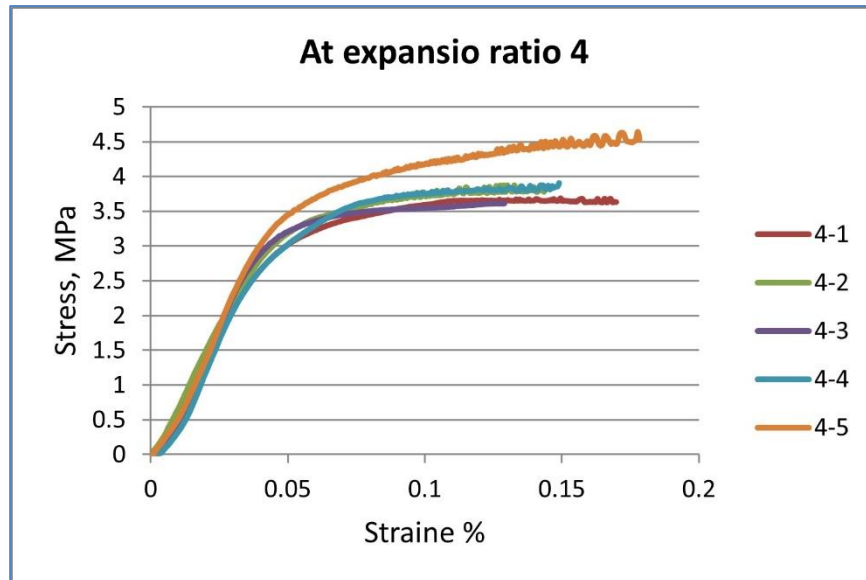


Figure 9. The stress-strain state of the resin at volumetric expansion ratio 4.

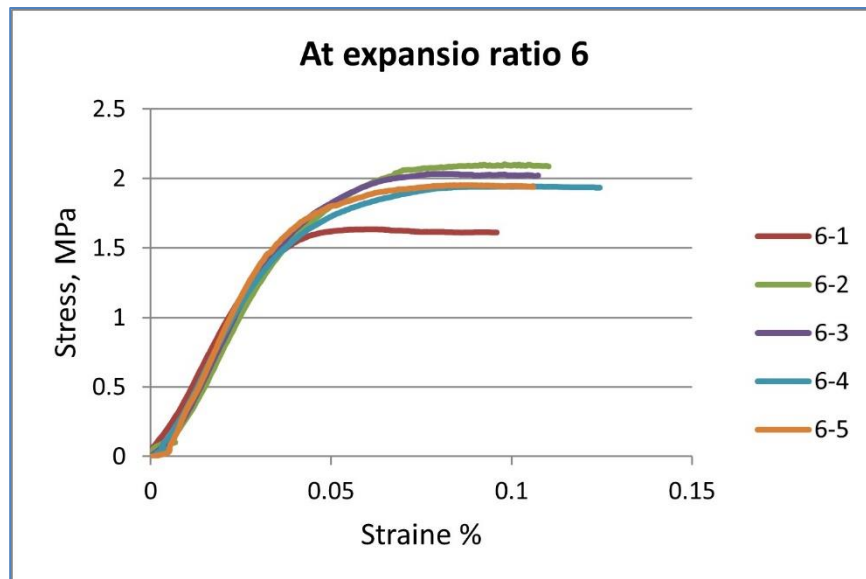


Figure 10. The stress-strain state of the resin at volumetric expansion ratio 6.

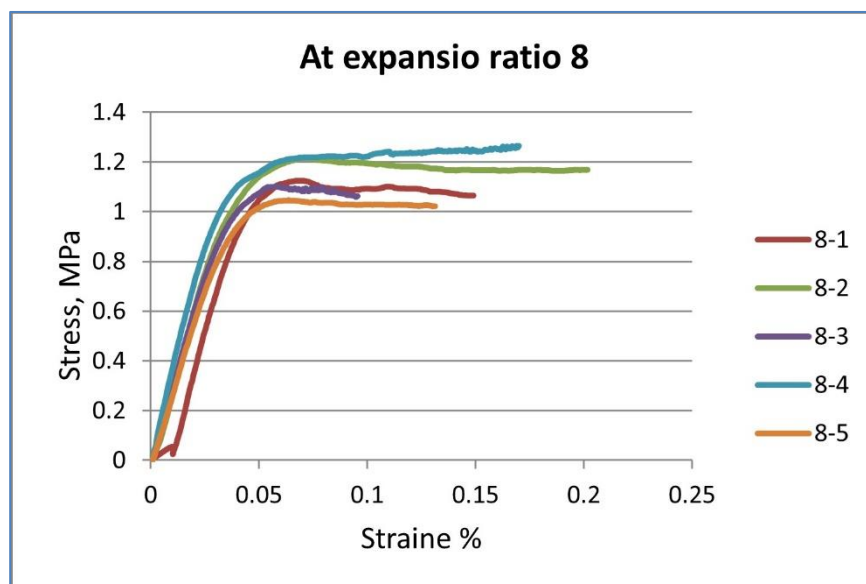


Figure 11. The stress-strain state of the resin at volumetric expansion ratio 8.

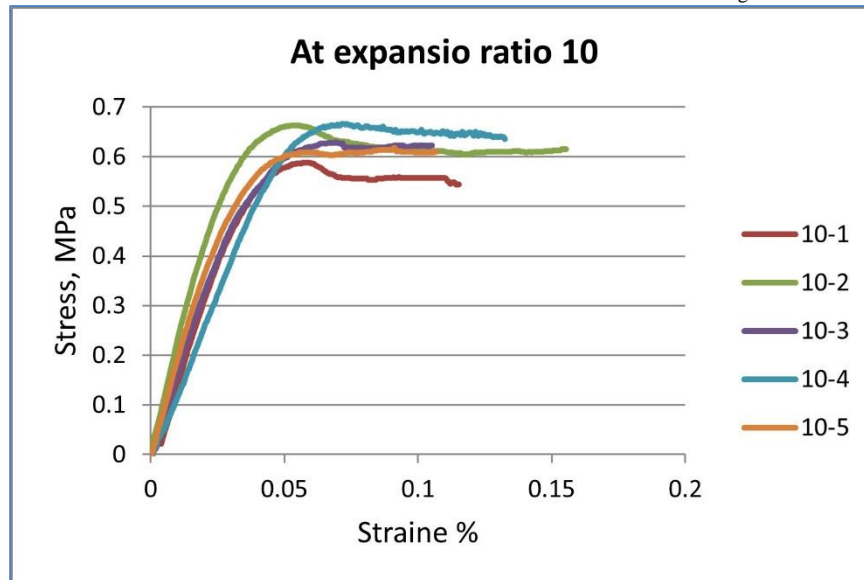


Figure 12. The stress-strain state of the resin at volumetric expansion ratio 10.

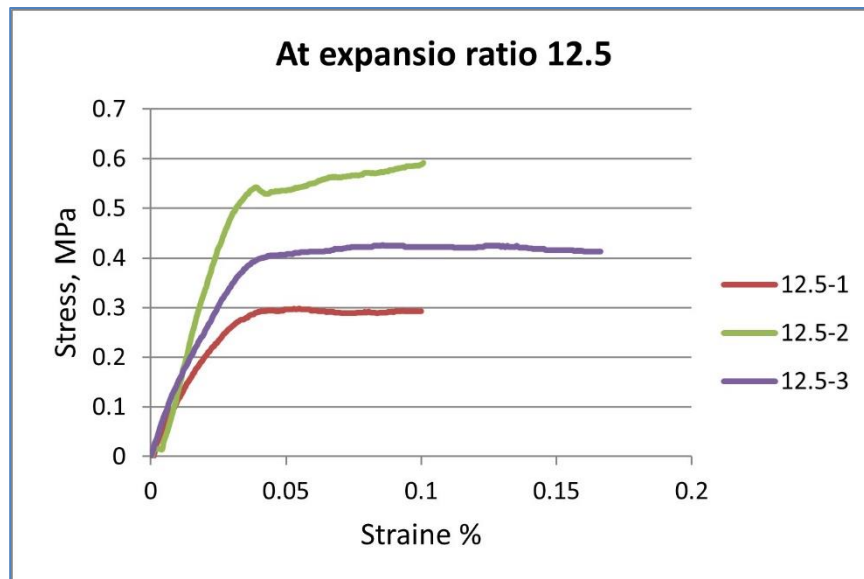


Figure 13. The stress-strain state of the resin at volumetric expansion ratio 12.5.

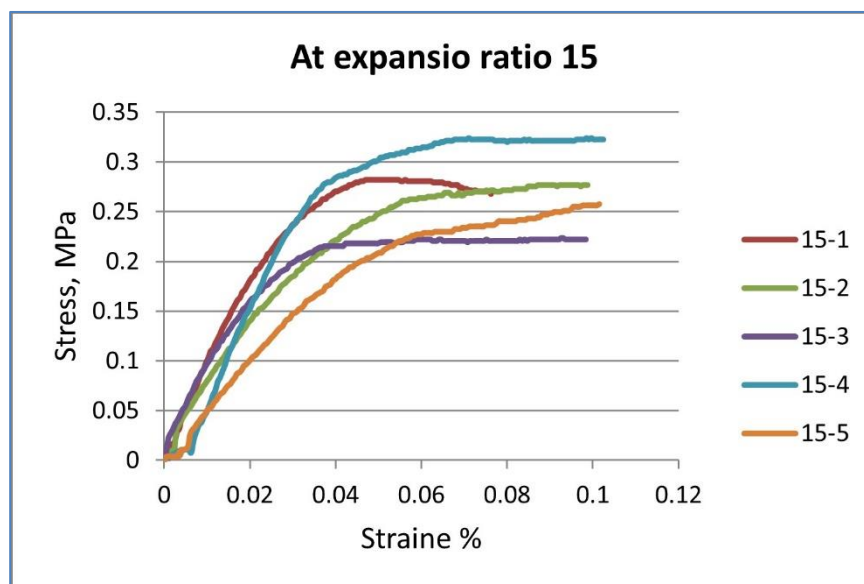


Figure 14. The stress-strain state of the resin at volumetric expansion ratio 15.

From the above, the obtained laboratory results are consistent with stress-strain state patterns categorized by Gibson [26], as shown in Fig. 7-a. Thus, the stress-strain state of the investigated resin seems to behave likely as an elastomeric foam under compression. This behavior of the material justifies the reverse of the expandable resin to its initial state after the release of the uniaxial compressive forces, as observed during the unconfined compression test of the investigated samples. The deformation of the samples (the buckling) shown in the Fig. 6-b is similar to the buckling elastic and not a shear failure. It occurs due to the nature of the closed-cell structure of PU foam under compression (filled by air, which is compressed and reverses to its original state unless reaching the densification).

Focusing on Fig. 8–14, the yield strain % of the investigated samples mostly ranged between 4–4.5 % based on the density of the samples tested except for the expansion ratio (3) where the yield strain % elongated up to approximately 6 %.

The resin under compression behaved linearly until reaching its yield strength, followed by the protracted plateau where the deformation (elastic buckling) occurred. The compression process in this investigation is limited to the linear part reaching the yield strength and the plateau part of the stress-strain state.

The elastic modulus has been calculated at a strain, which equals 50 % of the yield strain % of each sample using the following formula:

$$E = \frac{\sigma}{\varepsilon}$$

where: E is the elastic modulus; σ is the stress at the yield strain%; ε is the yield strain%.

A verification process of Young's modulus prediction values has been carried out through computing the regression between two points at the linear part of the stress-strain state. Further, according to [24, 26], the slope of the stress-strain curve in the elastic phase characterizes Young's modulus of the polyurethane foam. The three ways used for predicting the elastic modulus have mostly shown similar results.

The results were interpreted, determining the yield compressive strength, ultimate compressive strengths, and the modulus of elasticity of the resin according to its predetermined densities. The average yield, ultimate compressive strength, and the modulus of elasticity of the investigated resin for each obtained density are shown in Table 4.

Table 4. The average ultimate compressive strength and the elastic modulus of investigated resin under compression for each density obtained.

The resin's expansion ratios	The actual resin's density obtained, g/cm ³	The yield compressive strength, MPa	The ultimate compressive strength, MPa	The modulus of elasticity, MPa
3	0.349	5.145	6.756	104
4	0.255	2.886	3.943	73
6	0.184	1.597	1.933	44
8	0.128	1.020	1.150	30
10	0.088	0.558	0.636	18
12.5	0.066	0.407	0.447	14
15	0.056	0.236	0.275	9

The relationships between the density and the compressive strength of the resin, in addition to the relationship between the density and the modulus of elasticity under compression, are established and shown in Fig. 15, 16.

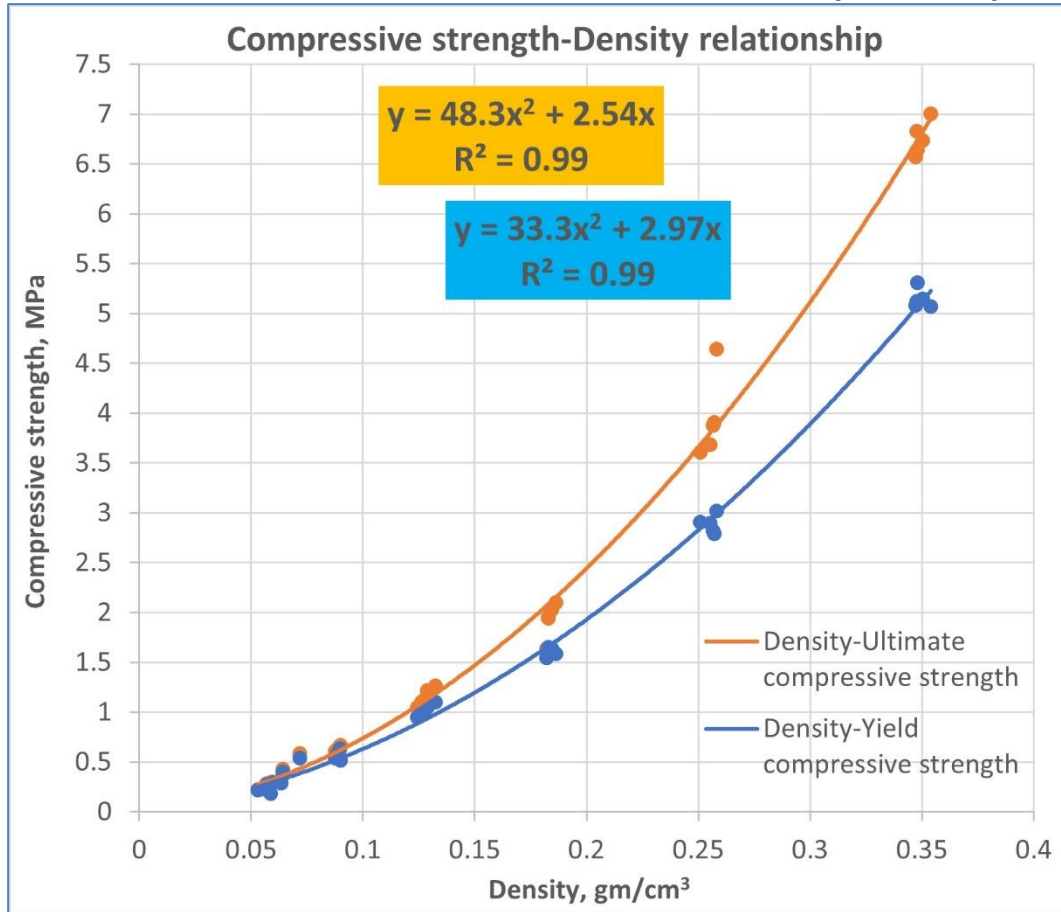


Figure 15. The relationship between the resin's density and its compressive strength obtained under compression.

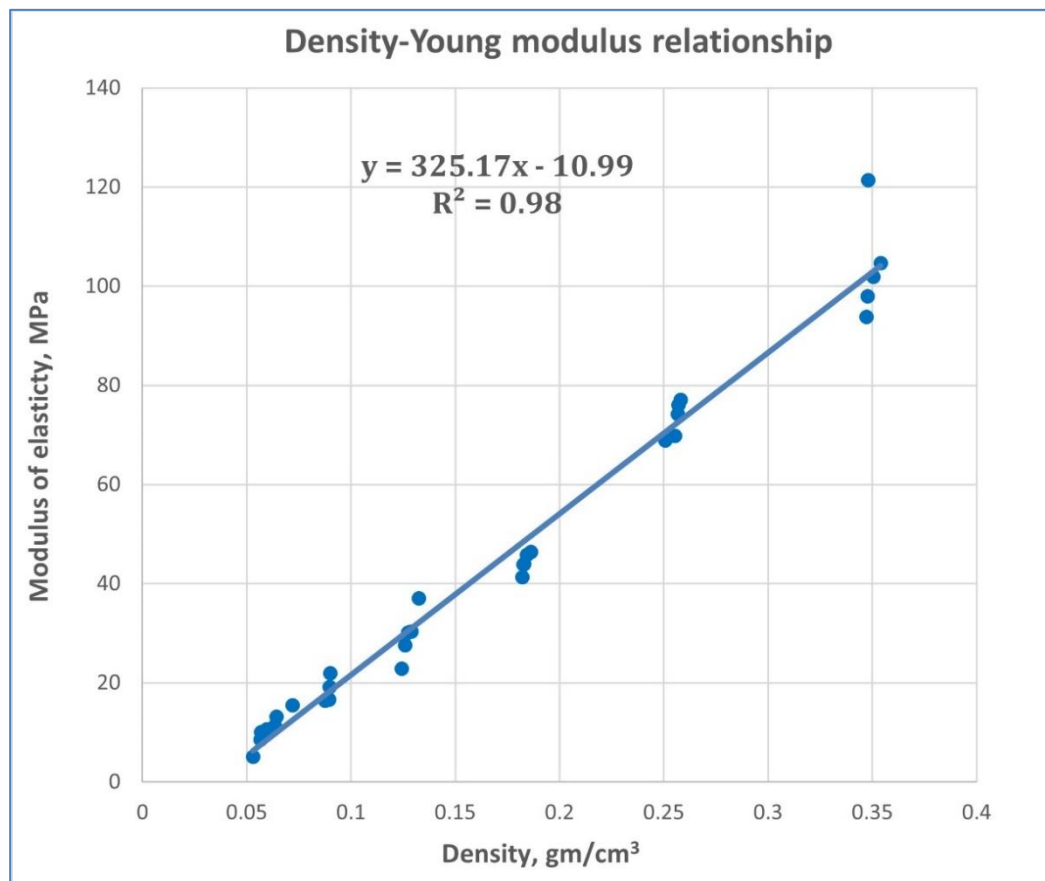


Figure 16. The relationship between the resin's density and its elastic modulus obtained under compression.

The obtained results prove that the investigated resin can be formed in various densities according to the amount of the injected resin, allowing a high spectrum of the mechanical properties in the soil massive ($E = 5\text{--}121$ MPa, ultimate compressive strength = $0.2\text{--}7$ MPa), respectively, at prespecified expansion ratios ranges (3–15 times). Consequently, this resin is considered a high strength elastic injected material compared to various injection materials used in the field of soil stabilization, taking into account the rapid lifting and strengthening processes, and the full control over desired results. Also, the high fluidity allows the resin to propagate in different types of soils according to their specifications.

Furthermore, the actual propagation of the resin and its density formed in the massive of the injected soils (in a homogeneous injection environment) depends mainly on the amount of the injected resin and the properties of the injected soil.

The obtained relationships play an essential role in the theoretical and practical applications of the injection process when applying the injection technology using an expandable polyurethane resin for the soil strengthening and foundation lifting process.

4. Conclusion

1. The mechanical properties of the expandable polyurethane resin of various densities based on its volumetric expansion have been obtained, determined its strength-density and young modulus-density relationships under compression within density ranges ($0.053\text{--}0.354$ gm/cm³) and volumetric expansion ratios (3-15) respectively, controlled by the amount of injectable resin. These relationships allow the prediction of the mechanical properties and the expansion volume of the injected resin through its density formed in the soil massive.

2. The obtained relationships prove the dependency of the resin's mechanical characteristics on its density based on its expansion nature controlled by its injected amount in a homogeneous injection environment. However, the actual density of the expandable resin formed in the massive of the injected soils is affected by other factors such as the injection pressure, the injection temperature, and the specification of the injected soil itself.

3. The high spectrum of the mechanical properties of the investigated resin, which depends on its expansion nature controlled volumetrically by its injected amount, leads to high control over the lifting process and gain the desired soil strengthening results, especially that the injection process is carried out in "shots" using the injection pistol.

5. Acknowledgment

The author would like to show his gratitude to the company MC-Bauchemie for providing the resin used for the experiment.

References

1. Sabri, M.M., Shashkin, K.G. Improvement of the soil deformation modulus using an expandable polyurethane resin. *Magazine of Civil Engineering*. 2018. 83(7). Pp. 222–234. DOI: 10.18720/MCE.83.20
2. Sabri, M.M., Shashkin, K.G., Zakharin, E., U.A.V. Soil stabilization and foundation restoration using an expandable polyurethane resin. *Magazine of Civil Engineering*. 2018. 82(6). Pp. 68–80. DOI: 10.18720/MCE.82.7
3. Sabri, M., Bugrov, A., Panov, S., D.V. Ground improvement using an expandable polyurethane resin. *MATEC Web of Conferences*. 2018. 245. Pp. 1–4. DOI: 10.1051/mateconf/201824501004
4. Buzzi, O., Fityus, S., Sloan, S.W. Use of expanding polyurethane resin to remediate expansive soil foundations. *Canadian Geotechnical Journal*. 2010. 47(6). Pp. 623–634. DOI: 10.1139/T09-132. URL: <http://www.nrcresearchpress.com/doi/10.1139/T09-132>
5. Nowamooz, H. Resin injection in clays with high plasticity. *Comptes Rendus – Mecanique*. 2016. 344(11–12). Pp. 797–806. DOI: 10.1016/j.crme.2016.09.001. URL: <http://dx.doi.org/10.1016/j.crme.2016.09.001>
6. Dalinchuk, V.S., Ilmenderov, M.S., Yarkin, V.V. Ustraneniye prosadki fundamentov s pomoshchyu tekhnologii SLAB LIFTING. *Stroitelstvo unikalnykh zdaniy i sooruzheniy*. 2015. 11(38). Pp. 15–26.
7. Rayevskiy, V.V. Rekonstruktsiya i remont vzletno – posadochnykh polos (VPP) i rulezhnykh dorozhek s primeneniye dvukhkomponentnoy penopoliuretanovoy smoly. *Perevod kapitalnogo remonta VPP v tekushchiy remont. Stroitelstvo unikalnykh zdaniy i sooruzheniy*. 2014. 11(26). Pp. 18–32.
8. Buzzi, O., Fityus, S., Sasaki, Y., Sloan, S. Structure and properties of expanding polyurethane foam in the context of foundation remediation in expansive soil. *Mechanics of Materials*. 2008. 40(12). Pp. 1012–1021. DOI: 10.1016/j.mechmat.2008.07.002
9. Valentino, R., Stevanoni, D. Micropiles made of reinforced polyurethane resins: Load tests and evaluation of the bearing capacity. *Electronic Journal of Geotechnical Engineering*. 2010. 15 J(November). Pp. 895–912.
10. Escolano Sánchez, F., Mazariegos de la Serna, A., Sánchez Lavín, J.R., Campo Yagüe, J.M. del, Sánchez, F.E., de la Serna, A.M., Lavín, J.R.S., Yagüe, J.M. del C. Underpinning of shallow foundations by expansive polyurethane resin injections. Case study: Cardinal Diego de Espinosa Palace in Segovia (Spain). *Revista de la construcción*. 2017. 16(3). Pp. 420–430. DOI: 10.7764/RD-LC.16.3.420. URL: <http://revistadelaconstruccion.uc.cl/index.php/rdlc/article/view/1039>
11. Popik, M., Trout, M., Brown, R.W. Improving soil stiffness beneath pavements using polyurethane injection. *TAC/ATC 2010 – 2010 Annual Conference and Exhibition of the Transportation Association of Canada: Adjusting to New Realities*. 2010. (610 mm).

12. CheLat, D., Ismacahyadi B., Mohamed J., Roslizayati, R., Tawaf, M.K. Performance Comparison between Polyurethane Injection Pile and Slab System against Lightweight Concrete as a Ground Improvement Using Finite Element Analysis. *Journal of Applied Science Research*. 2015. 11(20). Pp. 11–16.
13. Golpazir, I., Ghalandarzadeh, A., Jafari, Mohammad K., Mahdavi, M. Dynamic properties of polyurethane foam-sand mixtures using cyclic triaxial tests. *Construction and Building Materials*. 2016. 118. Pp. 104–115. DOI: 10.1016/j.conbuildmat.2016.05.035. URL: <http://dx.doi.org/10.1016/j.conbuildmat.2016.05.035>
14. Sidek N., Mohamed, K., Jais, I.B.M., Abu Bakar, I.A. Strength Characteristics Of Polyurethane (PU) With Modified Sand. *Applied Mechanics and Materials*. 2015. 773–774 (September). Pp. 1508–1512. DOI: 10.4028/www.scientific.net/amm.773-774.1508. URL: <http://www.scientific.net/AMM.773-774.1508>
15. Hellmeier, P., Soranzo, E., Wu, W., Niederbrucker, R., Paschetto, A. an Experimental Investigation Into the Performance of a Domestic Thermosyphon. 2011 Pan-Am CGS, Geotechnical conference. 2011.
16. Hess, J. Master of Science thesis: In-Situ Testing of Uretek ' s Injectable Barrier SM as a Mechanism for Groundwater Control by. University of South Florida, 2016.
17. Sidek, N., Bakar, I.A.A., Azman, A.A., Rahman, A.S.A., Austin, W.A. Strength characteristic of polyurethane with variation of polyol to isocyanate mix ratio : A numerical analysis. *Proceedings - 2017 IEEE 2nd International Conference on Automatic Control and Intelligent Systems, I2CACIS 2017*. 2017. 2017-Decem(January 2018). Pp. 31–34. DOI: 10.1109/I2CACIS.2017.8239028
18. Sai Tejaswi, L., Aswathi, T.S., Poongothai, A. Rectification of settled foundations. *Proceedings of 6th IRF International Conference, Chennai, India*. 2014. Pp. 68–72.
19. Escolano Sánchez, F., Mazariegos de la Serna, A., Sánchez Lavín, J.R., Campo Yagüe, J.M. del. Underpinning of shallow foundations by expansive polyurethane resin injections. Case study: Cardinal Diego de Espinosa Palace in Segovia (Spain). *Revista de la construcción*. 2017. 16(3). Pp. 420–430. DOI: 10.7764/RDLC.16.3.420. URL: <http://revistadelaconstruccion.uc.cl/index.php/rdlc/article/view/1039>
20. Yenco, A. Master of Science thesis: Decision Tree For Ground Improvement In Transportation Applications. University of Akron, 2013.
21. Apuani, T., Giani, G.P., D'Attoli, M., Fischanger, F., Morelli, G., Ranieri, G., Santarato, G. Assessment of the Efficiency of Consolidation Treatment through Injections of Expanding Resins by Geotechnical Tests and 3D Electrical Resistivity Tomography. *Scientific World Journal*. 2015. 2015. DOI: 10.1155/2015/237930
22. Wiyono, P., Faimun, Suprobo, P., Kristijanto, H. Characterization of physical and mechanical properties of rigid polyurethane foam. *ARNP Journal of Engineering and Applied Sciences*. 2016. 11(24). Pp. 14398–14405.
23. Qiu, D., He, Y., Yu, Z. Investigation on compression mechanical properties of rigid polyurethane foam treated under random vibration condition: An experimental and numerical simulation study. *Materials*. 2019. 12(20). DOI: 10.3390/ma12203385
24. Mane, J.V., Chandra, S., Sharma, S., Ali, H., Chavan, V.M., Manjunath, B.S., Patel, R.J. Mechanical Property Evaluation of Polyurethane Foam under Quasi-static and Dynamic Strain Rates- An Experimental Study. *Procedia Engineering*. 2017. 173. Pp. 726–731. DOI: 10.1016/j.proeng.2016.12.160. URL: <http://dx.doi.org/10.1016/j.proeng.2016.12.160>
25. Tu, Z.H., Shim, V.P.W., Lim, C.T. Plastic deformation modes in rigid polyurethane foam under static loading. *International Journal of Solids and Structures*. 2001. 38(50–51). Pp. 9267–9279. DOI: 10.1016/S0020-7683(01)00213-X
26. Gibson, L.J., Ashby, M.F. *Cellular solids – Structure Properties*. Cambridge University Press. Cambridge., 1997.

Contacts:

Mohanad Muayad Sabri, mohanad.m.sabri@gmail.com

Konstantin Shashkin, cshashkin@yandex.ru



DOI: 10.18720/MCE.98.12

Improved gradient projection method for parametric optimisation of bar structures

V.V. Yurchenko^a, I.D. Peleshko^b

^a Kyiv National University of Construction and Architecture, Kyiv, Ukraine

^b Lviv Polytechnic National University, Lviv, Ukraine

* E-mail: vitalinay@rambler.ru

Keywords: parametric optimization, bar structures, nonlinear programming, gradient projection method, finite element analysis

Abstract. Numerical optimization and the finite element method have been developed together to make possible the emergence of structural optimization as a potential design tool. The main research goal of this paper is the development of mathematical support and a numerical algorithm to solve parametric optimization problems of structures with orientation on software implementation in a computer-aided design system. The paper considers parametric optimization problems for bar structures formulated as nonlinear programming ones. The method of the objective function gradient projection onto the active constraints surface with simultaneous correction of the constraints violations has been used to solve the parametric optimization problem. Equivalent Householder transformations of the resolving equations of the method have been proposed. They increase numerical efficiency of the algorithm developed based on the considered method. Additionally, proposed improvement for the gradient projection method also consists of equivalent Givens transformations of the resolving equations. They ensure acceleration of the iterative searching process in the specified cases described by the paper due to decreasing the amount of calculations. The comparison of the optimization results of truss structures presented by the paper confirms the validity of the optimum solutions obtained using proposed improvement of the gradient projection method. The efficiency of the proposed improvement of the gradient projection method has been also confirmed taking into account the number of iterations and absolute value of the maximum violation in the constraints.

1. Introduction

Over the past 50 years, numerical optimization and the finite element method have individually made significant advances and have together been developed to make possible the emergence of structural optimization as a potential design tool [1]. In recent years, great efforts have been also devoted to integrate optimization procedures into the CAD facilities. With these new developments, lots of computer packages are now able to solve relatively complicated industrial design problems using different structural optimization techniques [2].

Applied optimum design problems for bar structures in some cases are formulated as parametric optimization problems, namely as searching problems for unknown structural parameters, which provide an extreme value of the specified objective function in the feasible region defined by the specified constraints. In this case, structural optimization is performed by variation of the structural parameters when the structural topology, cross-section types and node type connections of the bars, the support conditions of the bar system, as well as loading patterns and load design values are prescribed and constants.

Kibkalo et al. in the paper [3] formulated a parametric optimization problem for thin-walled bar structures and considered methods to solve them. The searching for the optimum solution has been performed by varying the structural parameters providing the required load-carrying capacity of structural members and the minimum value of manufacturing costs.

Alekseytsev has described the process of developing a parametrical-optimization algorithm for steel trusses in the paper [4]. Parametric optimization has been performed taking into account strength, stability and stiffness constraints formulated for all truss members. The objective function has been formulated depending

Yurchenko, V.V., Peleshko, I.D. Improved gradient projection method for parametric optimisation of bar structures. Magazine of Civil Engineering. 2020. 98(6). Article No. 9812. DOI: 10.18720/MCE.98.12



This work is licensed under a CC BY-NC 4.0

on the specific manufacturing of the truss panel joints in term of the manufacturing cost calculated based on the labor costs and materials used.

Serpik et al. in the paper [5] developed an algorithm for parametric optimization of steel flat rod systems. The optimization problem has been formulated as a structural weight minimization problem taking into account strength and displacement constraints, as well as overall stability constraints. The cross-sectional dimensions of the truss members and the coordinates of the truss panel joints have been considered as design variables. The structural analysis of internal forces and displacements for considered structures has been performed using the finite element method. An iterative procedure for searching for optimum solution has been proposed in [6].

Sergeyev et al. in the paper [7] formulated a parametric optimization problem with constraints on faultless operation probability of bar structures with random defects. The weight of the bar structures has been considered as the objective function. Initial global imperfections have been considered as small independent random variables distributed according to normal distribution law, as well as buckling load value has been also considered as a random variable.

The mathematical model of the parametric optimization problem of structures includes a set of design variables, an objective function, as well as constraints, which reflect generally non-linear dependences between them [8]. If the objective function and constraints of the mathematical model are continuously differentiable functions, as well as the search space is smooth, then the parametric optimization problems are successfully solved using gradient projection non-linear methods [9]. The gradient projection methods operate with the first derivatives or gradients only both of the objective function and constraints. The methods are based on the iterative construction of such a sequence of the approximations of design variables that provides convergence to the optimum solution (optimum values of the structural parameters) [10].

Additionally, a sensitivity analysis is a useful optional feature that could be used in scope of the numerical algorithms developed based on the gradients methods [11]. Thus, in the paper [12] Sergeyev et al. formulated a parametric optimization problem of linearly elastic space frame structures taking into account the stress and multiple natural frequency constraints. The cross-sectional parameters of structural members as well as node positions of the bar structures has been considered as design variables. The sensitivity analysis of multiple frequencies has been performed using analytic differentiation with respect to the design variables. The optimal design of the structure has been obtained by solving a sequence of quadratic programming problems.

Although many papers are published on the parametric optimization of structures, the development of a general computer program for the design and optimization of structures according to specified design codes remains an actual task. Therefore, the main *research goal* of this paper is the development of mathematical support and a numerical algorithm to solve parametric optimization problems of structures with orientation on software implementation in a computer-aided design system.

One of the effective methods to solve parametric optimization problems for structures is gradient projection methods, as shown by the review of scientific researches presented above. That is why, in this paper, a gradient projection method is considered as *investigated object*. The following research tasks are formulated: to propose an improvement of the gradient projection method that ensures the increase of the numerical efficiency of the algorithm developed based on the considered method, as well as the acceleration of the iterative searching process due to decreasing the amount of calculations.

2. Methods

2.1. Parametric optimization problem formulation

Let us consider a parametric optimization problem of a structure consisting of bar members. It can be formulated as presented below: to find optimum values for geometrical parameters of the structure, bar's cross-section dimensions and initial pre-stressing forces introduced into the redundant members of the bar system, which provide the extreme value of the determined optimality criterion and satisfy all load-bearing capacities and stiffness requirements. We assume, that the structural topology, cross-section types and node type connections of the bars, the support conditions of the bar system, as well as loading patterns and load design values are prescribed and constants.

The formulated parametric optimization problem can be stated as a non-linear programming task in the following mathematical terms: to find unknown structural parameters $\vec{X} = \{X_i\}^T$, $i = \overline{1, N_X}$, providing the least value of the determined objective function:

$$f^* = f(\vec{X}^*) = \min_{\vec{X} \in \mathfrak{S}_{\mathbb{N}}} f(\vec{X}), \quad (1.1)$$

in a feasible region (search space) \mathfrak{S} defined by the following system of constraints:

$$\Psi(\vec{X}) = \left\{ \psi_{\kappa}(\vec{X}) = 0 \mid \kappa = \overline{1, N_{EC}} \right\}; \quad (1.2)$$

$$\Phi(\vec{X}) = \left\{ \phi_{\eta}(\vec{X}) \leq 0 \mid \eta = \overline{N_{EC} + 1, N_{IC}} \right\}; \quad (1.3)$$

where \vec{X} is the vector of the design variables (unknown structural parameters); f , ψ_{κ} , ϕ_{η} are the continuous functions of the vector argument; \vec{X}^* is the optimum solution or optimum point (the vector of optimum values of the structural parameters); f^* is the optimum value of the optimum criterion (objective function); N_{EC} is the number of constraints-equalities $\psi_{\kappa}(\vec{X})$, whose define hyperplanes of the feasible solutions; N_{IC} is the number of constraints-inequalities $\phi_{\eta}(\vec{X})$, whose define a feasible region in the design space \mathfrak{S} .

The vector of the design variables can consist of a set of unknown geometrical parameters of the structure, a set of unknown cross-sectional dimensions of the structural members, as well as a set of unknown initial pre-stressing forces introduced into the specified redundant members of the structure.

The specific technical-and-economic index (material weight, material cost, construction cost etc.) or another determined indicator can be considered as the objective function Eq. (1.1) taking into account the ability to formulate its analytical expression as a function of design variables \vec{X} .

Load-bearing capacities constraints (strength and stability inequalities) for all design sections of the structural members subjected to all design load combinations at the ultimate limit state as well as displacements constraints (stiffness inequalities) for the specified nodes of the bar system subjected to all design load combinations at the serviceability limit state should be included into the system of constraints Eqs. (1.2) – (1.3). The design internal forces in the bar structural members used in the strength and stability inequalities of the system Eqs. (1.2) – (1.3) are considered as state variables depending on design variables \vec{X} and can be calculated from the linear equations system of the finite element method [13]. The node displacement of the bar system used in stiffness inequalities of the system Eqs. (1.2) – (1.3) are also considered as state variables depending on design variables \vec{X} and can be also calculated from the linear equations system of the finite element method [13]. Additional requirements, whose describe structural, technological and serviceability particularities of the considered structure, as well as constraints on the building functional volume can be also included into the system Eqs. (1.2) – (1.3).

2.2. An improved gradient projection method for solving the parametric optimization problem

The parametric optimization problem stated as non-linear programming task by Eqs. (1.1) – (1.3) can be solved using a gradient projection method. The method of *objective function gradient projection onto the active constraints surface with simultaneous correction of the constraints violations* ensures effective searching for solution of the non-linear programming tasks occurred when optimum designing of the structures [14].

The gradient projection method operates with the first derivatives or gradients only of both the objective function Eq. (1.1) and constraints Eqs. (1.2) – (1.3). The method is based on the iterative construction of such sequence Eq. (2.1) of the approximations of design variables $\vec{X} = \{X_{\iota}\}^T$, $\iota = \overline{1, N_X}$, that provides the convergence to the optimum solution (optimum values of the structural parameters):

$$\vec{X}_{k+1} = \vec{X}_k + \Delta \vec{X}_k, \quad (2.1)$$

where $\vec{X}_k = \{X_{\iota}\}^T$, $\iota = \overline{1, N_X}$ is the current approximation to the optimum solution \vec{X}^* that satisfies both constraints-equalities Eq. (1.2) and constraints-inequalities Eq. (1.3) with the extreme value of the objective function Eq. (1.1); $\Delta \vec{X}_k = \{\Delta X_{\iota}\}^T$, $\iota = \overline{1, N_X}$, is the increment vector for the current values of the design variables \vec{X}_k ; k is the iteration's index. The start point of the iterative searching process $\vec{X}_{k=0}$ can be assigned as engineering estimation of the admissible design of the structure.

The active constraints only of constraints system Eqs. (1.2) – (1.3) should be considered at each iteration.

A set of active constraints numbers \mathbf{A} calculated for the current approximation \vec{X}_k to the optimum solution (current design of the structure) is determined as:

$$\mathbf{A} = \mathbf{\kappa} \cup \mathbf{\eta}, \quad \mathbf{\kappa} = \left\{ \kappa \mid \left| \psi_{\kappa}(\vec{X}_t) \right| \geq -\varepsilon \right\}, \quad \mathbf{\eta} = \left\{ N_{EC} + \eta \mid \phi_{\eta}(\vec{X}_t) \geq -\varepsilon \right\}. \quad (2.2)$$

where ε is a small positive number introduced here in order to diminish the oscillations on movement alongside of the active constraints surface.

The increment vector $\Delta\vec{X}_k$ for the current values of the design variables \vec{X}_k can be determined by the following equation:

$$\Delta\vec{X}_k = \Delta\vec{X}_{\perp}^k + \Delta\vec{X}_{\parallel}^k, \quad (2.3)$$

where $\Delta\vec{X}_{\perp}^k$ is the vector calculated subject to the condition of elimination the constraint's violations; $\Delta\vec{X}_{\parallel}^k$ is the vector determined taking into consideration the improvement of the objective function value. Vectors $\Delta\vec{X}_{\parallel}^k$ and $\Delta\vec{X}_{\perp}^k$ are directed parallel and perpendicularly accordingly to the subspace with the vectors basis of the linear-independent constraint's gradients, such that:

$$\left(\Delta\vec{X}_{\perp}^k \right)^T \Delta\vec{X}_{\parallel}^k = 0. \quad (2.4)$$

The values of the constraint's violations for the current approximation \vec{X}_k of the design variables are accumulated into the following vector:

$$\mathbf{V} = \left(\psi_{\kappa}(\vec{X}) \forall \kappa \in \mathbf{\kappa}; \phi_{\eta}(\vec{X}) \forall \eta \in \mathbf{\eta} \right).$$

Let us introduce a set \mathbf{L} , $\mathbf{L} \subseteq \mathbf{A}$, of the constraint's numbers, such that the gradients of the constraints at the current approximation \vec{X}_k to the optimum solution are linear-independent.

Component $\Delta\vec{X}_{\perp}^k$ is calculated from the equation presented below:

$$\Delta\vec{X}_{\perp}^k = [\nabla \varphi] \vec{\mu}_{\perp}. \quad (2.5)$$

where $[\nabla \varphi]$ is the matrix that consists of components $\frac{\partial \psi_{\kappa}}{\partial X_t}$ and $\frac{\partial \phi_{\eta}}{\partial X_t}$, here $t = \overline{1, N_X}$, $\kappa \in \mathbf{L}$, $\eta \in \mathbf{L}$;

$\vec{\mu}_{\perp}$ is the column-vector that defines the design variables increment subject to the condition of elimination the constraint's violations. Vector $\vec{\mu}_{\perp}$ can be calculated as presented below.

In order to correct constraint's violations \mathbf{V} , vector $\Delta\vec{X}_{\perp}^k$ to a first approximation should also satisfy Taylor's theorem for the continuously differentiable multivariable function in the vicinity of point \vec{X}_k for each constraint from set \mathbf{L} , namely:

$$-\mathbf{V} = [\nabla \varphi]^T \Delta\vec{X}_{\perp}^k. \quad (2.6)$$

With substitution of Eq. (2.5) into Eq. (2.6) we obtain the system of equations to determine column-vector $\vec{\mu}_{\perp}$:

$$[\nabla \varphi]^T [\nabla \varphi] \vec{\mu}_{\perp} = -\mathbf{V}. \quad (2.7)$$

Component $\Delta\vec{X}_{\parallel}^k$ is determined using the following equation:

$$\Delta\vec{X}_{\parallel}^k = \xi \times \vec{p} = \xi \left(\vec{\nabla} f - [\nabla \varphi] \vec{\mu}_{\parallel} \right), \quad (2.8)$$

where $\vec{\nabla} f$ is the vector of the objective function gradient in the current point (current approximation of the design variables) \vec{X}_k ; \vec{p} is the projection of the objective function gradient vector onto the active constraints surface in the current point \vec{X}_k ; $\vec{\mu}_{\parallel}$ is the column-vector that defines the design variable's increment subject

to the improvement of the objective function value. Column-vector $\vec{\mu}_{||}$ can be calculated approximately using the least-square method by the following equation:

$$[\nabla \varphi] \vec{\mu}_{||} \approx \nabla \vec{f}, \quad (2.9)$$

or from the equation presented below:

$$[\nabla \varphi]^T [\nabla \varphi] \vec{\mu}_{||} = [\nabla \varphi]^T \nabla \vec{f}; \quad (2.10)$$

where ξ is the step parameter, which can be calculated subject to the desired increment Δf of the objective function on movement along the direction of the objective function anti-gradient. The increment Δf can be assign as 5...25% from the current value of the objective function $f(\vec{X}_t)$:

$$\Delta f = \xi (\nabla \vec{f})^T \nabla \vec{f}, \quad \xi = \frac{\Delta f}{(\nabla \vec{f})^T \nabla \vec{f}}, \quad (2.11)$$

where in case of minimization Eq. (1.1) Δf and ξ accordingly have negative values. The parameter ξ can be also calculated using the dependency presented below:

$$\xi = \frac{\Delta f}{(\vec{p})^T \nabla \vec{f}}, \quad (2.12)$$

that follows from the condition of attainment the desired increment of the objective function Δf on the movement along the direction of the objective function anti-gradient projection onto the active constraints surface. Step parameter ξ can be also selected as a result of numerical experiments performed for each type of the structure individually [15, 16].

Fig. 2.1 presents a graphical illustration for step to the point \vec{X}_{k+1} depending on location of the current approximation \vec{X}_k in the two-dimension search space.

Using Eq. (2.5) and Eq. (2.8), Eq. (2.3) can be rewritten as presented below:

$$\Delta \vec{X}_k = [\nabla \varphi] \vec{\mu}_{\perp} + \xi (\nabla \vec{f} - [\nabla \varphi] \vec{\mu}_{||}), \quad (2.13)$$

or

$$\Delta \vec{X}_k = \xi \nabla \vec{f} + [\nabla \varphi] (\vec{\mu}_{\perp} - \xi \vec{\mu}_{||}), \quad (2.14)$$

where column-vectors $\vec{\mu}_{\perp}$ and $\vec{\mu}_{||}$ are calculated using Eq. (2.7) and Eq. (2.9) or Eq. (2.10), respectively.

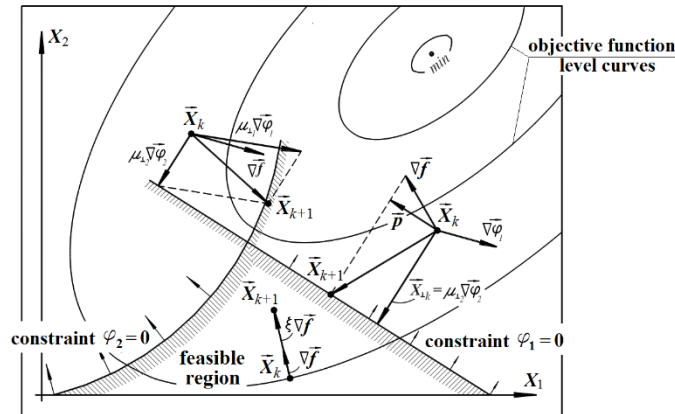


Figure 2.1. Step to the next point \vec{X}_{k+1} depending on location of the current approximation \vec{X}_k for two design variables X_1 and X_2 .

The linear-independent constraints of the system Eqs. (1.2) – (1.3) should be detected when constructing the matrix of the active constraints gradients $[\nabla \varphi]$ used by Eq. (2.7) and Eq. (2.9) or Eq. (2.10). Selection of the linear-independent constraints can be performed based on the equivalent transformations of the resolving equations of the gradient projection method using the non-degenerate transformation matrix \mathbf{H} , such that the sub-diagonal elements of the matrix $\mathbf{H}[\nabla \varphi]$ equal to zero. Besides,

$$\mathbf{H}^T \mathbf{H} = \mathbf{I}; \quad (2.15)$$

$$\mathbf{H} = \mathbf{H}_t \times \dots \times \mathbf{H}_i \times \dots \times \mathbf{H}_2 \times \mathbf{H}_1; \quad (2.16)$$

where \mathbf{I} is the unit matrix; t is the total number of the linear-independent gradients of the active constraints, \mathbf{H}_i is the transformation matrix, such that $\mathbf{H}_i^T \mathbf{H}_i = \mathbf{I}$, at the same time the sub-diagonal element are equal to zero in matrix $\mathbf{H}_i \times \mathbf{H}_{i-1} \times \dots \times \mathbf{H}_2 \times \mathbf{H}_1 \times [\nabla \varphi]$ for column's numbers $\overline{1, i}$. Described conditions are satisfied by the orthogonal matrix of the elementary mapping (Householder's transformation) [17, 18].

Let us present here the following algorithm to form set \mathbf{L} and to construct matrix $\mathbf{H}[\nabla \varphi]$.

1. $i=0$, $\mathbf{L} = \emptyset$ and $[\nabla \Phi]_0 = [\nabla \varphi]$ should be assumed, where $[\nabla \varphi]$ is the matrix that comprises from the column-gradients of all active constraints. All columns of matrix $[\nabla \Phi]_0$ should be marked as 'not used' (or linear-independent).

2. $i = i + 1$.

3. Among all 'not used' columns of matrix $[\nabla \Phi]_{i-1}$, whose correspond to the constraints-equalities Eq. (1.2), one j^{th} column with extreme value of the specified criterion should be selected (e.g., the following

criterion $\ell_j^2 = \sum_{k=i}^{N_X} g_{kj}^2$ can be considered as such criterion, where g_{kj} are the j^{th} column's components of matrix $[\nabla \Phi]_{i-1}$). At the same time, all k^{th} columns of matrix $[\nabla \Phi]_{i-1}$, for whose the following inequality

$\ell_k^2 \leq \varepsilon_1$ met, should be marked as 'used', here ε_1 is a small positive number. In case when no constraints-equalities exist or all constraints-equalities Eq. (1.2) are marked as 'used', the selection of j^{th} column should be performed among all 'not used' columns of matrix $[\nabla \Phi]_{i-1}$, whose correspond to the constraints-inequalities Eq. (1.3). If $\ell_j^2 \leq \varepsilon_1$, then generation of set \mathbf{L} and matrix $\mathbf{H}[\nabla \varphi]$ is finished.

$\mathbf{H}[\nabla \varphi] = [\nabla \varphi]_{i-1}$. In case of $\ell_j^2 \leq \varepsilon_1$ and $i=1$ (i. e. $\mathbf{L} = \emptyset$), there is a contradiction in the system of constraints Eqs. (1.2) – (1.3). In other case, moving to the next step performs.

4. k^{th} number of the constraint, that corresponds to the j^{th} column number, should be included into set \mathbf{L} , $\mathbf{L} \leftarrow \mathbf{L} + \{k\}$.

5. Calculate $[\nabla \Phi]_i = \mathbf{H}_i [\nabla \Phi]_{i-1}$. It is reasonable to execute the multiplication only for 'not used' columns. It should be noted, when using Householder's transformation matrix \mathbf{H}_i is not constructed evidently [18]. At the same time, matrix $[\nabla \Phi]_i$ can be constructed within the ranges of matrix $[\nabla \Phi]_{i-1}$ when no additional memory is needed.

6. If $i=1$, then $[\nabla \varphi]_i = \vec{q}_j$, where \vec{q}_j is j^{th} column-vector of matrix $[\nabla \Phi]_i$. When $i > 1$ $[\nabla \varphi]_i$ is constructed using extension of the matrix $[\nabla \varphi]_{i-1}$ by the column-vector \vec{q}_j . j^{th} column of matrix $[\nabla \Phi]_i$ is selected as 'used', then moving to the step 2 performs.

Using Householder's transformations described above triangular structure of the nonzero elements of matrix $\mathbf{H}[\nabla \varphi]$ is formed step-by-step. Besides, Eq. (2.7) and Eq. (2.9) can be rewritten as follow:

$$([\nabla \varphi]^T \mathbf{H}^T)(\mathbf{H}[\nabla \varphi])\vec{\mu}_{\perp} = -\mathbf{V}; \quad (2.17)$$

$$\mathbf{H}[\nabla \varphi]\vec{\mu}_{\parallel} \approx \mathbf{H}\nabla \vec{f}. \quad (2.18)$$

In order to calculate column-vectors $\vec{\mu}_\perp$ and $\vec{\mu}_\parallel$, it is required only to perform forward and backward substitutions in Eq. (2.17) and Eq. (2.18).

To accelerate the convergence of the minimization algorithm presented above, h^{th} columns should be excluded from matrix $\mathbf{H}[\nabla\varphi]$. These columns correspond to those constraints from Eq. (1.3), for which the following inequality satisfies:

$$\mu_{\perp h} - \xi \times \mu_{\parallel h} > 0. \quad (2.19)$$

Actually, if $\mu_{\perp h} - \xi_2 \mu_{\parallel h} > 0$, then the return onto the active constraints surface from the feasible region \mathfrak{S} is performed with simultaneous degradation of the objective function value (see Fig. 2.2, b). At the same time, in case of:

$$\mu_{\perp h} - \xi_1 \mu_{\parallel h} < 0, \quad (2.20)$$

both the improvement of the objective function value and the return from the inadmissible region onto the active constraints surface are performed (see Fig. 2.2, a).

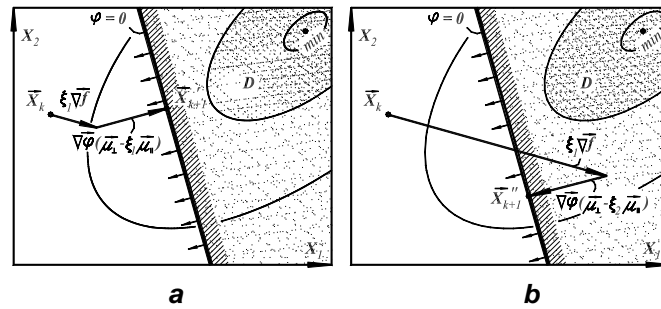


Figure 2.2. The selection of the constraints-inequalities:

$$\mathbf{a} - \mu_{\perp h} - \xi_1 \mu_{\parallel h} < 0; \quad \mathbf{b} - \mu_{\perp h} - \xi_2 \mu_{\parallel h} > 0.$$

When excluding h^{th} columns from matrix $\mathbf{H}[\nabla\varphi]$ corresponded to those constraints for whose Eq. (2.13) is satisfied, the matrix $(\mathbf{H}[\nabla\varphi])_{red}$ with a broken (non-triangular) structure of the non-zero elements is obtained. The set \mathbf{L} of the linear-independent active constraints numbers transforms into the set \mathbf{L}_{red} respectively. At the same time, the vector of the constraint's violations \mathbf{V} reduced into the vector \mathbf{V}_{red} accordingly.

In order to restore triangular structure of the matrix $(\mathbf{H}[\nabla\varphi])_{red}$ with zero sub-diagonal elements, Givens transformations (Givens rotations) [19, 18] can be used. Givens transformations for the matrix $(\mathbf{H}[\nabla\varphi])_{red}$ consist of construction such square matrix \mathbf{G}_{wz} , for which corresponded wz^{th} element of matrix $\mathbf{G}_{wz}(\mathbf{H}[\nabla\varphi])_{red}$ returns zero (see Fig. 2.3) [20]. Since $c^2 + s^2 = 1$ by definition, it follows:

$$(\mathbf{G}_{wz})^T \mathbf{G}_{wz} = \mathbf{I}. \quad (2.21)$$

An obvious method to calculate c and s for d^{th} non-zero sub-diagonal element and for a^{th} diagonal element is presented below:

$$c = \frac{a}{\sqrt{a^2 + d^2}}, \quad s = \frac{d}{\sqrt{a^2 + d^2}}; \quad (2.22)$$

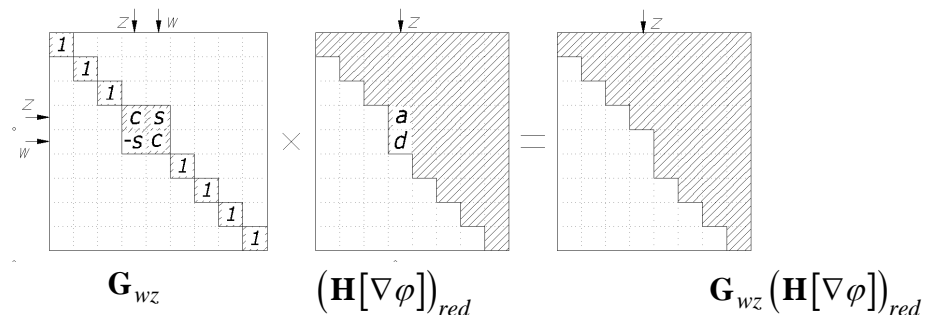


Figure 2.3. Scheme for Givens rotations (non-zero elements of the matrixes are hatched).

The Givens matrix \mathbf{G} can be calculated similarly to the matrix \mathbf{H} using the following equation:

$$\mathbf{G} = \mathbf{G}_\gamma \times \dots \times \mathbf{G}_i \times \dots \times \mathbf{G}_2 \times \mathbf{G}_1. \quad (2.23)$$

where γ is the number of the Givens transformations. So, Givens transformations should be executed several times (with different values z and w), while the matrix $\mathbf{G}_{wz}(\mathbf{H}[\nabla\varphi])_{red}$ has no all zero sub-diagonal elements (for example presented by Fig. 2.3, $\gamma = 5$).

Taking into account Givens transformations, Eq. (2.17) and Eq. (2.18) for column-vectors $(\vec{\mu}_\perp)_{red}$ and $(\vec{\mu}_\parallel)_{red}$ can be rewritten as:

$$([\nabla\varphi]^T \mathbf{H}^T)_{red} \mathbf{G}^T \mathbf{G} (\mathbf{H}[\nabla\varphi])_{red} (\vec{\mu}_\perp)_{red} = -\mathbf{V}_{red}; \quad (2.24)$$

$$\mathbf{G} (\mathbf{H}[\nabla\varphi])_{red} (\vec{\mu}_\parallel)_{red} \approx \mathbf{G} \mathbf{H} \nabla f; \quad (2.25)$$

and the main resolving equation of the gradient projection method Eq. (2.13) and Eq. (2.14) can be rewritten as presented below:

$$\Delta \vec{X}_k = (\mathbf{H}[\nabla\varphi])_{red} (\vec{\mu}_\perp)_{red} + \xi \left(\nabla f - (\mathbf{H}[\nabla\varphi])_{red} (\vec{\mu}_\parallel)_{red} \right), \quad (2.26)$$

or

$$\Delta \vec{X}_k = \xi \nabla f + (\mathbf{H}[\nabla\varphi])_{red} \left((\vec{\mu}_\perp)_{red} - \xi (\vec{\mu}_\parallel)_{red} \right). \quad (2.27)$$

The proposed improvement for the method of the objective function gradient projection onto the active constraints surface with simultaneous correction of the constraints violations consists of equivalent transformations of the resolving equations using Householder transformations. The transformations with matrix \mathbf{H} presented by Eq. (2.24) and Eq. (2.25) of the resolving equations of the gradient projection method Eq. (2.7) and Eq. (2.9) increase the numerical efficiency of the algorithm developed based on the gradient projection method described above.

Additionally, the proposed improvement for the gradient projection method includes equivalent transformations of the resolving equations using Givens rotations. The transformations with matrix \mathbf{G} presented by Eq. (2.24) and Eq. (2.25) ensure acceleration of the iterative searching process Eq. (2.1) in case when Eq. (2.19) takes into account due to decreasing the amount of calculations.

It should be noted that the lengths of the gradient vectors for the objective function Eq. (1.1), as well as for constraints Eqs. (1.2) – (1.3), remain as they were in scope of the proposed equivalent transformations ensuring the dependability of the optimization algorithm.

The determination the convergence criterion is the final question when using the iterative searching for the optimum point Eq. (2.1) described above. Considering the geometrical content of the gradient steepest descent method, we can assume that at the permissible point \vec{X}_k the component of the increment vector $\Delta \vec{X}_\parallel^k$ for the design variables should be vanish, $\Delta \vec{X}_\parallel^k \rightarrow 0$, in case of approximation to the optimum solution of the non-linear programming task presented by Eqs. (1.1) – (1.3). So, the following convergence criterion of the iterative procedure Eq. (2.1) can be assigned:

$$\|\Delta \vec{X}_\parallel^k\| = \sqrt{\sum_{i=1}^{N_X} (\Delta X_{\parallel,i}^k)^2} < \varepsilon_1, \quad (2.28)$$

where ε_1 is a small positive number.

Taking into consideration Eq. (2.28), let us formulate the following stop criteria in the iterative searching procedure of Eq. (2.1).

Stop criterion 1: when the objective function gradient in the current approximation \vec{X}_k is close to zero indicating on extreme character of the current approximation, as well as there are no violated constraints:

$$\begin{cases} \mathbf{\Sigma} = \emptyset, \\ -\varepsilon \geq \nabla f \geq +\varepsilon; \end{cases} \quad (2.29)$$

where Σ is the set of the violated constraints numbers, $\Sigma = \left\{ s \mid \left| \psi_s(\vec{X}_k) \right| > \varepsilon; \phi_s(\vec{X}_k) > \varepsilon \right\}$;

Stop criterion 2: when the projection of the objective function gradient in the current approximation \vec{X}_k onto the active constraints surface is close to zero (objective function gradient is perpendicular to the active constraints surface) indicating impossible further improvement of the objective function value, as well as there are no violated constraints:

$$\begin{cases} \Sigma = \emptyset; \\ -\varepsilon \geq \vec{p} \geq +\varepsilon; \end{cases} \quad (2.30)$$

Stop criterion 3: when in the current approximation \vec{X}_k of the iterative searching procedure Eq. (2.3) the total number of the active constraints t equals to the number of design variables N_X , as well as all active constraints are ε -active (both not violated constraints and those ones for whose inequality Eq. (2.13) met):

$$\begin{cases} \Sigma = \emptyset; \\ t = N_X; \\ \mu_{\perp f} - \xi \times \mu_{\parallel f} < 0, \forall f \in \mathbf{L}. \end{cases} \quad (2.31)$$

This stop criterion for the iteration process Eq. (2.1) corresponds to the case when the current approximation $\vec{X}_k = \left(X_t^k \right)^T, t = \overline{1, N_X}$, to the optimum solution is located at the intersection of the constraints (i.e., vertex). In this case, no correction of the constraints violations is needed and further improvement of the objective function value is not possible.

Stop criterion 4: when the objective function values within two consecutive iterations are the same with acceptable accuracy subject to the absence of the violated constraints:

$$\begin{cases} \Sigma = \emptyset; \\ f(\vec{X}_{k-1}) \approx f(\vec{X}_k). \end{cases} \quad (2.32)$$

3. Results and Discussion

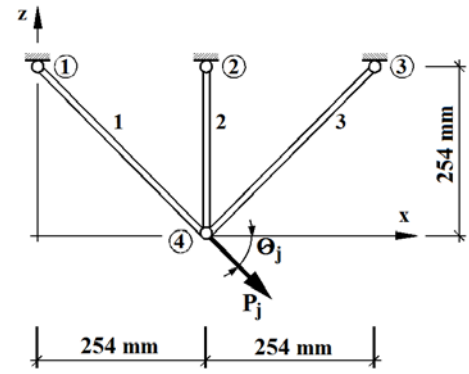
In order to estimate an efficiency of the new methods or algorithms, a comparison with alternative methods or algorithms presented by other authors using different optimization techniques should be performed. Criteria to implement such comparison are described, e.g. by Haug & Arora [15] and Crowder et al. [21]. Many of these criteria, such as robustness, amount of functions calculations, requirements to the computer memory, numbers of iterations etc. cannot be used due to lack of corresponded information in the technical literature. Therefore, an efficiency estimation of the method of objective function gradient projection onto the active constraints surface with simultaneous correction of the constraints violations presented above will be based on the comparison of the optimization results obtained using proposed improvement of the gradient projection method, as well as of the results presented by the literature and widely used for testing. The initial data and mathematical models of the parametric optimization problems considered below were assumed as the same as described in the literature.

3.1. Parametric optimization of a three-bar truss

Optimization of a three-bar truss (see Fig. 3.1) has been firstly solved by Schmit [22] using a non-linear programming method. Besides, the task has been also considered by Haug and Arora [15]. The parametric optimization problem is formulated as searching for optimum cross-sectional areas b_1 , b_2 and b_3 of the truss bars providing the least value of the truss weight subject to normal stresses and flexural stability constraints, as well as displacements and eigenvalue constraints. The load cases for the considered truss are presented in Table 3.1. Initial data for optimization of the truss are shown in Table 3.2.

Table 3.1. Load cases for considered truss.

Load case j	1	2	3
$\theta_j, ^\circ$	45	90	135
$P_j \times 10^3$ [pound-force]	40	30	20
P_j [kN]	177.9897	133.4922	88.9948


Figure 3.1. Three-bar truss.
Table 3.2. Initial data for optimization of the truss.

Unit weight of the truss material ρg	0.1 pound/inch ³ = 0.027154 N/cm ³
Modulus of elasticity E	10^7 pound/inch ² = 6.8971×10^6 N/cm ²
Allowable stresses value σ_1^a, σ_3^a for the 1 st and 3 rd truss members	5000 pound-force/inch ² = 3.4486 kN/cm ²
Allowable stresses value σ_2^a for the 2 nd truss member	2000 pound-force/inch ² = 1.3794 kN/cm ²
Non-dimensional factor β used to calculate second moment area of inertia for each truss member, $I_i = \beta b_i$	1.0
Ultimate vertical z^a and horizontal x^a displacements of the truss nodes	0.005 inch = 0.0127 cm
Lower limit value for eigenvalue	$\zeta_0 = 1.872 \cdot 10^8$

The objective function can be written as presented below:

$$\psi_0 = \rho g l (b_1 \sqrt{2} + b_2 + b_3 \sqrt{2}) \rightarrow \min; \quad (3.1)$$

where b_1 , b_2 and b_3 are cross-sectional areas of the truss bars; l is the truss height, $l = 25.4$ cm (see Fig. 3.1). Let us formulate strength constraints for each truss members for all load cases as follows:

$$\psi_{3(i-1)+j} = \frac{|N_i^j|}{b_i \sigma_i^a} - 1 \leq 0; \quad (3.2)$$

where N_i^j is the axial force for i^{th} truss member subjected to j^{th} load case, $i = \overline{1, 3}$, $j = \overline{1, 3}$. Besides, let include to the system of constraints the inequalities for the positive values of the design variables:

$$\psi_{9+i} = -b_i \leq 0; \quad (3.3)$$

Flexural buckling constraints for all truss members can be written using Hooke's law as presented below:

$$\psi_{12+3(i-1)+j} = -\frac{(x_4^j + z_4^j) l}{\pi^2 \beta b_i} - 1 \leq 0; \quad (3.4)$$

where x_4^j , z_4^j are linear displacements for node 4 of the truss subjected to j^{th} load case along the directions of Ox and Oz axes respectively. The constraints on the minimum values of the eigenvalues can be written analytically using calculation results of the eigenvalues stability problem for the considered truss:

$$\psi_{22} = \frac{2\sqrt{2} \rho l^2 \zeta_0 \left(\frac{b_1 + b_3}{b_2} \sqrt{2} + 1 \right)}{3E \left(\frac{b_1 + b_3}{b_2} + \sqrt{2} - \sqrt{\left(\frac{b_1 - b_3}{b_2} \right)^2 + 2} \right)} - 1 \leq 0. \quad (3.5)$$

Let also formulate displacements constraints for 4th truss node in the plane xOz :

$$\psi_{22+j} = -1 - \frac{x_4^j}{x^a} \leq 0; \quad (3.6)$$

$$\psi_{25+j} = \frac{x_4^j}{x^a} - 1 \leq 0; \quad (3.7)$$

$$\psi_{28+j} = -1 - \frac{z_4^j}{z^a} \leq 0; \quad (3.8)$$

$$\psi_{31+j} = \frac{z_4^j}{z^a} - 1 \leq 0. \quad (3.9)$$

Starting from start values of the design variables $\bar{b}^0 = (64.516, 32.258, 32.258)^T \text{ cm}^2$ with truss weight $G^0 = 116.602 \text{ N}$, an optimum solution $\bar{b}^* = (57.4878, 12.4482, 27.4299)^T \text{ cm}^2$ with the optimum weight $G^* = 91.383 \text{ N}$ has been obtained. The comparison of the optimization results for the considered three-bar truss obtained by Haug and Arora [15] and in this article is presented in Table 3.3. Good correlation of obtained optimization results with the results of the other authors confirms the validity of the optimum solutions calculated using the proposed improvement of the gradient projection method.

The step-by-step characteristics of the iterative searching for optimum design of the three-bar truss are presented in Table 3.4. Eleven iterations have been performed. The iterative searching process for the optimum point was stopped due to the following stop criterion: increment of the design variables within two consecutive iterations was less than 0.0001, whereas there were no violated constraints.

Table 3.3. Comparison of the optimization results for the three-bar truss.

Source	Start and optimum cross-section areas [cm ²] for truss member			Truss weight [N]
	1	2	3	
Start values by Haug and Arora [15]	64.516	32.258	32.258	116.602
Optimum values by Haug and Arora [15]	59.2257	13.9355	24.8387	91.588
Optimum values by this paper	57.4878	12.4482	27.4299	91.383

* truss member's numbers are indicated in Fig. 3.1

Table 3.4. Step-by-step characteristics of the iterative searching for optimum design of the three-bar truss.

Iteration number	Current values of the design variables [cm ²]			Objective function value [kN]	Numbers of the active constraints	Maximum violation of the constraints
	b_1	b_2	b_3			
0	64.5160	32.2580	32.2580	0.1166	—	—
1	44.5160	22.2580	22.2580	0.0805	15	0.35835
2	60.7847	12.2580	12.2580	0.0797	10, 15, 18, 22, 24, 33, 34	0.46276
3	40.7847	14.8577	22.2580	0.0717	15, 18, 22, 26	0.42237
4	55.5763	15.8613	21.5250	0.0861	15, 22	0.10076
5	57.3934	13.0115	26.3367	0.0906	15, 22	0.01189
6	57.5871	12.5536	27.2368	0.0914	15, 22	0.00027
7	57.4967	12.4569	27.4140	0.0914	15, 22	$9.67 \cdot 10^{-6}$
8	57.4885	12.4489	27.4288	0.0914	15, 22	$7.55 \cdot 10^{-8}$
9	57.4878	12.4483	27.4299	0.0914	15, 22	$1.43 \cdot 10^{-9}$
10	57.4878	12.4483	27.4299	0.0914	15, 22	$8.74 \cdot 10^{-11}$
11	57.4878	12.4483	27.4299	0.0914	15, 22	$6.55 \cdot 10^{-12}$

3.2. Optimization of a ten-bar cantilever truss

A parametric optimization problem of a ten-bar cantilever truss (see Fig. 3.2) is widely used in the literature [15, 23, 24, 25] in order to compare different methods for solving optimization problems. The

parametric optimization problem is formulated as follows: to find unknown cross-sectional areas for each truss member $\vec{b} = (b_i)^T$, $i = \overline{1,10}$, with weight minimization of the truss subjected to stresses constraints in all truss bars, node displacements constraints, as well as constraints on the minimal cross-section areas. A start value $b_0 = 1.0 \text{ inch}^2 = 6.4516 \text{ cm}^2$ was used as a start approximation for variable cross-sections areas for all bars of the considered truss.

The considered truss undergoes two load cases, as shown in Fig. 3.2 and presented in Table 3.5. Initial data for optimization of the truss are presented in Table 3.6.

Table 3.5. Load cases for ten-bar cantilever truss.

Load case number	Node number (Fig. 3.2)	Point load along axis Oz , $\times 10^3$ [pound-force]	Point load along axis Oz [kN]
1	2	-100.0	-444.82
	4	-100.0	-444.82
	1	50.0	222.41
2	2	-150.0	-667.23
	3	50.0	222.41
	4	-150.0	-667.23

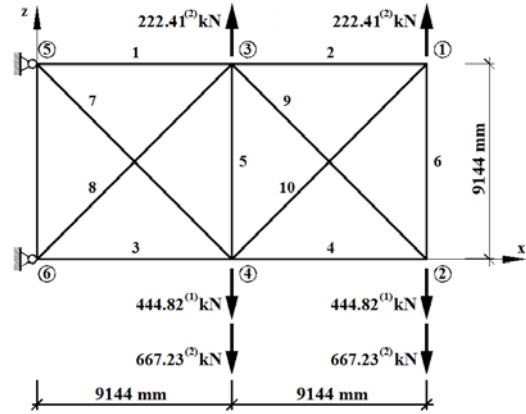


Figure 3.2. Ten-bar cantilever truss.

Table 3.6. Initial data for optimization of the ten-bar truss.

Unit weight of the truss material ρg	0.1 pound/inch ³ = 0.027143 N/cm ³
Modulus of elasticity E	10 ⁷ pound/inch ² = 6.8948 $\times 10^6$ N/cm ²
Non-dimensional factor β used to calculate second moment area of inertia for each truss member, $I_i = \beta b_i^2$	1.0
Lower limit value b^L for cross-sectional areas for all truss bars	0.10 inch ² = 0.64516 cm ²
Allowable stresses value for the all truss member σ^a	25000 pound-force/inch ² = 17.236 kN/cm ²
Ultimate vertical z^a displacements of the truss nodes	$\pm 2 \text{ inch} = \pm 5.08 \text{ cm}$

Variable cross-section areas for each truss member $\vec{b} = (b_i)^T$, $i = \overline{1,10}$, were considered as design variables. The objective function can be written as presented below:

$$\psi_0 = \rho g l \left(b_1 + b_2 + b_3 + b_4 + b_5 + b_6 + \sqrt{2} (b_7 + b_8 + b_9 + b_{10}) \right) \rightarrow \min; \quad (3.10)$$

where l is the truss height, $l = 914.4 \text{ cm}$ (see Fig. 3.2). Constraints on lower limit value for variable cross-sectional areas for all truss bars are written as follows:

$$\psi_i = 1 - \frac{b_i}{b_i^L} \leq 0. \quad (3.11)$$

Stresses constraints can be formulated as presented below:

$$\psi_{10+i} = \frac{|N_i|}{b_i \sigma_i^a} - 1 \leq 0. \quad (3.12)$$

where N_i is the axial force in the i^{th} truss member. Displacement constraints for the truss nodes are written as follows:

$$\psi_{20+j} = -1 - \frac{z_j}{z^a} \leq 0; \quad (3.13)$$

$$\psi_{24+j} = \frac{z_j}{z^a} - 1 \leq 0; \quad (3.14)$$

where x_j , z_j are linear displacements of j^{th} truss node, $j = \overline{1,4}$.

Starting from the initial truss design with start weight $G^0 = 1.867$ kN, an optimal solution with the optimum weight of $G^* = 22.514$ kN has been obtained for the truss subjected to the first load case. Additionally, starting from the initial truss design with the start weight of $G^0 = 1.867$ kN, an optimal solution with the optimum weight of $G^* = 20.806$ kN has been obtained for the truss subjected to the second load case. For both loaded cases, the iterative searching process for the optimum point was stopped due to the following stop criterion: the increment of the design variables within two consecutive iterations was less than 0.0001, as well as there were no violated constraints.

Table 3.7. Comparison of the optimization results for the ten-bar cantilever truss.

Bar number, i	Design variable	Start values for design variables [cm ²]	Optimal cross-section area for i^{th} truss member [cm ²]			
			for the first load case		for the second load case	
			Haug&Arora [15]	This paper	Haug&Arora [15]	This paper
1	b_1	6.4516	193.7480	196.7185	152.0255	151.8842
2	b_2	6.4516	0.6452	0.6452	0.6452	0.6452
3	b_3	6.4516	150.1545	149.6227	163.0771	163.1232
4	b_4	6.4516	98.6192	98.1744	92.5353	92.7578
5	b_5	6.4516	0.6452	0.6452	0.6452	0.6452
6	b_6	6.4516	3.5903	3.5536	12.7084	12.7079
7	b_7	6.4516	48.1825	48.0919	80.0063	79.8721
8	b_8	6.4516	136.7610	135.7063	82.9031	82.7963
9	b_9	6.4516	139.4707	138.8988	130.8707	131.1797
10	b_{10}	6.4516	0.6452	0.6452	0.6452	0.6452
Truss weight [kN]		1.867	22.523	22.511	20.808	20.807
Number of active constraints			4	5	4	6
Numbers of active constraints			2, 5, 10, 22	2, 5, 10, 15, 21	2, 10, 15, 22	2, 5, 10, 15, 16, 22
Modulus of the maximum violation in the constraints			$0.27 \cdot 10^{-4}$	$6.35 \cdot 10^{-7}$	$0.17 \cdot 10^{-3}$	$1.19 \cdot 10^{-7}$

Table 3.8. Comparison of the optimization results for the ten-bar cantilever truss.

Source of information	Optimum weight [kN]			
	Load case 1		Load case 2	
	Stresses constraints only	All constraints	Stresses constraints only	All constraints
This paper	7.087	22.511	7.404	20.807
Haug & Arora [15]	7.089	22.523	7.411	20.808
Schmit & Miura [25]	7.089	22.591	7.407	20.811
Rizzi [24]	7.089	22.590	7.407	20.811
Dobbs & Nelson [23]	7.217	22.605	–	22.514

Table 3.7 presents comparison of the optimization results for considered ten-bar truss obtained by Haug and Arora [15] and in this article. Table 3.8 shows a comparison of the optimization results for the ten-bar cantilever truss obtained using the proposed improved method of objective function gradient projection onto the active constraints surface with simultaneous correction of the constraints violations with optimization results presented by the literature [15, 23, 24, 25].

Good correlation of obtained optimization results with the results of the other authors confirms the validity of the optimum solutions calculated using proposed improvement of the gradient projection method. The efficiency of the proposed improvement of the gradient projection method has been also confirmed taking into account the number of iterations and absolute value of the maximum violation in the constraints. The deviations available in some presented results can be explained by using a numerical approach to the iterative searching with specified accuracy.

3.3. Optimization of a 24-bar transmission tower

A parametric optimization problem for a transmission tower (see Fig. 3.3) has been considered by Haug and Arora [15]. The transmission tower is subjected to 2 load cases, as shown in Table 3.9. The initial data for optimization of the tower are presented in Table 3.10. Taking into account the symmetry of the structural form, the vector of the design variables has been reduced to 7 variable cross-section areas for 25 structural members of the considered tower (see Table 3.11). The parametric optimization problem is formulated as searching for optimum cross-sectional areas $\bar{X} = (X_i)^T$, $i = \overline{1, 7}$, of the tower structural members, whose provide the least weight of the tower subjected to stresses constraints, node displacements constraints, as well as constraints on the minimal cross-section areas.

A start value $A_0 = 1.0 \text{ inch}^2 = 6.4516 \text{ cm}^2$ was used as a start approximation for the variable cross-sections areas for all members of the considered tower. The dimensions of the optimization problem comprised 7 design variables and 129 constraints.

Table 3.9. Load cases for the transmission tower.

Load case number	Node number (Fig. 3.3)	Point load along axis [kN]		
		$0x$	$0y$	$0z$
1	1	2.2241	—	—
	2	2.2241	—	—
	3	4.4482	-22.241	44.4822
	4	—	-22.241	44.4822
2	3	—	-22.241	88.9644
	4	—	-22.241	-88.9644

The positive direction of the point loads coincides with the positive direction of the corresponded axes

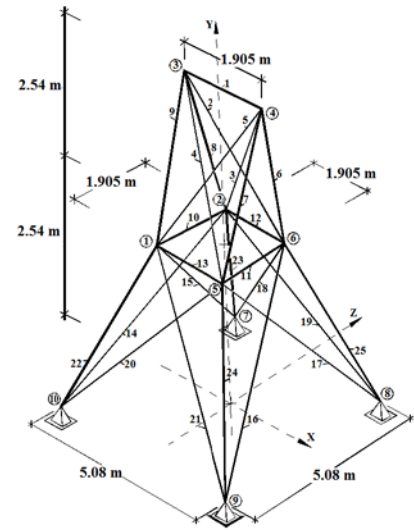


Figure 3.3. Design model of the transmission tower.

Table 3.10. Initial data for optimization of the transmission tower.

Unit weight of the tower material ρg	0.1 pound/inch ³ =0.027154 N/cm ³
Modulus of elasticity E	10^7 pound/inch ² = 6.8971×10^6 N/cm ²
Non-dimensional factor β used to calculate second moment area of inertia for each tower structural member $I_i = \beta b_i^2$	1.0
Lower limit value A^L for cross-sectional areas for all tower members	0.01 inch ² =0.0645 cm ²
Ultimate node displacements of the tower x^a, y^a, z^a	0.35 inch=0.889 cm
Allowable stresses value for the all tower member σ^a	± 40000 pound/inch ² = ± 27.5885 kN/cm ²

Table 3.11. Comparison of the optimization results for the transmission tower.

Design variable	Tower structural members*	Optimal cross-section areas for tower members [cm ²]	
		Haug and Arora [15]	This paper
A_1	1	0.0645	0.0655
A_2	2, 3, 4, 5	13.2103	13.1754
A_3	6, 7, 8, 9	19.3322	19.3654
A_4	10, 11, 12, 13	0.0645	0.0645
A_5	14, 15, 16, 17	4.4213	4.4056
A_6	18, 19, 20, 21	10.4626	10.4669
A_7	22, 23, 24, 25	17.2335	17.2343
Tower weight [kN]		2.4250	2.4245

*bar's numbers are indicated in Fig. 3.3

At the continuum optimum point there were 5 active constraints: constraints on lower limit value for

variable cross-sectional area for 10th, 11th, 12th and 13th tower members; 3rd and 4th node displacement constraint of the tower along axis Oz for both load cases. The iterative searching process for the optimum point was stopped due to the following stop criterion: increment of the design variables within two consecutive iterations was less than 1×10^{-6} , as well as there were no violated constraints.

The comparison of the optimization results for the transmission tower is presented by Table 3.11. Good correlation of obtained results with the results of the other authors confirms the validity of the optimum solutions calculated using the proposed improvement of the gradient projection method. Start values of the design variables have no influence on the optimum solutions for the considered non-linear problems, validating thus the accuracy of the obtained optimum solutions. The efficiency of the proposed improvement of the gradient projection method has been also confirmed taking into account the number of iterations and absolute value of the maximum violation in the constraints.

4. Conclusion

The paper considers parametric optimization problems for the bar structures formulated as nonlinear programming task. The method of the objective function gradient projection onto the active constraints surface with simultaneous correction of the constraints violations has been used to solve the parametric optimization problem.

Equivalent Householder transformations of the resolving equations of the method have been proposed. They increase numerical efficiency of the algorithm developed based on the considered method.

Equivalent transformations (Givens rotations) of the resolving equations of the method have been also proposed. They ensure acceleration of the iterative searching process in the specified cases described by the paper due to decreasing the amount of calculations.

Lengths of the gradient vectors for objective function, as well as for constraints remain as they were in scope of the proposed equivalent transformations ensuring the reliability of the optimization algorithm.

In order to estimate an efficiency of the proposed improvement of the gradient projection method, a comparison of the obtained optimization results with the results presented by the literature and widely used for testing has been performed. Good correlation of obtained results with the results of the other authors confirms the validity of the optimum solutions calculated using the proposed improvement of the gradient projection method. The efficiency of the proposed improvement of the gradient projection method has been also confirmed taking into account the number of iterations and absolute value of the maximum violation in the constraints.

5. Acknowledgement

Authors would like to thank the two anonymous reviewers for their critically reading the manuscript and suggesting substantial improvements.

References

1. Jelusic, P., Kravanja, S. Optimal design of timber-concrete composite floors based on the multi-parametric MINLP optimization. *Composite Structures*. 2017. Vol. 179. Pp. 285–293. DOI: 10.1016/j.compstruct.2017.07.062
2. Degertekin, S.O., Lamberti, L. Sizing, layout and topology design optimization of truss structures using the Jaya algorithm. *Applied soft computing*. 2018. Vol. 70. Pp. 903–928. DOI: 10.1016/j.asoc.2017.10.001
3. Kibkalo, A., Lebedeva, M., Volkov, M. Methods of parametric optimization of thin-walled structures and parameters which influence on it. *MATEC Web of Conferences*. 2016. No. 53. No. 01051. DOI: 10.1051/mateconf/20165301051
4. Alekseytsev, A.V. Evolutionary optimization of steel trusses with the nodal joints of rods. *Magazine of Civil Engineering*. 2013. No. 40(5). Pp. 28–37. (rus). DOI: 10.5862/MCE.40.3
5. Serpik, I.N., Alekseytsev, A.V., Balabin, P.Yu., Kurchenko, N.S. Flat rod systems: optimization with overall stability control. *Magazine of Civil Engineering*. 2017. No. 76(8). Pp. 181–192. DOI: 10.18720/MCE.76.16
6. Serpik, I.N., Alekseytsev, A.V. Optimization of frame structures with possibility of emergency actions. *Magazine of Civil Engineering*. 2013. No. 44(9). Pp. 23–29. (rus). DOI: 10.5862/MCE.44.3
7. Sergeev, O.A., Kiselev, V.G., Sergeeva, S.A. Overall instability and optimization of bar structures with random defects in case of constraints on faultless operation probability. *Magazine of Civil Engineering*. 2013. No. 44(9). Pp. 30–41. (rus). DOI: 10.5862/MCE.44.4
8. Permyakov, V.O., Yurchenko, V.V., Peleshko, I.D. An optimum structural computer-aided design using hybrid genetic algorithm. *Proceeding of the International Conference "Progress in Steel, Composite and Aluminium Structures"*. Taylor & Francis Group. London, 2006. Pp. 819–826.
9. Perelmuter, A.V., Yurchenko, V.V. Parametric optimization of steel shell towers of high-power wind turbines. *Procedia Engineering*. 2013. No. 57. Pp. 895–905. DOI: 10.1016/j.proeng.2013.04.114
10. Yurchenko, V.V., Peleshko, I.D., Beliaev, N.A. Parametric optimization of steel truss with hollow structural members based on update gradient method. *Proceedings of International Conference "Design, Fabrication and Economy of Metal Structures"*. Springer Berlin Heidelberg, 2013. Pp. 103–109. DOI: 10.1007/978-3-642-36691-8_16

11. Kuci, E., Henrotte, F., Duysinx, P., Geuzaine, C. Design sensitivity analysis for shape optimization based on the Lie derivative. Computer methods in applied mechanics and engineering. 2017. Vol. 317. Pp. 702–722. DOI: 10.1016/j.cma.2016.12.036
12. Sergeyev, O.A., Kiselev, V.G., Sergeyeva, S.A. Optimal design of 3D frame structures taking into account the stress and multiple natural frequency constraints. Magazine of Civil Engineering. 2016. No. 61(1). Pp. 74–81. DOI: 10.5862/MCE.61.7
13. Huebner, K.H., Dewhirst, D.L., Smith, D.E., Byrom, T.G. The finite element method for engineers. 4th ed. John Wiley & Sons, 2001. 744 p.
14. Peleshko, I.D., Yurchenko, V.V. An optimum structural computer-aided design using update gradient method. Proceedings of the 8th International Conference "Modern Building Materials, Structures and Techniques". Faculty of Civil Engineering, Vilnius Gediminas Technical University, 2004. Pp. 860–865.
15. Haug, E.J., Arora, J.S. Applied optimal design: mechanical and structural systems. John Wiley & Sons, 1979. 520 p.
16. Reklaitis, G.V., Ravindran, A., Ragsdell, K.M. Engineering optimization. Methods and applications. Wiley, 2006. 688 p.
17. Golub, G.H., Van Loan, C.F. Matrix Computations. 3rd ed. The Johns Hopkins University Press. Baltimore and London, 1996. 694 p.
18. Wilkinson, J.H., Reinsch, C. Handbook for Automatic Computation. Volume II: Linear Algebra. Heidelberg New York Springer-Verlag Berlin. 1971. 441 p. DOI: 10.1137/1014116
19. Bindel, D., Demmel, J., Kahan, W., Marques, O. On computing Givens rotations reliably and efficiently. ACM Transactions on Mathematical Software. 2002. Vol. 28. No. 2. Pp. 206–238.
20. Press, W.H., Teukolsky, S.A., Vetterling, W.T., Flannery, B. P. Givens method. Numerical recipes: the art of scientific computing. 3rd ed. New York: Cambridge University Press. 2007. 1235 p.
21. Crowder, N.P., Denbo, R.S., Mulvey, J.M. Reporting computational experiments in mathematical programming. Mathematical Programming. 1978. Vol. 15. Pp. 316–329.
22. Schmit, L.A., Goble, G.G., Fox, R.L., Lason, L., Moses, F., Razani, R. Structural synthesis: Summer course notes. Vol. 1. Case institute of technology. Cleveland, Ohio, 1965.
23. Dobbs, M.W., Nelson, R.B. Application of optimality criteria to automated structural design. AIAA Journal. 1976. Vol. 14(10). Pp. 1436–1443.
24. Rizzi, P. The optimization of structures with complex constraints via a general optimality criteria method. Ph. D. thesis. Stanford University. Palo Alto, CA, 1976.
25. Schmit, L.A., Miura, H.A. New structural analysis. Synthesis capability. ACCESS 1. AIAA Journal. 1976. Vol. 14(5). Pp. 661–671.

Contacts:

Vitalina Yurchenko, vitalinay@rambler.ru

Ivan Peleshko, ipeleshko@hotmail.com

© Yurchenko V.V., Peleshko I. D., 2020



ПОЛИТЕХ

Санкт-Петербургский
политехнический университет
Петра Великого

Инженерно-строительный институт
Центр дополнительных профессиональных программ

195251, г. Санкт-Петербург, Политехническая ул., 29,
тел/факс: 552-94-60, www.stroikursi.spbstu.ru,
stroikursi@mail.ru

**Приглашает специалистов проектных и строительных организаций,
не имеющих базового профильного высшего образования
на курсы профессиональной переподготовки (от 500 часов)
по направлению «Строительство» по программам:**

П-01 «Промышленное и гражданское строительство»

Программа включает учебные разделы:

- Основы строительного дела
- Инженерное оборудование зданий и сооружений
- Технология и контроль качества строительства
- Основы проектирования зданий и сооружений
- Автоматизация проектных работ с использованием AutoCAD
- Автоматизация сметного дела в строительстве
- Управление строительной организацией
- Управление инвестиционно-строительными проектами. Выполнение функций технического заказчика

П-02 «Экономика и управление в строительстве»

Программа включает учебные разделы:

- Основы строительного дела
- Инженерное оборудование зданий и сооружений
- Технология и контроль качества строительства
- Управление инвестиционно-строительными проектами. Выполнение функций технического заказчика и генерального подрядчика
- Управление строительной организацией
- Экономика и ценообразование в строительстве
- Управление строительной организацией
- Организация, управление и планирование в строительстве
- Автоматизация сметного дела в строительстве

П-03 «Инженерные системы зданий и сооружений»

Программа включает учебные разделы:

- Основы механики жидкости и газа
- Инженерное оборудование зданий и сооружений
- Проектирование, монтаж и эксплуатация систем вентиляции и кондиционирования
- Проектирование, монтаж и эксплуатация систем отопления и теплоснабжения
- Проектирование, монтаж и эксплуатация систем водоснабжения и водоотведения
- Автоматизация проектных работ с использованием AutoCAD
- Электроснабжение и электрооборудование объектов

П-04 «Проектирование и конструирование зданий и сооружений»

Программа включает учебные разделы:

- Основы сопротивления материалов и механики стержневых систем
- Проектирование и расчет оснований и фундаментов зданий и сооружений
- Проектирование и расчет железобетонных конструкций
- Проектирование и расчет металлических конструкций
- Проектирование зданий и сооружений с использованием AutoCAD
- Расчет строительных конструкций с использованием SCAD Office

П-05 «Контроль качества строительства»

Программа включает учебные разделы:

- Основы строительного дела
- Инженерное оборудование зданий и сооружений
- Технология и контроль качества строительства
- Проектирование и расчет железобетонных конструкций
- Проектирование и расчет металлических конструкций
- Обследование строительных конструкций зданий и сооружений
- Выполнение функций технического заказчика и генерального подрядчика

По окончании курса слушателю выдается диплом о профессиональной переподготовке
установленного образца, дающий право на ведение профессиональной деятельности

